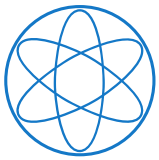


TUM School of Natural Sciences
TECHNISCHE UNIVERSITÄT MÜNCHEN

# Turbulence measurements at the ASDEX Upgrade tokamak for a comprehensive validation of the gyrokinetic turbulence code GENE

Klara Höfler

Vollständiger Abdruck der von der TUM School of Natural Sciences der Technischen Universität München zur Erlangung des akademischen Grades einer Doktorin der Naturwissenschaften genehmigten Dissertation.

| | |
|---|---|
| Vorsitzender: | Prof. Dr. Michael Knap |
| Prüfer der Dissertation: | 1. Prof. Dr. Ulrich Stroth |
| | 2. Prof. Dr. Peter Manz |

Die Dissertation wurde am 09.09.2022 bei der Technischen Universität München eingereicht und durch die TUM School of Natural Sciences am 18.10.2022 angenommen.

TUM School of Natural Sciences
TECHNISCHE UNIVERSITÄT MÜNCHEN

# Turbulence measurements at the ASDEX Upgrade tokamak for a comprehensive validation of the gyrokinetic turbulence code GENE

Author: Klara Höfler
Supervisor: Prof. Dr. Ulrich Stroth
Advisor: Dr. Tim Happel

Submission Date: September 9th, 2022

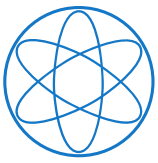


MAX-PLANCK-INSTITUT FÜR PLASMAPHYSIK

EUROfusion

# Abstract

Nuclear fusion has the potential to become a game changer in clean and safe electricity production. Magnetic confinement fusion plasmas need to exceed a threshold in the product of temperature, density and energy confinement time to ignite. Turbulence is the main driver of heat and particle transport, which reduce all three of these quantities, and thus deteriorate the performance of fusion plasmas.

To extrapolate our current turbulence models to reactor-type fusion plasmas we need turbulence codes, which are validated by experiments. Validation work has already been done for a single or a small number of turbulence observables, showing agreement, but also highlighting areas where disagreement helps to point to new physics discoveries. Individual observables were matched within the error bars of the physics inputs. When increasing the number of observables, this may, however, reveal "false positives" where a better match in signal A deteriorates the agreement with signal B. Hence, a comprehensive validation should involve as many observables as possible at the same time – a challenging goal for both experiment and theory.

The present thesis studies a comprehensive set of multi-field and scale-resolved turbulence data from two different plasma scenarios at the ASDEX Upgrade tokamak. All observables are measured in the same radial region in which the turbulence drive is changed by variation of the electron cyclotron resonance heating (ECRH) deposition position. This comparison of two slightly different turbulence regimes, which both have to be matched by the simulations, intends to further constrain code validation and thus improves the quality of this study. In order to maximize the number of observables, all turbulence quantities accessible with the current diagnostic hardware at ASDEX Upgrade are measured. Doppler reflectometers in both X-mode and O-mode polarization measure the electron density wavenumber spectrum and scale-resolved radial correlation length of electron density fluctuations. A correlation electron cyclotron emission (CECE) radiometer measures the relative fluctuation amplitude and radial correlation length of electron temperature fluctuations. When both diagnostics probe on the same line of sight and in perpendicular incidence, they measure the cross-phase between electron density and electron temperature fluctuations. Whereas the electron temperature fluctuation amplitude increases for increasing normalized electron temperature and density gradient, a surprising decrease of the density fluctuation amplitude is observed. Interestingly, the radial correlation length and the cross-phase, however, do not change from one scenario to the other.

In this study all of the above mentioned measurements are compared to nonlinear simulations done with the gyrokinetic code GENE. Synthetic diagnostic modeling is applied to account for

diagnostic effects on measurements. Doppler reflectometry measurements are modeled with the IPF-FD3D fullwave code, synthetic CECE modeling is supported using the ECE forward model for radiation transport, ECRad. Not only the absolute values of the measured quantities, but also the trends between the plasma scenarios are successfully reproduced by the code and the synthetic diagnostic modeling.

In addition to these extensive turbulence studies, the present thesis focuses on poloidally resolved measurements of the propagation velocity of density fluctuations perpendicular to the magnetic field. A profound understanding of this velocity directly serves the purpose of fundamental turbulence understanding, as shear flows are the main players to decorrelate turbulence. Observations at other plasma devices revealed deviations from the expected poloidal dependence of the perpendicular velocity. However, no such asymmetry is observed in ASDEX Upgrade. This finding is accompanied by a sensitivity study of uncertainties connected to the Doppler reflectometer data analysis. These uncertainties can explain potential poloidal asymmetries to some extent, but cannot resolve the source of asymmetries at magnitudes such as observed at other machines.

In summary, the validation efforts of this work significantly go beyond previous studies. They constitute a considerable step in the understanding of plasma turbulence and turbulent transport, which is crucial for successful prediction and realization of a novel fusion reactor.

# Zusammenfassung

Kernfusion hat das Potential die Energieerzeugung radikal in Richtung Nachhaltigkeit und $CO_2$-Neutralität zu verändern. Das Produkts aus Dichte, Temperatur und Energieeinschlusszeit muss bei magnetisch eingeschlossenen Fusionsplasmen einen Schwellenwert überschreiten, damit das Plasma zündet. Die Effizienz eines Fusionskraftwerkes wird dabei durch Transportverluste durch Turbulenz drastisch beschränkt.

Um das Verhalten der Turbulenz beim Design künftiger Reaktoren möglichst präzise vorhersagen zu können, müssen die verwendeten Turbulenzmodelle mit Hilfe von Experimenten überprüft werden. Zahlreiche vergangene und gegenwärtige Studien zur Validierung von Turbulenz-Codes ergaben für einzelne Messgrößen innerhalb der Unsicherheiten eine Übereinstimmung zwischen Modell und Experiment. Ebenso konnten durch die Feststellung etwaiger Unterschiede zwischen Theorie und Messung neue physikalische Erkenntnisse gewonnen werden. Durch die Erhöhung der Anzahl der zu vergleichenden Messgrößen wurden Fälle aufgedeckt, wo eine bessere Übereinstimmung von Größe A die Übereinstimmung von Größe B verschlechtert. Deshalb sollten sorgfältige Vergleichsstudien zwischen Modell und Experiment so viele Messgrößen wie möglich gleichzeitig berücksichtigen, was sowohl auf experimenteller als auch theoretischer Ebene herausfordernd ist.

In der vorliegenden Arbeit wird ein umfassender Satz an Messgrößen gewonnen, der sowohl Fluktuationen der Elektronendichte als auch der Elektronentemperatur beinhaltet, welche mitunter skalenaufgelöst verfügbar sind. Untersucht werden zwei Plasmaszenarien, die sich in der räumlichen Deposition der Elektronenzyklotronresonanzheizung unterscheiden. Der Messbereich befindet sich dabei an jenem radialen Ort, an welchem sich die beiden Szenarien am stärksten unterscheiden. Die Aussagekraft des zu validierenden Simulationscodes kann durch die Wahl zweier Plasmaszenarien weitreichender analysiert werden, als bei der Berücksichtigung nur eines Szenarios, da er auch den unterschiedlichen Turbulenzantrieb in beiden Szenarien gleichermaßen gut modellieren muss. Durch das vollständige Ausschöpfen aller experimentellen Messmöglichkeiten kann eine große Anzahl an Messgrößen gleichzeitig untersucht werden. Mehrere Doppler Reflektometer in X-Mode- als auch O-Mode-Polarisation messen Wellenzahlspektren der Elektronendichte und deren Korrelationslängen für verschiedene Turbulenzskalen. Ein Radiometer zur Korrelationsmessung der Elektronenzyklotronstrahlung erfasst die relative Fluktuationsamplitude der Elektronentemperatur, sowie die zugehörige Korrelationslänge. Der gleichzeitige Betrieb beider Diagnostiken entlang der selben Sichtlinie senkrecht zum einschließenden Magnetfeld ermöglicht zusätzlich die Messung der Kreuzphase zwischen Fluktuationen der Elektronendichte und Elektronentemperatur. Während die Fluktuationsamplitude der Elektronentemperatur mit zunehmendem normierten Elektronentemperaturgradienten ansteigt, fällt die Fluktuationsampli-

tude der Elektronendichte überraschend ab. Die Korrelationslängen und die Kreuzphase ändern sich hingegen kaum.

Diese Studie vergleicht alle oben genannten Messgrößen mit nichtlinearen Simulationen des gyrokinetischen Codes GENE. Für die optimale Vergleichbarkeit werden in bisher einmaligem Umfang synthetische Diagnostiken eingesetzt. Es zeigt sich, dass diese Methode unerlässlich ist, um etwaige Diagnostikeffekte miteinzubeziehen. Die Doppler Reflektometer-Messungen werden vom Vollwellencode IPF-FD3D modelliert, die Korrelationsmessungen der Elektronzyklotronstrahlung mit dem ECRad-Vorwärtsmodell für Strahlungstransport. Die gyrokinetischen Turbulenzsimulationen und die darauf angewandten synthetischen Diagnostikmodelle reproduzieren hierbei neben den Absolutwerten der Messgrößen auch die Trends zwischen den beiden Plasmaszenarien.

Neben diesen umfassenden Turbulenzstudien beschäftigt sich die vorliegende Arbeit auch mit poloidal aufgelösten Messungen der Senkrechtgeschwindigkeit von Dichtefluktuationen. Das tiefgreifende Verständnis dieser Geschwindigkeit geht direkt mit dem erfolgreichen Modellieren der Turbulenz einher, da Scherströmungen hauptverantwortlich für die Dekorrelation der Turbulenz sind. Im Gegensatz zu Studien an anderen Experimenten werden hier keine Asymmetrien beobachtet, was im Einklang mit theoretischen Überlegungen steht. Eine begleitende Sensitivitätsanalyse zum Einfluss der Unsicherheiten der Datenauswertung auf die Senkrechtgeschwindigkeit kann potentielle Asymmetrien teilweise erklären, jedoch keine Erklärung für Asymmetrien, von der Größe wie sie bei anderen Maschinen beobachtet werden, finden.

Zusammenfassend übersteigt die hier präsentierte Validierungsarbeit deutlich die Komplexität bisheriger Studien und trägt damit wesentlich zu einer verbesserten Extrapolierbarkeit der Turbulenz- und der turbulenten Transportphänomene hin zu einem Fusionsreaktor bei.

# Contents

# 1 Introduction

In present days the issue of climate change and global warming is omnipresent. Since the first years of the industrialization the average temperature on earth rose by 1°C from 1850 until now [1], which is attributed to anthropogenic greenhouse gas emission. $CO_2$ constitutes the largest fraction of greenhouse gases, followed by methane. Without major changes to our ways of living, the temperature rise is predicted to continue to an extent that it will cause one of the largest mass extinctions our planet has seen [2]. Currently the main sources of $CO_2$ emission in the European Union are energy production (24 % of total emission), transport (18 %) and industry (17 %) [3]. Energy production and transport both largely rely on the burning of fossil fuels. Next to severe greenhouse gas emission they additionally pollute the atmosphere with fine dust and also contaminate large areas of soil when the exploitation of the vanishing natural deposits requires controversial techniques, such as fracking [4].

Therefore, there is large scientific consensus that alternatives must be found, which enable environmentally friendly and sustainable energy production. On the one side there are renewable energy sources, such as solar cells, wind turbines and water power plants [5]. However, they bear the disadvantage to require a multiple of the continuous energy consumption to be stored for days without sun and wind. The technology for energy storage on these unprecedented large scales remains a topic of current research with no comprehensive solution. On the other side of greenhouse gas free energy production there are fission and fusion where energy is produced by splitting and fusing of atomic nuclei. Fission increasingly shifts out of focus due to its potentially disastrous accidents, which can radioactively contaminate wide regions for hundreds of thousands of years on the one hand and the unsolved issue of final storage of radioactive waste on the other hand. The intrinsically different design of fusion power plants prohibits these accidents, whereas in addition fusion reactions do not produce these large amounts of long-living radioactive waste [6].

Facing the urgent need for alternatives to nowadays' energy production, scientists carry out multi-pronged research on both power storage and base load power plant technology independent of external constraints such as the weather. This thesis focuses on the latter, nuclear fusion for energy production.

## 1.1 General introduction to nuclear fusion

Nuclear fusion is the process that powers stars. In the Sun, the most common fusion reaction is the proton-proton chain because hydrogen makes up for 74 % of its mass [7]. For applications on Earth the choice of nuclei to fuse is more flexible. The most attractive reaction is the fusion of a deuterium (D) nucleus with a tritium (T) nucleus to a helium nucleus (He) and a neutron (n),

$$ {}^{2}_{1}\mathrm{D} + {}^{3}_{1}\mathrm{T} \rightarrow {}^{4}_{2}\mathrm{He}\,(3.5\,\mathrm{MeV}) + {}^{0}_{1}\mathrm{n}\,(14.1\,\mathrm{MeV}) $$

because of its relatively large fusion cross-section and energy output [8]. In order to fuse two positively charged nuclei, they must be provided with a large amount of energy to overcome their Coulomb repulsion and experience the attracting force of the strong interaction. The Lawson criterion [9] formulates a threshold for the product of particle temperature $T$, density $n$ and energy confinement time $\tau_\mathrm{E}$ that must be exceeded for net energy production from fusion. Higher temperatures imply higher energies to overcome the Coulomb repulsion, whereas higher densities and confinement times increase the probability for fusion reactions. Note that $\tau_\mathrm{E} = W_\mathrm{plasma}/P_\mathrm{heat}$ with the plasma energy $W_\mathrm{plasma}$ and heating power $P_\mathrm{heat}$. For typical particle temperatures in a fusion reactor, such as 15 keV, the triple product of $T$, $n$ and $\tau_\mathrm{E}$ must exceed

$$ Tn\tau_\mathrm{E} > 3 \cdot 10^{21}\,\mathrm{keV\,s\,m^{-3}}. \tag{1.1} $$

For reasonable densities in the order of $n \approx 10^{20}\,\mathrm{m^{-3}}$ this implies energy confinement times on the order of seconds. At these temperatures, D, T and He are fully ionized and together with their electrons they form a plasma[1].

## 1.2 Magnetically confined plasma

In order to reach the conditions of Eq. 1.1, these hot charged atomic nuclei and electrons, the plasma, needs proper confinement. The solar plasma is confined by the gravitational force. For application on Earth there is inertial fusion on the one hand where the plasma is compressed on a very fast timescale, such as done in hydrogen bombs. The other approach, called magnetic confinement, uses strong magnetic fields to confine the charged particles. One of the benefits of this approach is the ability to operate in steady state and thus produce energy continuously. It takes advantage of the fact that charged particles are bound to magnetic field lines. In the force free case they can move freely along a field line, whereas their motion perpendicular to the field is constrained to a gyration around the field lines. The *gyrofrequency* or *cyclotron frequency* $\omega_c$ and the *Larmor radius* $\rho_\mathrm{L}$ of this gyration relate via

$$ \omega_\mathrm{c} = \frac{|q|B}{m}, \quad \rho_\mathrm{L} = \frac{v_{\perp,\mathrm{c}}}{\omega_\mathrm{c}} = \frac{mv_{\perp,\mathrm{c}}}{|q|B} = \frac{\sqrt{2mT}}{|q|B}. \tag{1.2} $$

[1] Formally if in addition criteria related to Debye shielding are met [10], which is the case for the plasmas in the context of this thesis.

$q$ and $m$ are the particle charge and mass, respectively, $B$ is the magnetic field strength. The last step of Eq. 1.2 assumes a thermal plasma in which the velocity of the gyration $v_{\perp,\mathrm{c}}$ is expressed in terms of the thermal energy[2].

In the case of external forces, the particles additionally experience drifts perpendicular to the magnetic field lines. The drift most relevant for this thesis is the $E \times B$ drift with velocity

$$\mathrm{v}_{E\times B} = \frac{\mathbf{E}\times\mathbf{B}}{B^2}, \tag{1.3}$$

caused by an electric field $\mathbf{E}$. Other potential sources for drifts such as spatially in-homogeneous magnetic fields, forces like gravity and temporally varying electric fields are in detail discussed in the literature [10]. Note that since the plasma consists of charged particles, electric fields can be shielded as long as they vary slower than the plasma frequency

$$\omega_\mathrm{p} = \sqrt{\frac{e^2 n_\mathrm{e}}{\epsilon_0 m_\mathrm{e}}}, \tag{1.4}$$

where the subscript $e$ refers to *electrons*. This fundamental plasma property also affects the propagation of electromagnetic waves in the plasma. Depending on the orientation between the wave's electric field and the confining magnetic field one speaks of different wave polarizations. Wave propagation can only take place above a critical *cutoff frequency* which depends on the polarization. Further details on the polarizations and their dispersion relations will be discussed in Sec. 4.1.

## 1.3 The tokamak

Following the EUROfusion Roadmap [11], the two most promising magnetic confinement configurations are the *tokamak* and the *stellarator*. This thesis focuses on the first one. Both have in common their toroidal shape and a strong toroidal magnetic field produced by external coils. However, due to the plasma drifts, a purely toroidal magnetic field is not sufficient for confinement. For successful confinement, the magnetic field needs an additional poloidal component. Figure 1.1(a) shows this magnetic field for the tokamak concept. The planar toroidal field coils produce the toroidal field. The transformer induces a toroidal plasma current, in red, which in turn produces a poloidal magnetic field. The black lines illustrate the superposition of toroidal and poloidal field: a helically twisted magnetic field. Additional vertical field coils further stabilize the configuration. The duration of plasma operation in a tokamak is limited by the time the transformer can maintain the current in the plasma. For steady state power production, research is ongoing to operate the tokamak non-inductively [12, 13]. In a stellarator the helically twisted magnetic field stems from external coils only and thus allows steady state operation without a plasma current. Historically the tokamak concept has been pursued more intensely, since it

[2] In plasma physics the temperature is usually expressed in units of energy.

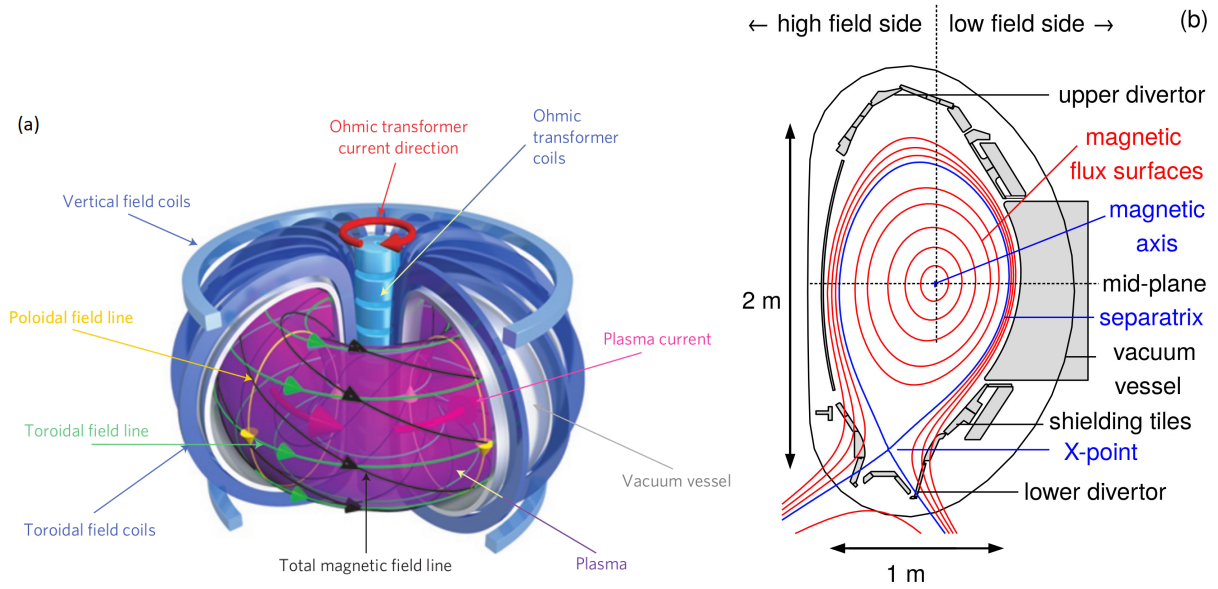


**Figure 1.1:** Schematics of the tokamak principle in (a) (from [6]): the helically twisted magnetic field consists of a toroidal component produced by external coils and a poloidal component as the result of a large toroidal plasma current. This current is induced by a transformer. Poloidal cross-section of the ASDEX Upgrade tokamak in (b): vessel structure in black and magnetic flux surfaces in red. For details refer to the text.

is easier to build and first results were very encouraging. Therefore, stellarators are about one generation behind.

Figure 1.1(b) depicts a poloidal cross-section of the ASDEX Upgrade tokamak. The vacuum vessel is shown in black and the tiles for heat protection in grey. The red lines indicate the *magnetic flux surfaces*, which are regions of constant poloidal magnetic flux $\Psi$

$$\Psi = \int \mathrm{d}\mathbf{A}_{\mathrm{tor}} \cdot \mathbf{B}_{\mathrm{pol}}. \tag{1.5}$$

$\mathbf{A}_{\mathrm{tor}}$ is the toroidal plane and $\mathbf{B}_{\mathrm{pol}}$ the poloidal magnetic field. A magnetic field line always stays on the same magnetic flux surface. Since transport along the magnetic field lines is very fast compared to perpendicular to them, pressure and electric potential can be assumed constant on the magnetic flux surfaces. The separatrix (blue line) separates the region of closed nested magnetic flux surfaces, the *confined region*, from the region where the magnetic field lines cross the wall. The most common spatial coordinate for experimental tokamak research is the poloidal magnetic flux coordinate

$$\rho_{\mathrm{pol}}(\mathbf{r}) = \sqrt{\frac{\Psi(\mathbf{r}) - \Psi_{\mathrm{axis}}}{\Psi_{\mathrm{sep}} - \Psi_{\mathrm{axis}}}}, \tag{1.6}$$

with $\Psi_{\mathrm{axis}}$ and $\Psi_{\mathrm{sep}}$ the magnetic flux on the magnetic axis and separatrix, respectively. The value of $\rho_{\mathrm{pol}}$ is 0 on the magnetic axis and 1 at the separatrix. The region where $\rho_{\mathrm{pol}} > 1$ is termed *scrape off layer*. Here the magnetic field lines hit the *divertor*, transporting the particles along the field lines directly to the target, where cold plasma particles and impurities can be pumped out. Depending on whether the upper or lower divertor is closer to the X-point of the

separatrix, the magnetic geometry is called *upper single null (USN)* or *lower single null (LSN)*. The magnetic equilibrium depicted in Fig. 1.1(b) is a LSN type. When referring to certain regions in the plasma it is useful to distinguish between the *low field side (LFS)* and the *high field side (HFS)* and to define the *midplane* as the horizontal plane that goes through the magnetic axis.

The experiments performed in this thesis are conducted at the *ASDEX Upgrade (AUG) tokamak*, a medium sized tokamak located in Garching, Germany. It started physics operation in 1991 as successor of the ASDEX tokamak. The particularity of the ASDEX-line is the divertor, a groundbreaking idea to spatially separate the contact zone between plasma and wall from the confined plasma. This separation maximizes the draining efficiency of impurities and thus produces cleaner plasmas. The use of a divertor facilitates the transition into a high confinement mode, the *H-mode*, with increased plasma temperature, density and energy confinement time compared to the low confinement mode, the *L-mode* [14]. Typical parameters of interest of a tokamak are the major radius, $R$, the distance between the transformer and the magnetic axis (AUG: $R = 1.65$ m) and the minor radius, $r$, the distance between the magnetic axis and the separatrix (AUG: $r \approx 0.5$ m). The standard magnetic field strength at AUG is 2.5 T on the magnetic axis (maximum 3.4 T), with a standard plasma current of 0.8 MA (maximum 1.2 MA) [15].

## 1.4 Transport and turbulence

On the way towards a burning plasma scientists need to develop scenarios and technology to increase all quantities of the triple product in Eq. 1.1. This implies a reduction of energy transport from the core plasma across the separatrix into the scrape off layer. On a macroscopic level the local heat transport depends on the local temperature gradient $\nabla T$, the local particle density and other local quantities summarized in the heat transport coefficient $\chi$. The local particle transport $\Gamma$ is a function of the density gradient $\nabla n$ and the particle transport coefficient $D$.

$$\mathbf{q} = -\chi n \nabla T, \ \mathbf{\Gamma} = -D \nabla n \tag{1.7}$$

On the microscopic level it is turbulence that predominantly drives transport [16, 17]. There is a zoo of various different micro-instabilities driving fluctuations in plasma density, temperature, magnetic field, electrostatic potential, etc. The characteristics of the particular turbulence regime enter into Eq. 1.7 via the transport coefficients. A more detailed description of the most important micro-instabilities that lead to turbulence will be given in Sec. 2.3.

## 1.5 Validation of turbulence simulations

In order to predict and optimize the performance of future fusion power plants, scientists need reliable codes that correctly model the plasma behavior. As described above, turbulence is

the main driver of heat and particle transport and directly determines the energy confiment. There are plenty of different theoretical approaches to model turbulence. They range from computationally expensive and very comprehensive gyrokinetic codes, such as GENE [18] and GYRO [19], to more reduced but computationally easier manageable codes, such as the gyrofluid codes TGLF [20, 21] and GEMR [22, 23]. They all have in common their need of verification and validation [24]. Verification denotes the comparison of simulation results from different codes with similar input. Validation refers to the process of benchmarking the simulation results of a code against experimental measurements. This thesis focuses on the latter one, aiming to validate one of the leading codes, GENE, which itself has been verified against other codes [25–28].

Most validation efforts follow the same strategy, which is discussed in detail in Refs. [24, 29] and a tutorial on validation [30] and shall be outlined here. All investigations build on dedicated experiments, which enable both unambiguous turbulence measurements and good knowledge of background plasma parameters, such as ion and electron temperature and electron density, the *kinetic profiles*. These plasma parameters serve as input for simulations. The input is varied within experimental uncertainties to obtain the best match between the simulation results and the experimental heat fluxes and turbulence measurements. Some validation studies, such as comparisons between measurements at the DIII-D tokamak and simulations from the GYRO code [31], in addition run pre-experiment simulations to accompany the design of the experiment. This for instance allows to focus on particular turbulence characteristics, such as the dominance of a particular micro-instability. Still, experimental studies to isolate a particular effect, which in simulation shows interesting features, are difficult. Therefore, this thesis does not run pre-experiment simulations. It rather relies on experimentally accessible external control parameters to produce similar but not identical plasma scenarios: the radial location of the heating power deposition. Section 6.1 will discuss the details of the design of two scenarios that differ in the underlying mixture of micro-instabilities. The implementation of more than one scenario aims to further constrain the simulation results, since differences in experiment must translate into analogous differences in simulations.

An additional possibility to constrain and thus improve validation efforts is to increase the number of observables, which are compared between experiment and simulation [24, 32]. For a code it is easier to reproduce the experimental observation of only one turbulence quantity varying the kinetic input parameters, than simultaneously matching several parameters. An increasing number of turbulence quantities may reveal "false positives" where a better match in signal A deteriorates the agreement with signal B. It is in addition advantageous to do multi-field comparisons [30, 32]. In addition, a diligent code validation takes into account the diagnostics' measurement principles when comparing experiment and simulation. This *synthetic diagnostic modeling* mimics a range of effects, such as the intrinsic spatial or spectral filtering of the measurement diagnostic [33], its possibly nonlinear diagnostic response etc. and thus has been shown to be an indispensable tool for code validation for both electron density fluctuation measurements [34, 35] and additionally electron temperature fluctuation measurements [36].

The study in the context of this thesis exploits all measurement diagnostics available for the radial region of interest to capture the maximum number of turbulence observables. To my knowledge the amount of different turbulence parameters used here for validation is unprecedented so far. Details on the experiments and measured turbulence characteristics will follow in Chap. 6. The comparison to GENE including state of the art synthetic diagnostic modeling is described in Chap. 7.

## 1.6 Scope of this thesis

Although single fusion reactions commonly occur in magnetic confinement fusion experiments, fusion power plants so far only exist on paper. In order to reliably predict the performance of fusion reactors, the processes found in existing machines must be extrapolated to larger scales. For prediction one needs verified and validated simulation codes that are benchmarked against other models and – most important – against experiment. In the past there have been numerous validation efforts where a single or a small number of turbulence parameters were compared between experiment and simulation. However, the significance of such studies increases with the number of turbulence parameters compared. Hence this thesis focuses on experimental measurements of a large variety of turbulence quantities and compares them to the comprehensive state of the art turbulence code GENE. First, Chap. 2 gives a basic introduction into the most important concepts of turbulence on both physics and analysis side. Chapter 3 follows with a discussion of the experimental setup, different methods of plasma heating and the measurement principles of the diagnostics that are used in this thesis. The most important diagnostic for these studies, Doppler reflectometry, is introduced in detail in Chap. 4. Chapter 5 deals with one particular measurement quantity of Doppler reflectometry: the velocity of electron density fluctuations perpendicular to the confining magnetic field. A comprehensive study of a large data set of different turbulence quantities in experiment follows in Chap. 6. These experimental findings are compared to simulations in Chap. 7. Finally the thesis concludes with a summary and outlook in Chap. 8.

# 2 Turbulent transport in theory, experiment and simulation

Turbulence denotes a chaotic motion of fluids or gases and involves a large variety of different structure sizes. This chapter first touches on a mathematical description of turbulence and the interaction between different scales via cascades. It then illuminates the origin of plasma turbulence, micro-instabilities that lead to fluctuations, and relates plasma flows and turbulence. Then it discusses characteristic parameters of turbulence, which will be later on measured in experiment and compared to simulation results. An introduction into the mathematical tool kit that aims to characterize turbulence behavior is given next. This chapter concludes with the introduction of a simulation code for plasma turbulence.

## 2.1 Mathematical description of turbulence

Despite its stochastic character, turbulence can be approached by analytic mathematical models. This section follows the argumentation in Refs. [10, 37] to introduce basic concepts of turbulence description. The flow velocity $\mathbf{v}$ of a neutral incompressible fluid is described by the *Navier-Stokes equation*,

$$\rho_\mathrm{m}\left(\frac{\partial}{\partial t}+\mathbf{v}\cdot\nabla\right)\mathbf{v}=-\nabla p+\rho_\mathrm{m}\mathbf{g}+\eta\Delta\mathbf{v}. \tag{2.1}$$

The left hand side denotes the inertia: the mass density $\rho_\mathrm{m}$ and its acceleration in the co-moving frame. The terms on the right hand side correspond to the force density of a pressure $p$, the gravitational force density including the gravitational constant $\mathbf{g}$ and the friction force density from a viscosity $\eta$. The nonlinearity of the second term on the left side drives turbulence. The viscosity term on the right hand side dissipates turbulence. Reformulating Eq. 2.1 allows to characterize turbulence by a single scalar, the *Reynolds number*

$$Re=\frac{LU}{\eta/\rho_\mathrm{m}} \tag{2.2}$$

with the characteristic size $L$ and velocity $U$ of the flow. The numerator corresponds to the driving nonlinear term and the denominator to the dissipating viscosity term. Thus, $Re$ is a measure whether turbulence is expected and at which strength: flows with $Re \ll 1$ are *laminar* and flows with $Re \gg 1$ *turbulent*.

The nonlinear velocity term in the Navier-Stokes equation, $(\mathbf{v} \cdot \nabla)\mathbf{v}$, makes it complicated to analytically solve it. Thus, mathematical models of neutral fluid turbulence often need to apply prior approximations to simplify the problem and equations. Still, solutions are mostly attained using vast numerical approaches and computational power. In plasma turbulence, however, the Coulomb forces between charged particles and Lorentz forces due to currents drastically increase the degree of difficulty. The complex geometry of magnetically confined plasmas further challenges the theoretical description.

One concept to model magnetic-confinement-plasma turbulence is to approach the problem by using kinetic theory. It treats the plasma as a many-particle system and calculates the spatio-temporal evolution of a particle distribution function $f = f(\mathbf{r}, \mathbf{v}) = f(x, y, z, v_x, v_y, v_z)$ via the *Vlasov equation*

$$\frac{\partial}{\partial t} f(\mathbf{r}, \mathbf{v}) + \mathbf{v} \cdot \nabla f(\mathbf{r}, \mathbf{v}) + q/m(\mathbf{E} + \mathbf{v} \times \mathbf{B}) \cdot \nabla_{\mathrm{v}} f(\mathbf{r}, \mathbf{v}) = 0, \tag{2.3}$$

where $\nabla_{\mathrm{v}}$ is the derivative in velocity space. This alternative plasma description using kinetic theory bears the advantage to enable a straight forward reduction of dimensions in phase space and save computation power in simulations. The commonly applied *gyrokinetic approach* simplifies the gyration of charged particles around the magnetic field lines: the gyromotion of charged particles is approximated by a charged ring of radius $\rho_L$ traveling along the field lines. This approximation neglects one velocity component and reduces the number of phase space dimensions to five. The turbulence simulations presented in this thesis build on this gyrokinetic approach. They use the GENE code [18], which will be introduced in Sec. 2.8.

## 2.2 Turbulence cascade

The energy distribution of different *turbulent scales* or *eddy sizes* in three-dimensional isotropic turbulence results from the conservation of energy. The Kolmogorov model [38] describes an injection scale, where energy is injected into the system, and a dissipation scale, located at smaller scales, where the energy is dissipated. Both scales are connected via an energy transfer range, also called inertial range, from large to small scales. The energy within this energy cascade, $E$, scales with the the inverse scale size, $k$, as $E \propto k^{-5/3}$. In the inertial range energy is neither injected nor dissipated.

Turbulence in magnetically confined fusion plasmas, however, is not isotropic in all three dimensions: transport along the magnetic field lines is much faster than perpendicular to them, causing the turbulent structures to elongate along the magnetic field lines. The turbulent dynamics thus happen mostly in the plane perpendicular to the magnetic field and are approximately two-dimensional. In two dimensions not only the energy, but also the enstrophy $\Omega = \nabla \times \mathbf{v}$ is conserved. A direct consequence is that the energy cascade is directed from the injection scale to larger scales, thus in the opposite direction than in three dimensions. This inverse energy cascade again exhibits $E \propto k^{-5/3}$. Only a small fraction of energy is transferred to smaller scales via the

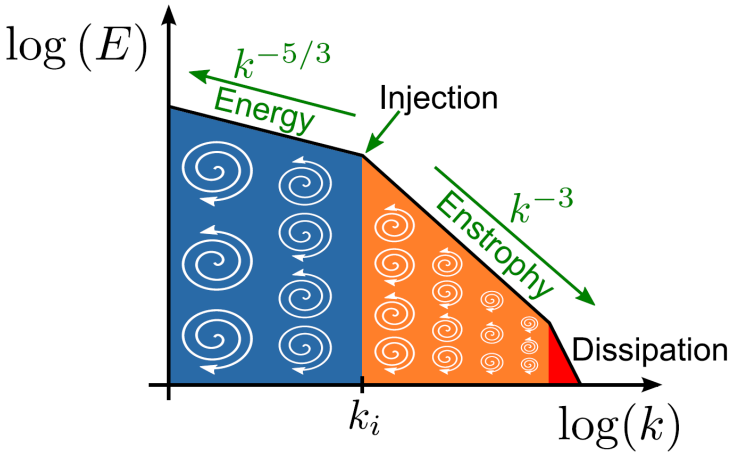


**Figure 2.1:** Fluctuation energy distribution for different turbulence wavenumbers: energy is injected into the system at the injection scale $k_\mathrm{i}$, the fluctuation amplitude decreases with decreasing structure size. From [40].

enstrophy cascade, which scales with $E \propto k^{-3}$. A description of this *dual cascade* goes back to Kraichnan [39]. Figure 2.1 visualizes the corresponding two-dimensional wavenumber spectrum: a localized energy injection scale, $k_\mathrm{i}$, separates the energy cascade at large structures from the enstrophy cascades at smaller structures. The interaction between the turbulence and spatial fluid boundaries prohibits an accumulation of energy at the largest structures. Even though less pronounced than in three dimensions, at very small structures energy is dissipated.

In the model mentioned above the injection and dissipation of energy takes place very localized in $k$-space. However, in a plasma, energy is injected at multiple different scales by a variety of micro-instabilities (c.f. Sec. 2.3) that co-exist. In addition, there is a broad range of scales where turbulence interacts with for instance low frequency flow oscillations, such as *zonal flows* [41] and *geodesic acoustic modes* (GAMs) [42]. The determination of the superposition of the underlying micro-instability or the rate of energy transfer to zonal flows and GAMs sensitively depends on the background plasma parameters and usually needs computational modeling.

## 2.3 Linear micro-instabilities

The following introduces the three most important micro-instabilities, which drive turbulence for the studies in this thesis: the *ion temperature gradient mode (ITG)*, the *electron temperature gradient mode (ETG)* and the *trapped electron mode (TEM)*. The underlying mechanisms of the growth of ITG, ETG and TEM are the *interchange instability* (ITG, ETG, TEM) and the *drift wave* (TEM). A complete list and discussion of the different types of instabilities can be found in the literature, such as [10, 37].

Interchange instabilities are in general driven by pressure gradients, in the case of ITG and ETG by the ion and electron temperature gradient, respectively [43–46]. The system is unstable where the temperature gradient is anti-parallel to the radius of curvature of the magnetic field. This

| Instability | scale size | driven by | damped by | propagation direction |
|---|---|---|---|---|
| ITG | $k_\perp \rho_\mathrm{s} \approx 1$ | $L_{T_\mathrm{i}}$ | $L_\mathrm{n}$ | ion diamagnetic |
| ETG | $k_\perp \rho_\mathrm{s} > 1$ | $L_{T_\mathrm{e}}$ | $L_\mathrm{n}$ | electron diamagnetic |
| TEM | $k_\perp \rho_\mathrm{s} \approx 1$ | $L_{T_\mathrm{e}}$,$L_\mathrm{n}$ | - | electron diamagnetic |

**Table 2.1:** Characteristic scale sizes, driving and damping terms and the propagation direction of the ITG, ETG and TEM instabilities.

is the case on the low field side of a tokamak. Thus, turbulence is most pronounced on the low field side and gradually decreases when going towards the high field side, which is stable. This poloidal dependence of the turbulence is termed ballooning character.

The TEM instability is caused by magnetically trapped particles, which cannot move freely along a magnetic field line. It exhibits both characteristics of a drift wave and an interchange instability [37, 47, 48]. As the trapped particles mainly occur on the low field side, the TEM is ballooned as well.

The micro-instabilities differ in the characteristic scale size, the driving and damping terms, as well as the direction of propagation. Turbulence studies of magnetically confined plasmas usually consider the characteristic scale size in perpendicular direction to the magnetic field and to the normal of the flux surface, $k_\perp$, since this is well accessible in experiment. This scale size is often normalized to the hybrid Larmor radius $\rho_\mathrm{s}$ with

$$\rho_\mathrm{s} = \frac{\sqrt{T_\mathrm{e} m_\mathrm{i}}}{eB}. \tag{2.4}$$

$T_\mathrm{e}$ is the local electron temperature, $m_\mathrm{i}$ the mass of the ions, $e$ the elementary charge and $B$ the local magnetic field. The turbulence driving and possible damping terms are expressed using *normalized gradients*

$$\left| \frac{R \nabla X}{X} \right| = \frac{R}{L_X} \tag{2.5}$$

with $X = T_\mathrm{i}, T_\mathrm{e}, n_\mathrm{e}$ and the machine major radius $R$. $L_X$ is termed the gradient length of $X$. The direction of the propagation velocity of turbulence is referred to the diamagnetic drift direction. The latter denotes the direction of the diamagnetic drift velocity $\mathbf{v}_\mathrm{dia}$

$$\mathbf{v}_\mathrm{dia} = -\frac{\nabla p \times \mathbf{B}}{qnB^2}. \tag{2.6}$$

The diamagnetic drift direction has different signs for ions ($q > 0$) and electrons ($q < 0$). Typical scales, driving and damping terms and the propagation directions of ITG, ETG and TEM are listed in Tab. 2.1. Similar features for other instabilities can be found in Ref. [49].

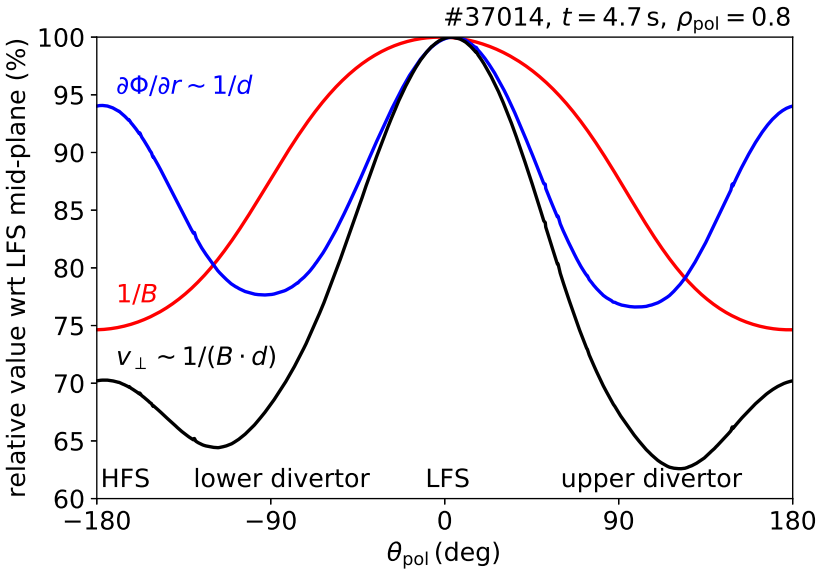


**Figure 2.2:** Intrinsic poloidal variation of the $E \times B$ drift velocity in black. Its components are the inverse distance between flux surfaces (blue) and the inverse magnetic field (red), respectively.

## 2.4 Plasma flow perpendicular to the magnetic field and turbulence decorrelation

Magnetically confined plasmas are subject to strong flows in different directions. To some extent the toroidal rotation velocity $v_{\mathrm{tor}}$ results from the Ohmic plasma current, c.f. Sec. 1.3. Other sources for rotation are tangentially injected neutral beam injection (c.f. Sec. 3.1) or intrinsic plasma effects, such as plasma drifts. Note that all these other sources can also contribute to the poloidal rotation velocity $v_{\mathrm{pol}}$. Experimental turbulence studies, however, often use a coordinate system that does not distinguish between toroidal and poloidal direction. They rather define a *direction parallel to the magnetic field*, and two directions perpendicular to it; the *radial direction* that is perpendicular to the flux surface and the *perpendicular direction* or *binormal direction* that is perpendicular to the normal vector of the magnetic flux surface. The diagnostic principle in the context of this thesis is mainly sensitive to the flow velocity in perpendicular direction, $v_\perp$ with

$$v_\perp = v_{E\times B} + v_{\mathrm{ph}}. \tag{2.7}$$

$v_{E\times B}$ is the drift velocity due to the radial electric field $E_{\mathrm{r}}$ (c.f. Eq. 1.3) and $v_{\mathrm{ph}}$ the intrinsic turbulence phase velocity, which is a result of the underlying mix of micro-instabilities [50]. Later in this thesis, the poloidal variation of $v_{E\times B}$ will be of interest. Therefore, the radial electric field is expressed as the local gradient of the electrostatic potential, $\Phi$. Plugging $E = \partial\Phi/\partial r$ into Eq. 1.3 yields

$$v_{E\times B} = -\frac{1}{B}\frac{\partial\Phi}{\partial r}. \tag{2.8}$$

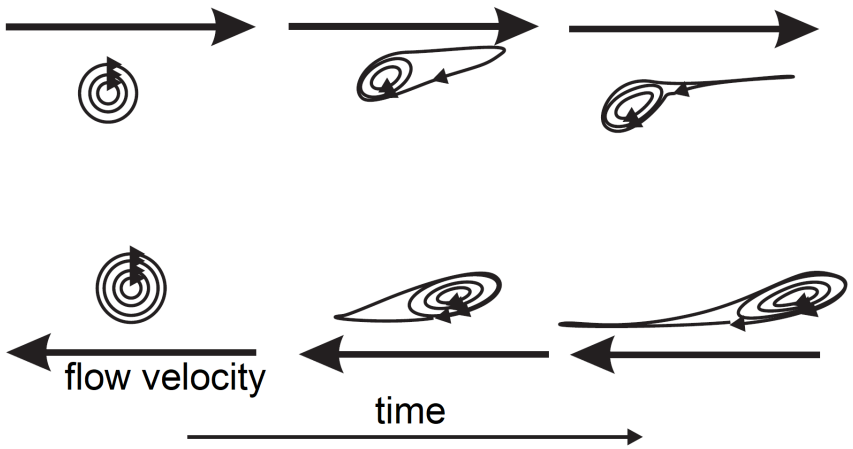


**Figure 2.3:** Schematics of the generation of a zonal flow by the vortex thinninc mechanism. Modified from [54].

Figure 2.2 depicts the poloidal variation of both $1/B$ and $\partial\Phi/\partial r$: $1/B$ (red) is proportional to the local major radius $R$, $\Phi$ is poloidally constant, but the distance between the flux surfaces in the denominator, $d$, is not (blue). At the midplane at the LFS, i.e. at poloidal angle $\theta_{\mathrm{pol}} = 0°$, $v_{E\times B}$ (black) has a maximum, since $B$ has a minimum and the flux surfaces are compressed due to the Shafranov shift, which minimizes $d$ [51]. For positive (negative) poloidal angles, which refer to regions above (below) the midplane, $v_{E\times B}$ gradually decreases towards the upper (lower) divertor. Towards the HFS the velocity again increases towards a local maximum.

A detailed understanding of the perpendicular propagation velocity, or plasma flows in general, is motivated by their strong interaction with turbulence. Sheared plasma flows are the main player to suppress turbulence and transport via decorrelation and dissipation [52–55]. The turbulent energy of the eddy can be transferred into shear flows, such as zonal flows [41, 54] via the Reynold's stress tensor [56]. Figure 2.3 schematically depicts the interaction between turbulent eddies and a zonal flow. As time goes by (left to right) the eddies elongate, tilt, thin and by this transfer energy to the zonal flow. This mechanism decreases both the turbulence level and the correlation length, i.e. the characteristic turbulence size, perpendicular to the flow. Flows and turbulence carry out limit-cycle oscillations similar to a predator-prey relationship: the strength of the shear flow increases with increasing turbulence level, then starts to stagnate and decrease once it has consumed too much turbulence energy, resulting finally in an new increase of turbulence.

## 2.5 Turbulent transport

Fluctuations of the plasma temperature, density and potential cause transport. For the electrostatic case the turbulent electron particle flux $\Gamma_{\mathrm{e}}$ and the turbulent electron heat flux $Q_{\mathrm{e}}$ yield [17]

$$\Gamma_{\mathrm{e}} = \frac{\langle \delta E_{\mathrm{pol}} \delta n_{\mathrm{e}} \rangle}{B_{\mathrm{tor}}} \tag{2.9}$$

and

$$Q_\mathrm{e} = \frac{3 n_\mathrm{e} T_\mathrm{e}}{2 B_\mathrm{tor}} \left( \frac{\langle \delta E_\mathrm{pol} \delta T_\mathrm{e} \rangle}{T_\mathrm{e}} + \frac{\langle \delta E_\mathrm{pol} \delta n_\mathrm{e} \rangle}{n_\mathrm{e}} \right). \tag{2.10}$$

$\delta E_\mathrm{pol}$, $\delta T_\mathrm{e}$ and $\delta n_\mathrm{e}$ refer to the fluctuation amplitudes of the poloidal electric field, the electron temperature and the electron density, respectively. $\langle \cdot \rangle$ denotes ensemble averaging and $B_\mathrm{tor}$ the magnetic field in toroidal direction. The contributions from electron temperature fluctuations or electron density fluctuations to the transport depend on the phase relation (c.f. Sec. 2.7) between $\delta E_\mathrm{pol}$, $\delta T_\mathrm{e}$ and $\delta n_\mathrm{e}$. Whereas a range of diagnostics exist to measure $\delta n_\mathrm{e}$ and $\delta T_\mathrm{e}$, fluctuations of the electric field or potential, are only experimentally accessible in the plasma edge. Thus, neither the phase angle between electric field and electron temperature fluctuations, nor between electric field and electron density fluctuations can be experimentally determined in the plasma core. However, the cross-phase between electron density and temperature fluctuations can provide useful information about the turbulence and the models behind [57, 58], even though it does not enter directly into Eqs. 2.9 and 2.10.

## 2.6 Experimentally accessible turbulence features

Thanks to a broad range of turbulence diagnostics, of which an overview is available in Ref. [59], there is a variety of experimentally accessible turbulence quantities. The following discusses the quantities of interest in this thesis. Turbulence diagnostics do not necessarily measure the mean value of a quantity like temperature or density, but rather detect their fluctuating part. The root mean square (RMS) of the signal is defined as the *fluctuation amplitude*. The comparison of the fluctuation amplitude among different turbulence scales informs about *wavenumber spectra*. Measuring fluctuations at slightly separated points in space allows to infer the *correlation length* of turbulence. In fully developed turbulence, the correlation length is the distance over which turbulence remains correlated, which is usually on the order of the eddy diameter [53]. In this thesis the correlation length is defined as the half width half maximum (HWHM) of the spatial decay of the cross-correlation coefficient. Note that also the spectral dependence of the turbulence energy is a measure of the correlation length [60, 61]. The simultaneous detection of two fluctuating fields at the same location allows to determine their cross-phase. Even though it is experimentally challenging to access, the cross-phase is an important indicator for the transport level [17].

## 2.7 Tools to analyze turbulence

In order to extract the turbulence quantities mentioned above from the measured raw data or simulation output, different analysis techniques are necessary. A very useful mathematical

operation to visualize fluctuating features in measurement or simulation data $x(t)$ is the Fourier transform FT. The square of a Fourier transform, which (in Fourier space) is the product of the Fourier transform $\mathrm{FT}[x(t)]$ with its complex conjugate $\mathrm{FT}[x(t)]^*$, is referred to as the power spectrum $S(f)$ with

$$S(f) = \mathrm{FT}[x(t)] \cdot \mathrm{FT}[x(t)]^*. \tag{2.11}$$

It quantifies the fluctuation power depending on the frequency $f$. To decrease statistical errors and improve the signal quality it can be useful to apply ensemble averaging. Here the measurement timetrace is split into bins of equal number of samples $n_{\mathrm{fft}}$, which optionally overlap. Typically $n_{\mathrm{fft}}$ is a power of two, such as 1024 or 2048. The Fourier transforms of all these bins are averaged.

In the analysis of fluctuating quantities it is often not only one fluctuating quantity, but the relationship between two (or more) time series that is of interest. The coherence

$$\gamma(f) = \frac{(\mathrm{FT}[x_1(t)]^* \cdot \mathrm{FT}[x_2(t)])^2}{S_1(f) \cdot S_2(f)} \tag{2.12}$$

describes the 'similarity' of two signals $x_1(t)$ and $x_2(t)$ in Fourier space. Its absolute value ranges from zero (signals incoherent for this frequency) to one (identical signals). The phase of the coherence, termed *cross-phase* or $\alpha_{x_1,x_2}$, indicates the phase shift between the two signals $x_1(t)$ and $x_2(t)$ for each fluctuation frequency. For a finite length of signals, such as inevitably available from experiment, the absolute coherence does not drop below a noise level, which depends on the number of samples. Again, noise can be reduced by using ensemble averaging.

The function to describe the 'similarity' of two signals in time is the normalized cross-correlation function $c(\tau)$ with

$$c(\tau) = \frac{\int_{-\infty}^{\infty} x_1(t)^* x_2(t+\tau)\mathrm{d}t}{\sqrt{\left(\int_{-\infty}^{\infty} |x_1(t)|^2 \mathrm{d}t\right)\left(\int_{-\infty}^{\infty} |x_2(t)|^2 \mathrm{d}t\right)}}. \tag{2.13}$$

It is of interest when two time series $x_1(t)$ and $x_2(t)$ see similar events with a certain time delay. $c(\tau_{\mathrm{s}}) = 1$ refers to two identical signals that are shifted in time by $\tau_{\mathrm{s}}$, whereas a value of zero indicates no correlation. Via the Wiener-Khinchin theorem the normalized cross-correlation function reformulates into

$$c(\tau) = \frac{\mathrm{IFT}[\mathrm{FT}[x(1)]^* \cdot \mathrm{FT}[x_2(t)]]}{\sqrt{E_{\mathrm{x}1} E_{\mathrm{x}2}}}. \tag{2.14}$$

IFT is the inverse Fourier transform, $E_{\mathrm{x}}$ is the energy of the signal, which is its auto-correlation function at zero lag,

$$E_{\mathrm{x}} = \int_{-\infty}^{\infty} |x(t)|^2 \mathrm{d}t = \mathrm{IFT}[\mathrm{FT}[x(t)]^* \cdot \mathrm{FT}[x(t)]]|_{\tau=0}\,. \tag{2.15}$$

The maximum of the normalized cross-correlation function of two signals with a time shift $\tau_{\mathrm{s}}$ is located at $\tau = \tau_{\mathrm{s}}$. This time delay directly relates to the derivative of the coherence's phase $\alpha$

with respect to frequency $f$ via

$$\tau_\mathrm{s} = \frac{1}{2\pi}\frac{\mathrm{d}\alpha}{\mathrm{d}f} = \frac{s}{v_\mathrm{prop}}. \tag{2.16}$$

The first equal sign of Eq. 2.16 indicates that correlating two measurement signals that detect the same turbulent feature with a time lag $\tau_\mathrm{s}$ thus produces a linearly ramping cross-phase. The second equals sign of Eq. 2.16 relates $\tau_\mathrm{s}$ to the propagation velocity of this feature, $v_\mathrm{prop}$, and the spatial distance of the measurement locations $s$.

For cases where spurious noise leads to undesired correlation, the signals can be filtered in Fourier space beforehand. If $x_{1,2}(t) \in \mathbb{R}$ there is a range of adequate filter functions, $Y_\mathrm{filt}$, to assign a new filtered time series $x_\mathrm{filtered}$ as

$$x_\mathrm{filtered} = \mathrm{IFT}[\mathrm{FT}[x(t)] \cdot Y_\mathrm{filt}(f)]. \tag{2.17}$$

Commonly used filter functions are for instance the Butterworth or Chebychev filters that are (close to) unity in the frequency range of interest $[f_1, f_2]$ and (close to) zero otherwise. If $x_{1,2}(t) \in \mathbb{C}$, however, the power spectra are not symmetric in frequency space and thus cannot be filtered directly with the above mentioned symmetric filter functions. The raw signal $x(t)$ must be *demodulated* first, thus multiplied by the complex $\exp(-i2\pi f_\mathrm{C} t)$ with $f_\mathrm{C} = (f_1 + f_2)/2$ and $t$ the time base of $x(t)$. The demodulation shifts the power spectrum in Fourier space: the previous frequency $f_\mathrm{C}$ now is located at zero frequency, such that the symmetric filter functions can be applied. The filtered signal is thus

$$x_\mathrm{filtered} = \mathrm{IFT}[\mathrm{FT}[x(t) \cdot \exp(-i2\pi f_\mathrm{C} t)] \cdot Y_\mathrm{filt}(f)] \exp(i2\pi f_\mathrm{C} t). \tag{2.18}$$

The tool kit presented here is especially useful for signals where turbulence features are the dominant contribution to the fluctuating part of the signal. In case the measured signal is dominated by incoherent noise, the above introduced correlation techniques give lower coherence and cross-correlation values than for pure turbulence response. The correlation techniques must therefore be slightly adapted to the specific physics behind the measurement principle. This will be of importance for the CECE diagnostic and discussed separately in Sec. 3.4.

## 2.8 Modeling plasma turbulence – the GENE code

Due to its chaotic behavior – related to the nonlinear term of Eq. 2.1 – the modeling of turbulence is computationally highly expensive. Turbulence simulations, being already challenging for neutral fluids, become increasingly difficult for the case of charged plasma particles. One method to reduce the complexity of the problem and thus to make it accessible for simulations is to use the gyrokinetic approach (c.f. Sec. 2.1). The gyrokinetic approach reduces the six-dimensional phase space (three dimensions in space and three dimensions in velocity) to five dimensions to save a large amount of computing power: the gyration of plasma particles is approximated by the dynamics of charged rings. This approach holds for phenomena that occur on time-scales

slower than the gyrofrequency, which is usually justified for turbulence fluctuations. Note that the averaging of the gyromotion is only done in the time domain, but not in space. More detailed introductions to the gyrokinetic approach and the gyrokinetic equations can be found in dedicated PhD theses on the gyrokinetic code GENE, such as Refs. [62–64].

There is a large number of different codes, which are currently used to model turbulence in the core plasma region using the gyrokinetic approach; GENE [18, 65, 66], CGYRO [67], GKW [68], GYSELA [69], ORB5 [70], GENE-3D [71] and EUTERPE [72]. Additionally, recent code efforts extend gyrokinetic turbulence modeling towards the edge plasma and the scrape off layer: GRILLIX [73] and GENE-X [74]. The simulations in the present thesis are done using the GENE code.

The Gyrokinetic Electromagnetic Numerical Experiment (GENE) code is a nonlinear gyrokinetic plasma turbulence code [18, 65, 66]. It solves the Vlasov and Maxwell equations numerically to simulate turbulence in magnetic fusion and astrophysical plasmas. GENE can simulate turbulence both locally in a so-called flux-tube on a given flux surface, as well as globally over the full radial domain up to the separatrix [75, 76]. It can solve the gyrokinetic equations both linearly (*linear runs*) and nonlinearly (*nonlinear runs*) [66]. Depending on the spatio-temporal resolution of the simulations, they are ion or electron scale, referring to the ion or electron gyromotion, respectively. The simulations in the context of this thesis are typically local and include electromagnetic effects, i.e. also model fluctuations of the magnetic field. They mostly model two species; plasma ions and electrons, whereas few tests with a third species, boron ions, have been performed and are currently ongoing. In this thesis collisions are taken into account by a linearized Landau-Boltzmann operator, of which details can be found in Ref. [77]. The simulations additionally include the experimental toroidal plasma rotation and $E \times B$ shear and consider the experimental flux surface shapes.

# 3 Experimental setup and diagnostics

This chapter introduces methods for plasma heating and diagnosis. Given the high temperatures in the confined region, the approaches for both power injection and measurement principles are based on the usage of electromagnetic waves or neutral particles.

## 3.1 Plasma heating

Fusion power plants with deuterium and tritium plasmas maintain high temperatures by fusion processes and corresponding alpha particle heating. AUG mostly operates in deuterium (sometimes hydrogen or helium) and thus needs external heating to sustain a plasma. The following briefly discusses different techniques for plasma heating. More details can be found in the literature [78–82].

Tokamak plasmas inherently heat up by resistive dissipation of the toroidal plasma current [79]. This simple source of energy injection is termed *Ohmic heating*. The plasma resistivity is proportional to $T^{-3/2}$ such that for higher temperatures Ohmic heating becomes less effective and auxiliary heating is needed to further heat up the plasma. The power density of Ohmic heating is largest in the plasma center.

The energy of gyrating plasma particles can be increased by the interaction with electromgnetic waves [83]. *Electron cyclotron resonance heating* (ECRH) works by injecting microwaves at the gyrofrequency of electrons or higher harmonics, which transfer their energy to the resonant gyrating electrons. Due to the radially decreasing magnetic field in a tokamak, the gyrofrequency, $\omega_{\mathrm{c,e}} \propto B \propto 1/R$, changes with major radius. Therefore, ECRH power injected at a certain frequency heats the plasma very locally. In the experiments in the scope of this thesis, ECRH is used to change the local electron temperature gradient and thus the turbulence drive in the measurement region. Note that wave heating can also be used to heat ions, but this is not of relevance for the experiments in this thesis.

*Neutral beam injection* (NBI) heats the plasma by injecting neutral hydrogen isotopes into the plasma that have a higher kinetic energy than the thermal plasma ions [84, 85]. The particles transfer their energy to the plasma bulk ions either by charge exchange processes, where the slow plasma ion is given the electron of the fast neutral particle, or by ionization of the neutral particle after a collision with a plasma electron. The experiments in the context of this thesis use deuterium, which is mostly (60 %) accelerated as single atoms at an energy of 50 keV, and

partially (40 %) as molecule consisting of two or three atoms. The latter only have half or a third of that energy, respectively, since only single atoms enter the plasma. These atoms are tangentially injected to drive plasma rotation (c.f. Sec. 6.1.1). In addition, short blips of high power NBI enable to measure the ion temperature (c.f. Sec. 3.2.5).

## 3.2 AUG standard diagnostics

The experiments and simulations in the context of this thesis need knowledge of a variety of plasma parameters. This section touches the relevant measurement diagnostics and their working principles.

### 3.2.1 Electron cyclotron emission radiometry

The gyromotion of a charged particle around a magnetic field line is an accelerated movement. Hence, the particles emit Bremsstrahlung at the gyrofrequency and its higher harmonics. The radiation coming from one electron at a certain point in space is repeatedly absorbed and re-emitted by other electrons close by, which have a similar $\omega_{\mathrm{c,e}}$. The plasma regions under consideration in this thesis are *optically thick*, meaning that the absorption and emission processes occur often enough that it is black body radiation that leaves the plasma. Its intensity [79]

$$I(\omega) = \frac{\omega^2 T_{\mathrm{e}}(R)}{8\pi^3 c^2} \tag{3.1}$$

as a function of the frequency $\omega$ directly depends on the electron temperature. The spatial position of the source of radiation is localized via the spatial dependence of $\omega_{\mathrm{c,e}} \propto B$. The *electron cyclotron emission* (ECE) *radiometers* at AUG [86] are sensitive to the second harmonic emission in X-mode wave polarization (for more details on wave polarizations see Sec. 4.1).

### 3.2.2 Thomson scattering diagnostic

*Thomson scattering* denotes the process of wave scattering on charged particles that start to oscillate and emit light at the frequency of the wave. In AUG a laser is shot through the plasma to invoke this effect. The intensity of the Thomson scattered radiation is a measure for the electron density. Its Doppler shift relative to the injected laser frequency corresponds to the thermal motion of the electrons and thus the electron temperature [87].

### 3.2.3 Infrared laser interferometry

Electromagnetic waves propagating at frequencies in the same order of magnitude as (but strictly higher than) the cutoff frequency experience dispersion that depends on the local plasma param-

eters. *Interferometry* sends a laser beam through the plasma. On its way the beam's phase velocity increases depending on the local electron density. The phase shift between the probing and a reference beam directly relates to the electron density integrated along the line of sight of the interferometer [79]. The AUG interferometers consist of deuterium cyanide (DCN) lasers, which pass through the plasma along different lines of sight [88].

### 3.2.4 Lithium beam emission spectroscopy

The *lithium beam emission spectroscopy* (Li-BES) diagnostic injects a beam of neutral lithium particles into the plasma and measures the interaction between the beam and the plasma electrons [89]. The collisions with the electrons either ionize the lithium particles or excite their electrons into higher atomic states. The excited state that is most occupied is 2p. It relaxes back to 2s via de-excitation and emission of a photon. The number of these photons with respect to the injected particles is a measure of the plasma density. Since lithium neutrals cannot penetrate deeply into the plasma, this diagnostic is particularly suited for edge density measurements. AUG uses a probabilistic lithium beam data analysis [90].

### 3.2.5 Charge exchange recombination spectroscopy

One way of interaction of externally injected neutral particles with the plasma ions is charge exchange, c.f. Sec. 3.1. *Charge exchange recombination spectroscopy* (CXRS) observes the interaction of fast neutral particles, which are injected by the NBI, with the plasma. The original plasma ion is left in an excited state with one more electron than before. In the case of deuterium it is then neutral and leaves the plasma, however, in the case of an impurity species it stays positively charged and thus confined. The excited state of the impurity atom decays via photon emission at characteristic frequencies [91]. The Doppler broadening of these spectral lines is a measure for the bulk thermal temperature of the emitting ions, their Doppler shift corresponds to the plasma velocity parallel to the line of sight and their intensity relates to the impurity density [92, 93].

CXRS is commonly used to determine the radial electric field of the plasma, $E_\mathrm{r}$, from the radial force balance

$$q\left(\mathbf{E} + \mathrm{v} \times \mathbf{B}\right) - \nabla p = 0 \tag{3.2}$$

or

$$E_\mathrm{r} = v_{\mathrm{tor},\alpha} B_\mathrm{pol} - v_{\mathrm{pol},\alpha} B_\mathrm{tor} + \frac{1}{n_\alpha Z_\alpha e} \frac{\partial p_\alpha}{\partial r}. \tag{3.3}$$

$B_\mathrm{tor}$ and $B_\mathrm{pol}$ are the toroidal and poloidal magnetic field components, $v_{\mathrm{tor},\alpha}$ and $v_{\mathrm{pol},\alpha}$ are the toroidal and poloidal velocity components of the bulk ion species $\alpha$ on which charge exchange processes are measured. $n_\alpha$, $Z_\alpha$ and $p_\alpha$ are the impurity density, charge number and pressure.

In the plasma core, the dominant contribution to $E_\mathrm{r}$ is the toroidal velocity term. In the experiments performed here, $v_{\mathrm{pol},\alpha}$ could not be measured due to hardware unavailability and thus $E_\mathrm{r}$ from CXRS is approximated as

$$E_\mathrm{r} \approx v_{\mathrm{tor},\alpha} B_\mathrm{pol} + \frac{1}{n_\alpha Z_\alpha e} \frac{\partial p_\alpha}{\partial r}. \tag{3.4}$$

This assumption is supported by a previous analysis of several L-mode plasma discharges [94] where $-1.5\,\mathrm{km/s} < v_{\mathrm{pol},\alpha} < 2.0\,\mathrm{km/s}$, which is in quantitative agreement to findings at other tokamaks [95–98].

### 3.2.6 Integrated data analysis

The above mentioned diagnostics provide redundant measurements of the same physical quantities. The Bayesian probability theory can be used to combine data from different measurement techniques to find the most probable plasma profiles.

The electron density and temperature profiles in the experiments of this thesis are inferred using the AUG's *integrated data analysis* (IDA) framework [99]. The input data stems from ECE radiometry, Thomson scattering, DCN laser interferometry and Li-BES. The resulting profile is a spline fit with pre-determined radial knot positions. In turbulence studies the quantities of interest are the normalized gradients. Integrated data analysis is used for this thesis with a reduced number of spline knots compared to Ref. [99]. This adaptation shifts the focus of standard IDA from determining the most probable absolute value towards smoother gradients with less spatial variation.

The ion temperature and toroidal rotation profiles used in the following are fitted using Gaussian process regression, based on the experimental data of different CXR spectrometers [100]. At AUG these fits are commonly called *IDI* (relating 'IDA' from above to 'ion').

Combining the information of most realistic kinetic profile fits from IDA and IDI with magnetic measurements enables the reconstruction of a pressure constrained magnetic equilibrium [101]. In AUG nomenclature this equilibrium is referred to as *IDE* (relating 'IDA' to 'equilibrium').

### 3.2.7 Bolometer

*Bolometers* measure the power that is emitted from the plasma as radiation. They consist of thin films of metal, semiconductors or pyrolectric material. The rate of change in the film's temperature is a measure for the absorbed power. Using a large amount of lines of sight through the plasma allows tomographic reconstruction of the radiation pattern and thus spatially resolved information of the radiated power [102].

## 3.3 AUG turbulence diagnostics

There is a large number of diagnostics that can measure turbulence features, c.f. Ref. [59]. In this thesis, the two main diagnostics to measure turbulence at AUG are Doppler reflectometry [103, 104] and correlation electron cyclotron emission radiometry [105, 106], both microwave diagnostics [107, 108]. Note that AUG has a variety of other powerful diagnostics to measure turbulence, such as more Doppler reflectometers [109], perpendicular incidence reflectometers [110], poloidal correlation reflectometers [111], Langmuir probes [112], a helium beam [113] and an imaging heavy ion beam probe [114]. These, however, could not be considered in this thesis, since their measurement range does not cover the radial region of interest or they were temporally unavailable. Doppler reflectometry measures the amplitude and the velocity of electron density fluctuations. Being the most important diagnostic in the context of this thesis, it is introduced in detail in Chap. 4.

## 3.4 Correlation electron cyclotron emission radiometry

*Correlation electron cyclotron emission* (CECE) radiometers [115, 116] measure absolute electron temperature fluctuation levels and their radial correlation lengths by correlation of closely spaced ECE channels. In the context of this thesis the CECE radiometry is of comparable importance as Doppler reflectometry, hence, it shall be in detail discussed in this section.

### 3.4.1 Principle of CECE and its implementation at AUG

The CECE diagnostic uses several ECE radiometer (c.f. Sec. 3.2.1) channels. Whereas the ECE diagnoses the absolute temperature, the CECE correlates the cyclotron radiation from two close locations to extract temperature fluctuations. Figure 3.1 sketches the CECE measurement principle: two plasma volumes emit ECE radiation at slightly different wavelengths. These signals are correlated to infer the turbulent fluctuation dynamics. The necessity of this correlation shall be illuminated in the following: other than traditional turbulence diagnostics, such as for instance reflectometers, of which the measurement signal's fluctuating part only stems from density fluctuations (and in part from hardware noise), the electron cyclotron radiation has a significant contribution from the (strongly fluctuating) intrinsic thermal noise or black body radiation. Since for two close-by but non-overlapping CECE channels turbulence is coherent, but thermal noise is not, correlating two channels allows to extract the broadband temperature fluctuations and thus reduce the uncorrelated intrinsic noise. The main difference between an ECE and a CECE radiometer is the narrower filter bandwidth, $B_{\mathrm{IF}}$, of the latter, which improves the correlation. The CECE system at AUG [105, 106] measures at 24 radial positions with filters with $B_{\mathrm{IF}} = 200$ MHz for the measurements presented in this thesis. Its standard location is in sector 9 of AUG. For concurrent and spatially overlapping measurements of density fluctuations it is also temporarily installed at sector 11 for the presented study. The lines of sight in both sectors

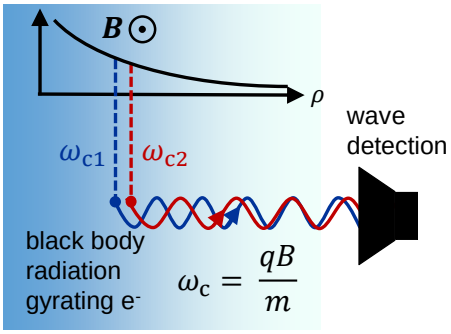


**Figure 3.1:** Schematics of the CECE diagnostic measurement principle: the cyclotron radiation from two locations is correlated to extract electron temperature fluctuations.

ensure perpendicular incidence probing. Since CECE radiometers measure the cyclotron radiation that is emitted from a finite plasma volume, they are sensitive to large turbulent structures only, as all structures that are smaller than the measurement volume cannot be resolved.

### 3.4.2 Data analysis

To measure temperature fluctuation amplitudes as a radial profile, each channel is correlated with the next neighboring channel. The integral of the coherence $\gamma_c$ in the frequency range of the broadband turbulence, $f_1$ to $f_2$, connects to the absolute temperature fluctuation amplitude $\delta T_e/T_e$. The most straight forward way to calculate $\delta T_e/T_e$ from the coherence is [106, 117],

$$\frac{\delta T_e}{T_e} = \sqrt{\frac{2}{B_{IF}} \int_{f_1}^{f_2} (\gamma_c(f) - \gamma_{bg})\, \mathrm{d}f}. \tag{3.5}$$

$\gamma_{bg}$ is a non-zero (background) noise component, which is determined in a frequency region far from the broadband turbulence feature. Equation 3.5 assumes the thermal black body radiation to largely exceed the turbulence information [106]. Going one step further and analytically separating the thermal noise from the turbulence signal enables to derive a formula in which the temperature fluctuations only come from turbulence contributions and thermal noise is analytically excluded. Thereby the assumption that thermal noise is much greater than the turbulence signal becomes superfluous. This more general expression reads [106]

$$\frac{\delta T_e}{T_e} = \sqrt{\frac{2}{B_{IF}} \int_{f_1}^{f_2} \frac{(|\gamma_c(f)| - |\gamma_{bg}|)}{1 - (|\gamma_c(f)| - |\gamma_{bg}|)} \mathrm{d}f}. \tag{3.6}$$

Whereas a previous publication on AUG CECE data analysis [106] compares the use of the real part of the coherence to the absolute coherence and in that study it was decided for the real part, this thesis uses the absolute value as it gives more reasonable results. Note that for the same reason also a recent AUG study using CECE [118] uses absolute values. The uncertainty

of the temperature fluctuation amplitude as derived in Ref. [118] reads

$$\sigma_{\delta T_\mathrm{e}/T_\mathrm{e}} = \frac{1}{\delta T_\mathrm{e}/T_\mathrm{e}} \frac{1}{B_\mathrm{IF}} \int_{f_1}^{f_2} \frac{\sigma_{\gamma_\mathrm{c}}(f)}{(1-|\gamma_\mathrm{c}(f)-\gamma_\mathrm{bg}|)^2} \mathrm{d}f. \tag{3.7}$$

In the case of discrete frequency steps, $\mathrm{d}f$ is the frequency resolution of the coherence. $\sigma_{\gamma_\mathrm{c}}$ is the uncertainty of the coherence:

$$\sigma_{\gamma_\mathrm{c}}(f) = \frac{1}{\sqrt{2n_\mathrm{d}}}(1-|\gamma_\mathrm{c}(f)|^2), \tag{3.8}$$

with the number of independent ensemble averaging windows $n_\mathrm{d}$.

The analysis of radial correlation lengths from CECE is more convoluted than for electron temperature fluctuations and shall be tackled in the following. In general, the correlation length is inferred by correlating one channel with several other channels in the close neighborhood. The integral of the coherence between the channel and a neighboring channel decreases with the radial distance between the channels. This is a direct measure for the spatial decorrelation of turbulence. The first AUG study of the radial correlation length from CECE [119] uses a straight forward way: first the temperature fluctuation amplitude for CECE channel pairs with increasing radial separation is calculated. Second a Gaussian function is fitted to the plot of the amplitude versus the radial separation to extract a correlation length. Following the approach of Ref. [106] to analytically derive an equation for the temperature fluctuation amplitude without thermal noise contributions, Ref. [118] derives an equation to calculate radial correlation lengths and analytically exclude the thermal noise contributions. It expresses the maximum $C_\mathrm{max}$ of a hypothetical normalized cross-correlation without thermal noise and assumes it to be at zero lag, i.e. $\tau_\mathrm{max} = 0$. This assumption is justified, since for the AUG CECE data acquisition system the sampling time is larger than (or equal) $\tau_\mathrm{max}$. A short form of the equation for $C_\mathrm{max}$ between channels X and Y from Ref. [118] is

$$C_\mathrm{max} = \frac{\mathcal{T}_\mathrm{e,xy}}{\sqrt{\mathcal{N}_\mathrm{e,x}^2 \mathcal{N}_\mathrm{e,y}^2}}. \tag{3.9}$$

In the broader sense, $\mathcal{T}_\mathrm{e,xy}$ resembles a temperature fluctuation amplitude between the two non-directly-neighboring channels X and Y:

$$\mathcal{T}_\mathrm{e,xy} = \frac{2}{B'_\mathrm{IF,xy}} \int_{f_1}^{f_2} (\gamma_\mathrm{c,xy}(f) - \gamma_\mathrm{bg,xy}) \mathrm{d}f \tag{3.10}$$

using an average filter bandwidth $B'_\mathrm{IF,xy} = \sqrt{B_\mathrm{IF,x} B_\mathrm{IF,y}}$. Figure 3.2 visualizes the computation of $\mathcal{T}_\mathrm{e,xy}$ for one representative channel pair X and Y. The radial distance between X and Y is defined as indicated by the grey arrow in Fig. 3.2. $\mathcal{N}_\mathrm{e,x}$ and $\mathcal{N}_\mathrm{e,y}$ denote the average relative temperature fluctuation levels at the radial position of X and Y, respectively. Since CECE radiometers intrinsically measure temperature fluctuation levels between channels, rather than at the specific position of one channel, $\mathcal{N}_\mathrm{e,x}$ and $\mathcal{N}_\mathrm{e,y}$ make use of both of their direct neighboring channels to calculate the fluctuation amplitude and then take the average value. The bottom left

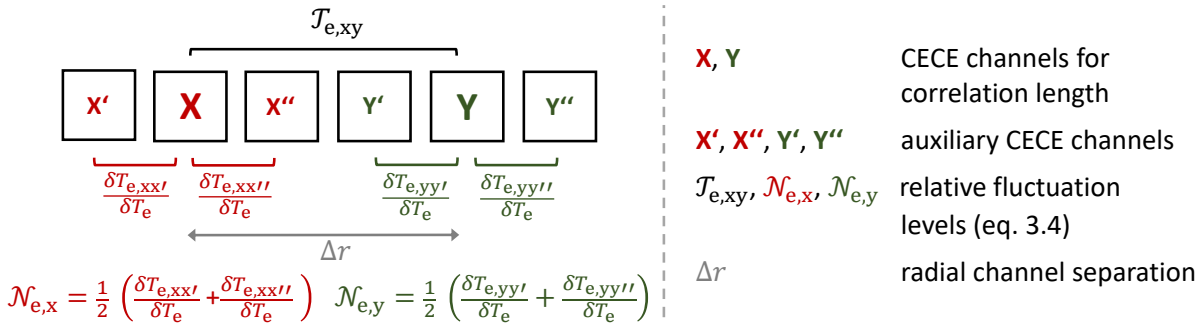


**Figure 3.2:** Visualization of radial correlation length analysis with CECE: channel X and Y with spatial distance $\Delta r$ are correlated. For details refer to the text.

of Fig. 3.2 attempts to illustrate this technique: channel X is allocated two auxiliary channels, X′ and X″, to its left and right. $\mathcal{N}_{e,x}$ is the mean value of $\delta T_{e,xx'}/T_{e,x}$ and $\delta T_{e,xx''}/T_{e,x}$, whereas $\delta T_{e,xx'}/T_{e,x}$ and $\delta T_{e,xx''}/T_{e,x}$ equal the relative fluctuation amplitudes from Eq. 3.5. The full expression of $\mathcal{N}_{e,x}$ reads:

$$\begin{aligned}\mathcal{N}_{e,x} &= \frac{1}{2}\left(\frac{\delta T_{e,xx'}}{T_{e,x}} + \frac{\delta T_{e,xx''}}{T_{e,x}}\right) \\ &= \frac{1}{2}\left(\sqrt{\frac{2}{B_{IF}}\int_{f_1}^{f_2}(\gamma_{c,xx'}(f) - \gamma_{bg,xx'})\mathrm{d}f} + \sqrt{\frac{2}{B_{IF}}\int_{f_1}^{f_2}(\gamma_{c,xx''}(f) - \gamma_{bg,xx''})\mathrm{d}f}\right)\end{aligned} \tag{3.11}$$

The same holds for Y and its auxiliary channels Y′ and Y″. The use of these auxiliary channels restricts the application of this technique to channel pairs X and Y that have at least one other channel in-between them. This prevents X and Y becoming auxiliary channels of each other. Note that the derivation of Eq. 3.9 needs to reintroduce the assumption that thermal noise is much greater than turbulence features. Therefore, following Ref. [118] for the sake of consistency $\delta T_e/T_e$ shall in the context of radial correlation lengths be calculated using Eq. 3.5 instead of Eq. 3.6.

### 3.4.3 Synthetic diagnostic modeling

In order to compare the CECE measurements to turbulence simulations, synthetic diagnostic modeling is used. The idea is to artificially mimic the measurement principle of the diagnostic on the simulated turbulence fields, such as from GENE. In the case of CECE this implies that the finite spot sizes of electron cyclotron emission are taken into account. The simulated turbulence within these volumes is spatially averaged, giving time-traces of synthetic CECE channels. These individual channels are located at the same radial and vertical position as in the experiment. Correlating the channels gives cross-power-spectra that correspond to the experimentally obtained frequency spectra.

The spot sizes from which the ECE radiation is emitted require knowledge of both the diagnostic antenna pattern as well as physics behind ECE radiation and wave propagation. The latter are calculated by the ECE model ECRad [120] and the beam tracing code TORBEAM [121, 122]. For the specific discharges and radial positions, the beam width in poloidal direction is $w_\mathrm{P} = 15.4-19.3\,\mathrm{mm}$. The filter bandwidth restricts the radial extent of the measurement volume to $w_\mathrm{R} = 4.1-4.2\,\mathrm{mm}$. This translates into a wavenumber sensitivity of $k_\mathrm{P} < 3.3-4.1\,\mathrm{cm}^{-1}$ in poloidal and $k_\mathrm{r} < 15.0-15.3\,\mathrm{cm}^{-1}$ in radial direction.

# 4 Doppler reflectometry

*Doppler reflectometry* or *Doppler backscattering* is a versatile diagnostic technique to study local characteristics of density fluctuations. Microwaves are obliquely injected into the plasma and backscattered off turbulence eddies. The intensity of the backscattered wave is proportional to the fluctuation amplitude, whereas the Doppler shifted wave frequency is a measure of the propagation velocity of turbulent structures. A range of turbulence scales can be accessed and investigated depending on the injection angle and the probing frequency. Simultaneous measurements of two Doppler reflectometer channels at closely spaced points allow for correlation analysis and determination of radial correlation lengths of the density fluctuations, as well as the tilt angle of the turbulent eddies.

First experimental works go back to [123–127]. They found the phase of a perpendicular incidence reflectometer – which there is a measure for the cutoff position – to temporally change when probing in oblique incidence with respect to the magnetic flux surfaces. This *phase runaway* was related to the plasma rotation. Nowadays Doppler reflectometers are quasi standard diagnostics at larger magnetic confinement fusion devices [109, 128–135]. This chapter first introduces the theory behind wave propagation in a magnetized plasma. It then focuses on the measurement principle of Doppler reflectometry and afterwards discusses the hardware setup. It concludes with the data analysis and with the modeling of the measurement.

## 4.1 Theoretical background of wave propagation

Electromagnetic waves propagating through a plasma do not stay unaffected from the presence of charged particles, which interact with the oscillating electric field. In addition, the confining magnetic field can influence the wave propagation. The wave injection or detection in a tokamak takes place perpendicular to the confining magnetic field, $\mathbf{B}$. There are two solutions of the wave equation for propagation perpendicular to $\mathbf{B}$: the *ordinary wave* (O-mode) where the electric field of the wave $\mathbf{E}_\mathrm{w}$ oscillates in the direction parallel to $\mathbf{B}$, $\mathbf{E}_\mathrm{w} \parallel \mathbf{B}$, and the *extra-ordinary wave* (X-mode), where $\mathbf{E}_\mathrm{w} \perp \mathbf{B}$. The derivation of their dispersion relations and the solutions from the wave-equation for other geometries can be found in the literature [10, 108]. The refractive index of O-mode waves, $N_\mathrm{O}$, reads

$$N_\mathrm{O} = \frac{kc}{\omega} = \sqrt{1 - \frac{\omega_\mathrm{p}^2}{\omega^2}}, \tag{4.1}$$

where $\omega$ and $k$ are the (angular) wave frequency and wavenumber, respectively, and $c$ is the speed of light in vacuum. It only depends on the local electron density via the plasma frequency of the electrons, $\omega_\mathrm{p}$ (c.f. Eq. 1.4). The refractive index of X-mode waves, $N_\mathrm{X}$, reads

$$N_\mathrm{X} = \frac{kc}{\omega} = \sqrt{\frac{(\omega^2 - \omega_\mathrm{L}^2)(\omega^2 - \omega_\mathrm{R}^2)}{(\omega^2 - \omega_\mathrm{UH}^2)(\omega^2 - \omega_\mathrm{LH}^2)}}. \tag{4.2}$$

$\omega_\mathrm{R}$ and $\omega_\mathrm{L}$ are the cutoff frequencies of the right- and left-handed circularly polarized wave, respectively:

$$\omega_\mathrm{R,L} = \frac{1}{2}\left(\sqrt{\omega_\mathrm{c,e}^2 + 4\omega_\mathrm{p}^2} \pm \omega_\mathrm{c,e}\right).$$

$\omega_\mathrm{c,e}$ and $\omega_\mathrm{c,i}$ refer to the cyclotron frequency of the electrons and ions, respectively (c.f. Eq. 1.2). The resonances of the X-waves, the lower hybrid and upper hybrid frequencies, are given by

$$\omega_\mathrm{LH} = \omega_\mathrm{c,e}\sqrt{\frac{\omega_\mathrm{c,i}^2}{\omega_\mathrm{c,e}^2 + \omega_\mathrm{p}^2}}, \quad \omega_\mathrm{UH} = \sqrt{\omega_\mathrm{c,e}^2 + \omega_\mathrm{p}^2}.$$

Eq. 4.2 has various solutions from which the highest frequency branch is interesting for most reflectometer application. Note that in addition to its dependence on the electron density, $N_\mathrm{X}$ also depends on the background magnetic field, which enters via the cyclotron frequency. The wave frequency at zero refractive index is termed *cutoff frequency*. For oblique wave injection, the refractive index does not reach zero, thus the cutoff here refers to the minimum refractive index. Solving Eq. 4.1 and the highest frequency branch in Eq. 4.2 for the cutoff frequency gives a higher cutoff frequency in X-mode than in O-mode for the same density. Therefore, Doppler reflectometers probing in X-mode need higher probing frequencies than in O-mode to reach the same spatial point. In general, the probing frequency determines the radial measurement location and the probing angle determines the poloidal location and the turbulence scale size to measure at, but they are not completely disentangled.

## 4.2 Physics principle

Doppler reflectometers obliquely inject microwaves into the plasma at an angle, $\theta_0$, with respect to the normal of the vacuum-plasma interface. Figure 4.1(a) shows a sketch of the setup. The blue shaded area indicates a plasma with a gradient in electron density perpendicular to a magnetic field. An antenna (black) injects a microwave. On the way, the refractive index decreases with the electron density (and with the magnetic field for X-mode), c.f. Sec. 4.1. The wave is thus refracted and bent following Fresnel's principle. At the point of minimum refractive index, in the following termed *turning point* or *cutoff position*, the density fluctuations scatter the wave. Doppler reflectometers are optimized to detect the first order backscattered component, i.e. the $-1^\mathrm{st}$ order. Due to conservation of momentum, the perpendicular wavenumber of these turbulence structures, $k_\perp$, relates to the wavenumber of the microwave at the cutoff, $k_\mathrm{i}$ as

$$k_\perp = 2k_\mathrm{i}. \tag{4.3}$$

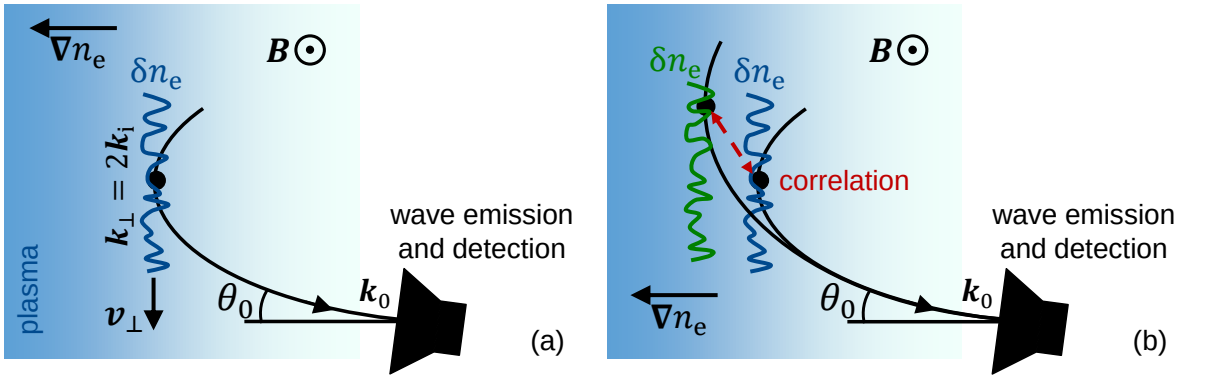


**Figure 4.1:** Principle of Doppler reflectometry in (a): a microwave beam (black) is injected into the plasma and backscattered off density fluctuations (blue). Correlating two Doppler reflectometers in (b) allows to estimate the spatial decorrelation of turbulence. For details refer to the text.

In slab geometry the wavenumber of the incident beam, $k_0$, and $k_\perp$ relate via the Bragg condition for $-1^{\text{st}}$ order

$$k_\perp = 2k_0 \sin\theta_0. \tag{4.4}$$

The backscattered $-1^{\text{st}}$ component follows the path of the incident wave path back to the launching antenna and is detected there. The intensity of the backscattered wave is proportional to $\delta n_e^2$. Its Doppler shift, $\omega_D$, relates to the propagation velocity of density fluctuations via the scalar product of the plasma velocity and the wavevector, $\mathbf{k}$

$$\omega_D = \mathbf{v}\cdot\mathbf{k} = v_\parallel k_\parallel + v_\perp k_\perp + v_r k_r \approx v_\perp k_\perp. \tag{4.5}$$

The approximation on the right side is commonly used for Doppler reflectometers [109, 126]: $k_\perp \gg k_\parallel$ holds because the turbulence structures are elongated in direction of the magnetic field much more than perpendicular to it. $k_\perp \gg k_\parallel$ is additionally ensured by the injection of microwaves perpendicular to background magnetic field. The relation $v_\perp > v_r$ is usually satisfied since turbulence motion perpendicular to the field is dominated by the direction along flux surfaces over the radial direction. Furthermore, $k_r \approx 0$ holds at the cutoff.

As mentioned in Eq. 2.7, the perpendicular velocity measured by Doppler reflectometers comprises the $E\times B$ drift velocity, $v_{E\times B}$ (c.f. Eq. 1.3), and the phase velocity of the turbulence, $v_{ph}$, which depends on the probed turbulence structure size. Previous experiments performed at AUG [136] found $v_{ph} \ll v_{E\times B}$ and thus $v_\perp = v_{E\times B} + v_{ph} \approx v_{E\times B}$ although this is not true for all cases [137, 138]. The experiments discussed in Sec. 5.1.3 confirm the finding of a much smaller phase velocity than the perpendicular propagation velocity, as also reported by other tokamaks [125, 128, 139–143]. A possible explanation is that the observed high levels of small-scale vorticity fluctuations can damp linear features such as growth rates of instabilities and thus lead to a small and dispersionless $v_{ph}$ [50].

Due to the non-trivial magnetic geometry of a tokamak, the determination of $k_\perp$ is more complicated than the simple slab case in Eq. 4.4. Numerical codes are necessary to model the

propagation and backscattering of the wave in the plasma. The most comprehensive tool is the fullwave simulation, which solves Maxwell's equations of the wave on a spatial grid, c.f. Sec. 4.6. Due to its high computational cost, routine Doppler reflectometer analysis employs ray tracing or beam tracing codes that solve the dispersion relation on a spatial grid to estimate $k_\perp$ and are thus faster and cheaper, c.f. Sec. 4.4.2.

Simultaneous measurements with two Doppler reflectometers allow to measure correlation lengths of the electron density fluctuations. Figure 4.1(b) indicates how two Doppler reflectometer beams of slightly different probing frequencies measure at two nearby locations. Varying the distance between the two locations enables the observation of the spatial decorrelation of turbulence.

The backscattering process takes place at an extended spatial and spectral region. The turbulent structures within the finite spectral resolution contribute to a broadening of the Doppler peak, c.f. Sec. 4.4. The peak additionally broadens from the different velocities within the finite radial interval of wave backscattering. Fullwave simulations show that the region of maximum interaction between microwave and turbulence has a spatial and spectral extent that is described by an Airy function [144, 145]. Furthermore, there is an optimum beam width of the injected microwaves, which maximizes the spatial and spectral resolution [146, 147]. The ellipsoidal launching mirror [103] mentioned above is optimized for operating close to this beam width for W-band frequencies. The resolution additionally depends on the radius of curvature of the plasma [146–148], which, however, cannot be experimentally varied that easily. A recent study using fullwave simulations [145] gives generic expressions to approximate the spectral and spatial uncertainties from fullwave simulations. However, it is emphasized that these formulae in particular deviate for cases with large angles of incidence (in Ref. [145] called *banana cases*). Thus, this thesis uses the 3-ray method to estimate the uncertainties of ray tracing, c.f. Sec. 4.4.2.

## 4.3 Hardware setup

Figure 4.2 shows a sketch of the hardware setup of one of the AUG Doppler reflectometers in sector 11. The ex-vessel hardware on the right consists of two parts: the emitting section depicted on the top and the receiving section on the bottom.

The key elements of the emitting section, also referred to as *RF section* (radio frequency), are a synthesizer (grey) and a multiplier (dark yellow). The synthesizer feeds a sinusoidal signal with frequency $f_{\mathrm{S,RF}}$ (12.0−18.5 GHz) into the multiplier. The latter multiplies by 4 to reach V-band microwave frequencies (50–75 GHz) or by 6 to reach W-band microwave frequencies (75–104 GHz) with a power of around 10 dBm. Oversized waveguides (orange) guide the microwaves into the vacuum vessel on the left. A planar mirror passes them onto an ellipsoidal mirror, which can be steered by an in-vessel piezoelectric motor (green). Sample rays for two mirror positions indicate the measurement region in the poloidal cross-section of AUG. Note that the launching mirror is not aligned in poloidal direction, but perpendicular to the helically twisted magnetic field to ensure $k_\parallel \approx 0$. The launching angle of the mirror, $\theta_{\mathrm{m}}$, is defined as the angle between the injected

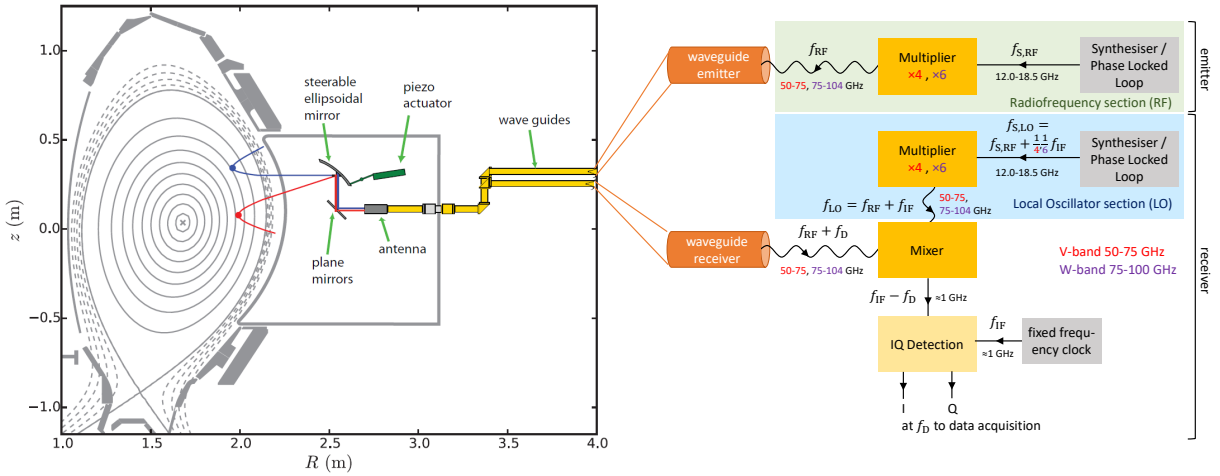


**Figure 4.2:** Setup of the AUG Doppler reflectometer, with the in- and ex-vessel components on the left and right, respectively. Left part modified from [149]. For details refer to the text.

ray and the horizontal plane, counting positive angles upwards. The microwaves backscattered off the density fluctuations travel back to the launching mirror and are guided out of the plasma via a second planar mirror. This configuration, where the emitting and the receiving branches use two different waveguides, is called bistatic. The usage of one common waveguide for both is referred to as monostatic.

The microwaves coming from the plasma oscillate at the original launching frequency, $f_{\mathrm{RF}}$, plus $f_{\mathrm{D}}$, the Doppler shift from the turbulence (order of $\pm$ few MHz). As $f_{\mathrm{RF}} + f_{\mathrm{D}}$ is beyond the sampling frequency of the data acquisition (DAQ), the signal is downconverted by a mixer. For downconversion the mixer uses a reference signal given by a local oscillator signal (LO). This LO wave is produced identically to the RF wave and has a frequency $f_{\mathrm{LO}} = f_{\mathrm{RF}} + f_{\mathrm{IF}}$. The resulting frequency from the mixing process, $f_{\mathrm{IF}} - f_{\mathrm{D}}$, is fed to a heterodyne IQ detection for a second downconversion process. The IQ detection can distinguish signals with positive and negative Doppler shifts and encodes this information into a complex signal, $V = I + iQ$ with the in-phase term $I$ and quadrature term $Q$.

Preferably, all Doppler reflectometer components exhibit a flat frequency response. However, typically this is not the case for the full frequency range. Therefore, for these studies a power calibration was performed. For this purpose the multiplier in the RF section feeds its output (via an attenuator) directly into the mixer in the LO section and all probing frequencies are stepped in fine intervals. The power as acquired by the DAQs varies less than 4 dB for the three reflectometer channels in use: one W-band and two V-band Doppler reflectometers. This weak frequency dependence is comparable to the power deviations that are imposed by the oversized waveguides, the vacuum window and the in-vessel mirror system. Due to practical reasons the calibration of the latter components is not done. Thus, a general power calibration is not applied in the context of this study, but a dedicated calibration in post-processing is used, which is discussed in Sec. 6.3.

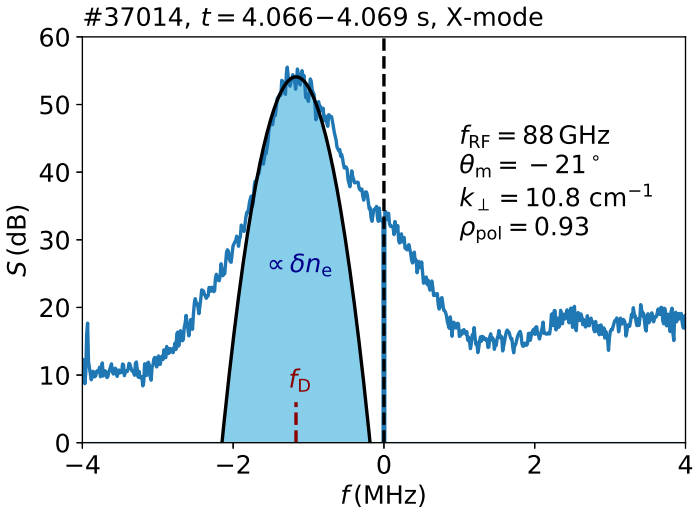


**Figure 4.3:** A sample spectrum of the IQ signal from Doppler reflectometers, probing in X-mode polarization. The center frequency, $f_\mathrm{D}$, of the Gaussian fit on the spectral contribution of interest is a measure for the propagation velocity of density fluctuations, the area below it corresponds to the fluctuation amplitude.

## 4.4 Data analysis

This section focuses on the analysis of the IQ signal to extract information about the electron density fluctuations.

### 4.4.1 The spectrum of the backscattered wave

The spectrum of the IQ signal gives information about both the fluctuation amplitude and the propagation velocity of density fluctuations perpendicular to the magnetic field. Figure 4.3 depicts an experimental spectrum measured by the W-band Doppler reflectometer probing in X-mode at 88 GHz with a launching angle of $\theta_\mathrm{m} = -21°$. It is calculated using averaging with $n_\mathrm{fft} = 2048$ samples. The Doppler shifted component is fitted with a Gaussian function, whereas also other fit functions can be used [150]. The frequency of the peak $f_\mathrm{D}$ corresponds to the propagation velocity (c.f. Eq. 4.5), the area below the fit function corresponds to the fluctuation amplitude. As the process of the backscattering of the wave from the plasma is rather complex, it is difficult to accurately determine the power fraction that is backscattered into the antenna. Therefore, Doppler reflectometers do not measure absolute, but relative fluctuation amplitudes. The vertical offset in Fig. 4.3 is thus arbitrary.

The extraction of the Doppler peak from a spectrum that includes unwanted features that are symmetric in frequency can be tackled by fitting only the asymmetric part of the spectrum, as explained in the following. In general, the power spectrum can be expressed via a Fourier series with sine and cosine Fourier coefficients. The total power spectrum is a superposition of the symmetric power spectrum produced by the cosine coefficients and an asymmetric power

spectrum produced by the sine coefficients. The Doppler shifted measurement signal only comprises asymmetric contributions to the spectrum. In spectra with strong and/or broad central components, which are often close to symmetric, considering and fitting only the asymmetric spectrum can significantly increase the data quality. This method only applies for large Doppler shifts [40].

In the ideal case, turbulence features of interest dominate the IQ signal. Then the RMS of the measurement data corresponds to the fluctuation amplitude. The temporal derivative of the phase $\mathrm{d}\left(\arctan\left[I(t)/Q(t)\right]\right)/\mathrm{d}t = \mathrm{d}\phi/\mathrm{d}t$ corresponds to the velocity. This approach has been applied to experimental data in early works [150, 151] where the histogram of the phase derivative matches the spectrum.

In the non-ideal case, the spectrum may contain additional unwanted features. These possibly include noise from the hardware directly or from external sources. In addition, there could be contributions from another wave polarization and thus a different place in the plasma, from an antenna side lobe or from an asymmetry in the microwave mixer. Furthermore, diagnostic effects may impact the shape of the IQ spectrum. Most of these cases can be tackled in data analysis by for instance restricting the frequency interval to fit the Doppler shift. In the present study there will be one case where an unwanted spectral feature limits the extraction of the turbulence signal (c.f. Sec. 6.5).

### 4.4.2 Ray tracing – the TORBEAM code

To model the path of the wave through the plasma and to estimate the probed turbulence wavenumber, $k_\perp$, it is usually sufficient to use the ray tracing, or the closely related beam tracing approximation where the propagating waves are modeled as rays without thickness or as beam with a spatial extension, respectively. For this purpose, Maxwell's equations are reduced to a set of first-order ordinary differential equations. This thesis uses the beam tracing code TORBEAM [121, 122] for spatial localization of the beam and the cutoff position, as well as the probed turbulence wavenumber. TORBEAM takes into account diffraction effects to model both a beam or a ray. For further reading on beam and ray tracing, see Ref. [152].

The input quantities for ray tracing with TORBEAM are: the magnetic equilibrium, the electron density and electron temperature profiles and characteristics of the beam, such as launching position, launching angle, polarization, consideration of relativistic effects, etc. Due to the low temperature in L-mode plasmas, the TORBEAM runs for this thesis do not include relativistic effects and thus do not need $T_\mathrm{e}$ as input. TORBEAM returns the spatial trajectory of the microwave ray including the local wavenumbers and refractive indices in perpendicular and parallel direction. As the plasmas under consideration are stationary over several seconds, the same average magnetic field and density is used for all data points and only the beam properties change. The so-called *3-ray method* serves as an estimate for the ray tracing uncertainties. Here, in addition to the central ray, two rays are injected with a vertical offset of $\pm 7\lambda$, where $\lambda = 2\pi/k_0$.

The radial distance between the turning points of the rays and their difference in $k_\perp$ serve as an estimate for the radial and spectral uncertainties. The 3-ray method relates to the optimization of the ellipsoidal launching mirror, such that the microwave beam is focused at the probing position and consists of plane wave fronts to reduce both the spatial and the spectral resolution to a minimum [146, 147]. The offset of $\pm 7\lambda$ corresponds to the ideal beam width at the cutoff that maximizes the spectral resolution for this application.

### 4.4.3 Correlation and eddy tilt angle

This thesis will, among others, study the correlation of two Doppler reflectometer channels to extract the radial correlation length and eddy tilt angle of electron density fluctuations. The coherence between two nearby probing Doppler reflectometers has a maximum around the Doppler frequency. The quantity of interest to measure the degree of correlation, thus also called *correlation coefficient*, is the maximum of the absolute of the normalized cross-correlation function. Its spatial dependence is a measure for the decorrelation of turbulence.

The analysis technique to extract the tilt angle of turbulence structures is related. It uses the time delay of the maximum of the absolute normalized cross-correlation function, $\tau_{\max}$. $\tau_{\max}$ comprises two contributions: the first one relates to the spatial distance between the measurement locations in perpendicular direction, $\Delta y_{\mathrm{ray}}$, the second refers to the tilt of the turbulence structures. A detailed derivation has been done in the context of a recent AUG study [153, 154], which expresses the tilt angle $\beta$ with respect to the radial direction as

$$\tan(\beta) = \frac{\tau v_\perp}{\Delta r} - \frac{\Delta y_{\mathrm{ray}}}{\Delta r}. \tag{4.6}$$

$\Delta r$ is the spatial distance of the measurement locations of reference and hopping channels in radial direction. The inclusion of slightly different $k_\perp$ from different hopping channel positions into Eq. 4.6 likely does not distort the calculation of the tilt angle, since Refs. [153, 154] average over a wide spectral range to extract one common tilt angle for all structure sizes.

## 4.5 Diagnostic effects

The fluctuation power and propagation velocity measured with Doppler reflectometry do not always scale linearly with the area below the Gaussian fit or its Doppler shift.

### 4.5.1 Power response regimes

Due to enhanced scattering of the microwaves off density fluctuations, the power of the backscattered wave and thus of the IQ signal does not always linearly depend on the underlying turbulence level. An estimate whether the diagnostic response is linear or nonlinear is expressed by the non-

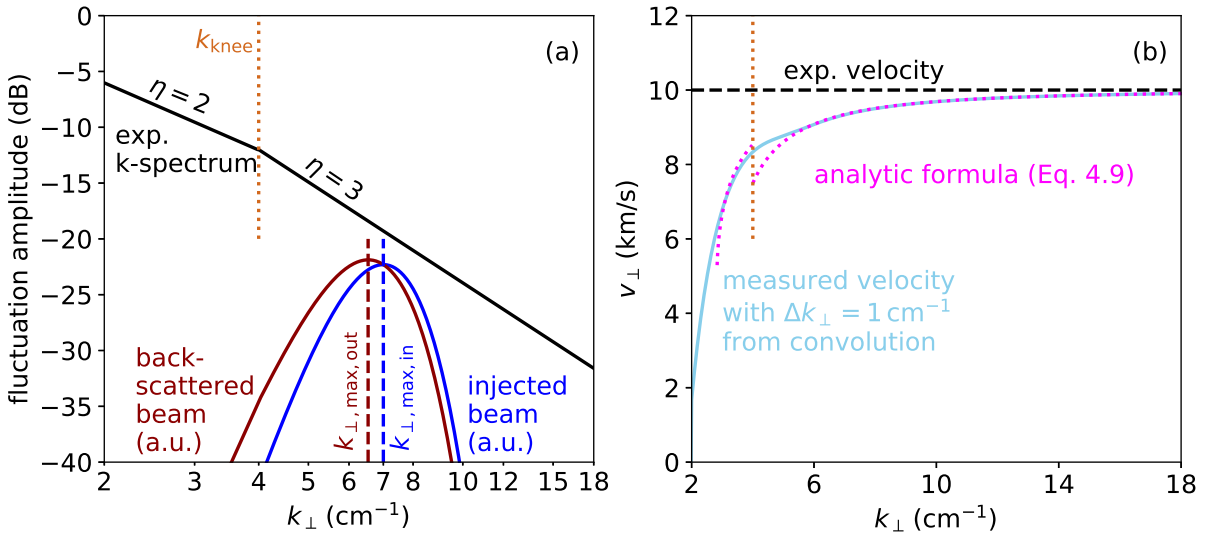


**Figure 4.4:** Sample wavenumber spectrum with a knee position separating two ranges of different spectral indices in (a). The backscattered Gaussian beam (dark red) is the product of the injected beam (blue) and the wavenumber spectrum. $k_{\perp,\mathrm{max,in}}$ and $k_{\perp,\mathrm{max,out}}$ are the $k_\perp$ values where the intensity of the injected and backscattered beams have their maximum. For typical wavenumber spectra $k_{\perp,\mathrm{max,out}} < k_{\perp,\mathrm{max,in}}$ holds. Thus, the measured perpendicular velocity underestimates the actual velocity. This deviation can be approximated by an analytic formula (b).

linearity parameter $\gamma$ [155]:

$$\gamma = \left(\frac{\delta n_\mathrm{e}}{n_\mathrm{e}}\right)^2 \frac{G^2 \omega^2 x_\mathrm{c} l_\mathrm{cx}}{c^2} \ln\left(\frac{x_\mathrm{c}}{l_\mathrm{cx}}\right). \tag{4.7}$$

Here $\delta n_\mathrm{e}/n_\mathrm{e}$ is the RMS of density fluctuations, $x_\mathrm{c}$ the distance of the cutoff to the plasma periphery, $l_\mathrm{cx}$ the radial correlation length of the density fluctuations and $G$ a polarization dependent scaling factor with

$$G = \begin{cases} 1 & \text{for O-mode} \\ \frac{(\omega^2-2\omega_\mathrm{p}^2)(\omega^2-\omega_\mathrm{c}^2)+\omega_\mathrm{p}^4}{(\omega^2-\omega_\mathrm{p}^2-\omega_\mathrm{c}^2)} & \text{for X-mode.} \end{cases} \tag{4.8}$$

The determination of $\gamma$ requires knowledge of the absolute fluctuation amplitude and the average radial correlation length of density fluctuations, which in this thesis are provided by gyrokinetic simulations. The nonlinear power response deserves particular consideration when measuring a range of different fluctuation levels, such as wavenumber spectra. Thus, it will be taken into account using fullwave simulations (c.f. Sec. 4.6) when comparing the measurement to the simulation in Sec. 7.5.

### 4.5.2 Diagnostic effect on perpendicular velocity measurement

Mathematically, the measurement with Doppler reflectometry corresponds to a convolution of the injected microwave beam with the turbulence field. Figure 4.4(a) illustrates the effect in

$k$-space: a sample wavenumber spectrum with a knee at $k_{\mathrm{knee}} = 4\,\mathrm{cm}^{-1}$ and spectral indices $\eta = 2$ and 3 (not to be confused with the viscosity in Sec. 2.1) is plotted in black. The injected Gaussian microwave beam is shown in blue and its maximum, $k_{\perp,\mathrm{max,in}}$ is indicated with a dashed blue line. The convolution of this beam with the turbulence corresponds to a multiplication in $k$-space: the backscattered beam is indicated by the the dark red curve with a maximum $k_{\perp,\mathrm{max,out}} < k_{\perp,\mathrm{max,in}}$. This difference between $k_{\perp,\mathrm{max,in}}$ and $k_{\perp,\mathrm{max,out}}$ causes an underestimation of the actual propagation velocity in measurements by a factor $X$. An analytic expression is derived in Refs. [156, 157]:

$$X = \frac{1}{2}\left(1 + \sqrt{1 - 4\eta\left(\frac{\Delta k_\perp}{k_\perp}\right)^2}\right). \tag{4.9}$$

The velocity underestimation is directly related to the finite spectral resolution $\Delta k_\perp$ ($1\,\mathrm{cm}^{-1}$ in Fig. 4.4). The degree of deviation depends on the spectral index. Figure 4.4(b) shows the experimental reference velocity in black. The sky blue curve depicts the measured velocity, i.e. the mean of Gaussian fits on the backscattered beams, c.f. the dark red curve in (a). For a constant spectral resolution the effect is not independent of the probing $k_\perp$, but strongest for small $k_\perp$. The estimated velocity from the analytic expression in Eq. 4.9 (magenta) reproduces the convolved velocity well. The jump at the $k_\perp$ value of the knee position corresponds to the transition from one spectral index to the other.

## 4.6 Modeling Doppler reflectometer measurements – the IPF-FD3D code

In the context of this thesis the two-dimensional fullwave code *IPF-FD3D* [158, 159] simulates the Doppler reflectometer measurements on the turbulence simulations done with GENE. It assumes the turbulence to be frozen and to change much slower than the travel time of the wave. IPF-FD3D thus simulates the wave propagation through the plasma and the backscattering process off density fluctuations for each time frame of the GENE turbulence field. It solves Maxwell's equations and the electron equation of motion in a cold plasma using a finite difference time domain approach. In addition to the background plasma parameters of electron density and magnetic field, the code requires multidimensional input of the underlying turbulence. Given a certain set of probing frequencies and launching angles it calculates the electromagnetic field of the wave and the I and Q signal that a Doppler reflectometer would measure. Due to solving Maxwell's equations, IPF-FD3D takes into account both the nonlinear power response [35] and the underestimation of the perpendicular velocity [156, 157].

# 5 Poloidally resolved measurements of the perpendicular velocity

The poloidal dependence of the perpendicular velocity measured by Doppler reflectometry, $v_\perp$, is believed to mostly follow the poloidal trend of the $E \times B$ velocity, since it dominates the measurement (c.f. Sec. 2.4 and Sec. 4.2). However, poloidal asymmetries of $v_\perp$ have been reported on the TEXTOR tokamak [160] using correlation reflectometry and on the Tore Supra tokamak [161] and the TJ-II heliac [162] using Doppler reflectometry, which cannot be explained by the poloidal variation of the $E \times B$ velocity. References [160, 161] find a faster plasma flow at the midplane than at the top and a decreasing asymmetry from the edge towards the plasma center. The poloidal asymmetry in Ref. [162] is particularly strong for low plasma densities and reverses depending on the magnetic configuration. Suggestions to explain the observed asymmetries range from ripple effects, viscous spreading of asymmetries from the plasma edge to the core or large scale asymmetric zonal flows in Ref. [161] to electrostatic potential variations across one flux surface in Ref. [162]. Nevertheless, a final explanation of the surprising poloidal asymmetries in the perpendicular propagation velocity of density fluctuations remains a subject of current research.

This chapter discusses measurements of the perpendicular velocity for an extended poloidal region in AUG. Due to hardware constraints all investigations use X-mode probing. Some theoretical considerations will, however, also include the O-mode. This chapter tightly follows the structure and argumentation of Ref. [163], which contains most of the results presented here.

## 5.1 Analysis of a sample discharge

A dedicated L-mode deuterium plasma discharge serves for measurements of the poloidal dependence of $v_\perp$. This plasma is nearly the same as the *steep gradient scenario* of Chap. 6, whereas the only difference lies in the density control, which leads to slightly different kinetic profiles.

### 5.1.1 Plasma scenario

Figure 5.1 shows time traces of important plasma parameters for the flat top phase under consideration. The constant plasma current and magnetic field are shown in Fig. 5.1(a). The ECRH, NBI and Ohmic heating powers are depicted in Fig. 5.1(b) together with the estimated radiated

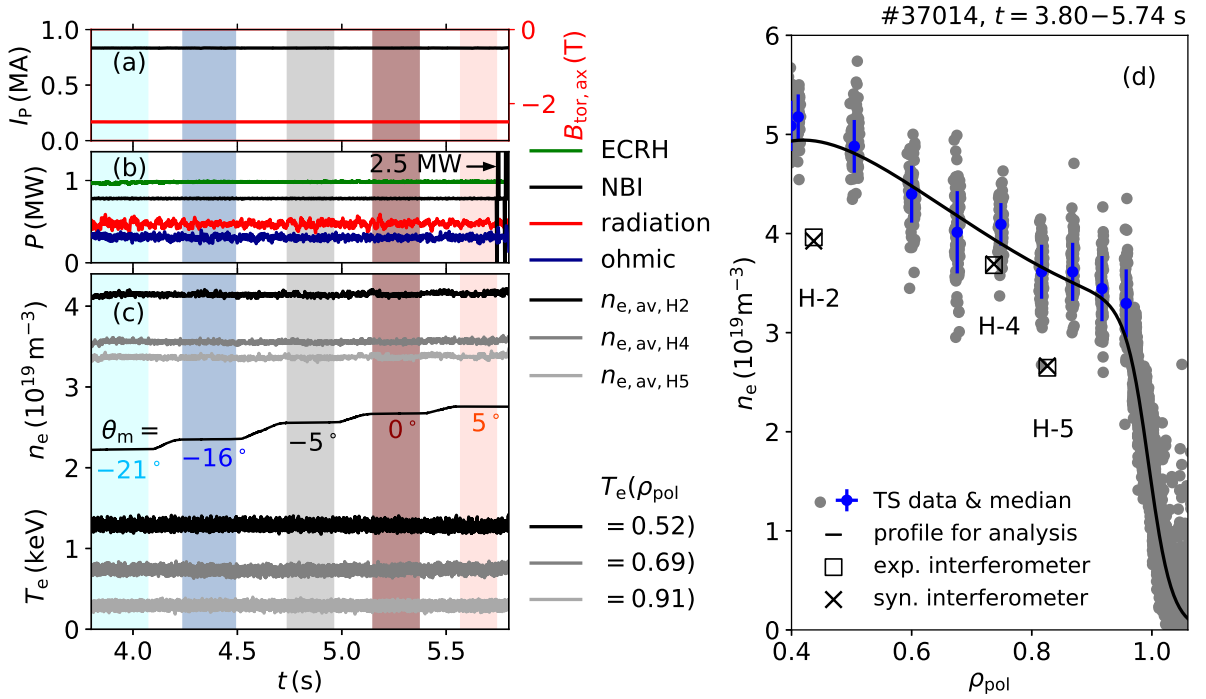


**Figure 5.1:** Time traces of important plasma parameters in the flat top phase under investigation: plasma current and magnetic field in (a), power sources and sinks in (b), orientation of the launching mirror of the Doppler reflectometer, electron temperature and density in (c). The density profile in (d) serves as input for localization of the measurement positions via ray tracing.

power in the confined region. The NBI blips at the end are required for CXRS measurements. The upper time traces in Fig. 5.1(c) show the line averaged density from three interferometers with different lines of sight. Time traces of the electron temperature at three radially different ECE channel locations are depicted in Fig. 5.1(c) at the bottom. To collect $v_\perp$ data at different poloidal angles, the mirror of the Doppler reflectometer system is steered to five different angles $\theta_m$. The middle of Fig. 5.1(c) indicates the corresponding mirror trajectory where the colored areas indicate phases of constant launching angle used for the subsequent analysis. The probing wave frequency is scanned in plateaus of 5 ms to obtain the radial measurement coverage within these time windows.

The input density profile for ray tracing determines, together with the magnetic field, the radial localization of the measurements and the resolvable turbulence scale. A commonly used fit function for kinetic profiles from AUG is the tanh, extended with polynomial functions. Details can be found in Refs. [164, 165], whereas this thesis uses polynomials up to $5^{th}$ order in the plasma core. Figure 5.1(d) depicts the fit as black line on top of Thomson scattering (TS) measurements in grey and their mean values in the core in blue. The time averaged measurement values of the three interferometer lines of sight are plotted as open squares. Their radial position corresponds to the innermost magnetic flux surface that is intersected by the corresponding interferometer channel. The spatial localization of both TS and interferometry uses the IDE equilibrium. The crosses depict the values of virtual interferometers applied on the modified tanh function,

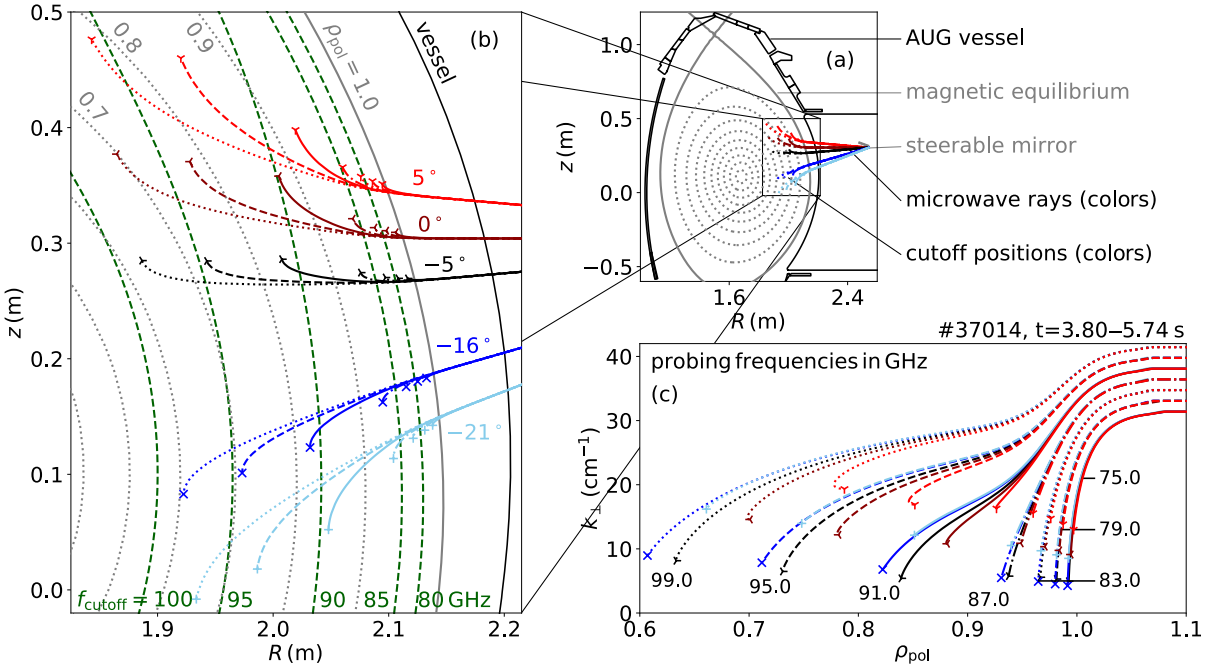


**Figure 5.2:** Poloidal cross-section of AUG in (a) and a zoom (b) with flux surfaces (grey) and vessel components (black). Microwaves are launched into the plasma with different mirror angles (red, black, blue) and different frequencies (line styles). The probed perpendicular wavenumber of the turbulence (twice the wavenumber of the wave, c.f. Eq. 4.3) in (c) decreases with beam propagation into the plasma.

demonstrating that it is in excellent agreement with the accurate experimental interferometer data. This underlines that TS and interferometer measurements are consistent.

### 5.1.2 Ray tracing

The density profile fit and the IDE equilibrium serve as input for simulation of the ray trajectory with TORBEAM. Since this study later focuses on the impact of ray tracing on poloidal asymmetries, the following discusses in detail the basics of this wave propagation through the plasma. Figure 5.2 depicts the ray paths for all five mirror positions and for seven sample probing frequencies. In addition, it illustrates the poloidal cross-section of AUG with the vacuum vessel in black and magnetic flux surfaces in grey. The different mirror angles are colored in blue, black and red, whereas the probing frequencies differ in line styles. All rays are launched from a common position on the rotation axis of the mirror. Figure 5.2(b) zooms into the measurement region and in addition to the before mentioned quantities shows the specific ray turning points as symbols as well as contour lines of the cutoff layers in green. Since the cutoff frequencies correspond to perpendicular incidence waves and thus $N = 0$, the ray trajectories with oblique incidence turn at larger radii for $N \to 0$. Due to the magnetic field dependence in the X-mode dispersion relation, the cutoff layers do not have the same shape as the magnetic flux surfaces, as would be the case for O-mode.

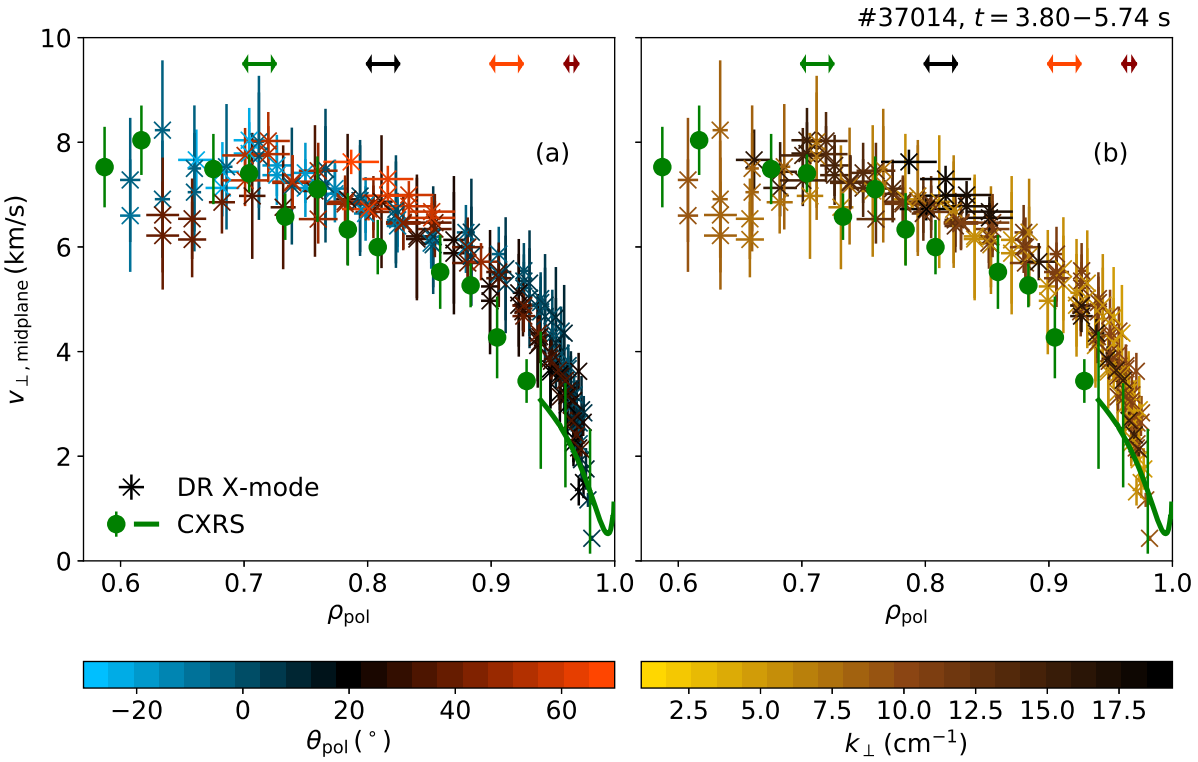


**Figure 5.3:** Radial profiles of the perpendicular velocity of density fluctuations mapped to the midplane. Colors in (a) refer to the poloidal angle, colors in (b) to the probed inverse structure size. There is no poloidal variation of $v_{\perp,\mathrm{midplane}}$.

Outside the plasma, all microwave trajectories of the same launching angle lie on top of each other as the refractive index is $N = 1$. They start bending when the refractive index reduces. Similarly, all rays of the same frequency have the same vacuum wavenumber regardless of the launching angle. Figure 5.2(c) illustrates how the probed turbulence wavenumber (i.e. twice the wavenumber of the microwave) depends on the angle of incidence and thus the path through the plasma. Note that for O-mode, all curves of $k_\perp$ versus $\rho_{\mathrm{pol}}$ coincide for the same frequency (not shown). Depending on the launching angle, the O-mode curves end at different wavenumbers and thus different radii. It is the additional magnetic field dependence of the dispersion relation in X-mode that makes the X-mode curves split apart for different angles but equal frequencies. The interplay between density and magnetic field in X-mode wave propagation will receive more attention in Sec. 5.3.3 where the influence of the density profile on the trajectories is discussed.

### 5.1.3 Poloidal dependence of the perpendicular velocity profile

The Doppler reflectometer measurement of the perpendicular velocity comprises $k_\perp$ at the cutoff position and the frequency shift between the injected and the backscattered microwave. The latter is extracted for each probing frequency using a Gaussian fit to the asymmetric part of the power spectrum of the backscattered wave, as discussed in Sec. 4.4.1. The radial profile of $v_\perp$ is shown in Fig. 5.3(a) and colorcoded with the poloidal angle. Note that the intrinsic poloidal

variation of $v_{E\times B}$ is taken into account using Eq. 2.8 to map all velocities on the midplane, in order to enable the search for effects other than the expected ones (c.f. Fig. 2.2).

The corresponding velocities $v_{\perp,\mathrm{midplane}}$ measured at different poloidal locations agree within the uncertainties from the 3-point ray tracing. They do not indicate any poloidal asymmetry beyond the trivial poloidal variation of the $E \times B$ velocity in Fig. 2.2. The density fluctuations propagate into the ion diamagnetic direction, which is clockwise in the poloidal cross-section in Fig. 5.2(b) and corresponds to a positive $E_r$ pointing radially outwards [166]. Towards the edge plasma the density fluctuations at the midplane move slightly faster than on the top, which is, however, within the uncertainties and in particular sensitive to the choice of the density profile, c.f. Sec. 5.3.3.

The same $v_{\perp,\mathrm{midplane}}$ data are shown in Fig. 5.3(b) colorcoded with the inverse turbulence scale $k_\perp$. Beams injected close to (far away from) perpendicular incidence probe large (small) turbulence scales. The clear conclusion from Fig. 5.3(b) is that different turbulence scales propagate with the same velocity $v_{\perp,\mathrm{midplane}}$. As all velocity data are mapped to the midplane taking into account the poloidal dependence of the $E \times B$ velocity, $v_{\mathrm{ph}}$ must either be much smaller than $v_{E\times B}$ and/or follow the poloidal dependence of $v_{E\times B}$ within the scatter of the data.

Additionally, Fig. 5.3 shows $v_{E\times B}$ measurements from the CXRS diagnostic (green) that agree with the velocity from Doppler reflectometry, but are systematically lower. Due to hardware availability, the core CXRS measurements (full circles) only include the toroidal rotation velocity and the pressure term, c.f. Eq. 3.4. The slight difference between CXRS and Doppler reflectometry is attributed to the poloidal velocity contribution in Eq. 3.4 and to the turbulence phase velocity in Eq. 2.7. However, it cannot be disentangled which of the two contributions dominates. The error bars combine measurement uncertainties of the toroidal velocity and the standard deviation of the data's scatter during the NBI blip. The edge CXRS measurements (green line) include the full $E_r$ from Eq. 3.3. The uncertainties are depicted at three representative radial locations and are larger than for the core as they include the scatter of the poloidal velocity measurements. The velocity measurements from Doppler reflectometry and CXRS agree within the error bars. Only one data point of the core system at $\rho_{\mathrm{pol}} = 0.93$ deviates by 26 % which might be due to the increasing impact of the poloidal velocity towards the edge. The good agreement supports the observation of small poloidal velocities in the core and points towards $v_\perp \approx v_{E\times B}$ and thus $\Leftrightarrow v_{\mathrm{ph}} \ll v_{E\times B}$.

Figure 5.4(a) visualizes the poloidal trend of $v_{\perp,\mathrm{midplane}}$ for four radial regions, which are indicated as arrows in Fig. 5.3. Again the intrinsic poloidal dependence of the $E \times B$ velocity is considered and the data is mapped to the midplane. The mean and standard deviation of all $v_{\perp,\mathrm{midplane}}$ within a radial interval are shown by dotted lines and shaded areas, respectively. Although $k_\perp$ largely varies with the poloidal angle, $v_{\perp,\mathrm{midplane}}$ is constant over the poloidal region covered by the Doppler reflectometer.

| # | | $B_{\mathrm{tor,ax}}$ (T) | $I_{\mathrm{P}}$ (MA) | $n_{\mathrm{e,av,core}}$ ($10^{19}$ m$^{-3}$) | $P_{\mathrm{ECRH}}$ (MW) | $P_{\mathrm{NBI}}$ (MW) |
|---|---|---|---|---|---|---|
| 37014 | USN | −2.5 | 0.8 | 4.2 | 1.0 | 0.8 |
| 37021 | LSN | −2.5 | 0.8 | 2.5 | – | 0.8 |
| 37465 | LSN | −2.5 | 0.8 | 4.9 | – | – |
| 37802 | USN | −2.5 | 0.9 | 5.2 | 0.7 | – |

**Table 5.1:** Key plasma parameters of the L-mode plasmas presented in Fig. 5.4.

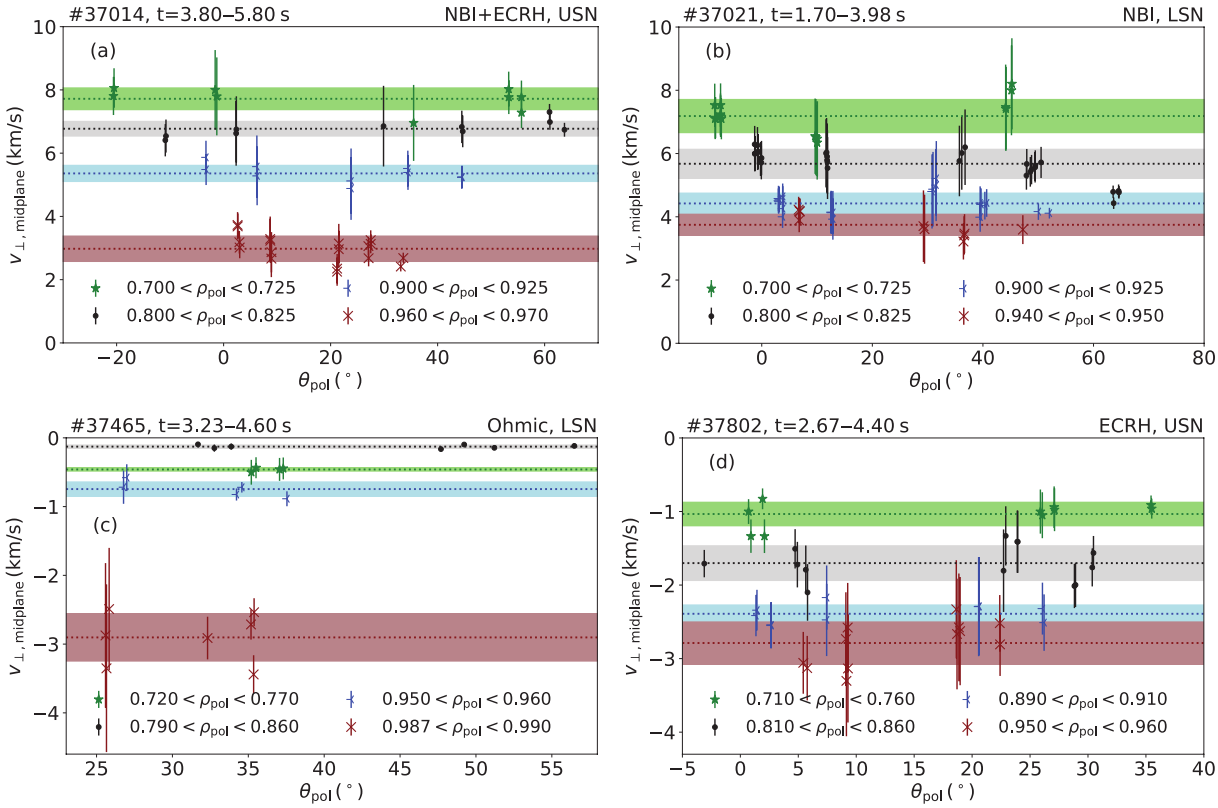


**Figure 5.4:** The perpendicular velocity mapped to the midplane versus the poloidal angle for four different L-mode plasmas. Magnetic configuration and heating method are varied between the plots. Colors correspond to the different radial intervals indicated in the legend. $v_{\perp,\mathrm{midplane}}$ does not depend on the poloidal angle outside the measurement uncertainties.

## 5.2 Measurements in various L-mode plasmas

Poloidally resolved measurements of $v_\perp$ were carried out in a variety of L-mode plasma scenarios. None shows poloidal asymmetries besides the intrinsic poloidal dependence of $v_\perp \approx v_{E\times B}$. The following discusses three representative discharges. Table 5.1 lists their key plasma parameters: they cover different magnetic configurations, USN and LSN, different heating mixes and a scan in density. $n_{\mathrm{e,av,core}}$ is the core averaged density from an interferometer with a central line of sight. The analysis of all discharges is identical to the analysis of discharge #37014 presented above. All discharges use the identical in- and ex-vessel Doppler reflectometry hardware system.

The corresponding perpendicular velocities mapped to the midplane are plotted in Fig. 5.4 versus the poloidal angle for different radial intervals. The different heating mixes (ECRH+NBI, NBI only, ECRH only, Ohmic) induce propagation velocities in both ion diamagnetic direction (ECRH+NBI in (a), NBI only in (b)) and electron diamagnetic direction (ECRH only in (d), Ohmic in (c)).

All four discharges confirm that – within the measurement region – $v_{\perp,\mathrm{midplane}}$ is not a function of $\theta_{\mathrm{pol}}$. Only the NBI heated discharge reveals a slight variation of $v_{\perp,\mathrm{midplane}}$ with $\theta_{\mathrm{pol}}$ for $\theta_{\mathrm{pol}} > 60°$. However, for this low density case the uncertainties associated to a variation of the electron density profile are particularly high. The variation is thus inside measurement errors and regarded insignificant. A discussion of these results is provided in Sec. 5.4.

## 5.3 Assessment of uncertainties of input for ray tracing

The observation that $v_\perp$ is not a function of $\theta_{\mathrm{pol}}$ depends sensitively on the magnetic equilibrium, the alignment and calibration of the optics and the density profile reconstruction. If not treated with care, each element can impose errors in the ray tracing and thus cause artificial poloidal asymmetries. This section quantifies the impact of uncertainties in the items mentioned above and their impact on the estimate of $\rho_{\mathrm{pol}}$ and $k_\perp$ via ray tracing, and thus on $v_\perp$ inferred from Doppler reflectometry measurements. It does not consider possible uncertainty propagation from the measurement and analysis of the Doppler shift of the backscattered signal to $v_\perp$, as these are regarded small compared to the impact of ray tracing. The change of the perpendicular velocity due to a change in $k_\perp$ is

$$\begin{aligned}\frac{\Delta v_\perp}{v_{\perp,\mathrm{ref}}} &= \frac{v_{\perp,\mathrm{test}} - v_{\perp,\mathrm{ref}}}{v_{\perp,\mathrm{ref}}} = \frac{2\pi f_{\mathrm{D}}/k_{\perp,\mathrm{test}} - 2\pi f_{\mathrm{D}}/k_{\perp,\mathrm{ref}}}{2\pi f_{\mathrm{D}}/k_{\perp,\mathrm{ref}}} \\ &= \frac{k_{\perp,\mathrm{ref}} - k_{\perp,\mathrm{test}}}{k_{\perp,\mathrm{test}}} = -\frac{\Delta k_\perp}{k_{\perp,\mathrm{test}}}.\end{aligned} \tag{5.1}$$

$v_{\perp,\mathrm{ref}}$ and $k_{\perp,\mathrm{ref}}$ are the reference perpendicular velocity and wavenumber (c.f. Figs. 5.2 and 5.3). $v_{\perp,\mathrm{test}}$ and $k_{\perp,\mathrm{test}}$ refer to the velocity and wavenumber based on ray tracing that is done for various optics positions, a different magnetic equilibrium or different density profiles. Equation 5.1 assumes that even though *ref* and *test* measure at different radii, they see identical Doppler shifts, $f_{\mathrm{D}}$, which is an approximation for velocity profiles that vary slowly with radius. Figure 5.5 illustrates the impact of the magnetic equilibrium, the optics alignment and the density profile on ray tracing for one representative radial position, $\rho_{\mathrm{pol}} = 0.8$, in discharge #37014. Each mirror angle is allocated a probing frequency that measures closest to $\rho_{\mathrm{pol}} = 0.8$. As shown in Fig. 5.3, the radial variation of $v_\perp$ is small at that radius, thus Eq. 5.1 holds in assuming the same $f_D$ for *ref* and *test*. The left plot focuses on the X-mode measurements that have been discussed so far. Even though no O-mode measurements were possible in the scope of this research, the study includes hypothetical O-mode data probing at the same radial position

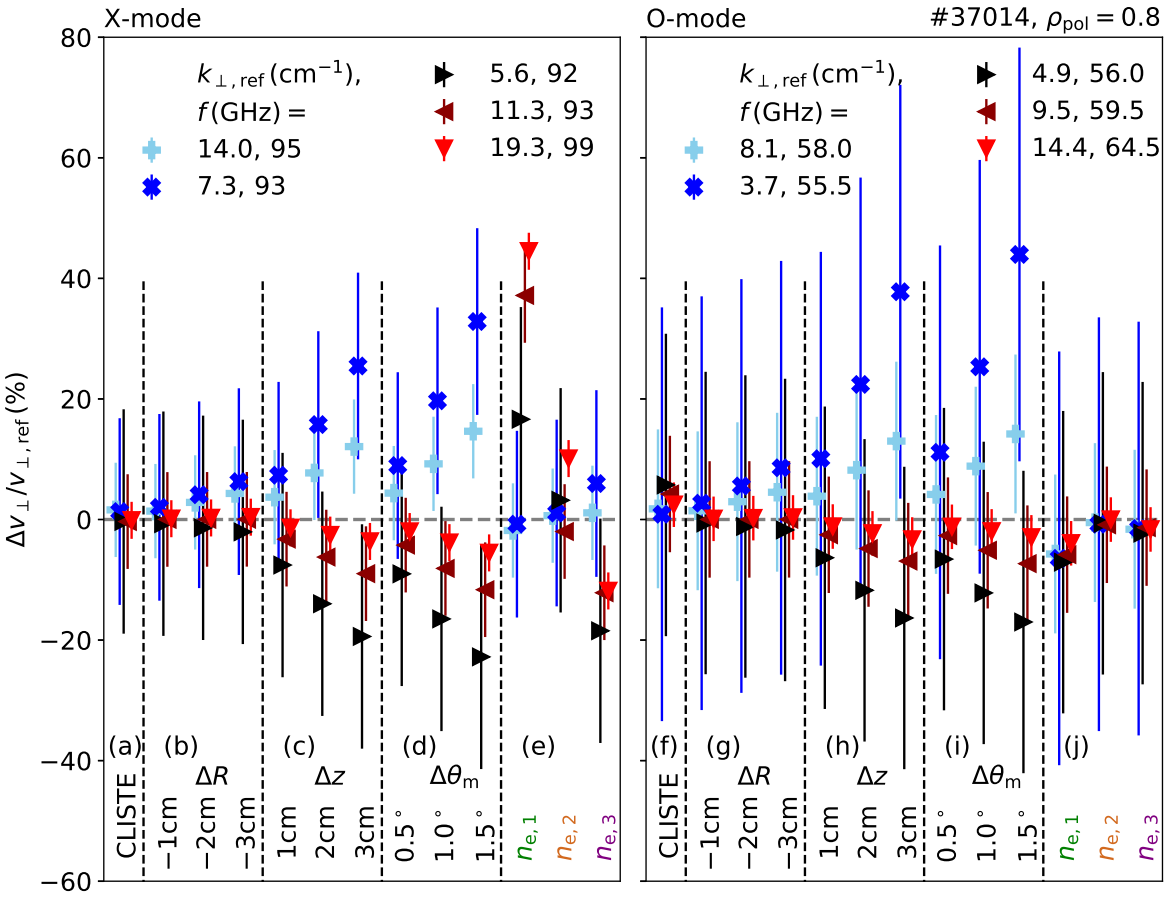


**Figure 5.5:** Relative perpendicular velocity changes caused by various effects: the choice of the magnetic equilibrium (a),(f), hardware misalignment in radial (b),(g) or vertical (c),(h) direction or with a systematic deviation in the injection angle (d),(i) or the choice of the density profile (e),(j). The distortion is strongest for small wavenumbers. X-mode measurements in (a)–(e) , O-mode measurements in (f)–(j).

in (b). A detailed discussion of the different features in Fig. 5.5 is done in the following. As before, the uncertainties are deduced using the 3-ray method on the reference case.

Since the discussion of more than one radial position is out of the scope of this thesis, the radial dependence of $\Delta v_\perp / v_{\perp,\mathrm{ref}}$ is briefly summarized here: misalignments in magnetic equilibrium and hardware impose velocity changes up to a maximum difference of 50 % with a slow radial variation. Velocity changes from the density reconstruction are comparable in magnitude and account up to 50 %, whereas the density profiles studied in the context of this thesis only impose velocity changes that are radially very localized.

### 5.3.1 Magnetic equilibrium

Both shape and location of the reconstructed magnetic flux surfaces influence the propagation of the microwave through the plasma. To assess the importance of their impact, two velocity profiles resulting from ray tracing using two different magnetic equilibria are compared: the above used IDE equilibrium and an equilibrium reconstructed with the CLISTE code [167],

which for this study does not take into account measured kinetic profiles but only considers measurements from magnetic diagnostics. Around $\rho_{\mathrm{pol}} = 0.8$ at the midplane of the low field side, the flux surfaces from the CLISTE equilibrium lie 1.5 cm radially outside the IDE flux surfaces (not shown). The relative change of the perpendicular velocity is within experimental uncertainties for both polarizations and is depicted in Figs. 5.5(a),(e). The observation that different equilibria influence the O-mode results stronger than waves in X-mode relates to the additional magnetic field dependence: X-mode waves are sensitive to both the magnitude and gradient of $B$ and via the density and its gradient to the shape of the flux surfaces, whereas O-mode waves only depend to the latter ones. Depending on which of these players changes to which extent, the two polarizations induce different velocity artifacts. In summary, both equilibria produce poloidally symmetric profiles and are equally suited for reconstructing perpendicular velocity profiles measured with Doppler reflectometry.

### 5.3.2 Hardware alignment

A misalignment of the antennas or the mirror system causes discrepancies in the localization of the cutoff position, since the beam is not injected from the radial and vertical position $R_0$ and $z_0$ with the injection angle $\theta_{\mathrm{m}}$ but from $R_0 + \Delta R$ and $z_0 + \Delta z$ with $\theta_{\mathrm{m}} + \Delta\theta_{\mathrm{m}}$. Figures 5.5(b)–(d),(g)–(i) depict the changes of the perpendicular velocity for misalignments $\Delta R$, $\Delta z$ and $\Delta\theta_{\mathrm{m}}$. Inaccurate antenna positioning in radial direction in (b) and (g) only slightly impacts the measured velocity, since the waves are launched far away from the plasma with a small angle to the horizontal plane. Thus, even a large inward shift of the launching mirror of the order of few cm causes deviations from the reference velocity profile that lie within the error bars. An erroneous antenna position in vertical direction in (c) and (h), however, can significantly impact the measured velocity. An unintended upwards shift of the launching mirror of $\Delta z = 1$ cm clearly distorts the velocity measurements, whereas for even larger offsets the deviations are outside the error bars. These deviations of the beam trajectory and thus of the measured $k_\perp$ are especially pronounced for small $k_\perp$, which coincide with small injection angles, $\theta_0$, with respect to the normal of the magnetic flux surface. Therefore, O-mode, which is probing at lower $k_\perp$ than X-mode, suffers more from hardware misalignments. This trend continues for deviations of the injection angle by $\Delta\theta_{\mathrm{m}}$, shown in Figs. 5.5(d),(i). Underestimating $\theta_{\mathrm{m}}$ by only 1° already leads to artificial asymmetries of the measured velocity outside the uncertainties. The sign of the distorted $k_\perp$ and thus the direction of velocity deviation depends whether the beam is launched above or below perpendicular incidence (perpendicular incidence corresponds to $\theta_{\mathrm{m}} \approx -10°$).

The position and alignment of the in-vessel mirror can only be determined in air and without magnetic field. The position of the mirror has uncertainties of 2 mm for $R$ and $z$ and 0.04° for $\theta_{\mathrm{m}}$. The uncertainties include the finite beam size of the optical laser used for calibration and the uncertainties of the three-dimensional measurement arm. After evacuation and baking, the AUG vacuum vessel distorts 0.7 mm in vertical direction and 0.7 mm in radial direction at the A-port of sector 9. Due to axisymmetry, this measurement also applies to sector 11, where the Doppler reflectometer is installed. The discussion of errors in the hardware alignment also

holds for the reversed case of a possible misplaced plasma equilibrium in horizontal or vertical direction. In summary, hardware misalignment, in particular deviations in the launching angle, can significantly distort the measured velocity and thus cause artificial asymmetries. The AUG calibration technique has measurement uncertainties of $\Delta\theta_\mathrm{m} = 0.04°$, whereas Figs. 5.5(b)–(d),(g)–(i) suggest that only distortions of the order of $\Delta\theta_\mathrm{m} = 0.5°$ cause artificially asymmetric velocity profiles outside of the error bars.

### 5.3.3 Density profiles

The beam propagation and $k_\perp$ of X-mode measurements depend on the local refractive index $N$ and its gradient $\nabla N$ and thus on the local electron density $n_\mathrm{e}$ and electron density gradient $\nabla n_\mathrm{e}$. For X-mode $N$ is additionally a function of the local magnetic field $B$, thus a variation of the density profile causes an artificial poloidally asymmetric change of the cutoff frequency. A change of the density thus induces artificial poloidally asymmetric changes of $k_\perp$ and consequently $v_\perp$. Doppler reflectometer measurements in low-density plasmas are particularly sensitive to deviations in the plasma density. The reason is that for low $n_\mathrm{e}$ the derivative of the cutoff frequency with respect to the density is higher than in high-$n_\mathrm{e}$ plasmas, c.f. Eq. 4.2. It is thus the interplay between density and magnetic field contributions to $N$ that causes more artificial asymmetries the more $B$ dominates $N$, i.e. for high $B$ or low $n_\mathrm{e}$. The other extreme case, where $n_\mathrm{e}$ fully dominates $N$, is O-mode probing, which does not suffer from artificial asymmetries caused by the choice of density profile.

To illustrate the influence of the density profile on poloidally resolved Doppler reflectometer measurements, three sample density profiles serve as input for ray tracing. They are snapshots at single points in time of the density analysis done by the IDA framework. Hence, they lie within experimental measurement uncertainties. However, both their absolute values as well as gradients differ significantly. Figure 5.6(a) depicts these profiles in colors and (b) shows the corresponding gradients with respect to the minor radius at the midplane. It must be pointed out that they are not the most likely profiles within the flat top phase of interest. Figure 5.6 also plots the TS and interferometer data for comparison, using the same conventions as in Fig. 5.1(d). For the sake of visibility, the experimental (squares) and synthetic (crosses) interferometer measurements of the different density profiles lie at slightly different radii. The radial region with the largest impact on the ray path and thus on $k_\perp$ is situated close to the cutoff, at slightly larger radii.

The impact of the choice of a density profile on poloidally resolved X-mode Doppler reflectometry measurements is plotted in Fig. 5.5(e). The green profile $n_\mathrm{e,1}$ has a flat gradient from $\rho_\mathrm{pol} = 0.85$ inwards and thus causes a strong artificial velocity asymmetry at $\rho_\mathrm{pol} = 0.8$. The $v_\mathrm{\perp,test}$ data on the left of Fig. 5.5(e) and the reference agree well at the midplane, but strongly deviate with increasing poloidal angle. The reason for the larger difference far from the midplane is the alignment of the cutoff layers of the two contributions: magnetic field and density. At the midplane they are aligned, but become increasingly misaligned for large poloidal angles (c.f. flux surfaces and cutoff layers in Fig. 5.2(b)). Thus, if changing only one of the contributions, here

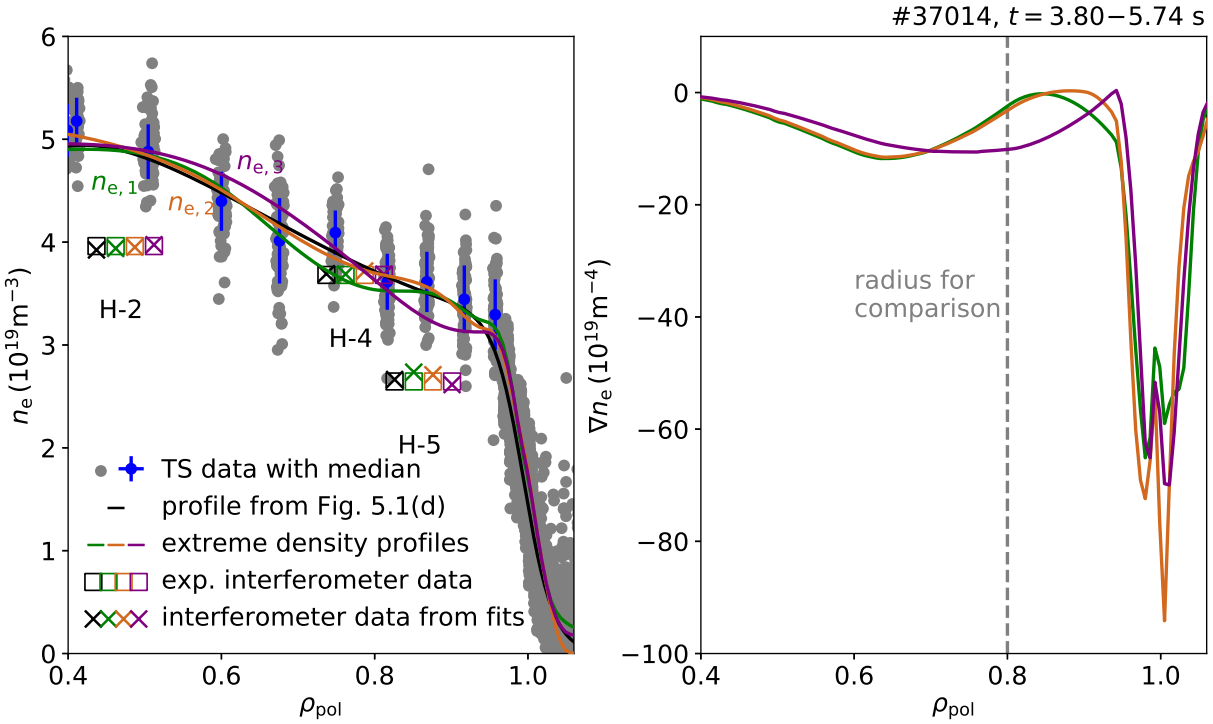


**Figure 5.6:** (a): The density profile from Fig. 5.1(d) in black on top of the TS measurement data in grey. Extreme IDA density profiles in colors. The squares depict interferometer measurements averaged over the flat top phase, × indicate synthetic interferometer measurements using the IDA density profiles. (b): the corresponding density gradients.

the density, the impact on the shape of the cutoff layer is stronger when they are misaligned. Profiles such as $n_{e,2}$ in orange cause less pronounced changes to $\Delta v_\perp / v_{\perp,\mathrm{ref}}$, since the density gradient outside and at $\rho_{\mathrm{pol}} = 0.8$ is similar to the gradient of the modified tanh function used for the reference velocity, c.f. Fig. 5.5(e) in the middle. The steep gradient of the purple density profile $n_{e,3}$ on the right of Fig. 5.5(e) induces reversed artificial asymmetries where the region above the midplane seems to propagate slower than the midplane. Again the poloidal region that is influenced most by the change in density of $n_{e,2}$ and $n_{e,3}$ is far from the midplane. Opposed to the equilibrium and hardware alignment where the artificial asymmetry varies slowly with radius, the density profile can result in very localized deviations from the reference velocity that mostly depend on the density gradient. The poloidally asymmetric $B$ causes measurements far from the midplane to particularly react on the density profile reconstruction, whereas measurements close to the midplane are more robust.

Figure 5.5(j) confirms the above discussion that measurements in O-mode do not suffer from artificial poloidal asymmetries that source from the density profile. Different density profiles impose an offset on the measured velocity that is common for all poloidal positions. Note that in Fig. 5.5(j) this offset slightly varies between the different $k_\perp$ since here the frequencies have 0.5 GHz resolution and thus do not all probe perfectly at $\rho_{\mathrm{pol}} = 0.8$.

To sum up, the density profile has the potential to induce significant velocity deviations in X-mode Doppler reflectometer measurements. There is in particular the representative case $n_{e,1}$,

where these velocity changes show a monotonic dependence on the poloidal angle and could be mistaken for a physics-based poloidal trend. Due to the different dispersion relation, O-mode measurements remain unaffected.

### 5.3.4 Intrinsic uncertainties from diagnostic effect

The diagnostic effect introduced in Sec. 4.5.2 can introduce artificial poloidal asymmetries, since the rotation of the turbulence field is slightly underestimated depending on the probed structure size. As this study does not find poloidal asymmetries, the diagnostic effect seems to be negligible or within uncertainties in these particular studies. This small impact of the diagnostic effect can have several reasons: first, the diagnostic effect influences in particular measurements at small $k_\perp$, which, since this study uses X-mode measurements, might not be reached. Second, a slowly decaying $k$-spectrum leads to a small influence of the diagnostic effect. For the discharges under investigation the shape of the $k$-spectra could not be accessed in experiment due to the limited lengths of the flat top phase. However, since Doppler reflectometry probing in X-mode in L-mode discharges tends to lie in the nonlinear power response regime, the effective $k$-spectra can well be relatively flat. The nonlinear power response regime in particular flattens the low $k_\perp$ range and thus counteracts the characteristic of the velocity diagnostic effect to be more pronounced at low $k_\perp$.

## 5.4 Discussion

The study in this chapter observes that the propagation velocity of density fluctuations perpendicular to the magnetic field only follows the poloidal trend of the $E \times B$ velocity. This finding agrees with the current model of the poloidal dependence of $v_\perp$ if $v_{\mathrm{ph}} \ll v_{E\times B}$ (which is usually fulfilled, c.f. Sec. 4.2). It, however, differs from reports from TEXTOR, Tore Supra and TJ-II where asymmetries have been found [160–162]. References [160, 161] see asymmetries that increase towards the edge when comparing top and midplane. Reference [162] observes a variety of asymmetries that reverse depending on the magnetic configuration. The question, why dedicated AUG studies do not find asymmetries other than studies at different machines remains unsolved. Velocity deviations up to a factor of 4, such as seen at Tore Supra, are outside of any conceivable error bars. Similar arguments apply to TJ-II studies that report velocity deviations up to a factor of 2.5 in addition to poloidally asymmetric density fluctuation amplitudes.

Due to hardware constraints, the AUG studies are restricted to a smaller poloidal range than Refs. [160–162], in particular towards the edge. Nevertheless, the measurements in the accessible region do not point towards a poloidal trend that would be expected if asymmetries were as pronounced as in Refs. [160–162]. A currently commissioned top launch reflectometer will shed more light on a poloidally extended region up to $\theta_{\mathrm{pol}} \approx 90°$ [168].

First AUG studies in the 2019 campaign [169] reported poloidal velocity asymmetries, which has to be put in context. These initial measurements had to rely on a launching mirror optimized for monostatic operation, but operated in bistatic. Thus, to obtain overlap of the emitting and receiving ray at the cutoff, a non-zero parallel component of the wavevector was necessary. The latter possibly resulted in a poloidal distortion particularly critical for small $k_\perp$.

The error bars in Fig. 5.3 and Fig. 5.5 give an optimistic lower limit for the magnitude of asymmetries that Doppler reflectometry can resolve. These uncertainties are estimated by the 3-ray method and are largest at small wavenumbers and decrease with increasing $k_\perp$. Velocity measurements close to perpendicular incidence are thus particularly sensitive to artificially induced asymmetries. Whereas hardware misalignment produces systematic asymmetries, the magnetic equilibrium and the density profile reconstruction potentially impose asymmetries that vary on a shot to shot basis.

More studies from different machines combining different diagnostics would be desirable to further study the poloidal dependence of the perpendicular velocity. This could include comparisons between Doppler reflectometer measurements and poloidal correlation reflectometer measurements. Additionally CXRS measurements that can experimentally access the full radial electric field (c.f. Eq. 3.3) in the core, such as done in Ref. [94], would be beneficial. Machines that find asymmetries depending on the plasma scenario could perform scans of different parameters, such as density and heating power, to address the underlying mechanisms for possible asymmetries.

# 6 Experimental measurements for code validation

A profound code validation effort needs well characterized experiments in the first place. To this end, this chapter presents measurements of several turbulence quantities in two slightly different plasma scenarios. The idea is to not only compare one plasma scenario to simulation outputs, but further constrain validation by including a variation of turbulence quantities with background plasma parameters that forces the gyrokinetic simulations to additionally model trends between different turbulence regimes. For these turbulence investigations, it is not only the turbulence quantities that are of interest, but also the knowledge of kinetic profiles and heat fluxes. Therefore, this chapter first introduces general plasma parameters of the scenarios under investigation, such as kinetic profiles of electron and ion temperature, electron density and toroidal rotation, as well as heat flux profiles. Next it discusses the diagnostic settings of Doppler reflectometry and CECE radiometry to both carefully and efficiently measure a large set of turbulence parameters. The major part of this chapter consists of a profound experimental investigation of these turbulence quantities. The final section focuses on additional plasma scenarios and discusses the reaction of turbulence to further gradient variations.

## 6.1 Plasma scenarios

The turbulence measurements are carried out in two slightly different L-mode deuterium plasmas, which have to be matched by simulations. This improves the validation by adding the trends between the scenarios as constraints for a match. The approach to change kinetic gradients by variation of the heating and to measure the impact on turbulence parameters has already been employed by previous studies at DIII-D [170–174] and at AUG [138]. For the two plasmas in this thesis, all external control parameters but one are identical. The deposition location of the ECRH power is varied. This results in different electron temperature gradients and also affects the profiles and gradient of the electron density, ion temperature and toroidal rotation. The magnetic equilibrium, the total heating power and the line averaged density do not change significantly. A sketch of the ECRH deposition profiles is shown in Fig. 6.1. Heating only inside (red solid line) or only outside (blue solid line) the measurement region (shaded in grey) produces two scenarios of different kinetic gradients and therefore different turbulence drive. The dashed lines indicate the steeper and flatter electron temperature profiles resulting from the heating location variation. In the following the two scenarios will be termed *steep* (red colors) and *flat*

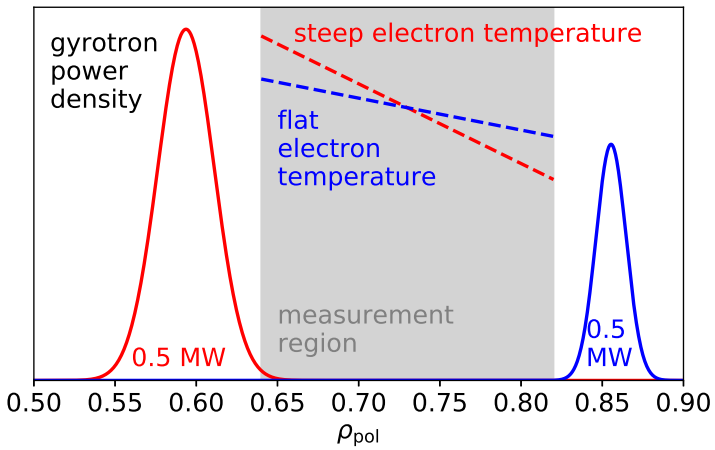


**Figure 6.1:** Sketch of the heat deposition and electron temperature profile variation: the heating location and thus the electron temperature profiles differ between the two scenarios and lead to a different mixture of turbulence instabilities.

(blue colors) profile scenario with the ECRH position inside and outside the measurement region, respectively.

### 6.1.1 Scenario development

When designing the two plasma scenarios, several constraints have to be met in order to ensure

1. fully developed plasma turbulence, which allows meaningful turbulence measurements,
2. spatial overlap between the sensitive area of the turbulence diagnostics and the region of interest between the deposition locations and
3. turbulence conditions, which maximize the signal to noise ratio for the turbulence diagnostics.

Criterion 1 is met by using a plasma in L-mode. This in turn sets an upper limit to the external heating power. 0.5 MW of ECRH power is used for the temperature gradient variation as indicated in Fig. 6.1, plus an additional 0.8 MW of NBI power (see criterion 3). In LSN this amount of heating power does not produce an L-mode plasma, thus the discharges use the USN magnetic configuration. Due to the different upper divertor conditions, an additional gyrotron at 0.5 MW must heat in the central plasma to avoid tungsten accumulation.

The turbulence measurements are carried out using Doppler reflectometers in O-mode (measurement location density-dependent) and X-mode (density- and magnetic field-dependent) as well as CECE radiometers (magnetic field-dependent). Thus, criterion 2 constrains the magnetic field strength and equilibrium, as well as the electron density.

Focusing first on Doppler reflectometer signals, criterion 3 requires NBI heating: the beams drive plasma rotation and thus increase the separation between the Doppler shifted signal of interest and a possible DC component of the spectrum. On the CECE side, criterion 3 constrains the density, as temperature fluctuations decrease for increasing density. This last point turns out to be the most challenging one, as CECE favors low density and thus directly conflicts with localizing the O-mode Doppler reflectometers (criterion 2), which needs the density to be above a certain threshold. As a compromise the lowest possible electron density to still enable O-mode measurements is used. This inevitable compromise is only just met, as will be seen in the following sections: the electron temperature fluctuations are at the limit of what can be experimentally resolved with the AUG CECE system. Note that for the Doppler reflectometer there is no negative impact from the choice of density, since any density value above the cutoff – and below the density that corresponds to the highest probing beam frequency – is sufficient.

### 6.1.2 Time traces

In order to measure the comprehensive set of turbulence data, which will be analyzed in the following, a number of identical plasma discharges are carried out. For a detailed discussion why all turbulence quantities presented in this thesis cannot be measured in only one plasma discharge, refer to Sec. 6.2. Most of the discharges have been carried out consecutively on the same day. Due to diagnostic availability, a small set of turbulence measurements has been performed later in reproducible plasma discharges. All time traces and kinetic profiles shown in the following correspond to measurements on the first and major set of discharges. All simulations that are to follow are based on them.

The time traces of several key plasma parameters are shown in Fig. 6.2 for both scenarios. Red/blue colors correspond to discharge #38420/#38423 in the steep/flat profile case, respectively. The measurement phase during the stationary flat top phase is indicated by vertical grey lines. Figure 6.2(a) shows the toroidal plasma current, the on-axis toroidal magnetic field and the safety factor at 95 % of the normalized poloidal flux radius. They do not differ between scenarios, such that sometimes the lines from the flat scenario hide those of the steep scenario. The heating power (ECRH, NBI, Ohmic) and the power loss from radiation inside the confined plasma region are depicted in Fig. 6.2(b) and do not strongly deviate either. Time traces of the line averaged density measurements from a core and an edge interferometer channel are depicted in Fig. 6.2(c). The discharge was performed using density feedback control on the core interferometer channel to ensure a stationary density during the measurement phase and to obtain comparable densities in the two scenarios. Due to the impact of the ECRH deposition location on the density peaking, the edge interferometer measurements inevitably differ between the scenarios. Figure 6.2(d) shows the magnetic flux surfaces at $\rho_{\mathrm{pol}} = 0.1, 0.2, ..., 0.9, 1.0$ from the IDE equilibrium. No significant differences between the scenarios can be observed.

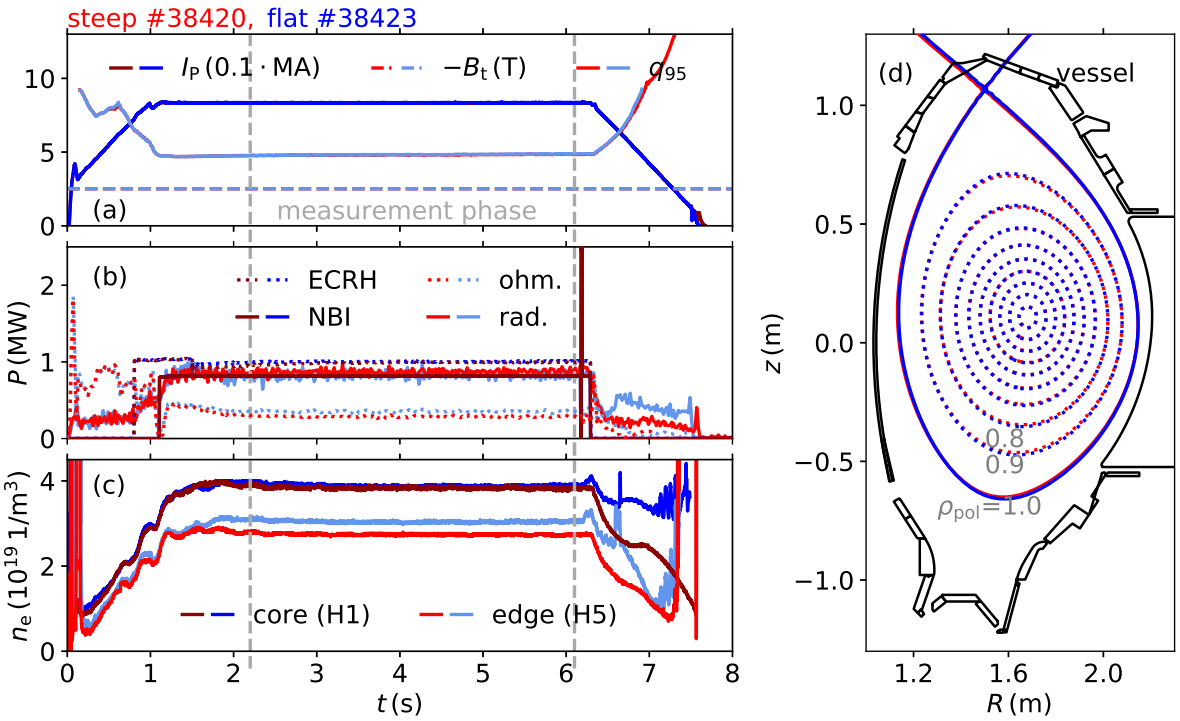


**Figure 6.2:** (a)–(c): Time traces of important plasma parameters of the steep (red) and the flat electron temperature profile discharge (blue). The magnetic equilibria (d) lie on top of each other.

### 6.1.3 Kinetic profiles

In the following the profiles of electron temperature and density, ion temperature and toroidal rotation are presented. The kinetic profile data of the steep scenario comes from #38419–21, in the flat scenario from #38419,22–23.

Figure 6.3(a) shows the ECE radiometer and TS diagnostic data of $T_e$ as dots. They include *all* measurement data from all discharges over the full flat top phase under consideration to illustrate the excellent reproducibility of the plasmas. For the sake of visibility, the median of 10 points is plotted. The edge TS diagnostic is radially shifted outwards by 6 mm in order to match the temperature profile as measured by ECE, such as routinely done at AUG. Figure 6.3(a) confirms the qualitative discussion of Fig. 6.1 that more central heating leads to steeper electron temperature profiles. TS measurements of $n_e$ are plotted in Fig. 6.3(b) with the same radial edge TS shift as discussed for $T_e$. Again, only every tenth point is plotted here. These measurements confirm the interferometer observation in Fig. 6.2(c) that the steep scenario exhibits lower $n_e$ at $\rho_{pol} = 0.95$. This behavior of density peaking agrees with previous studies on the effect of ECRH on the density profile [175] and has already been reported in past AUG studies of the change of the electron density fluctuation amplitude with the ECRH power [138]. $T_i$ data from CXRS is depicted in Fig. 6.3(c). The necessity to stay in L-mode prohibits to constantly operate an NBI beam at full power, thus 20 ms beam blips are used for CXRS measurements. As they come on top of 0.8 MW of background NBI power, no considerable distortion of the plasma temperature or rotation is observed during their on-time. The high-$T_e$ scenario goes in hand with a higher

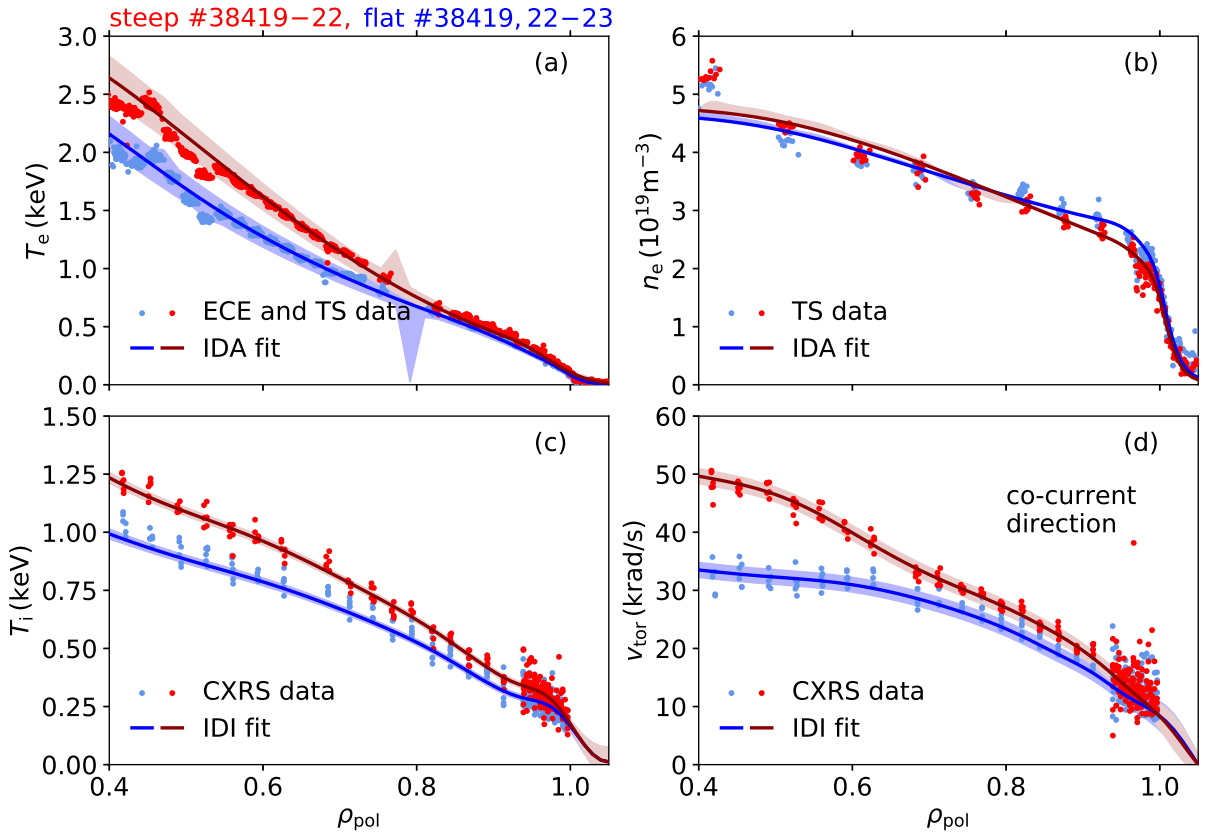


**Figure 6.3:** Profiles of the electron temperature (a), electron density (b), ion temperature (c) and toroidal rotation velocity (d) in the steady state measurement phases. The fits serve as input for simulations in Chap. 7.

$T_i$, as energy between both species is transferred via collisions. The toroidal rotation velocity measured by CXRS is shown in Fig. 6.3(d). The positive sign corresponds to a rotation in co-current (with respect to the plasma current) direction. The toroidal rotation shows a significant difference between both scenarios, which is, however, most pronounced at smaller radii than in the measurement region. Due to practical reasons, there are no measurements of the ion density available. This lack of information can be resolved by the plasma's quasi-neutrality and the effective charge state, $Z_{eff}$. In the steep scenario $Z_{eff} = 1.8$ and in the flat scenario $Z_{eff} = 1.7$.

As the turbulence simulations from GENE sensitively depend on all of these four quantities as input, several data fitting techniques have been investigated carefully and compared to each other. Polynomial fits of different order over both full radial profiles and parts of it, a commonly used fit at AUG with a modified tanh (which is especially suited for edge modeling), Gaussian process regression, spline fits on the measurement data and integrated data analysis were considered. Going through the pros and cons of all of them is out of the scope of this work, for which reason only the finally chosen method shall be motivated in the following.

In this work, integrated data analysis (c.f. Sec. 3.2.6) is the most convenient fitting technique because of the standardized work flow, the explicit use of probabilistic priors and the inclusion of various diagnostic forward models. The routine IDA provides profiles of $T_e$ and $n_e$ that

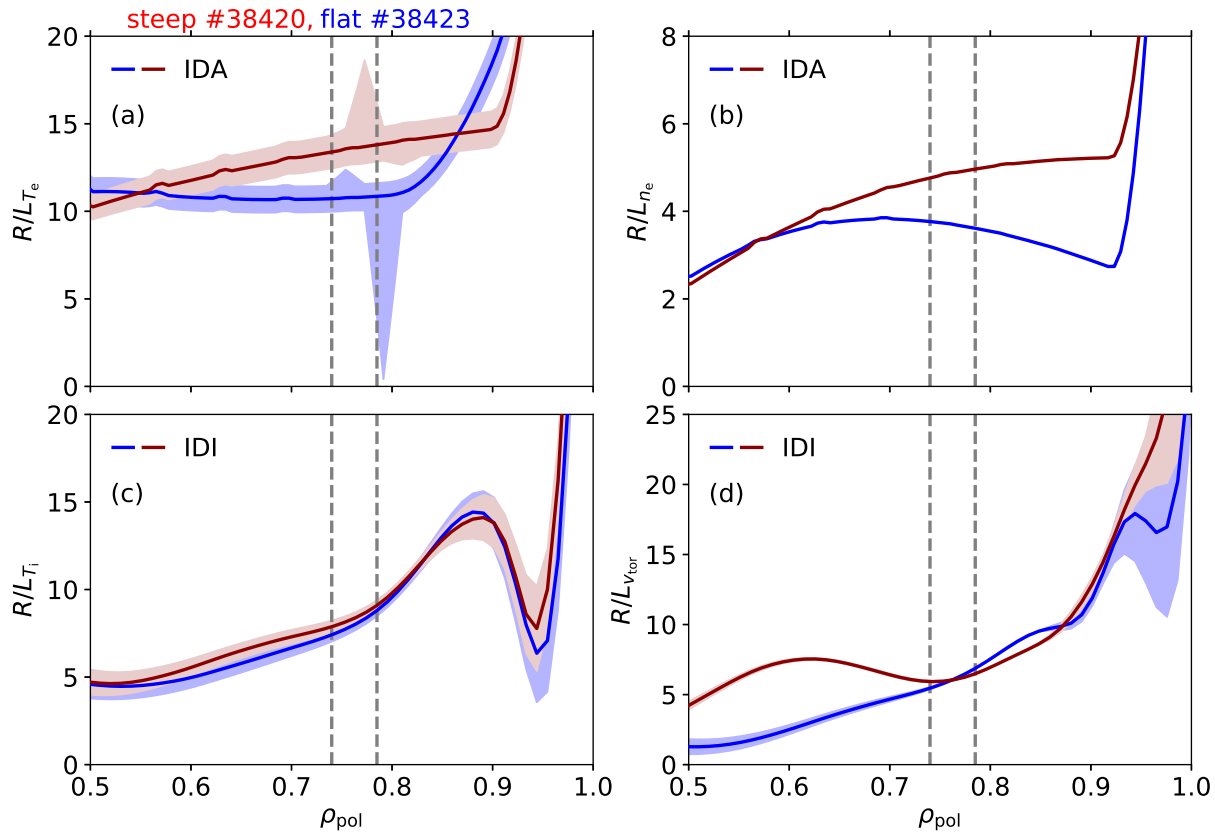


**Figure 6.4:** Radial profiles of the normalized gradients (c.f. Sec. 2.3) of electron and ion temperature (a),(c), electron density (b) and toroidal rotation velocity (d) of the two plasma scenarios.

| | change of | | | |
|---|---|---|---|---|
| $\rho_{pol}$ | $R/L_{T_e}$ | $R/L_{T_i}$ | $R/L_{n_e}$ | $R/L_{v_{tor}}$ |
| 0.740 | +11 % | +3 % | +12 % | +4 % |
| 0.785 | +12 % | +2 % | +16 % | −3 % |

**Table 6.1:** Relative change from the steep to the flat scenario of the normalized gradients for the two radii at which GENE simulations are done.

have a large number of radial spline knots ($T_e$: 19, $n_e$: 14) in order to give good estimates of the absolute values. The resulting gradients, however, strongly vary with radius. For gradient estimation, a strong radial variation points towards overfitting of the profiles and is not desired. Hence, for the present study a special set of IDA inputs has been developed which is particularly suited for GENE simulations due to a different radial spline knot spacing and its larger time average. Care is taken to make sure not to lack physics features in the profiles by not reducing the number of knots too much. After diligent analysis, the conclusion is that 10 knots for $T_e$ and 8 knots for $n_e$ produce the best compromise between accurate absolute values and gradients that vary smoothly with radius, whereas a time average of 400 ms turns out to be adequate. The uncertainties in the IDA profiles encompass only the uncertainties in the measured data

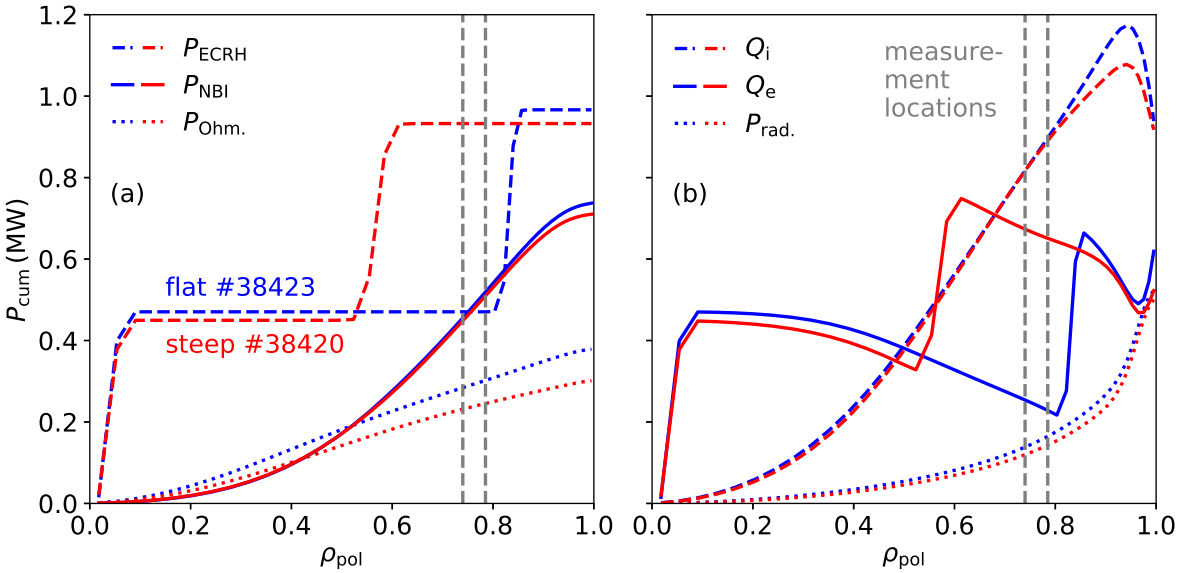


**Figure 6.5:** Radially integrated power sources (a) and heat fluxes and power loss (b) for both scenarios. For details refer to the text.

using the typical spatial resolution of the measurements. No uncertainties concerning the spatial coordinates of the measurements or uncertainties in the calibration are considered. The $T_i$ and $v_{tor}$ profiles are taken from the standard IDI evaluation. The fits shown in Fig. 6.3(b),(d) are the time average of all profiles within discharges #38419–23 to compensate the short measurement time during the NBI blip. The uncertainties are results of the Gaussian process regression of the IDI analysis. Note that the spatial mapping of all measurement data and corresponding fits mentioned above uses the IDE magnetic equilibrium.

The relevant physics quantity is the normalized gradient $R/L_X$ with $L_X = X/\nabla X$ (c.f. Sec. 2.3) of the kinetic profiles. It is shown in Fig. 6.4 for $T_e$ (a), $T_i$ (c), $n_e$ (b) and $v_{tor}$ (d) for both scenarios. The grey lines indicate the two radial locations where experimental measurement data will be compared to GENE simulations: $\rho_{pol} = 0.740$ and $\rho_{pol} = 0.785$. The normalized electron temperature gradient is larger for the steep profile scenario than for the flat one. As suggested by Fig. 6.2(b), also the normalized density gradient increases. The normalized gradients of $T_i$ and $v_{tor}$ do not change within the uncertainties in the measurement region. Table 6.1 lists the relative changes of the normalized gradients for both radial positions where GENE simulations are performed (dashed lines in Fig. 6.4) when going from the flat to the steep scenario.

### 6.1.4 Heat flux profiles

The experimental heat fluxes are of particular interest for code validation as they need to be reproduced by the turbulence simulations. Here they are calculated by the interpretative transport code TRANSP [176, 177] using the above shown kinetic profile fits as input. All power sources are shown in Fig. 6.5(a) versus radius as radially integrated values. Note that the slight difference

in the ECRH power magnitudes between the scenarios sources from slightly different gyrotron powers and tiny differences in temperature, density and magnetics. Figure 6.5(b) depicts the ion heat flux (dashed), the electron heat flux (full) and the radiated power (dotted). The electron heat flux follows roughly the curve of the radially integrated ECRH power. Its decrease with radius indicates two effects: heat transfer from electrons to ions and power losses of the electrons via radiation. The first simultaneously increases the ion heat flux. The ion heat flux resembles the radial shape of NBI and Ohmic heating, since ECRH only heats the electrons.

## 6.2 Diagnostic settings to measure various turbulence quantities

This section introduces the different settings of the two turbulence diagnostics used for this study, Doppler reflectometry and correlation electron cyclotron emission radiometry.

### 6.2.1 Doppler reflectometry settings

Doppler reflectometers are active diagnostics and can thus in general operate in a variety of different settings. The settings mainly depend on the particular turbulence quantity of interest, but also strongly vary with plasma scenario, radial region of interest and the time in which stationary plasma conditions are expected. In the context of this study all turbulence quantities accessible with Doppler reflectometry shall be measured for both scenarios. Investigating all of them within the full radial and poloidal measurement region accessible with the current Doppler reflectometer hardware (two V-band and one W-band on a common launching antenna) would need a multiple of the available discharge time. Thus, optimized diagnostic settings are necessary to obtain as much information as possible within a limited amount of time. The best choice of frequency and mirror patterns are shown in Figs. 6.6(a)–(i) for three different measurement procedures of interest. The corresponding measurement positions are indicated in the poloidal cross-sections in Figs. 6.6(j)–(l). The peculiarities of each case are listed in Tab. 6.2 and discussed in the following.

*Poloidal dependence of $v_\perp$:* These settings cover the whole radial and poloidal measurement region accessible (c.f. Fig. 6.6(j)) by stepping from the lowest frequency to the highest frequency available (X-mode with W-band in (a)) or highest frequency that can measure at a location where turbulence can be resolved (O-mode with V-bands in (d)). The perpendicular propagation velocity of electron density fluctuations, $v_\perp$, and the fluctuation level, $S$, are thus measured on a rough radial grid. The frequency patterns shown in (a) and (d) are repeated twice for each of the six constant mirror position (flat regions in (g)). Similar settings have been used extensively for studies of the poloidal dependence of $v_\perp$ in Chap. 5.

*k-spectra:* The frequency patterns in (b) and (e) repeat while the mirror moves slowly in (h). Following Eq. 4.4, the same frequency probes at larger radii for larger angles of incidence. This constrains the minimum and maximum frequency of the pattern, to make sure that the $\rho_{\mathrm{pol}}$ of

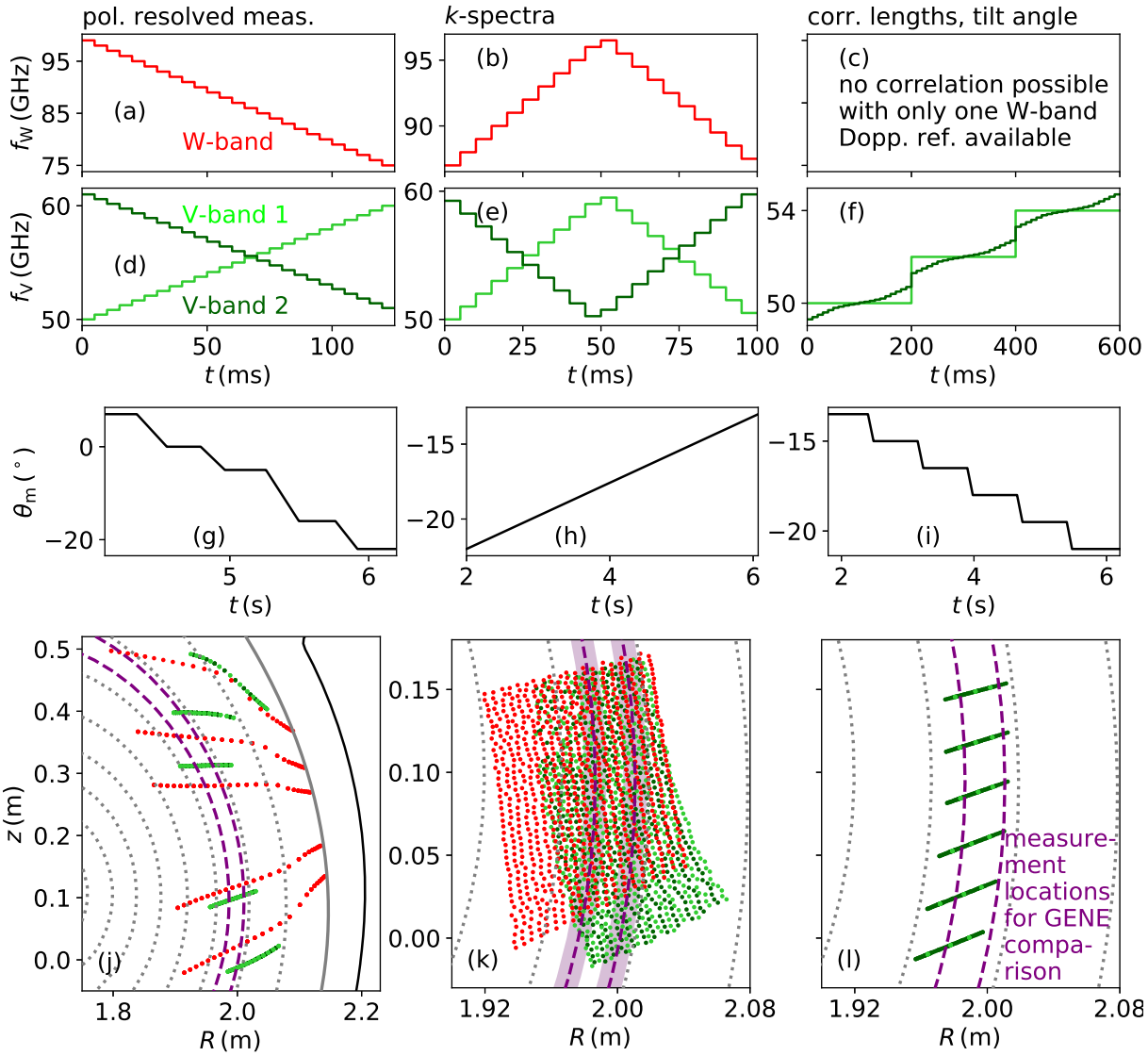


**Figure 6.6:** Doppler reflectometer settings for measurement of: poloidal dependence of the perpendicular velocity (left column), wavenumber spectra (center column), correlation lengths (right column). The frequency patterns of the W-band Doppler reflectometer (red) and V-band Doppler reflectometers (green) are shown in (a)–(c) and (d)–(f), respectively. The angle of the launching mirror is depicted in (g)–(i). The resulting measurement positions are plotted in poloidal cross-sections in (j)–(l) using the same coloring. The two radii at which GENE validation will be done are marked in purple dashed lines. (k) additionally marks the radial intervals from which measurement data will be used.

interest is within the measurement range for all poloidal positions. To measure the $k$-spectrum at one narrow radial interval requires steady state plasma conditions for several seconds.

*Correlation lengths and eddy tilting:* One channel, the *reference channel*, is kept at a fixed frequency (bright green in (f)), whereas the other one, the *hopping channel*, performs fine frequency steps around it (dark green in (f)). Thus, the hopping channel probes at radii closely around the reference channel's radial location. As discharge time is limited, a compromise between radial (number of frequency plateaus of the reference channel) and spectral (number of constant mirror

| | $v_\perp(\theta_{\mathrm{pol}})$ | $k$-spectra | correlation |
|---|---|---|---|
| Frequency plateaus and spacing | 25, rough (1 GHz) | 20, fine (0.25 GHz) | ref. channel: 3, rough, hop. channel: 3×20, fine |
| Radial extent | full radial region | narrow interval | 3 dedicated radii |
| Mirror plateaus and spacing | 5, very rough | continuous moving, very fine | 6, rough |
| Poloidal extent | full poloidal region | half of accessible region | dedicated poloidal regions |
| Difficulty, pre-measurement preparation | moderate, some preparation needed | advanced, significant preparation needed | advanced, significant preparation needed |
| Discharge(s) for GENE validation | 38419 | 38420, 38423, 38861, 38865 | 38421, 38422 (+38862, 38864) |

**Table 6.2:** A list of special Doppler reflectometer settings (rows) for investigation of different turbulence quantities (columns).

positions in (i)) resolution has to be found. Note that correlation using the W-band Doppler reflectometer works identical to that using the V-band, but cannot be done with only one channel available.

### 6.2.2 CECE settings

The radial probing region of the CECE radiometer is determined by the local oscillator frequency of the mixer. For discharges #38419–38426, the CECE system measured in sector 9 using 200 MHz bandpass filters. Figure 6.7(a) shows the probing locations obtained by calculation of the second harmonic cyclotron frequency from the IDE equilibrium. Possible refraction effects are checked by dedicated TORBEAM runs to be several orders of magnitudes smaller than uncertainties of the plasma equilibrium. Similar to Doppler reflectometry, CECE measurements need long stationary plasma phases to increase statistics and successfully separate turbulent fluctuations from the intrinsic thermal noise of ECE radiation.

### 6.2.3 Reflectometer + CECE settings for cross-phase measurements

Coupling a reflectometer and a CECE radiometer on the same line of sight into the plasma allows to measure the cross-phase between electron density and electron temperature fluctuations. In the case of this thesis, a CECE system was moved to the (Doppler) reflectometry section (sector 11) and the launching mirror steered to perpendicular incidence. In the following, the term *reflectometer* refers to probing in perpendicular incidence. Furthermore, when discussing cross-phase measurements, the signals of the CECE radiometer will be called *ECE signals*, since only a single channel is correlated with the reflectometer. Figure 6.7(b) shows the corresponding

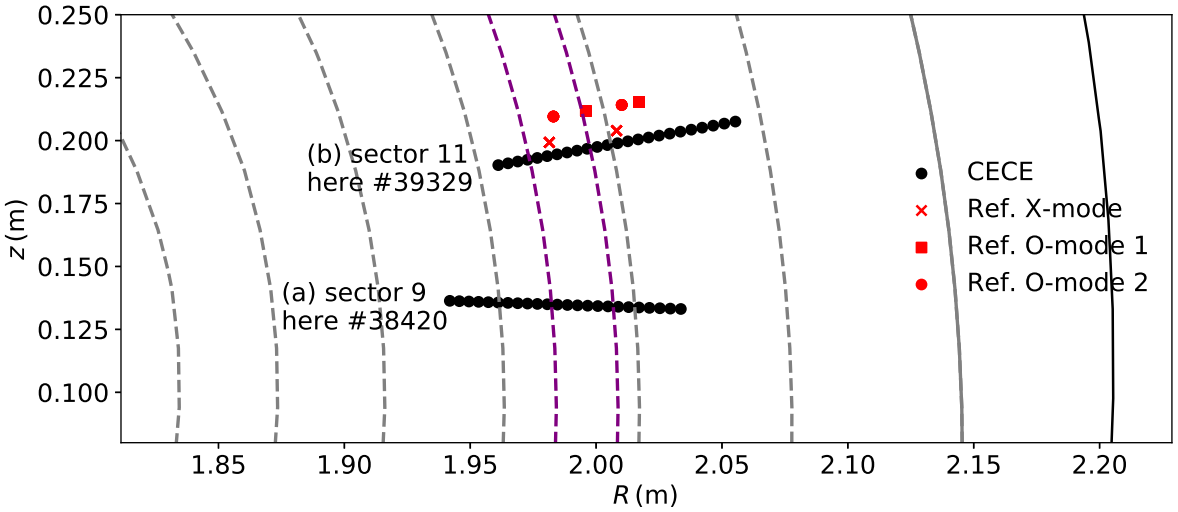


**Figure 6.7:** Poloidal cross-sections with (a) CECE measurement positions of the sector 9 system and (b) CECE measurement positions of the sector 11 system together with reflectometer measurement positions for cross-phase measurements.

measurement locations of the CECE array and the reflectometers probing in both X- and O-mode. The reason for the poloidal separation of the measurement locations is the different path of refraction of different launching frequencies and polarizations. To improve the signal to noise ratio of turbulence measurements, the reflectometers measure at a constant probing frequency for one second each.

## 6.3 Perpendicular wavenumber spectrum of electron density fluctuations

To analyze the wavenumber spectra of electron density fluctuations from Doppler reflectometry, the fluctuation amplitude for each pair of probing frequency and mirror angle in Figs. 6.6(b),(e),(h) is extracted. The Doppler spectra are calculated including ensemble averaging with $n_{\mathrm{fft}} = 4096$ (c.f Fig. 4.3). The radii of interest are, as before, $\rho_{\mathrm{pol}} = 0.740$ and $\rho_{\mathrm{pol}} = 0.785$. However, in the experiment it is practically impossible to locate measurements over a wide range of $k_\perp$ at exactly one radius, thus the following focuses on the intervals $\rho_{\mathrm{pol}} = 0.740 \pm 0.012$ and $\rho_{\mathrm{pol}} = 0.785 \pm 0.012$ (c.f. shaded area in Fig. 6.6(k)). The corresponding wavenumber spectra of all three Doppler reflectometer channels (X-mode $\leftrightarrow$ W-band, O-mode 1 $\leftrightarrow$ V-band 1, O-mode 2 $\leftrightarrow$ V-band 2) are depicted in Fig. 6.8 for both radial intervals (columns) and colorcoded for different probing frequencies. Measurements in the steep/flat scenario are depicted with stars/diamonds, whereas the offsets between all spectra are arbitrary. The X-mode $k$-spectra in Figs. 6.8(a)–(d) are acquired in discharges #38420 (steep scenario) and #38423 (flat scenario). Due to a hardware operating error (a saturation of the power level), the O-mode $k$-spectra of these discharges are limited to $k_\perp > 5\,\mathrm{cm}^{-1}$ and not used. The O-mode $k$-spectra are re-measured in identical repetitions of

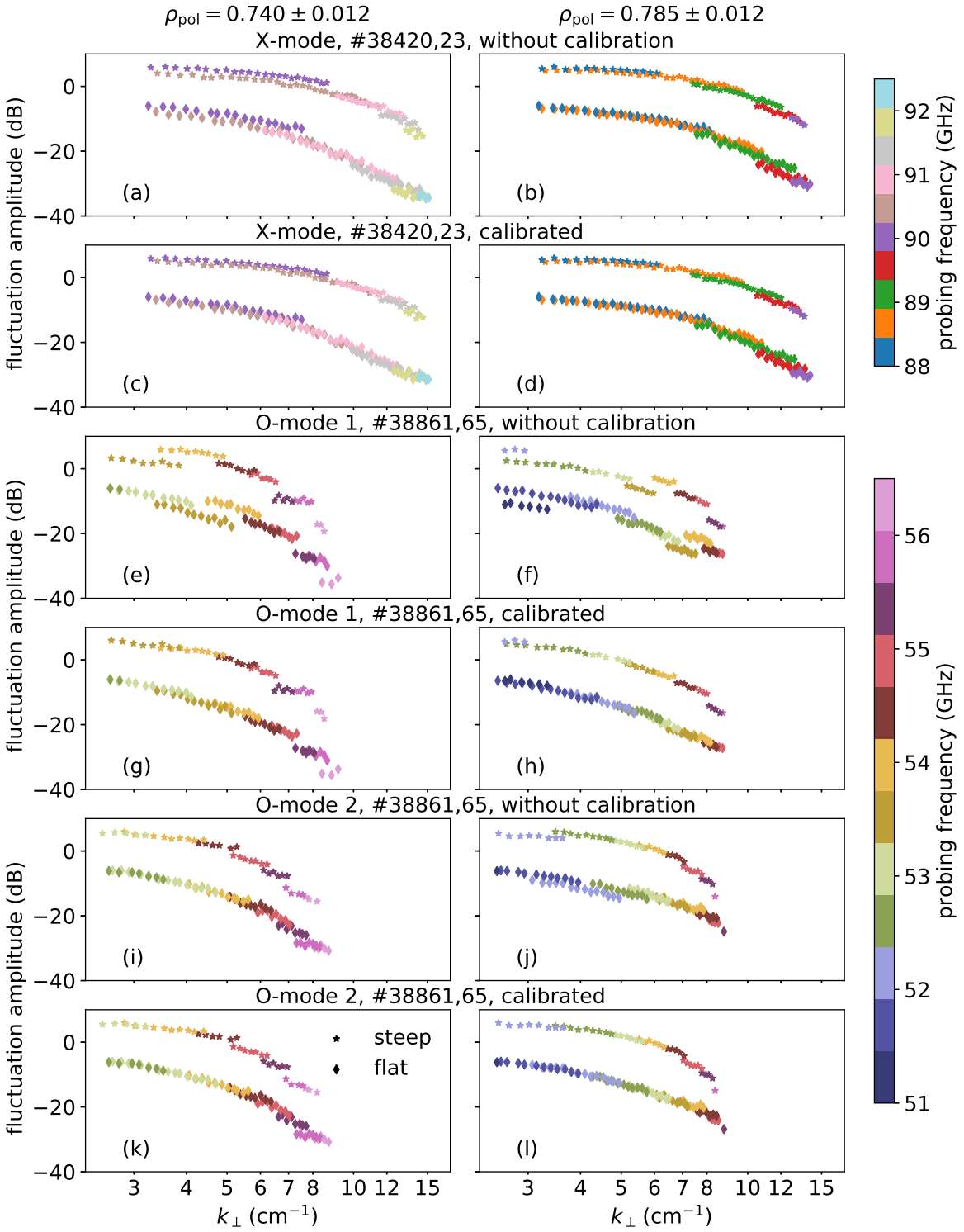


**Figure 6.8:** Wavenumber spectra in X-mode (a)–(d) and O-mode (e)–(l) for two radial intervals (columns), colorcoded with the probing frequencies. The uncalibrated spectra in the odd-numbered rows show pronounced steps with frequency, which disappear after manual calibration in the even rows. Stars depict data from the steep scenario, diamonds from the flat scenario. All offsets are arbitrary. For details refer to the text.

both scenarios (#38861: steep scenario and #38865: flat scenario) and plotted in (e)–(l). Good reproducibility of the repetition plasmas is accomplished, as not only the time traces but also the X-mode spectra of original and repetition scenario match very well.

Figure 6.8 depicts both the raw measurement data (first, third and fifth row) as well as calibrated data (second, fourth, sixth row) in order to illustrate the post-processing calibration. The uncalibrated $k$-spectra show a clear frequency dependence of the measured power which appear as pronounced steps in the O-mode 1 data and only present for some probing frequencies of the X-mode and the O-mode 2 system. A manual post-processing calibration tackles this frequency dependence by multiplying a frequency-dependent calibration factor on all data. This procedure is a valid tool as the scatter in the system clearly comes from different probing frequencies, in contrast to any other noise. The frequency dependence of the raw data must be a direct consequence of the missing calibration of the waveguides, antennas, mirrors etc., which is, however, not possible due to practical reasons.

Figure 6.9 compares the calibrated wavenumber spectra between different polarizations (different Doppler reflectometer channels as symbols), different scenarios (colors) and radial regions (columns). The offsets within each Doppler reflectometer channel relate to relative differences in the fluctuation amplitudes. The offsets between the channels are arbitrary, as pointed out before. The fluctuation level at the outer radius (right) exceeds the level at the inner radius (left) by an average factor of 1.5 for $k_\perp = 4\,\mathrm{cm}^{-1}$ and 3 for $k_\perp = 8\,\mathrm{cm}^{-1}$. This radial increase is in quantitative agreement with past AUG studies using Doppler reflectometry [138, 149]. It qualitatively agrees with experiments from Tore Supra [178, 179] and DIII-D [58, 180, 181], which reported a weaker radial dependence for a wide radial region. Surprisingly, however, the flat scenario exhibits a higher fluctuation amplitude than the steep scenario across the full measured wavenumber range. The difference is largest for intermediate scales, whereas at minimum and maximum $k_\perp$ of each wavenumber spectrum the fluctuation amplitudes of both scenarios become comparable. The difference of the shape of the X-mode and O-mode spectra origin from nonlinear diagnostic effects, which will be discussed later in this section.

The round shape of the wavenumber spectra relates to a two-dimensional fluid turbulence picture (c.f. Sec. 2.2), where various scales for energy injection and losses are present. Fitting the wavenumber spectra with straight lines, such as done in a past AUG study on wavenumber spectra [34], cannot decently recover the shape. Therefore, a general exponential fit function

$$\frac{\delta n_\mathrm{e}}{n_\mathrm{e}} = c \cdot \mathrm{e}^{-\delta \cdot k^p} \tag{6.1}$$

is used here. This function is not based on any specific turbulence model but has been motivated by measurements of $n_\mathrm{e}$ wavenumber spectra at Tore Supra [182–184], which use $p = 1$ and 2 to fit $\delta$. The corresponding fits are shown in Fig. 6.9 in black and dark red, respectively. Table 6.3 lists the relevant fitting parameters for all 12 spectra. For both radii, the exponent $p$ of the flat scenario exceeds that of the steep scenario, as the corresponding spectra are more curved. The specific curvature is a measure of the superposition of several close-by injection scales of the

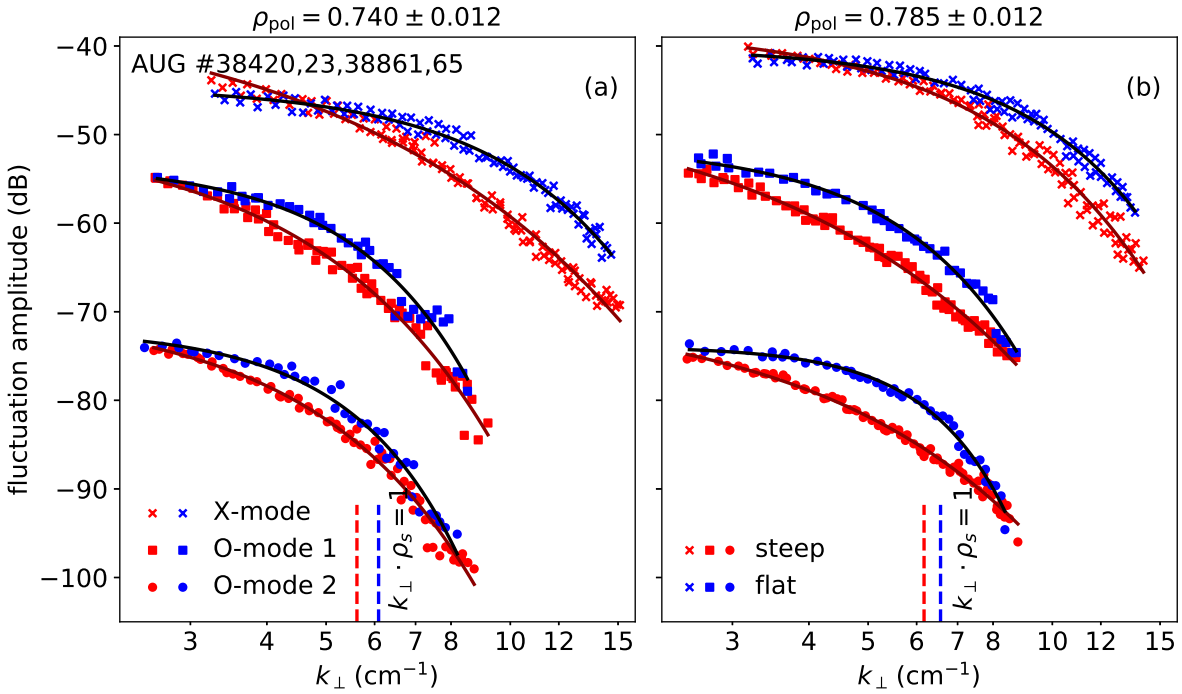


**Figure 6.9:** Wavenumber spectra measured with three Doppler reflectometers (one in X-mode, two in O-mode) at two radii (columns). The relative fluctuation levels in the flat scenario (blue) exceed the fluctuation levels of the steep scenario (red) for a wide range of scales.

| $\rho_{pol}$ | fit parameter | X-s, | O1-s | O2-s | X-f | O1-f | O2-f |
|---|---|---|---|---|---|---|---|
| 0.740 | $\delta$ | 0.64 | 0.43 | 0.19 | 0.026 | 0.026 | 0.028 |
| | $p$ | 0.97 | 1.3 | 1.7 | 1.9 | 2.5 | 2.6 |
| 0.785 | $\delta$ | 0.098 | 0.77 | 0.54 | 0.017 | 0.027 | 0.0024 |
| | $p$ | 1.6 | 1.0 | 1.1 | 2.1 | 2.4 | 3.5 |

**Table 6.3:** Fit parameters of a generalized exponential function on the spectra in Fig. 6.9. X, O1, O2 correspond to the Doppler reflectometer channels, s and f are steep and flat scenarios.

different micro-instabilities. Since the characteristic scales of the instabilities depend on $\rho_s$ (c.f. Tab. 2.1), the values where $k_\perp \rho_s = 1$ are indicated by dashed vertical lines in Fig. 6.9.

Figure 6.10 depicts the same spectra as Fig. 6.9 versus the dimensionless parameter $k_\perp \rho_s$ using identical conventions for colors and symbols. This choice of the horizontal axis is motivated by turbulence theories that often use dimensionless parameters. In general, the wavenumber spectra of both scenarios become increasingly similar when going to the dimensionless axis. A similar dependence of the wavenumber spectrum on $\rho_s$ has been observed for different $B$ in comparisons of deuterium and helium in Tore Supra [182]. For some scales, the steep scenario yields a larger fluctuation amplitude than the flat scenario, in particular at small $k_\perp \rho_s$ in X-mode and large

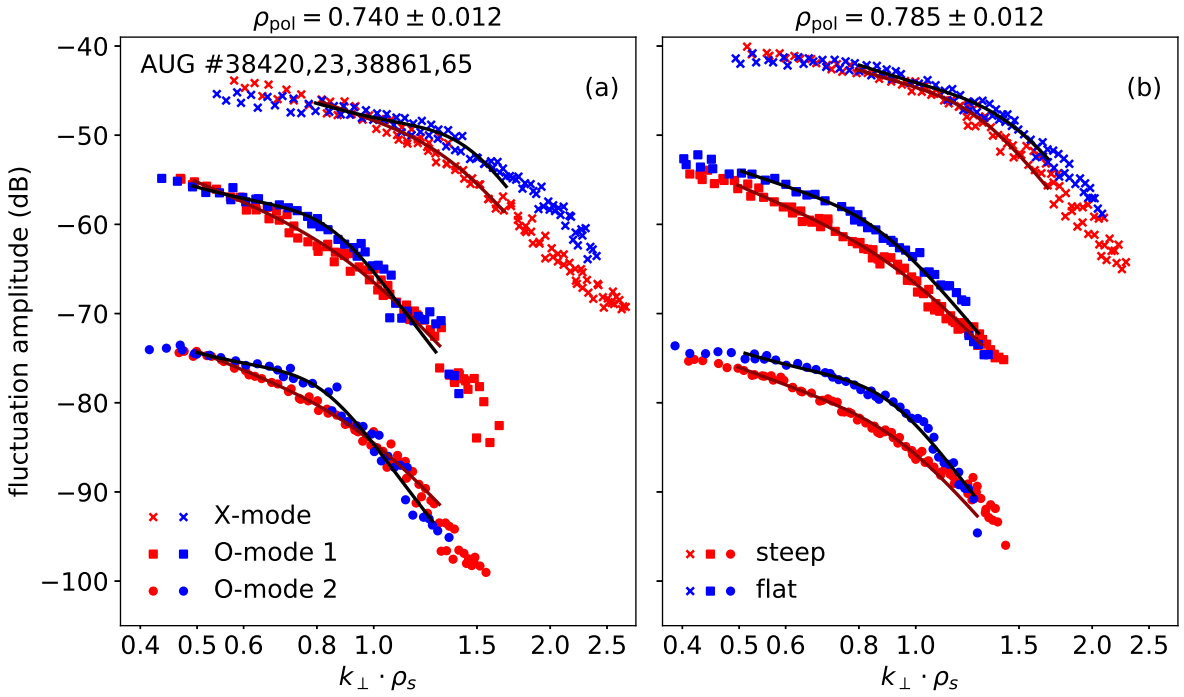


**Figure 6.10:** Wavenumber spectra measured with three Doppler reflectometers (one in X-mode, two in O-mode) at two radii (a),(b) in both plasma scenarios (steep scenario in red, flat scenario in blue) plotted versus the normalized wavenumber $k_\perp \cdot \rho_s$.

| $\rho_{pol}$ | fit parameter | X-s, | O1-s | O2-s | X-f | O1-f | O2-f |
|---|---|---|---|---|---|---|---|
| 0.740 | $\alpha$ | 0.55 | 1.2 | 1.1 | 0.47 | 1.3 | 1.4 |
| | $\beta$ | −1.7 | −2.8 | −4.0 | −1.7 | −4.6 | −5.2 |
| 0.785 | $\alpha$ | 0.59 | 0.98 | 0.91 | 0.46 | 1.4 | 1.2 |
| | $\beta$ | −2.0 | −2.3 | −2.6 | −1.6 | −5.0 | −4.5 |

**Table 6.4:** Fit parameters of the drift shell model on the spectra in Fig. 6.10. X, O1, O2 correspond to the Doppler reflectometer channels, s and f are steep and flat scenarios.

$k_\perp \rho_s$ in O-mode. Other than before, where a function was fitted that has best quantitative agreement with the data but was not motivated by a model, here an expression based on a model is applied. It relates to a spectral shell model for drift waves that describes the turbulence spectrum including local as well as disparate scale interactions [183, 185, 186] as

$$\frac{\delta n_e}{n_e} = \frac{c \cdot (k_\perp \rho_s)^{-3}}{(1 + \alpha k_\perp^2)^2 + \beta k_\perp}. \tag{6.2}$$

Core O-mode measurements at Tore Supra were reported to agree for $k_\perp \rho_s \in [0.7, 1.2]$ [184]. In the present study, the shell model reproduces the ranges $k_\perp \rho_s \in [0.5, 1.3]$ (O-mode) and $k_\perp \rho_s \in [0.8, 1.7]$ (X-mode) for most cases. Scales and ranges without agreement between experiment

| $\rho_{\mathrm{pol}}$ | X-s | X-f | O-s | O-f |
|---|---|---|---|---|
| 0.740 | 26 | 46 | 0.26 | 0.45 |
| 0.785 | 35 | 50 | 0.32 | 0.46 |

**Table 6.5:** Nonlinearity parameter, $\gamma$, (c.f. Eq. 4.7) for both radii and scenarios for O-mode and X-mode polarization, respectively.

and shell model might not necessarily point towards missing physics in the model, but could be affected by the nonlinear diagnostic response.

The difference of the shapes of the wavenumber spectra for O-mode and X-mode has been previously reported by AUG Doppler reflectometer measurements in both polarizations [34] and could be traced back to a diagnostic effect. This diagnostic effect is introduced in Sec. 4.5.1, together with a factor $\gamma$, which estimates whether Doppler reflectometry probes in the linear or nonlinear backscattering regime. For all $k$-spectra under investigation, $\gamma$ is listed in Tab. 6.5. The GENE simulations, which will be discussed in Chap. 7, provide information about the turbulence levels and the correlation lengths for calculating $\gamma$, whereas the remaining quantities are experimentally accessible. X-mode with $\gamma \gg 1$ probes in the nonlinear regime, O-mode with $\gamma < 1$ is close to the transition from linear to nonlinear. These two orders of magnitude difference in $\gamma$ between X-mode and O-mode could explain the different shapes, where the spectral slope in X-mode is flatter than in O-mode. Two orders of magnitude have also been observed by Ref. [34]. Hand in hand with the higher fluctuation amplitudes in the flat regime (c.f. Figs. 6.9 and 6.10), the corresponding diagnostic response is expected to be more nonlinear, as confirmed in Tab. 6.5 with higher values of $\gamma$. The same argument holds when comparing the two radial positions, where the fluctuation level at the outer radius exceeds the level at the inner radius.

## 6.4 Radial correlation length of electron density fluctuations

The measurements of the radial correlation length of density fluctuations for different turbulence structure sizes have been performed in discharges #38421 and #38422 with the two V-band Doppler reflectometers in O-mode polarization. As discussed for Fig. 6.6(f), the reference Doppler reflectometer channel probes at a constant radial position while the hopping channel probes at 20 radial positions around it. The raw heterodyne signals of both channels are correlated. As these Doppler reflectometer signals are complex-valued, there are several possibilities to either only correlate the $I$ or $Q$ signals alone, the amplitude $\sqrt{I^2+Q^2}$, the phase $\arctan(Q/I)$ or the full complex signal $I+iQ$. Different approaches were used and discussed in experiments at AUG [187, 188] and DIII-D [189] and fullwave simulations [190]. In the context of this study, all five methods have been compared (not shown), concluding that the full complex signal serves best for the following analysis. Before correlating the signals, they are filtered in frequency space, using the demodulation technique (c.f. Eq. 2.18) and a Butterworth filter of order 6. The frequency

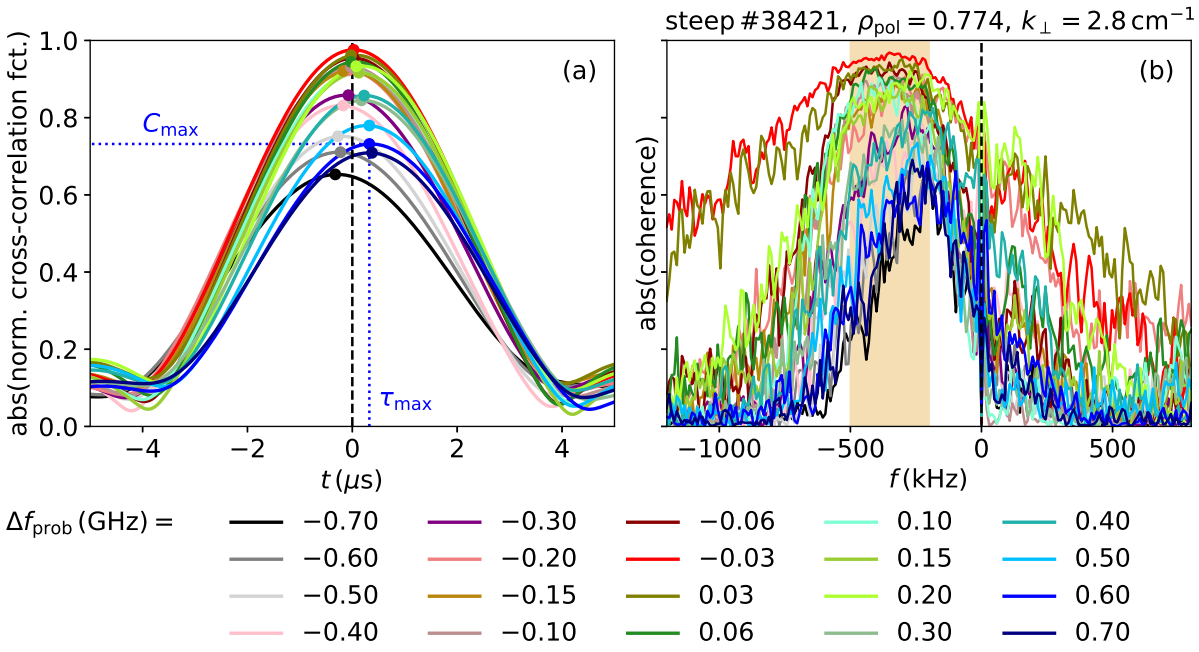


**Figure 6.11:** (a) normalized cross correlation function and (b) coherence for all 20 plateaus of the hopping channel, measured in the steep scenario at the outer radial position and $k_\perp = 2.8\,\mathrm{cm}^{-1}$. The colors indicate the probing frequency differences between hopping and reference channel, the shaded region is the frequency filter interval used for calculating the normalized cross correlation function.

intervals for filtering are centered around the Doppler peak and thus vary between different reference channel probing frequencies. To ensure comparability, all hopping channels around the same reference frequency use the same frequency filter intervals. For the same reason the width of the frequency interval remains constant at 300 kHz for all reference channel plateaus. Note that these measurements are unaffected by the power saturation mentioned in the previous section, as both V-band Doppler reflectometers show the same saturating behavior.

The correlation analysis follows Sec. 2.7 with $n_{\mathrm{fft}} = 2048$ without overlapping windows. The normalized cross correlation function is calculated for each combination of reference and hopping channel frequency using Eq. 2.13 for both scenarios, both radii and the 6 launching mirror angles. For the following illustration, one measurement set from the steep scenario at the outer radial position and $k_\perp = 2.8\,\mathrm{cm}^{-1}$ shows the analysis. Figure 6.11(a) depicts the corresponding absolute of the normalized cross correlation function for all 20 plateaus of the hopping channel. The frequency difference between the hopping channel and the reference channel, $\Delta f_{\mathrm{prob}}$, is marked in colors. For increasing radial distance (increasing absolute frequency difference) between the channels, the underlying turbulence decorrelates. Thus the maxima of the absolute normalized cross correlation functions $C_{\mathrm{max}}$ (dots) decrease with increasing $|\Delta f_{\mathrm{prob}}|$ and thus with spatial distance. The time lags corresponding to the maxima, $\tau_{\mathrm{max}}$, simultaneously increase, as it takes longer for turbulent features to propagate between measurement locations with larger spatial distance.

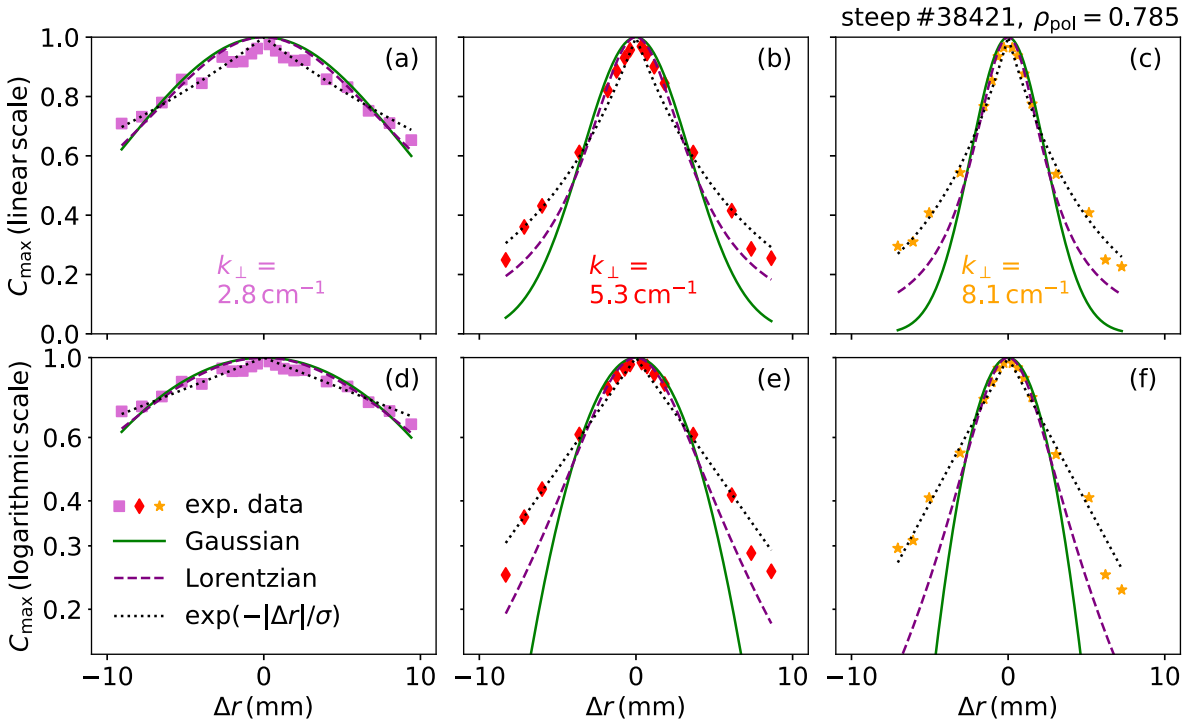


**Figure 6.12:** Maxima of the normalized cross correlation functions versus the radial distance between reference and hopping channels for three sample $k_\perp$ (columns) measured in the steep scenario, plotted in linear (top) and logarithmic (bottom) scale.

The coherence for the same 20 plateaus is calculated using Eq. 2.12 and shown in Fig. 6.11(b). It is largest for small probing frequency differences and decreases with increasing probing frequency difference. This behavior confirms the observation of Fig. 6.11(a) that for increasing radial separation turbulence decorrelates. The shaded region in Fig. 6.11(b) indicates the frequency range which is considered for the analysis of the normalized cross-correlation function, $C_{\max}$ and $\tau_{\max}$. An explanation why the coherence with frequency differences of $\pm 0.03$ GHz does not drop to zero as fast as the others could be the significant overlap of the beam patterns of reference and hopping channels.

To quantify a radial correlation *length*, dedicated TORBEAM runs translate the probing frequency differences into a spatial distance, in this case the component in radial direction $\Delta r$ i.e. perpendicular to the magnetic flux surfaces. Following the common AUG definition in Ref. [149], $\Delta r$ is positive for negative $\Delta f_{\text{prob}}$, in other words, when the hopping channel probes radially outside of the reference channel. Figure 6.12(a) plots the maxima of the cross correlation functions from Fig. 6.11(a) versus the radial distance between reference and hopping channel. The same is done in Figs. 6.12(b)–(c) for two more measurements in the same discharge and at the same radius, but with different $k_\perp$. The deliberately non-uniform frequency spacing results in more measurement points at small $\Delta r$ to better describe the region of high correlation. The data in Figs. 6.12(a)–(c) is fitted with three different functions: a Gaussian $\exp(-\Delta r^2/\sigma^2)$ in green, a Lorentzian $1/(1+(\Delta r/\gamma)^2)$ in purple and an exponential $\exp(-|\Delta r|/\sigma)$ in black. Their analytic formulae are modified such that $C_{\max}(\Delta r = 0) = 1$, which accounts for measuring identical

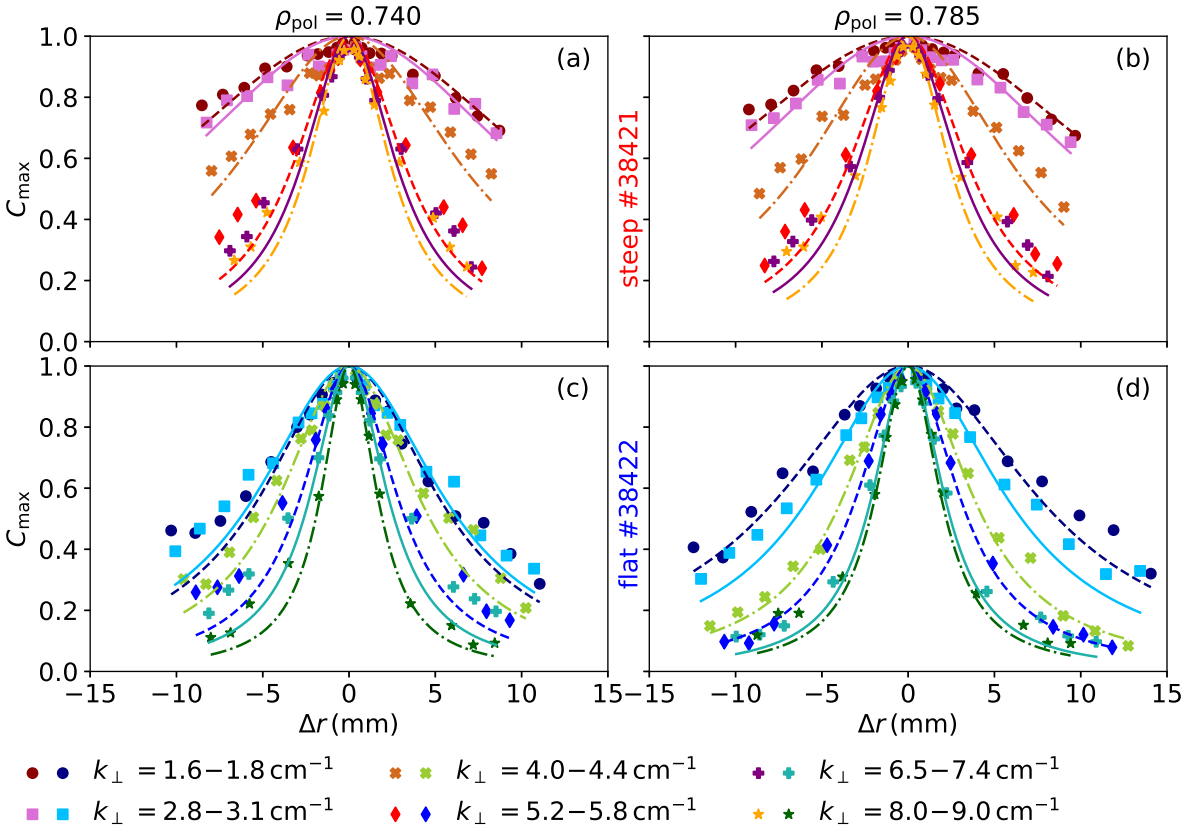


**Figure 6.13:** Maxima of the normalized cross correlation functions versus the radial distance between reference and hopping channels for several $k_\perp$ and for both scenarios (rows) and radial positions (columns).

signals at the same spatial point. Whereas the Gaussian and Lorentzian agree well with the measurement at small radial separation, they do not reproduce a second fall-off length at larger $|\Delta r|$. To primarily extract the inner fall-off length, these Gaussian and Lorentzian functions are fitted with weights $\propto C_{max}^2$, as done in previous AUG correlation studies using Doppler reflectometry [149]. In general both functions reproduce the spatial decay of $C_{max}$, but the Lorentzian function agrees better with the narrow shape for small $\Delta r$ and the wider wings for large $\Delta r$ and will thus be used in the following.

A side study (not shown) concludes that the choice of Lorentzian or Gaussian fit function only slightly impacts the quantitative results of the radial correlation lengths. To illustrate the two fall-off lengths clearer, the bottom row of Fig. 6.12 shows the same data as in the top row, but with a logarithmic scale. An exponential function fitted to equally weighted data points highlights a quasi linear decay in logarithmic scale. Note that, due to its discontinuous derivative at $\Delta r = 0\,mm$, the exponential function is not used as fit function for the radial correlation length analysis. The observation of more than one fall-off length confirms previous AUG correlation studies with Doppler reflectometry [188].

So far only measurements from one scenario at one radius and three $k_\perp$ have been discussed. Figure 6.13 presents both scenarios (rows), both radii of interest (columns) and all six $k_\perp$ (colors)

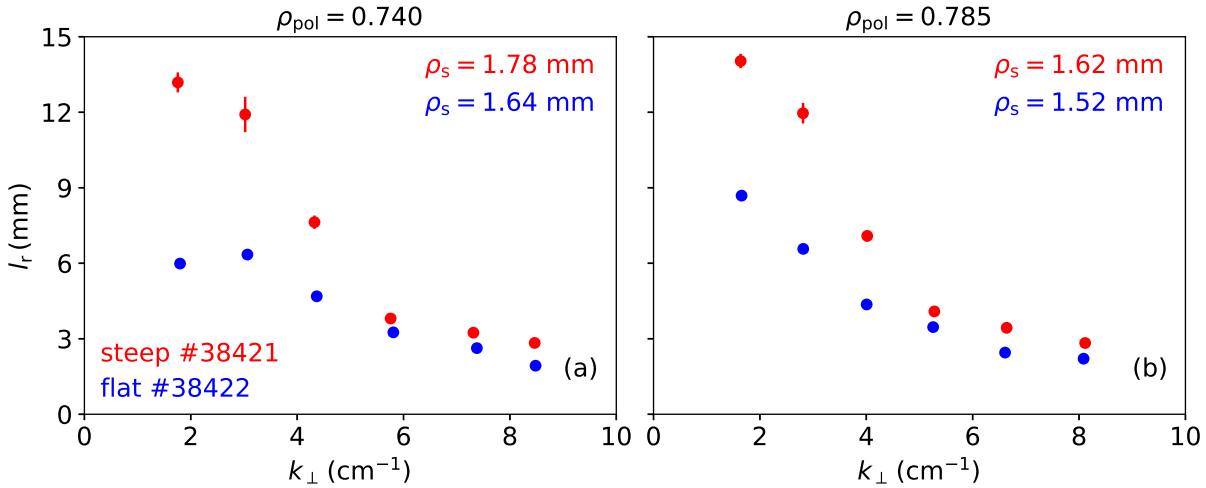


**Figure 6.14:** Radial correlation length of density fluctuations versus $k_\perp$. For small $k_\perp$ (large structure sizes) correlation lenghts are larger than for larger $k_\perp$ (small structures). $l_r$ of the steep scenario exceeds $l_r$ of the flat scenario. For details refer to the text.

with the probing frequency spacing from Fig. 6.11. Due to the steeper density gradient in the steep scenario on the top, the radial range covered by these frequency distances is narrower than in the flat scenario on the bottom. For all cases, $C_{max}$ consistently decreases with increasing channel separation. For small turbulence structures, $C_{max}$ decreases faster than for large structures, indicating that the turbulence decorrelation length depends on the scale size. Note that some points suffer from hardware noise and are not plotted. Following the previous discussion, the fitting curves in Fig. 6.13 are Lorentzian functions, using higher weighting of inner (low $|\Delta r|$) data points. The radial correlation lengths are the HWHM of the fit functions.

Figure 6.14 further elaborates the reciprocal dependence of the radial correlation lengths on $k_\perp$ and compares the measurements of both scenarios. This dependence indicates that the radial and poloidal eddy sizes are correlated. In general, the correlation lengths of the steep scenario (red) are larger than that of the flat scenario (blue) over the full range of turbulence scales. This trend links to the larger $\rho_s$ in the steep than in the flat scenario, as written in the plot. The observation that $l_r$ scales with $\rho_s$ is in line with several reports from DIII-D, like a $\rho_s$ scan in several limiter L-mode discharges [191], as well as detailed studies of single plasma discharges [181, 192]. An additional source for the smaller correlation length in the flat scenario might be the more nonlinear diagnostic response of the Doppler reflectometers, which was found both in TJ-II experiments [193] and fullwave simulations [190] to underestimate the measurement of the radial correlation length. The difference of the correlation lengths between the scenarios might not result from the change in heating power, since in the TFTR tokamak $l_r$ was found to slowly vary with changes in heating [194]. Comparing Figs. 6.14(a) and (b) does not indicate a clear difference between the radial positions. This indifference most likely stems from the spatial vicinity of the measurement positions, since other studies over a wider radial range at AUG [149, 187] and DIII-D [181] report a significant radial variation of $l_r$. As a side note it shall be mentioned that the term *radial* correlation length might need to be weakened: even though the spatial coordinate allocated to the measurement locations is in pure radial direction, any contributions from the

perpendicular distance between them cannot be taken into account. However, for later validation efforts this point will be fully tackled by synthetic diagnostic modeling.

## 6.5 Tilt angle of electron density fluctuations

The Doppler reflectometer settings used for radial correlation measurements provide the ideal basis for investigations of the tilt angle of turbulence eddies, $\beta$. The eddy tilt angle is inferred from the time delay between the two signals of reference and hopping channel and the spatial arrangement of the measurement positions, c.f. Eq. 4.6. For the definition and extraction of the time delay $\tau_{\max}$, i.e. the time shift of the maximum of the normalized cross-correlation function, the reader is referred to Fig. 6.11. The geometric quantities, such as the radial and perpendicular distance of the measurement locations, are obtained from TORBEAM runs. The perpendicular velocity as measured by Doppler reflectometry is taken from Fig. 6.17 as average of both radial positions.

As before in Fig. 6.12, three representative cases from the steep scenario at $\rho_{\mathrm{pol}} = 0.785$ are used for visualization of data evaluation in Fig. 6.15. The columns only differ in the probing wavenumber. The time delay between reference and hopping channel is shown in Figs. 6.15(a)–(c) versus the radial distance. It must be anticipated that the eddy tilt calculated in this study reveals a strong dependence on $k_\perp$. However, this dependence disagrees with previous AUG tilt angle measurements [153] and is hard to put into context with a theory of turbulence. Looking at the amplitude and phase of the coherence between the two channels sheds light on this discrepancy. To study it in more detail, the amplitude is plotted in Figs. 6.15(d)–(f) for five representative cases. The corresponding time delays are highlighted with full symbols in the upper plot. The single peak at low $k_\perp$ in (d) broadens for increasing $k_\perp$ in (e) and splits into two distinct peaks for high $k_\perp$ in (f). The two peaks in (f) are the real Doppler peak at higher frequencies and a spurious peak at low frequencies, in the following called *second peak*. The phase is shown in Figs. 6.15(g)–(i). It reveals an interesting feature at large $k_\perp$ in (i): the ramping of the phase differs for the two peaks.

The following discusses this important feature, since the ramping directly relates to different time lags between the signals via Eq. 2.16 and thus to the analysis of the tilt angle. The assumption is that for the lowest $k_\perp$ in (d), there is not only one peak, but two as well. However, they most likely superimpose and cannot be distinguished. Note that the time lags in (a) gather in quadrants one and three. When going to large wavenumbers in (f), the two peaks are clearly distinguished, whereas the time delays in (c) gather in quadrants two and four. For intermediate $k_\perp$ the peaks in (e) partially overlap. Thus the time delays (b) are ill-defined, since they include two contributions from the two peaks. As before, the normalized cross-correlation function and thus $\tau_{\max}$ is analyzed only in the shaded regions in Figs. 6.15(d)–(i), which are centered around the peak of the Doppler shifted spectrum of the backscattered wave (the correct Doppler shift is confirmed by CXRS measurements of the rotation velocity).

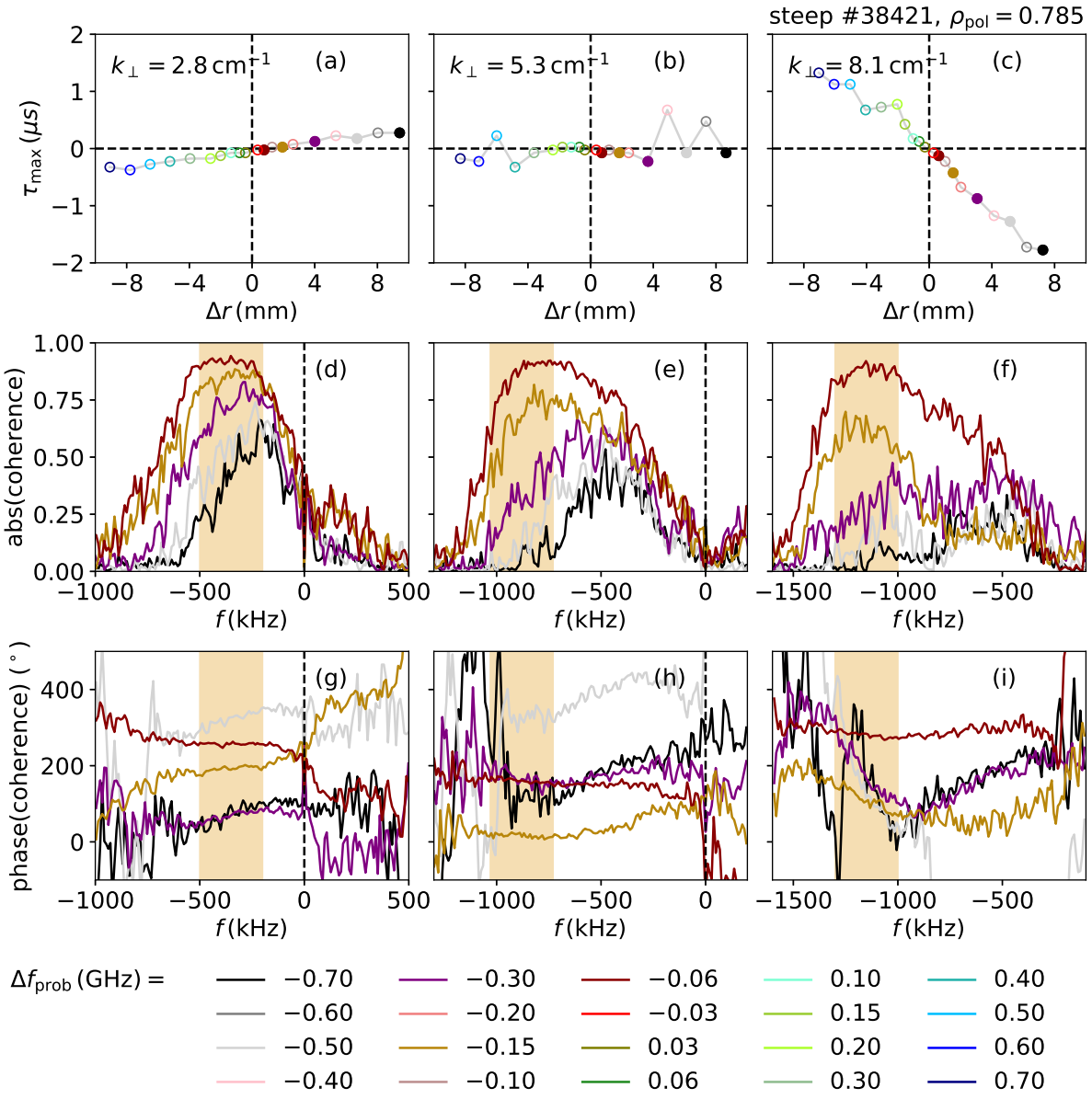


**Figure 6.15:** The time lags (a)–(c) with amplitude (d)–(f) and phase (g)–(i) of coherence between reference and hopping channel for all (time lag) and representative (coherence) probing frequency differences (colors), respectively, for three $k_\perp$. The frequency filter interval for calculation of the normalized cross correlation function is shown as shaded area. The time delays in (a)–(c) are extracted in the filter interval only.

For high $k_\perp$ both peaks and the time lags can be separated in the analysis. However, for intermediate and low $k_\perp$ the phase ramping is blurred by the second peak. The above mentioned $k_\perp$ dependence of $\beta$ sources from this superposition of two peaks. In general, the model for tilt angle analysis presented in Ref. [154] allows the slope of $\tau$ and $\Delta r$ (not to be confused with the slope of the phase of the coherence) to be positive and negative for the same eddy tilt angle but different $k_\perp$, but only for a specific arrangement of measurement positions. However, in the data presented in Figs. 6.15(a)–(c), the different slopes cannot be explained by one common tilt angle for all $k_\perp$. A correct analysis of $\beta$ will in the following only include time lags that unambiguously

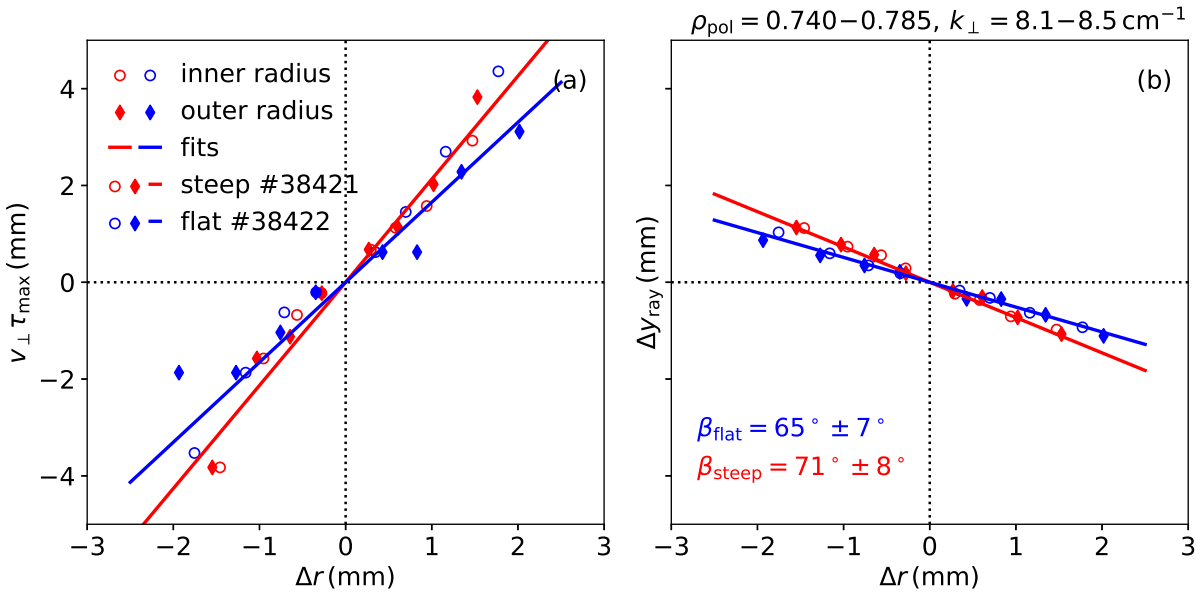


**Figure 6.16:** Relevant quantities for analysis of eddy tilt: velocity perpendicular to the magnetic field multiplied by the time lag between Doppler reflectometer signals in (a), poloidal distance between measurement points in (b). Both versus radial distance. The eddy tilt angle changes only little between scenarios. For details refer to the text.

correspond to the true Doppler peak. This is solely the case for the largest wavenumber, since there the two peaks can be clearly separated. Note that Ref. [154] using X-mode did not observe a second peak and hence could use the full $k_\perp$-range.

The wavenumber range in which the eddy tilt can be extracted in the context of this thesis is $k_\perp > 8\,\mathrm{cm}^{-1}$. Figure 6.16 shows $v_\perp \tau_{max}$ versus the radial separation $\Delta r$ in (a) and the perpendicular separation $\Delta y_{ray}$ versus $\Delta r$ in (b). Note that using the poloidal instead of perpendicular distance would introduce an error in the tilt angle of only $<1\,\%$. The names and definitions of these quantities are in line with the definitions in previous AUG works [149, 154]. Following Ref. [149] only the innermost points (here: $|\Delta r| < 2\,\mathrm{mm}$) contribute to the analysis. The open circles in Fig. 6.16 show the measurement data at the inner radius, the full diamonds at the outer. To improve statistics, both radii are fitted simultaneously with linear functions. The corresponding tilt angles of $71^\circ \pm 8^\circ$ in the steep and $65^\circ \pm 7^\circ$ in the flat scenario differ by $10\,\%$, which is inside the measurement uncertainties. These uncertainties go back on uncertainties of the fits and the perpendicular velocity.

The remainder of this section discusses several points that could lead to the second peak. The second peak is present for all radii and scenarios under investigation with O-mode Doppler reflectometry in the context of this thesis. However, neither of the listed sources is likely to cause the second peak, as will be argued. They are:

- *Antenna side lobe*: The launching antenna of the Doppler reflectometers is optimized for W-band frequencies. Potential consequences for probing in V-band frequencies are antenna side lobes that can cause additional spectral components. A side lobe appears as offset

in the angle of incidence of the launching beam. A dedicated sensitivity study using TORBEAM concludes that in order to match the spectral position of the second peak for all different launching angles, one would need different side lobe angles with a variation of 25 %. This variation does not fully exclude a side lobe as source for the peak, but still does not confirm it.

- *Contribution of X-mode waves*: Due to technical reasons, it is difficult to perfectly align the angle of the microwave electric field and the confining magnetic field. Therefore, a contribution from the other polarization, here X-mode, to the Doppler spectrum cannot generally be excluded and is checked manually: For X-mode upper hybrid waves (left-handed circular polarization) there is no cutoff in this combination of density and magnetic field strength, thus they cannot contribute. Right-hand X-mode waves have a cutoff located in the far SOL where another V-band Doppler reflectometer measuring in X-mode [109] observes negligible flow velocities at very small fluctuation amplitudes. Since the second peak in the O-mode signal corresponds to quite significant flow velocities, a contribution by the right-handed X-mode can likely be excluded.

- *Two co-existing turbulence modes*: Two co-existing comparably strong modes propagating at different phase velocities might cause two peaks. For a simultaneous existence of an ITG and a TEM mode, the total perpendicular velocity would yield the $E \times B$ velocity plus two corresponding phase velocities with different signs. In this case, however, the X-mode Doppler reflectometer would see two peaks as well when probing at the same $k_\perp$, which is not the case. Moreover, the magnitude of the second peak would be expected to change between the scenarios, since they have a different mixture of turbulence drive. This is not the case either. Finally, the accompanying GENE simulations do not predict two unstable modes at the same $k_\perp$.

- *Diagnostic effect from spectral resolution*: The diagnostic effect concerning the measurement of the perpendicular velocity, as discussed in Sec. 4.5.2, leads to a distortion in the Doppler spectrum. Depending on the particular spectral resolution of the Doppler reflectometer and the spectral index of the wavenumber spectrum, the Doppler spectrum can potentially be distorted. However, the analytic expression of Eq. 4.9 produces a peak with one maximum and non-Gaussian tails. It thus cannot reproduce the shape of the two separated peaks in the Doppler spectrum (not shown).

- *Doppler reflectometer hardware*: Even though to my knowledge the microwave components of the Doppler reflectometers should not introduce a second peak, it shall be mentioned that the second peak in these plasma discharges has been observed with two more V-band Doppler reflectometers [141] in O-mode polarization with completely independent microwave components and acquisition hardware. These two previous Doppler reflectometers used the same sector 11 waveguides and antenna systems in the plasma as the Doppler reflectometers used for this study. They measured in predecessor discharges of #38419–

26 and have been removed from AUG before the final discharges in the context of this study.

- *Higher order backscattering*: Following early works on Doppler reflectometry [126] higher order backscattered waves yield the same Doppler shift as the $-1^{\text{st}}$ contribution of interest and thus should not impose a second spectral peak.

In conclusion, the origin of the second peak remains unclear. Note that its existence does not significantly impact the analysis and spectral decay of the wavenumber spectra, since the magnitude of the second peak is smaller or comparable to the Doppler peak. The second peak possibly leads to a slight overestimation ($\lesssim 3$ dB) of the fluctuation amplitude at small $k_\perp$, where the peaks cannot be separated ($k_\perp < 5\,\text{cm}^{-1}$). Also it shall be anticipated that this second peak does not occur in the fullwave simulations discussed in Chap. 7.

## 6.6 Poloidally resolved measurement of the perpendicular velocity of electron density fluctuations

Directly following the extensive studies in Chap. 5, this section focuses on poloidally resolved measurements of $v_\perp$ in the steep and flat scenario. The discussion of this data is intentionally moved here, in order to share the same chapter as all other turbulence measurements of these scenarios. One dedicated discharge #38419 serves for Doppler reflectometry measurements at various specific poloidal positions and full radial coverage. The corresponding diagnostic settings and measurement regions are depicted in Figs. 6.6(a),(d),(g),(j). Since discharge #38419 is designed to measure full *radial* profiles for each launching mirror position, the *poloidal* resolution in $\theta_{\text{pol}}$ is limited due to lacking discharge time. However, the focus here is on two specific radial positions, therefore other discharges of the identical scenarios with much finer $\theta_{\text{pol}}$-spacing are added: #38420 and #38423 in which $k$-spectra are measured below perpendicular incidence (c.f. Sec. 6.3) and #38862 (steep) and #38864 (flat). Figure 6.17 shows X-mode measurements of all five above mentioned discharges. Their radial positions are located within $\Delta\rho_{\text{pol}} = 0.014$ around the radii of interest and are colorcoded with the plasma scenario. Following the argumentation of Sec. 5.1.3, all velocity data are mapped to the midplane using the poloidal dependence of the $E \times B$ velocity. The gap at $\theta_{\text{pol}} = 10{-}25°$ indicates the region where the Doppler reflectometer would probe at perpendicular incidence and thus cannot measure $v_\perp$. Interestingly, the velocity measured below perpendicular incidence slightly but systematically exceeds the velocity from above perpendicular incidence. Note that the measurements from above were acquired in the repetition discharges #38862 and #38864 with $\approx 3\,\%$ less rotation as measured by CXRS, which however, does not explain the observed discrepancy. The measurements above perpendicular incidence decrease for smaller poloidal angles (here smaller $k_\perp$) and thus qualitatively follow the model prediction discussed in Sec. 4.5.2 that, due to the finite spectral resolution of Doppler reflectometry and the wavenumber dependence of the turbulent fluctuation amplitude, the measured $v_\perp$ decreases with $k_\perp$. For below perpendicular incidence probing this is not the case. This

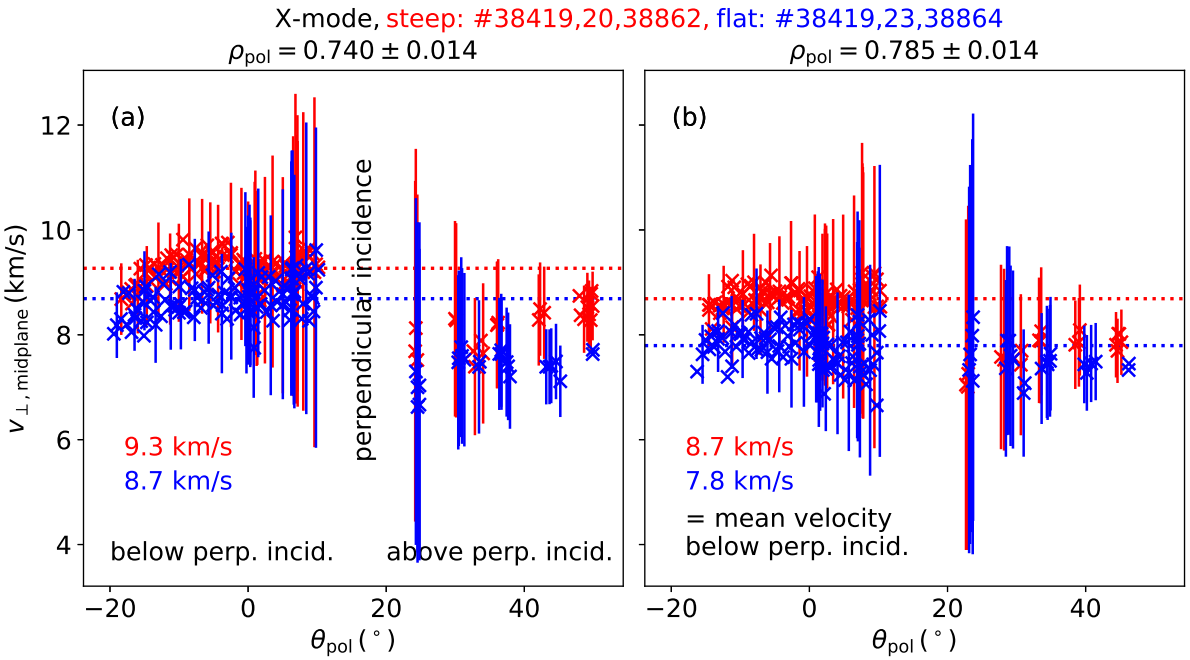


**Figure 6.17:** Perpendicular velocity of electron density fluctuations mapped to the midplane for various poloidal angles, measured with X-mode Doppler reflectometry in both scenarios and both radii.

observation might be related to the larger fluctuation amplitude in this region that increases the nonlinear diagnostic response of Doppler reflectometry, thus flattens the wavenumber spectrum and ultimately causes a less pronounced dependence of $v_\perp$ on $k_\perp$. Since most of the measurements in this thesis are performed below perpendicular incidence, the mean values of the data from below shall be of interest. They are drawn as dotted horizontal lines and decrease both with increasing radius and from the steep to the flat scenario.

In summary, the data plotted in (a) and (b) does not point towards a poloidal dependence of $v_{\perp,\mathrm{midplane}}$. It thus confirms the result from plasma discharge #37014 in Sec. 5.1, which is nearly identical to the steep scenario. As discussed in the previous section, for O-mode there is a second peak in the Doppler spectrum that distorts the Doppler peak for $k_\perp < 5\,\mathrm{cm}^{-1}$ and rules out a reliable extraction of $v_\perp$. Therefore, again a discussion of the poloidal dependence of O-mode velocity measurements is not possible. In conclusion, for the two turbulence reference scenarios the perpendicular velocity measured in X-mode polarization does not follow any poloidal trend other than the poloidal variation of the $E \times B$ velocity.

## 6.7 Frequency spectrum and fluctuation amplitude of electron temperature fluctuations

The CECE measurements in the context of this thesis are acquired in discharges #38420 (steep) and #38423 (flat), respectively. The full steady state phase enables averaging over a large temporal range to improve the signal to noise ratio. The plasma region under investigation is

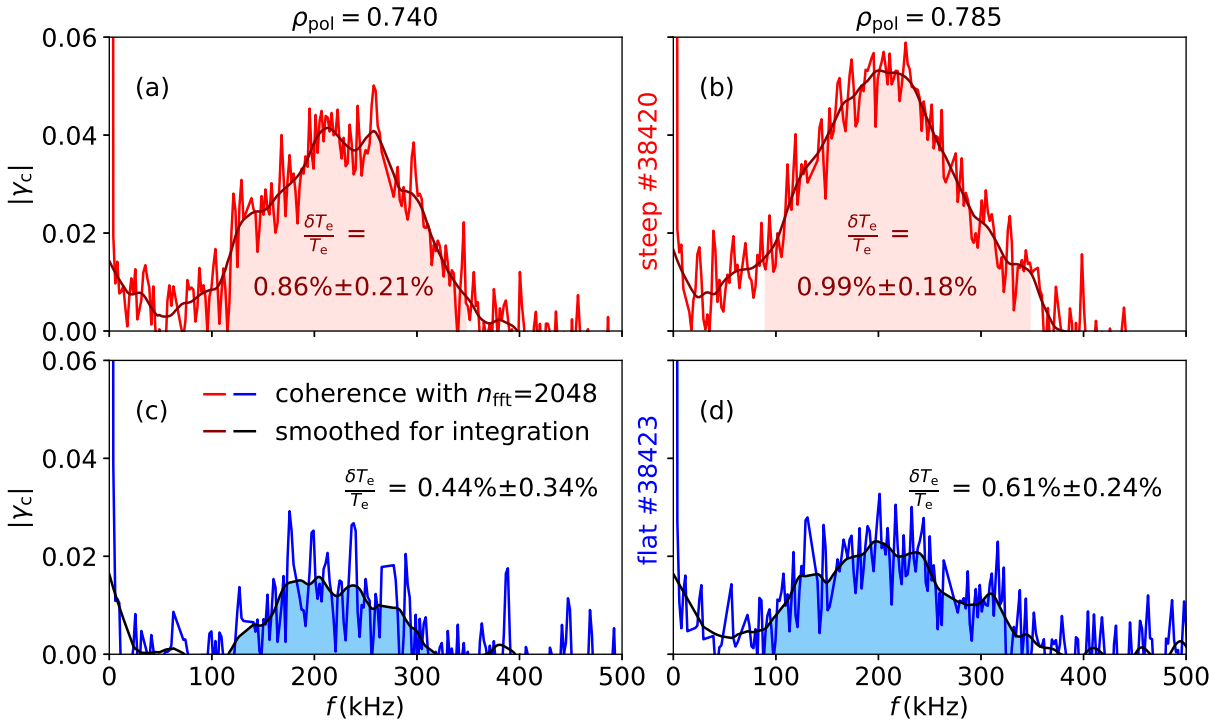


**Figure 6.18:** Coherence of adjacent CECE channels for both scenarios and radii. The fluctuation amplitude corresponds to the integral of the coherence (shaded area) and increases from flat to steep scenario. In addition, it increases with radius for both scenarios.

optically thick, such that contributions from electron density fluctuations are negligible. The calculation of the coherence between CECE channel pairs utilizes Eq. 2.12 with $n_{\mathrm{fft}} = 2048$ and 50 % overlap. Figure 6.18 depicts the coherence between neighboring channel pairs that measure closest to the radii of interest. Some spurious peaks due to hardware noise have been removed prior to this analysis. Due to non-ideal manufacturing, the band-pass filters of the CECE hardware slightly overlap, giving the coherence an offset. This offset is corrected by forcing the median coherence in the range 360 − 400 kHz to zero. This offset correction introduces artificial negative values for the coherence, which lack a physics interpretation and thus are treated as if being zero. The shape of the coherence spectrum is the same for all four cases. Its magnitude, however, increases with radius (from left to right) and from the flat scenario (bottom) to the steep scenario (top). Due to the large amount of NBI injection compared to other L-mode plasmas, the peak of the broadband turbulence feature shifts towards larger frequencies than in ECRH heated AUG L-modes [106, 118, 119]. This frequency shift is qualitatively recovered in a recent AUG study, which compares the edge turbulence of a purely ECRH heated discharge to that of an ECRH and NBI heated discharge [195]. The coherence maximum at the outer radius is slightly less shifted in frequency than at the inner radius, since the rotation velocity decreases with radius, c.f. Figs. 6.17 and 6.3(d).

Using Eq. 3.6, the coherence spectrum translates into a temperature fluctuation power spectrum. Its integral gives the relative temperature fluctuation amplitude. The integration boundaries are $f_1 = 90$ kHz and $f_2 = 350$ kHz for the flat scenario and $f_1 = 70$ kHz and $f_2 = 370$ kHz for the

steep scenario to capture the relevant turbulence features. The respective frequency intervals are shaded in Fig. 6.18 and the smoothed coherence, used for integration, depicted in dark colors. The resulting electron temperature fluctuation levels of the steep scenario exceed the levels of the flat scenario. For $\rho_{\mathrm{pol}} = 0.740$, the increase from flat to steep is a factor of 2, whereas at $\rho_{\mathrm{pol}} = 0.785$ a factor of 1.6 is observed. This trend supports a simple picture of turbulence in which fluctuation amplitudes increase with increasing normalized electron temperature gradient. This simple picture has also been confirmed in a range of DIII-D L-mode plasmas where the normalized electron temperature gradient is varied by means of ECRH power variation [173, 174]. Two slightly different studies at DIII-D that investigate the impact on the turbulence when adding ECRH to an NBI heated plasma [58, 180] observe an increasing temperature fluctuation amplitude with electron temperature, even though the normalized electron temperature gradient remains roughly constant. It is important to note that the density fluctuations behave inversely compared to the electron temperature fluctuations, c.f. Sec. 6.3. The radial increase of fluctuation amplitudes, however, is consistent for both electron temperature and density fluctuations. A radially increasing electron temperature fluctuation level is in line with CECE measurements over a wider radial region, performed at AUG [118, 119] and DIII-D [58, 180].

## 6.8 Radial correlation length of electron temperature fluctuations

The estimation of the radial correlation length of electron temperature fluctuations follows the procedure introduced in Sec. 3.4.2, as it analytically eliminates thermal noise contributions. Eq. 3.9 expresses the maximum of the normalized cross-correlation function depending purely on the underlying turbulence. Section 3.4.2 discusses a technique where one reference channel X at the radius of interest is correlated with different neighboring channels Y to quantify the decrease of correlation with increasing distance $\Delta r$ between X and Y. Unlike other AUG studies on the radial correlation length from CECE [118, 119] this thesis includes channels Y that are located both radially in- and outwards of X.

Figure 6.19 depicts the integrand and the prefactor of Eq. 3.10 for the inner radial position of the steep scenario in #38420. Here, the reference channel is correlated with four different channels radially outward (top row) and five different channels radially inward (bottom row). The plots visualize the decreasing correlation with increasing channel separation. Note that due to the normalization constraints, the direct neighbors of X do not contribute to the analysis, c.f. Sec. 3.4.2. Figure 6.19 shows power spectra versus frequency, of which the integral refers to the scalar number $\mathcal{T}_{\mathrm{e,xy}}$ in Eq. 3.9. The integration boundaries and the frequency interval for background subtraction equal those used for absolute fluctuation measurements in Sec. 6.7.

Due to the low electron temperature fluctuation amplitudes it is technically demanding to resolve the coherence between radially distant CECE channels. These experimental measurement difficulties are attempted to be compensated by increasing the statistics, such that the full analysis from Sec. 3.4.2 is applied to the three CECE channels closest to the radii of interest. A radial de-

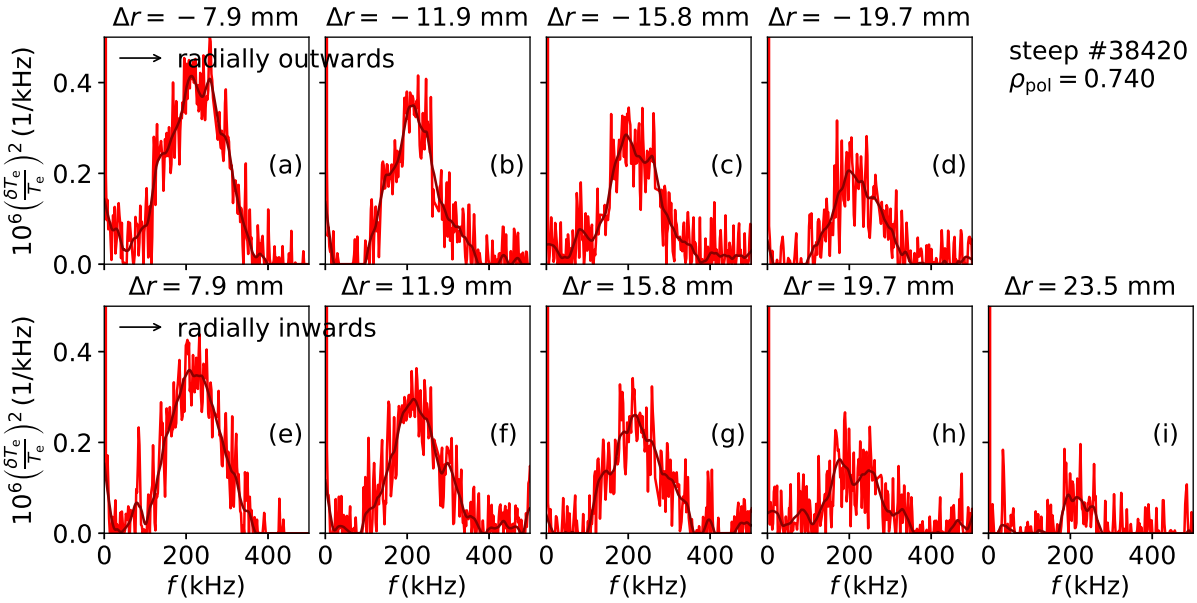


**Figure 6.19:** The integrand times the pre-factor of Eq. 3.10 plotted versus frequency for the illustration of turbulence decorrelation with channel separation: the area below the spectrum decreases with increasing channel separations. For details refer to the text.

pendence of the correlation length or radial changes in the antenna pattern within $\Delta\rho_{\mathrm{pol}} \approx 0.02$ are thus not resolved, but assumed smaller than experimental uncertainties for this study.

The radial correlation lengths are analyzed from #38420, $t = 2.2$–$6.2$ s in the steep scenario and in #38423, $t = 2.2-6.2$ s and #38419, $t = 2.2-3.9$ s for the flat scenario. In the flat scenario, the second discharge is included, as there the CECE channel array measures at another radial position. This improves statistics by correlating different hardware channels for the same radial position. Note that for the steep scenario, no such second discharge exists where the position of the CECE channel array is shifted.

The measured cross-correlation coefficients for all three reference channels around each of the radii of interest are plotted in Fig. 6.20 as open circles for both scenarios (rows) and radii (columns). Due to the reduced time resolution of the CECE DAQ system compared to the Doppler reflectometry DAQ, here the approximation $\max(c(\tau)) \approx c(\tau = 0)$ holds, where $c$ is the normalized cross-correlation function. The full circles indicate the mean values of each channel separation. This mean value does not distinguish between $Y$ being located radially in- or outside of $X$, since, due to the large scatter of the data a radial in-/outwards asymmetry is assumed to be smaller than the measurement uncertainty. The different number of measurement points for different $\Delta r$ are entirely related to the hardware configuration and wiring and thus not discussed. In the steep scenario coherent turbulence features are measured in channels up to a radial distance of 24 mm. However, in the flat scenario due to the low fluctuation amplitude there is only correlation within 12 mm. This, and in addition the larger scatter of the data, implies that no reliable correlation lengths can be extracted in the flat scenario.

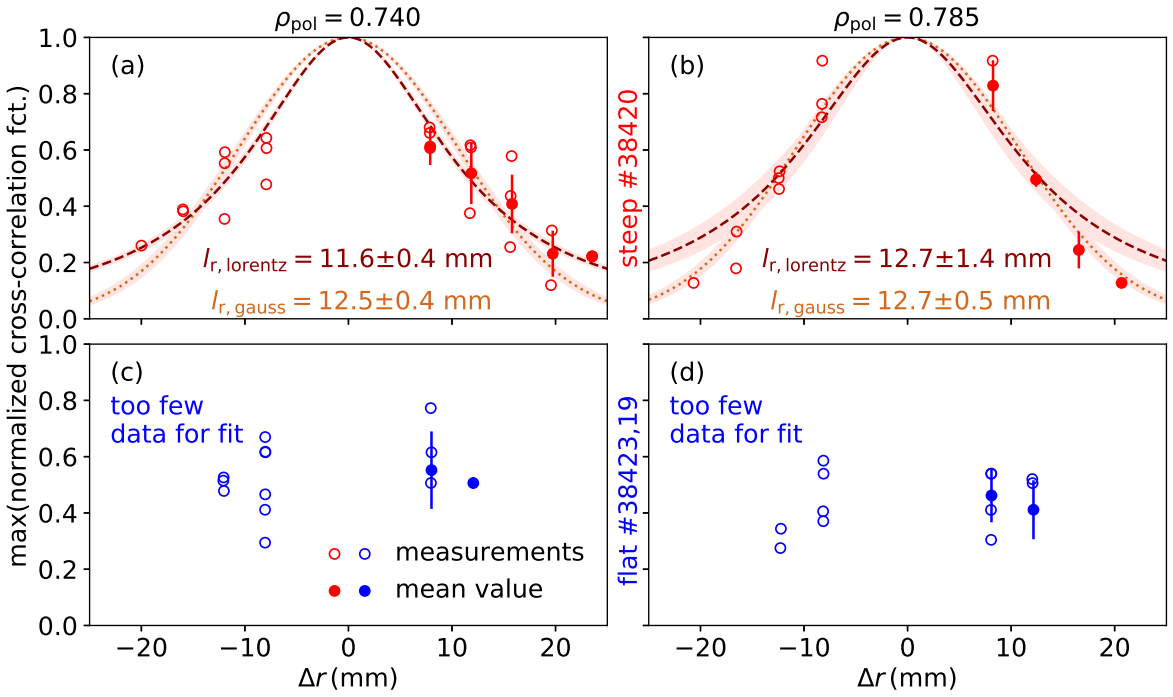


**Figure 6.20:** Radial correlation length of electron temperature fluctuations for both scenarios and radii. For details refer to the text.

The measured cross-correlation coefficients from the steep scenario are fitted with Lorentzian (dashed) and Gaussian (dotted) functions. Both functions give similar correlation lengths, which are, identically as for the density fluctuations, defined as HWHM. They are of the same order as in other AUG studies: slightly larger than those reported in Ref. [119] and slightly smaller than in Ref. [118]. Whereas for the inner radius, the spatial decay in Fig. 6.20(a) is better described by a Lorentzian than by a Gaussian, the opposite is true for the outer radius in Fig. 6.20(b). This observation is attributed to measurement uncertainties and thus is not discussed further.

A study of the spatial dependence of the maxima of the normalized cross-correlation functions in more detail shall be left for future work, which needs different plasma parameters (for instance lower density) with larger electron temperature fluctuations and thus stronger and more reliable signals. Note that Refs. [118, 119] used Gaussian fit functions. It shall be pointed out that Fig. 6.20 does not suggest a strong radial dependence of $l_r$ between the two positions of interest. This confirms a concurrent AUG study including CECE correlation lengths [118], where a weak radial variation is seen. The radial correlation length is $l_r \approx 7\rho_s$ for the inner radius and $l_r \approx 8\rho_s$ for the outer radius and thus again agrees with the finding in Ref. [118].

## 6.9 Cross-phase between electron density and temperature fluctuations

Measurements of the cross-phase between electron density and temperature fluctuations are performed using both O-mode and X-mode reflectometers. For this purpose, the CECE diagnostic is moved to the same line of sight as the reflectometers in sector 11. Due to this major hardware rearrangement, the discharges for cross-phase measurements did not take place on the same day as shots #38419–23. The flat scenario is repeated in #39329 and the steep scenario in #39399. Due to different machine conditions at the time of these repetition discharges, the radiative loss powers exceeded those in the previous discharges. Therefore, the ECRH power was increased to reproduce the heat fluxes and in turn the normalized gradients of the kinetic profiles of the original scenarios (c.f. Fig. 6.3). The normalized gradients and absolute values of the kinetic profiles deviate less than 8 %, for most quantities less than 4 %. All these values are well inside the experimental uncertainties.

For cross-phase measurements the reflectometer and the (C)ECE system probe the same volume in perpendicular incidence to the magnetic flux surfaces ($k_\perp \to 0$). The launching mirror position is chosen such that $k_\perp$ is minimized in the relevant radial interval. For simultaneous probing in both polarizations, the best values achievable are $k_\perp \approx 1.5\,\mathrm{cm}^{-1}$ in O-mode and $k_\perp \approx 1.3\,\mathrm{cm}^{-1}$ in X-mode. Due to the different dispersion relations, O-mode probes above perpendicular incidence and X-mode below. Thus $k_\perp \to 0$ is not possible for both polarizations simultaneously. Past AUG studies correlated the amplitude [119, 195] of the reflectometer signals with the ECE signals, whereas a study at DIII-D used the phase [58]. In the following, the reflectometer amplitude is used for correlation with the ECE measurements, as it gives larger coherences and thus more significant cross-phase measurements than using the reflectometer phase. This confirms previous reports from DIII-D [189].

A study using fullwave simulations found cases where (depending on the radii of curvature of the cutoff layer and the microwave beam) the amplitude of the reflectometer signal and the density fluctuations were not in phase [196]. An out-of-phase relation between the absolute reflectometer signal and the density fluctuations would lead to a sign change of the cross-phase angle. In the setup in this thesis, however, since both radii of curvature are positive, no adaptation of the sign is applied. For the sake of completeness, it shall be mentioned that the absolute value of the ECE signal is used, such that the signal becomes increasingly positive for increasing plasma temperature.

Each reflectometer channel is correlated with all of the (C)ECE channels. The structure size of the turbulence under investigation is found to be on the order of several cm, since $k_\perp \approx 0$. This is in line with the observation for the density fluctuations that the radial correlation length increases with decreasing $k_\perp$ (c.f. Fig. 6.14). Thus, a wide radial range of CECE channels sees correlation with the reflectometer. Therefore, both radial positions of interest, $\rho_{\mathrm{pol}} = 0.740$ and

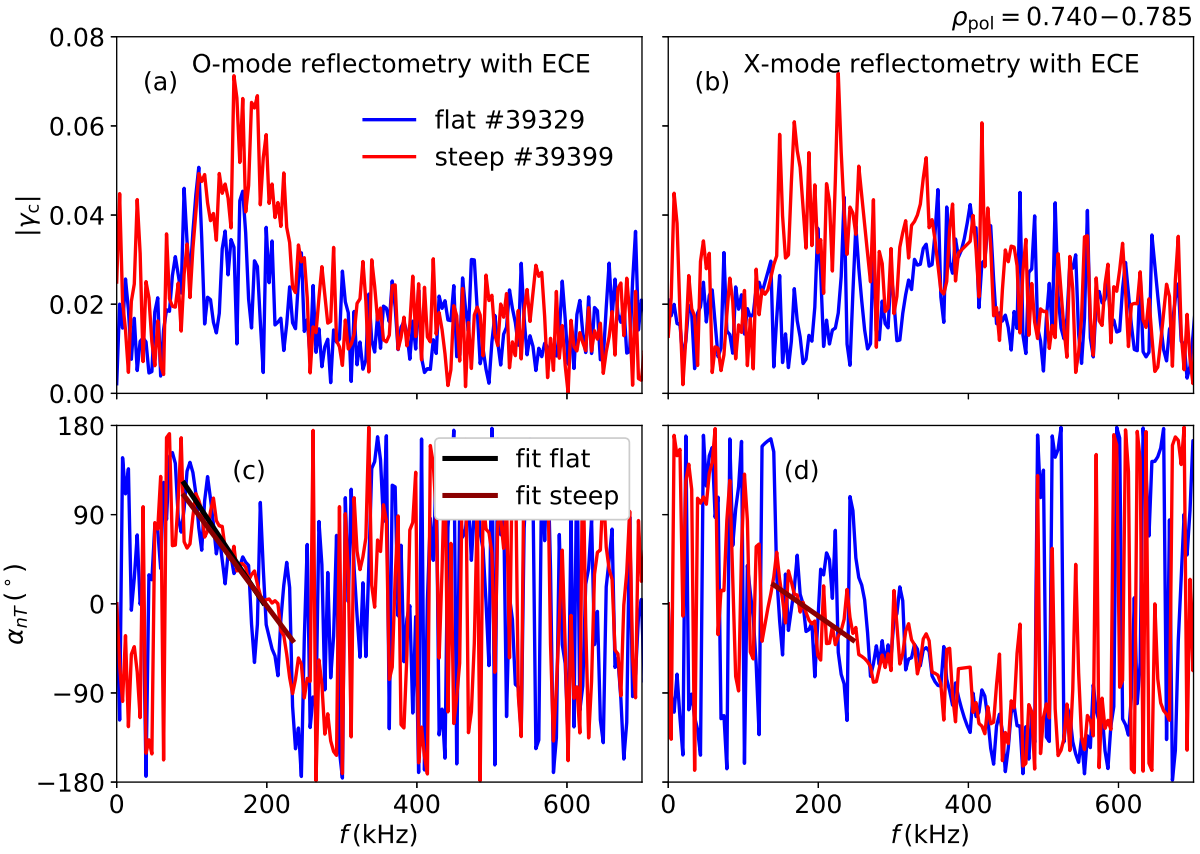


**Figure 6.21:** Coherence between (C)ECE and reflectometry probing in O-mode (a) and X-mode (b). The corresponding cross-phase ramps with frequency, which is partially understood. Most importantly for code validation, it does not change between steep and flat scenario. For details refer to the text.

$\rho_{pol} = 0.785$, are investigated simultaneously. In addition, due to limited discharge time, it was not possible to investigate the radial variation of the cross-phase.

In the following, the (C)ECE channel with largest coherence with the reflectometer amplitude (channel 8) is shown as representative for both radial positions. All three reflectometer channels measure coherent features with this channel. Figure 6.21(a) shows the coherence of the O-mode reflectometry measurements from V-band 1 with ECE channel 8. Correlation results using V-band 2 are not used in the following because for some cases the data is not fully understood. Figure 6.21(b) depicts the coherence between X-mode W-band reflectometry measurements and the ECE channel. The corresponding cross-phase between electron density and electron temperature fluctuations is shown in the bottom row of Fig. 6.21, for O-mode in (c) and X-mode in (d). As discussed in Sec. 2.7, it is defined as the phase angle of Eq. 2.12, where the reflectometer time trace enters as $x_1(t)$ and the ECE time trace as $x_2(t)$.

The coherence of O-mode reflectometry resembles the coherence of two CECE channels shown in Figs. 6.18 and 6.19: the reflectometer and radiometer measure coherent turbulence features at frequencies where also temperature fluctuations are coherent. For X-mode reflectometry, an additional peak arises at around 400 kHz which is currently not understood. Possible explanations range from coherent noise to turbulence features which are far below thermal noise in the CECE

correlation. A detailed discussion is left for future studies and is out of the scope of this thesis. Due to the unknown source of this second peak and the nonlinear diagnostic response of X-mode reflectometry, this study focuses on cross-phase measurements from O-mode reflectometry.

In general, the cross-phase has a defined value where the coherence is high and it is random where the coherence is low. For correlation with the O-mode reflectometer, the frequencies of interest range from 90 kHz to 200 kHz in the flat scenario and from 90 kHz to 240 kHz in the steep scenario. The cross-phase measurements of both scenarios coincide. However, they are not constant, but ramp with the frequency. Linear fits indicate a slope of $-1.0$ deg/kHz in the steep and $-1.1$ deg/kHz in the flat scenario. This corresponds to time lags of 2.8 $\mu$s (steep) and 3.0 $\mu$s (flat) between radiometer and reflectometer signals (via Eq. 2.16). Using the $v_\perp$ measured by Doppler reflectometry (c.f. Fig. 6.17), this translates into a poloidal offset of 2.5 cm for both scenarios. 60 % of this distance is explained by the poloidal separation of the measurement positions of reflectometer and radiometer in Fig. 6.7(b). The remaining distance could source from uncertainties in the magnetic equilibrium reconstruction or hardware misalignments similar to what is discussed in Sec. 5.3. Ramping phase angles due to a poloidal separation between CECE and reflectometer channels have previously been observed in synthetic diagnostic modeling on turbulence from GYRO, based on experimental measurements from DIII-D [31]. Even though the phase ramps, it is important to note that $\alpha_{nT}$ is the same for both scenarios. This observation does neither confirm reports at DIII-D [174], which observe a slight dependence of $\alpha_{nT}$ on the normalized electron temperature gradient, nor contradict them, since the underlying plasmas are expected to show a different mixture of micro-instabilities. Similarly, a different DIII-D study reports a change of the cross-phase for a variation of $T_\mathrm{e}/T_\mathrm{i}$ [180].

Even though the cross-phase between X-mode reflectometry and ECE will not be used for code validation, there are some features that provide additional information: only the steep scenario shows coherence between radiometry and reflectometry at the frequency range of CECE coherence, c.f. Fig. 6.18. The lack of coherence for the flat scenario originates from lower temperature fluctuation levels, and due to the larger density fluctuation amplitude from the more nonlinear diagnostic response in the reflectometer. The frequency range from 140 kHz to 250 kHz in the steep scenario displays a ramping phase with a slope of 0.6 deg/kHz, which corresponds to a time lag of 1.5 $\mu$s and a poloidal separation of 1.2 cm. This smaller phase ramping is consistent with the smaller poloidal offset between X-mode reflectometer and CECE channels compared to that of the O-mode reflectometer, c.f. Fig. 6.7(b). The other feature when comparing cross-phases investigated with O-mode and X-mode reflectometer is the different absolute value of the cross-phase. A possible explanation could be the polarization-dependent spatial extent of the reflectometer beam. Different spot sizes resolve different turbulence scales and thus take into account a different mixture of underlying turbulence instabilities, which in turn influences the value of the cross-phase.

In conclusion, the ramping of the cross-phase prohibits to extract an absolute value for $\alpha_{nT}$. However, a highly valuable observation can still be used for turbulence characterization: the

cross-phase in the respective frequency interval of interest does not change between the steep and the flat plasma scenario.

## 6.10 Additional gradient variation

This chapter so far investigated two plasma discharges that only differ in the location of ECRH deposition. The resulting changes in the normalized gradients of electron temperature and density drive the underlying micro-instabilities to a different extent, which may lead to different turbulence characteristics. This additionally constrains the input parameters of later simulations, as the normalized gradient of the steep scenario must be strictly larger than that of the flat scenario. Thus, having two plasma scenarios increases the robustness of code validation as it decreases the amount of possibilities to vary the input parameters until a match between experiment and simulation is obtained.

In addition to the two previously investigated scenarios, six more scenarios have been performed with different magnitudes of ECRH power, however, with a reduced number of observables. The ECRH deposition radii remain fixed at the inner and the outer position of the steep and the flat scenario, respectively. As will be shown in the following, the electron temperature gradient will become even steeper or flatter, respectively. This section discusses features of electron density and temperature fluctuations in these additional scenarios. The cross-phase between the electron density and temperature fluctuations could not be measured due to a lack of hardware availability. Since the extended scenarios do not cover the mirror launching angle for the highest $k_\perp$ that allowed to extract the eddy tilt angle in the original scenarios, the tilt angle cannot be extracted in these additional scenarios either.

### 6.10.1 Normalized gradients of extended scenarios

The extended gradient variation is performed in three discharges (#38424–26) that all have a steep and a flat gradient phase. The ECRH power is increased on a shot-to-shot basis. The flat top phase of each scenario has a length of $2-2.5$ s and enables turbulence measurements at a reduced radial range compared to the original scenarios. In the following, the scenarios are compared for $\rho_{\mathrm{pol}} = 0.77$. The kinetic profile fitting uses the same routines as discussed for the base case scenarios in Sec. 6.1.3.

Figure 6.22(a) depicts the variation of the normalized electron temperature gradient with heating power. Red points correspond to inner heating, blue to outer heating. The original two scenarios are marked as stars. Due to profile stiffness [197] in the case of inner heating, the normalized gradient does not change despite higher heating powers. The same effect is observed for the normalized electron density gradient for increasing inner heating in (b). For increasing heating power at the outer location, the normalized density gradient decreases and depends linearly on $R/L_{T_\mathrm{e}}$. The normalized ion temperature gradient remains less affected than those of $T_\mathrm{e}$ and

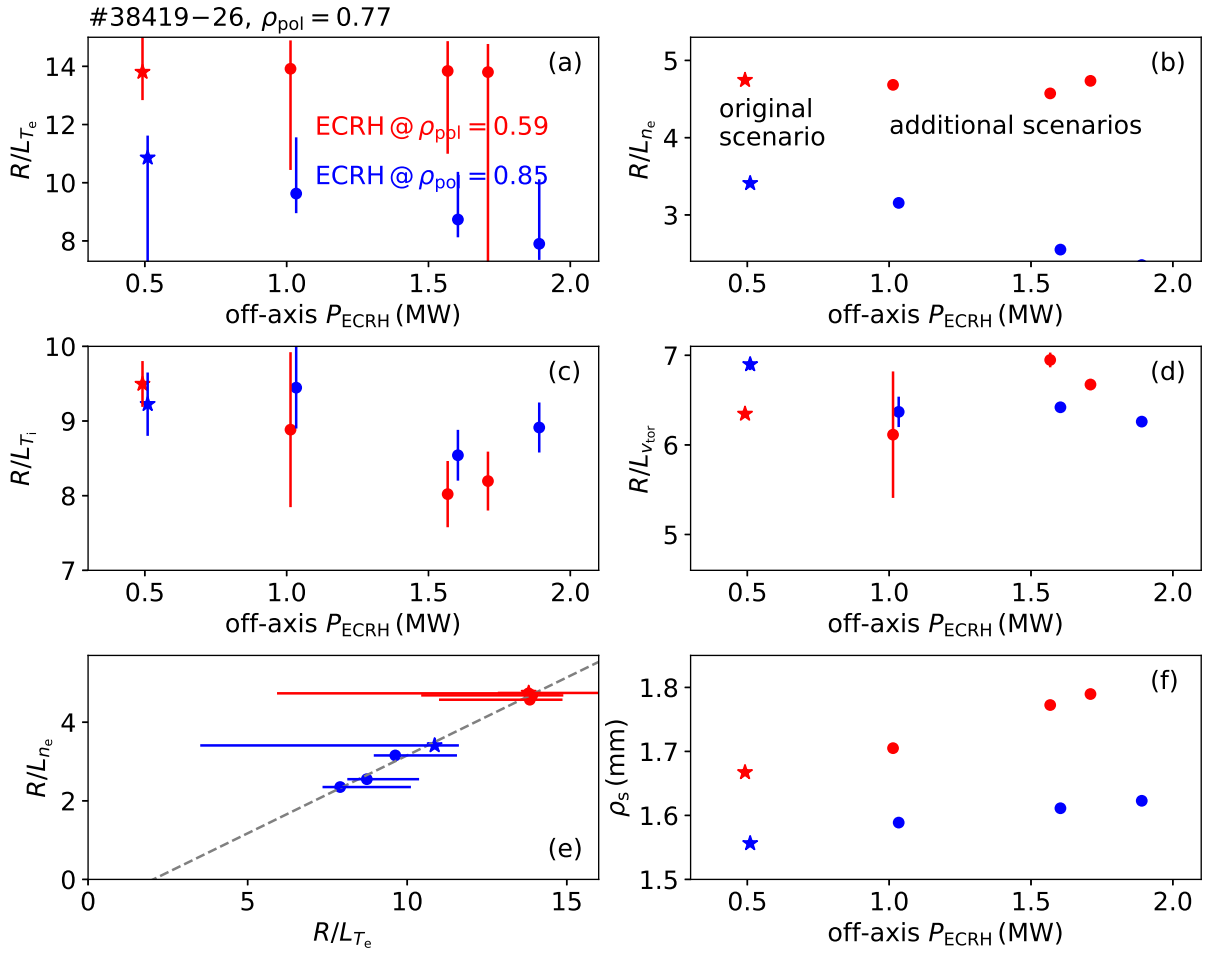


**Figure 6.22:** Normalized gradients of additional plasma scenarios where the ECRH power at both the inner (red) and outer (blue) position is further changed. Subplots (a)–(d) depict the normalized gradients of electron temperature, electron density, ion temperature and toroidal rotation velocity. (e) indicates that the normalized electron density gradient and electron gradient follows a linear dependence. The drift parameter increases with heating power in (f) and is systematically smaller for the flat scenario.

$n_e$, but slightly decreases with the increasing heating powers on both heating locations. The normalized gradient of the toroidal rotation velocity increases linearly for decreasing magnitude of outer heating but does not follow any trend for increasing inner heating. For both scenarios, the drift scale parameter $\rho_s$ increases with heating power and is systematically larger in the steep scenario.

In summary, the trend which has already been seen when comparing the base case flat and steep scenarios is continued: $R/L_{T_e}$ and $R/L_{n_e}$ react stronger than $R/L_{T_i}$ and $R/L_{v_{\mathrm{tor}}}$ and the normalized gradients in general become smaller for an increase of the heating power at the outer location. Due to a lack of time no TRANSP or GENE simulations have been performed for these scenarios. Nevertheless, these measurements give insights into the response of experimental turbulence parameters to broaden the overall picture.

### 6.10.2 Fluctuation amplitude of electron density fluctuations

The Doppler reflectometer settings of the extended gradient scenarios resemble those for radial correlation length measurements in Fig. 6.6: due to limited discharge time, the launching mirror is steered to two (#38424) or three (#38425–6) positions in each scenario, allowing for density fluctuation measurements at two or three specific values of $k_\perp$, respectively. The O-mode Doppler reflectometers follow the frequency pattern of a hopping and reference channel, such as shown in Fig. 6.6(f), the X-mode Doppler reflectometer performs a simple hopping pattern, such as depicted in Fig. 6.6(b).

Figure 6.23 shows the average fluctuation amplitudes at $\rho_{\mathrm{pol}} = 0.770 \pm 0.012$ for all scenarios. Scenarios with additional ECRH deposition at the inner (outer) position are colored in red (blue). Doppler reflectometry measurements in X-mode polarization include all three (two) $k_\perp$ ranges accessible by the three (two) launching mirror locations. In O-mode only the highest $k_\perp$ are considered, since the other measurements are affected by the saturation in the IQ detector in discharges #38419–26 (c.f. discussion for the wavenumber spectra in Sec. 6.3). The vertical offset between X-mode and O-mode measurements is arbitrarily chosen for better visibility. The error bars indicate the standard deviation of all data. Thus, they include both the radial dependence of the fluctuation amplitude within the considered interval as well as the scatter due to a possible intrinsic power dependence of the probing frequencies. Note that the calibration from Fig. 6.8 cannot be applied here because different probing frequencies had to be used for the extended scenarios. Thus, since a post-processing calibration needs a full $k$-spectrum rather than isolated values of $k_\perp$, no calibration can be applied here.

All data points measured at the same $k_\perp$ with the same polarization are connected with lines to illustrate the sequence of increasing inner and outer heating. The blue points of each of the four data groups (three X-mode, one O-mode) at smallest $R/L_{T_\mathrm{e}}$ correspond to the flat scenario with maximum ECRH power. The blue point with largest $R/L_{T_\mathrm{e}}$ corresponds to the original flat scenario from above. The red point that is connected by a red line to the original flat scenario corresponds to the original steep scenario.

As before, the density fluctuation level decreases with increasing $R/L_{T_\mathrm{e}}$. At low wavenumbers in X-mode, the fluctuation level remains constant for a wide range of normalized gradients and then suddenly drops for inner off-axis heating above 0.5 MW. For intermediate wavenumbers, the dependence on $R/L_{T_\mathrm{e}}$ is more gradual. The highest X-mode wavenumbers confirm the trend of intermediate $k_\perp$ when heating outside, but indicate a significantly lower and constant fluctuation amplitude for all points of inner heating. Whether the peak at $R/L_{T_\mathrm{e}} \approx 9$ is real or an effect of calibration or ray tracing is hard to disentangle and left open. The O-mode measurements indicate a constant fluctuation level for all points with outer heating. However, they confirm that for increasing heating power at the inner position the relative density fluctuation amplitude decreases.

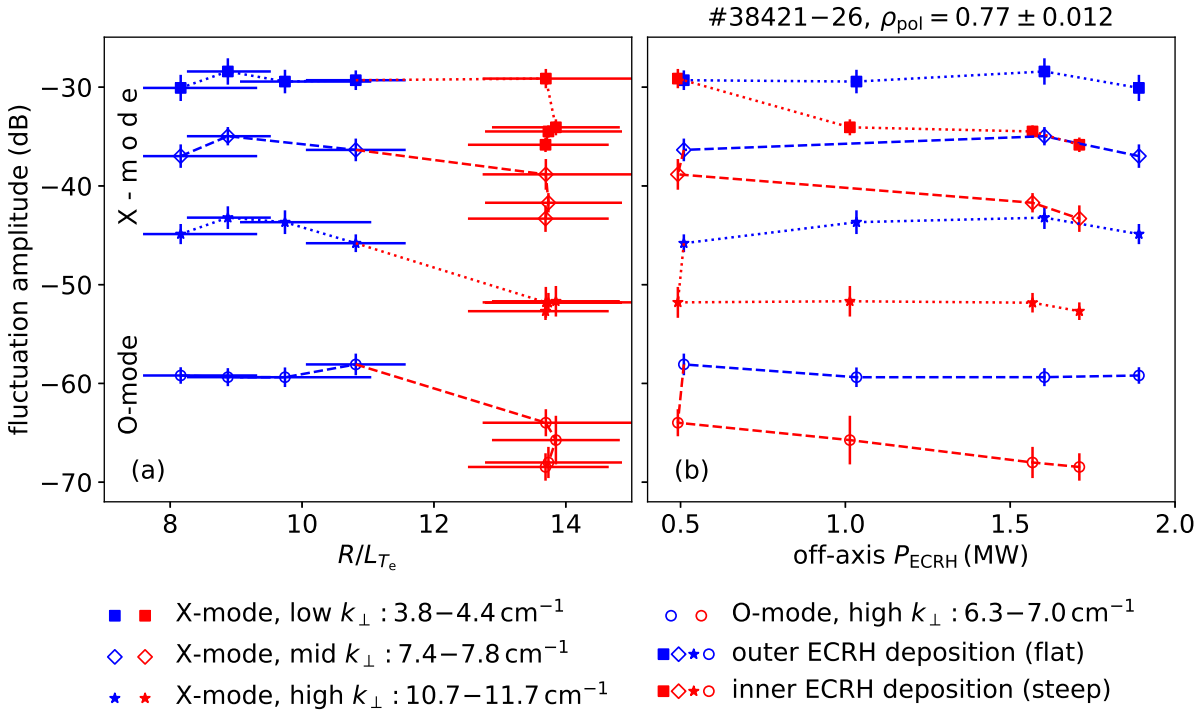


**Figure 6.23:** Amplitudes of electron density fluctuations for different plasma scenarios versus the normalized electron temperature gradient (a) and the off-axis heating power (b). The previously seen trend (c.f. Sec. 6.3) that flat (blue) scenarios have larger fluctuation amplitudes than the steep scenarios (red) continues.

Since $R/L_{T_\mathrm{e}}$ and $R/L_{n_\mathrm{e}}$ exhibit a linear dependence (c.f. Fig. 6.22(e)), the relation between the fluctuation amplitude and $R/L_{n_\mathrm{e}}$ is similar to the one plotted in Fig. 6.23(a). This opposes the simple mixing length model, which relates the turbulence amplitude to the gradient length and the inverse eddy structure size as $\delta n_\mathrm{e}/n_\mathrm{e} = 2\pi/(k_\perp L_\mathrm{n})$ [55].

In conclusion, it is interesting to see that for outer heating a further change of the normalized gradient only slightly changes the fluctuation level, whereas for inner heating the fluctuation level significantly decreases, even though $R/L_{T_\mathrm{e}}$ is constant. In general it shall be pointed out that the density fluctuation amplitude largely varies with radius. Hence, uncertainties in the density profile reconstruction, and thus the radial allocation of measurement points, can impact the comparison of density fluctuation levels between scenarios. A second source of scatter is that, due to the different density profiles, each scenario measures the fluctuation levels at a slightly different $k_\perp$. Still, the result that the density fluctuation amplitude in all outer heating scenarios exceeds the amplitude in inner heating ones remains a robust observation.

### 6.10.3 Radial correlation length of electron density fluctuations

Figure 6.24 depicts the correlation lengths measured at the same radius versus the normalized gradient of the electron temperature in (a) and density in (b). The analysis procedure for $l_\mathrm{r}$ is

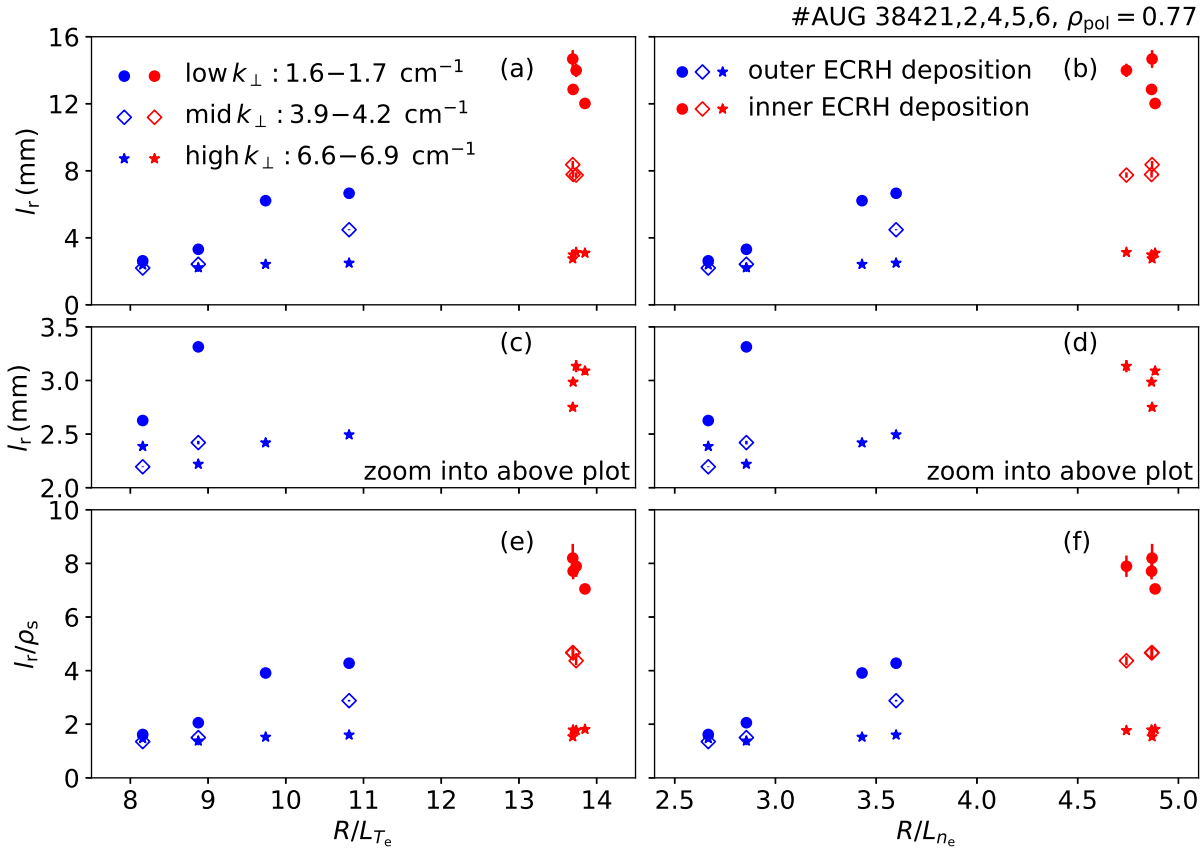


**Figure 6.24:** Radial correlation length of density fluctuations in plasma scenarios with different normalized electron temperature (a) and density (b) gradients, measured at the same radial position.

identical to that discussed in Sec. 6.4 for the base case scenarios. Again the measurements of the extended scenarios are separated into three $k_\perp$ ranges and marked by different symbols.

All scales indicate an increasing radial correlation length with $R/L_{T_e}$ and $R/L_{n_e}$. This increase is largest for low and intermediate wavenumbers where the correlation length increases by a factor of 4 from the lowest to highest $R/L$ scenario. Plots (c) and (d) are zooms into (a) and (b) to illustrate that measurements at the largest $k_\perp$ range vary by approximately 50 %. Experimental studies on density fluctuations in TJ-II [193] and fullwave simulations [190] reported a decrease of the measured correlation length with an increasingly nonlinear diagnostic response. Since in Fig. 6.23 fluctuation amplitudes are larger in the low $R/L_{T_e}$ scenarios, their diagnostic response is likely more nonlinear and could thus relate the smaller correlation length to the diagnostic response. However, since $\gamma \approx 1$ for O-mode, it could also be real physics. Comparing with Figs. 6.24(e),(f) suggests that the measured variation of the correlation length with the normalized gradient does not follow the trend of the drift scale parameter. To disentangle the impact of turbulence and diagnostic effects, respectively, is left for future work, since it would include additional turbulence modeling and fullwave simulations that are computationally too expensive for this thesis.

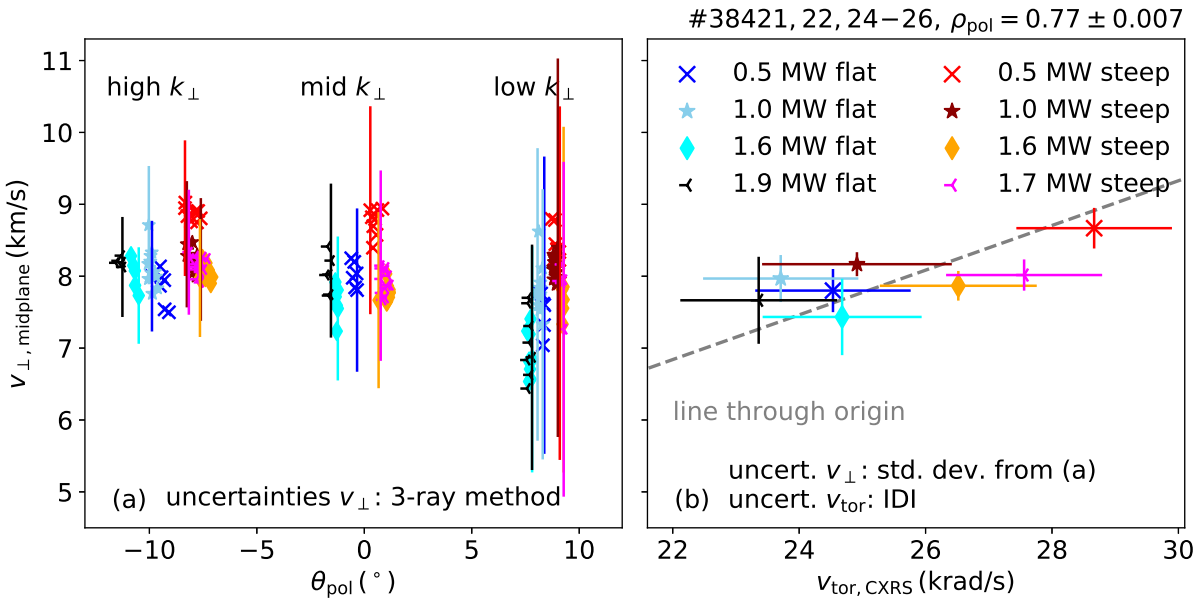


**Figure 6.25:** Perpendicular velocity of density fluctuations for different turbulence scenarios. The vertical axis measures the velocity as mapped to the midplane using the poloidal dependence of the $E \times B$ drift velocity. (a) indicates that there is no dependence on the poloidal angle, (b) suggests an approximately linear dependence with the toroidal rotation velocity from CXRS.

### 6.10.4 Poloidally resolved measurement of the perpendicular velocity of electron density fluctuations

The next quantity of interest in the extended scenarios is the perpendicular velocity of the density fluctuations and its poloidal variation. Figure 6.25(a) depicts X-mode measurements of the perpendicular velocity mapped to the midplane, $v_{\perp,\mathrm{midplane}}$, in all three wavenumber ranges under investigation versus the poloidal angle. The analysis of $v_\perp$ and the uncertainty calculation directly follow Chap. 5. Red and orange colors correspond to scenarios with inner heating, black and blue colors to scenarios with outer heating. For better visibility, the base case scenarios only include measurement data at the same mirror angles as the extended scenarios. The radial interval is smaller than in Fig. 6.17, since for the poloidal angles under consideration a finer radial resolution is available. The measurements in Fig. 6.25(a) confirm the observations in Chap. 5 and Sec. 6.6 that $v_\perp$ does not show a poloidal dependence other than that of the $E \times B$ velocity.

Figure 6.17(b) plots the poloidally averaged velocities versus the toroidal velocity from IDI. The dashed line crosses the origin of the coordinate system and is a fit through all points. The red points tend to lie at similar perpendicular velocities, but larger $v_{\mathrm{tor}}$ values than the blue points. Using Eq. 1.3 with the approximation $E_\mathrm{r} \approx v_{\mathrm{tor},\alpha} B_{\mathrm{pol}}$, the phase velocity can be roughly estimated as $v_{\mathrm{ph}} \approx v_{\mathrm{E\times B}} - v_{\mathrm{tor}} B_{\mathrm{pol}}/B$. The trend that the blue points occur at smaller toroidal velocities than the red points thus potentially indicates a lower phase velocity in the steep regime than in the flat regime, such that the phase velocity in the steep is less ion-diamagnetic directed than in the flat scenario. As will be discussed for the linear GENE runs in Sec. 7.3, this also holds for the two base case scenarios of flat and steep, where in Figs. 7.2(c),(d) the steep scenario shows

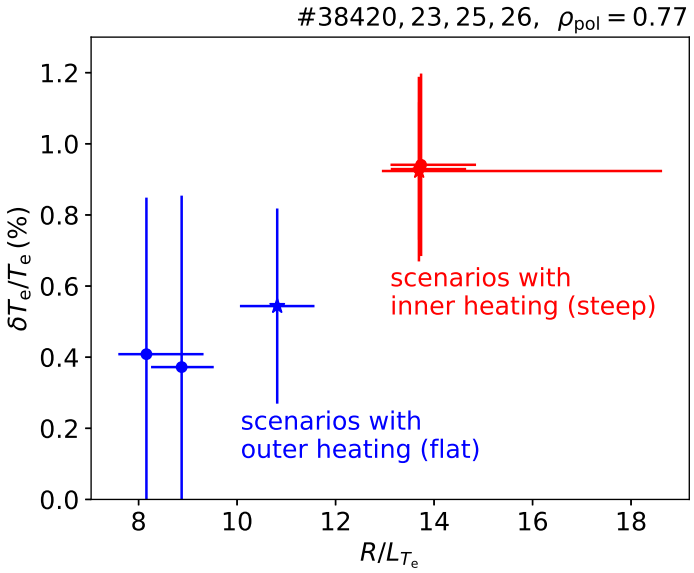


**Figure 6.26:** Temperature fluctuation amplitudes for various scenarios with different normalized electron temperature gradients, measured at the same radial position.

less propagation in ion diamagnetic direction than the flat scenario. However, it is important to note that the experimental observation is an estimate that lacks inclusion of the pressure term and the poloidal velocity into the electric field, c.f. Eq. 3.3, and thus must be treated with care.

Such as for the original two scenarios, the O-mode measurements suffer from the existence of the second peak (c.f. Sec. 6.5) and will not be considered here for investigations on the poloidal variation of the perpendicular velocity.

### 6.10.5 Fluctuation amplitude and radial correlation length of electron temperature fluctuations

The fluctuation amplitude of the electron temperature obtained by the analysis procedure used in Sec. 6.7 is plotted in Fig. 6.26. It follows the trend of the base case scenarios that the fluctuation level increases with the normalized gradient. In these additional scenarios the background of the coherence is subtracted in the same frequency interval as in the steep and the flat base case scenarios. The fluctuation power of the cases with inner/outer heating is integrated in the frequency interval of the base case steep/flat scenario, respectively. Note that the large uncertainties for the blue data points go back on the coherence between two neighboring channels being just slightly above the noise level (not shown). The trend of increasing fluctuation amplitude with $R/L_{T_e}$ supports the simple picture of the mixing length model. It, however, better matches the critical gradient model, which predicts the fluctuation amplitude to be quasi constant below a threshold in $R/L_{T_e}$ and to linearly increase with $R/L_{T_e}$ above the threshold. To determine this threshold this study would need more data points and/or better statistics. A similar study on DIII-D over a wide range of plasma parameters finds this critical gradient around $R/L_{T_e} \approx 5$ [173, 174].

The radial correlation length can only be extracted in the scenarios with inner heating since for outer heating the fluctuation levels are too low (c.f. discussion for the base case scenarios in Sec. 6.8). In line with the small change of the normalized electron temperature gradient, the radial correlation length does not differ between the three scenarios outside the measurement uncertainties (not shown). This observation agrees with the measurements of the radial correlation length of electron density fluctuations, which do not significantly differ between the steep scenarios as well.

## 6.11 Summary

A large set of turbulence quantities was presented for two plasma scenarios with inner and outer off-axis ECRH deposition, respectively. In addition, six plasma scenarios with a reduced coverage of turbulence measurements are analyzed to check whether the observed trends continue for more extreme cases, where the off-axis heating power is increased.

In terms of normalized gradients the scenarios differ mostly in the electron temperature and electron density domain, where the steep electron temperature gradient scenario exhibits larger values than the flat scenario. The ion temperature and toroidal rotation velocity do not change significantly. At the same time the ion heat flux varies only slightly. However, at the plasma radii analyzed, the electron heat flux of the steep scenario is a factor of $\approx 2$ larger than that of the flat scenario.

It is thus surprising to see that even though the normalized gradients increase from the flat to the steep scenario, the electron density fluctuation level drops for the whole range of accessible turbulence scales. The curvature of the spectrum in the flat scenario is stronger than that of the steep scenario. The additional scenarios mostly continue the trend of the fluctuation levels: the density fluctuation level decreases for increasing heating power being deposited at the inner position and remain approximately constant for increasing heating power at the outer position.

On the other side, the correlation lengths of electron density fluctuations vary only little. The steep scenario exhibits slightly higher $l_\mathrm{r}$ than the flat scenario, which is in line with the narrower $k$-spectrum and the larger drift scale parameter in the steep scenario. However, the additional scenarios see even smaller measured correlation lengths for increased heating even though $\rho_\mathrm{s}$ increases.

The eddy tilt angle of electron density fluctuations is extracted from the highest $k_\perp$ measurements and does not differ between the scenarios. The perpendicular velocity only follows the poloidal dependence of the $E \times B$ velocity. It is slightly larger in the steep scenario than in the flat scenario. This trend is, however, not continued in the additional scenarios that see similar velocities regardless of the heating power and the deposition location.

The electron temperature fluctuation level increases with increasing normalized temperature gradients by a factor of roughly 2 as does the electron heat flux. The power spectrum of the temperature fluctuations in the steep scenario peaks at higher frequency than that of the flat scenario, which is in line with the difference in the rotation velocity. In the additional scenarios, the electron density and temperature fluctuation levels show very different responses: for increasing inner heating power $R/L_{T_\mathrm{e}}$ and $\delta T_\mathrm{e}/T_\mathrm{e}$ remain unchanged, while $\delta n_\mathrm{e}$ decreases. For increasing outer heating power $R/L_{T_\mathrm{e}}$ and $\delta T_\mathrm{e}/T_\mathrm{e}$ decrease, but $\delta n_\mathrm{e}$ stays unchanged.

The radial correlation lengths of electron temperature fluctuations are subject to large measurement uncertainties. They can only be extracted in the steep scenario and yield similar values as the correlation lengths of density fluctuations at comparable turbulence scales.

The cross-phase between electron density and temperature fluctuations does not change between the scenarios. It ramps with frequency, which is partially attributed to the poloidal separation between the measurement positions, however, lacks a final explanation.

Next, this comprehensive set of data will be compared to dedicated GENE simulations in Chap. 7.

# 7 Validation studies of the gyrokinetic code GENE

This chapter presents gyrokinetic simulations of the GENE code, which model the plasma turbulence in the discharges of the previous chapter[1]. It first introduces general parameters and characteristics of the GENE simulations, followed by a detailed comparison between simulation output and experiment for each of the turbulence quantities of the previous chapter. This comparison includes synthetic diagnostic modeling using the codes IPF-FD3D[2] [158, 159], ECRad [120] and TORBEAM [121, 122]. The present study provides two plasma scenarios that are experimentally well characterized, using state of the art diagnostics and data evaluation methods. These scenarios can serve as a valuable basis for future code validation and verification efforts, similar to the cyclone base case [198] for linear gyrokinetic code comparisons.

## 7.1 Review of previous works

This work follows a long history of validation efforts of turbulence codes. This section attempts to highlight important studies in this field, focusing in particular on comparisons of measurements in the core of L-mode plasmas with gyrokinetic simulations. It emphasizes the last two decades, since in the early 2000s a range of gyrokinetic codes have been developed, which are still in use nowadays.

Early comparisons have been done on DIII-D using the GYRO code [19]. Reference [192] was the first to measure $l_\mathrm{r}$ of electron density fluctuations with reflectometry and compare the results to gyrokinetic simulations. Already back then, the community scanned the code inputs within the experimental error bars to test the sensitivity of the models. Slightly later Ref. [199] claimed to be the first to compare global gyrokinetic simulations with experiment, matching the transport coefficients within error bars. While studies of electron density fluctuations were done at an early stage, it took longer for the electron temperature domain.

[1] I would like to highly acknowledge the work of T. Görler from the theory department of IPP Garching for running the gyrokinetic simulations with GENE and providing me with its output; the turbulence fields (c.f. Fig. 7.1), linear stability analysis, heat fluxes and $k$-spectra, for analysis and interpretation.

[2] I would like to highly acknowledge the work of C. Lechte from the Plasma Turbulence Group of the University of Stuttgart for running the fullwave simulations with IPF-FD3D and providing me with the output for analysis and interpretation.

The first simultaneous measurements of electron temperature and density fluctuation profiles in a tokamak to be compared to gyrokinetic simulations have been performed on DIII-D [57]. The best match with GYRO was obtained at midradius, where experimental heat diffusivities and $\delta n_\mathrm{e}/n_\mathrm{e}$ was matched, while, however, overestimating $\delta T_\mathrm{e}/T_\mathrm{e}$ and the particle diffusivity. Besides, the awareness of the necessity of synthetic diagnostic modelling for comparisons was present [36]. Soon also the cross-phase between electron density and electron temperature fluctuations was successfully measured at DIII-D and compared to GYRO with good quantitative agreement, despite disagreements in the transport fluxes [58]. Later GENE runs on the same plasma scenario, however, could reproduce both the cross-phase values and the heat fluxes for slight variations in the input parameters [200]. Subsequent DIII-D studies simultaneously measured $\delta n_\mathrm{e}/n_\mathrm{e}$ and $\delta T_\mathrm{e}/T_\mathrm{e}$ in various plasma scenarios with different ECRH deposition profiles and thus $R/L_{T_\mathrm{e}}$ [170]. These measurements were extended in Ref. [171] and compared to both local and global GYRO simulations, which could reproduce the electron heat flux and low-$k$ $\delta T_\mathrm{e}/T_\mathrm{e}$ amplitudes, but underpredicted $Q_\mathrm{i}$ and disagreed with Doppler reflectometry measurements of $\delta n_\mathrm{e}/n_\mathrm{e}$ at intermediate $k$. This underprediction of the ion heat flux and that of the fluctuation level by GYRO was at that time termed *gyrokinetic shortfall*. It was investigated by dedicated GENE simulation, which were able to reproduce the experimental findings [200, 201]. Later studies [202] with an improved GYRO code confirmed the agreement found with GENE.

Following these promising validation studies, in the last decade a larger number of studies compared different quantities between various plasma scenarios in several fusion devices with a range of gyrokinetic codes. In a large-scale attempt to understand turbulence, three European devices, AUG, TCV and Tore Supra, joined to a *virtual institute* to work together on turbulence understanding [203]. This initiative helped prepare many of the tools used in this thesis. In addition, validation was thought of on the meta level, such as discussed in two reviews on best practices [24, 29] and one on validation metrics [204], as well as one recently written tutorial on code validation [30].

AUG turbulence measurements were compared to GENE [18, 65, 66], with early works focusing on electron density fluctuations and later works adding electron temperature fluctuations. An investigation of two plasma scenarios found that in a plasma with pure ITG drive the electron and ion heat fluxes could be matched together with the electron density fluctuation amplitude for the full extended radial region under investigation, however, for a mixture of ITG and TEM, only the fluctuation amplitudes were predicted correctly [138]. A subsequent study could match wavenumber spectra measured by Doppler reflectometers when applying synthetic diagnostic modeling by means of fullwave simulations [34]. What followed were comprehensive measurements of several turbulence quantities at the same radial position of an ECRH L-mode discharge, where $Q_\mathrm{e}$, $Q_\mathrm{i}$, $l_\mathrm{r}$ of electron temperature fluctuations and $\alpha_\mathrm{n,T}$ were matched within experimental uncertainties [119], leaving only $\delta T_\mathrm{e}/T_\mathrm{e}$ to be overpredicted by GENE. A concurrent study to the present work, focusing on isotopes, reported good agreement in all compared quantities, $Q_\mathrm{e}$, $Q_\mathrm{i}$, $\delta T_\mathrm{e}/T_\mathrm{e}$, $l_\mathrm{r}$ of electron temperature fluctuations and the absolute value of $\alpha_\mathrm{n,T}$, for both deuterium and hydrogen plasmas [118].

Validation efforts were also reported from Tore Supra when comparing heat fluxes and density fluctuations to GYRO. $k_\mathrm{r}$-spectra measurements from the fast swept reflectometer were matched in Ref. [179]. In addition, Ref. [178] matched $Q_\mathrm{e}$, $Q_\mathrm{i}$, $\delta n_\mathrm{e}/n_\mathrm{e}$ and poloidal and radial $k$-spectra from Doppler reflectometry.

On DIII-D, comparisons of both the electron density and the electron temperature fluctuation domain to GYRO simulations were done. Reference [180] could match $Q_\mathrm{e}$, $\delta n_\mathrm{e}/n_\mathrm{e}$ and $\alpha_\mathrm{n,T}$ for two plasma scenarios of different $T_\mathrm{e}/T_\mathrm{i}$, but did not find agreement for $Q_\mathrm{i}$ and $\delta T_\mathrm{e}/T_\mathrm{e}$. When comparing two-dimensional wavenumber spectra from beam emission spectroscopy to GYRO, Ref. [181] concluded on a reasonable prediction of trends, but no overall match. In a study on different plasma scenarios, the trends of how $Q_\mathrm{e}$ and $\delta T_\mathrm{e}/T_\mathrm{e}$ depend on $R/L_\mathrm{e}$ could be recovered by GYRO, however, simulations did not reproduce the typical behavior expected from the critical gradient model [172].

Alcator C-mod plasmas were compared to GYRO simulations as well. Reference [205] was the first to compare the impurity transport and could recover some trends. Later, good agreement of $Q_\mathrm{i}$ and the impurity particle transport were found, as well as trends in $(\delta T_\mathrm{e}/T_\mathrm{e})\,/\,(\delta n_\mathrm{e}/n_\mathrm{e})$ measured by CECE and a phase contrast imaging diagnostic were recovered [206]. Reference [207] reproduced $Q_\mathrm{i}$ and $\delta T_\mathrm{e}/T_\mathrm{e}$, but saw an underprediction of $Q_\mathrm{e}$ by simulations.

On the FT-2 tokamak, validation efforts were undertaken using the ELMFIRE code [208]. Reference [209] reported quantitative agreement of several transport phenomena related to electron density fluctuations measured by Doppler reflectometry. Later, also the poloidal variation of radial correlation length of electron density fluctuations was recovered [210].

On the MAST tokamak, measurements from beam emission spectroscopy were compared to the GS-2 code [211]. Reference [212] reported reasonable agreement for the correlation time and $l_\mathrm{r}$ of electron density fluctuations.

In addition to the above mentioned range of validation efforts, which include simultaneous comparison of several quantities, often covering more than one plasma scenario, comparisons of simulations with experimentally newly accessible turbulence quantities are of great importance. Reference [213] found multi-scale simulations with GYRO to match the experimental perturbative diffusivity of an Alcator C-Mod L-mode plasma within error bars. Reference [153] measured the eddy tilt angle of electron density fluctuations with Doppler reflectometry in two AUG L-mode discharges and found quantitative agreement with the GKW code [68].

In order to investigate the importance of multi-scale simulations, Ref. [214] compared Alcator C-mod measurements of both electron density and electron temperature fluctuations to GYRO simulations, which include a different number of scales. Reference [215] showed the first agreement between experiment and simulation of $Q_\mathrm{e}$ and electron scale frequency spectra for a plasma of the NSTX tokamak simulated by GYRO.

The present study exceeds the previous studies in the number of turbulence observables, simultaneously measured in two different plasma scenarios at the same two radial positions and in the extensive use of synthetic diagnostics. The GENE simulations at hand correctly model $Q_\mathrm{i}$, $k$-spectra and $l_\mathrm{r}$ of electron density fluctuations, $\delta T_\mathrm{e}/T_\mathrm{e}$ and $l_\mathrm{r}$ of electron temperature fluctuations. $\alpha_\mathrm{n,T}$ cannot be compared quantitatively, but the trend between the two scenarios is recovered. The only major disagreement is $Q_\mathrm{e}$, which is overpredicted by a factor of two, but follows the reduction from the steep to the flat scenario. Further simulations are ongoing to understand this deviation, i.e. by including the effect of impurities. In addition to the remarkably good overall agreement, all trends between the two plasma scenarios and radii are reproduced.

## 7.2 Simulation setup

The GENE (c.f. Sec. 2.8) simulations are performed in a local, i.e. flux-tube geometry and are restricted to ion gyroradius scales. The model includes electromagnetic fluctuations, collisions and the external $E \times B$ shear flow. Two species, electrons and ions, with realistic mass ratio are treated. Impurities are introduced through the effective atomic number $Z_\mathrm{eff}$ via the collision operator. Few tests with a third species (impurity ions), fully attributing the finite $Z_\mathrm{eff} - 1$ to the main impurity ions Boron, have been performed, initially finding that two species runs are sufficient. For simulations with increasing spectral resolution, considering the third species might improve the match. Since, due to computational constrains, these three species runs are currently ongoing, the following focuses on two species. To cover the full spatial and spectral range of experimental measurements, the simulation grid is finer than default, namely $N_x = 512$ points in radial direction, $N_z = 24$ points in toroidal direction. There are runs for both $N_{k_\mathrm{y}} = 48$ and $N_{k_\mathrm{y}} = 96$, the number of modes in poloidal direction. Since the latter is computationally more expensive, it is run on a shorter time interval. $N_{k_\mathrm{y}} = 96$ is thus only used for analysis of density fluctuations where this spectral resolution is necessary. The temperature fluctuation and cross-phase analyses use simulations with $N_{k_\mathrm{y}} = 48$ to profit from improved temporal statistics. The parallel velocity is scanned from $-3$ to 3 times the thermal ion velocity with a number of points $N_{v_\mathrm{par}} = 48$. The magnetic moment $\mu$ is resolved within 0 to 9 $T_0/B_\mathrm{ax}$ with number of points $N_\mu = 16$, where $T_0$ is the local temperature and $B_\mathrm{ax}$ the magnetic field on the magnetic axis.

The simulations build on the experimental parameters presented in Sec. 6.1 in Figs. 6.2, 6.3 and 6.4. The input includes the pressure constrained magnetic equilibrium IDE, transport analysis from the TRANSP code of the terms in the power balance equation yielding the experimental electron and ion heat fluxes to be reproduced by GENE. In GENE the normalized gradients are varied in order to obtain heat flux matching, c.f. Sec. 7.4.

The post-processing procedure of the GENE raw output data works as follows: it first interpolates the flux-tube data to fine-grained equidistant time steps. Next it translates from a co-moving frame to a lab frame by applying a phase factor. Finally it maps the flux-tube coordinates to cylindrical coordinates and extracts a poloidal cross-section. Figure 7.1 depicts a snapshot

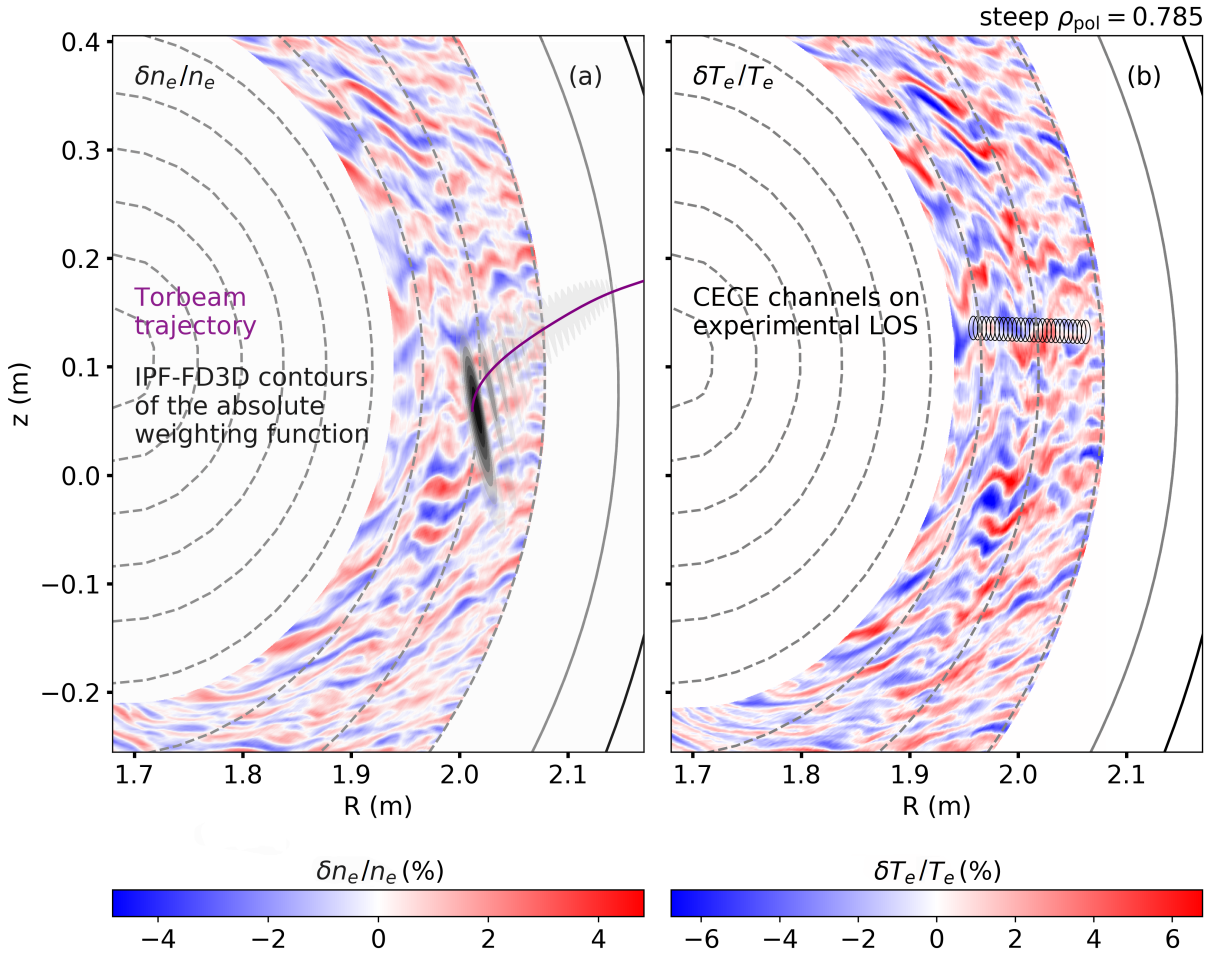


**Figure 7.1:** Poloidal cross-sections of AUG with density (a) and temperature (b) fluctuations from nonlinear flux-tube heat flux-matched GENE simulations of the steep scenario at the outer radius. Synthetic diagnostic modeling of Doppler reflectometer in (a): weighting function of fullwave simulations with IPF-FD3D and of CECE in (b): emission volumes. For details refer to the text and following sections.

of the relative electron density (a) and temperature fluctuations (b) of the steep scenario from nonlinear GENE runs for the kinetic profiles taken at $\rho_{\mathrm{pol}} = 0.785$ (c.f. Fig. 6.3) on top of the magnetic flux surfaces. In these flux-tube runs the kinetic profile's curvature is constant over the simulated radial interval. The turbulent structures of density fluctuations resemble those of the temperature fluctuations with slightly lower fluctuation amplitudes. In addition, Fig. 7.1 presents the principle of synthetic diagnostic modeling where a spatio (-temporal) filter is applied to best match the diagnostic specifications: the grey contours in Fig. 7.1(a) refer to the absolute of the weighting function of fullwave simulations with the IPF-FD3D code that agree with the purple trajectory modeled by TORBEAM. Since the wave electric field only swells at larger radii than the cutoff, the TORBEAM trajectory, which intersects the cutoff, slightly underestimates probing radius compared to the the more accurate fullwave simulations. The black ellipses in Fig. 7.1(b) indicate the experimental measurement locations of the CECE channels.

## 7.3 Linear stability analysis

Linear GENE runs serve to extract the dominant microinstabilities, which drive turbulence at different scales. These runs exist for both scenarios (steep, flat) and radial positions of interest ($\rho_{\mathrm{pol}} = 0.740$, 0.785) for ion and electron scales. The growth rates and real mode frequencies of the fastest growing modes are shown in Fig. 7.2 versus the inverse eddy scale size, $k_\perp$. Positive frequencies correspond to ITG-dominated turbulence, which moves in ion diamagnetic direction and negative frequencies to TEM- and ETG-dominated turbulence moving in electron diamagnetic direction. For the largest scales at $k_\perp \lesssim 0.4\,\mathrm{cm}^{-1}$ ($k_\perp \rho_\mathrm{s} \lesssim 0.1$) additionally microtearing modes could be relevant (more details on connections and co-existance of several microinstabilities are discussed in [216]). The growth rates are given in units of $c_\mathrm{s}/\alpha$ where $c_\mathrm{s}$ is the ion sound speed and $\alpha = \sqrt{\Psi_{\mathrm{tor,sep}}/\pi B_{\mathrm{ax}}}$ is a normalization factor with the separatrix toroidal magnetic flux $\Psi_{\mathrm{tor,sep}}$.

Figures 7.2(a),(b) suggest the turbulence to be more pronounced in the steep scenario, which is in line with the observation that all normalized kinetic gradients in the steep scenario exceed (or are equal to) those of the flat scenario, c.f. Fig. 6.4. For $0.4\,\mathrm{cm}^{-1} \lesssim k_\perp \lesssim 4.0\,\mathrm{cm}^{-1}$ ($0.1 \lesssim k_\perp \rho_\mathrm{s} \lesssim 1.0$) the turbulence is ITG-dominated for both scenarios and radii. The flat scenario plotted in blue colors remains ITG-dominated over a larger range of scales than the steep scenario in red. It transitions from ITG to ETG at higher $k_\perp \rho_\mathrm{s}$ than the steep scenario. For the smallest scales all cases are ETG-dominated.

To study the mixture of the different instabilities, the normalized kinetic gradients are varied within the error bars in several linear GENE runs (not shown). At ion scales all simulations with nominal normalized gradients predict ITG dominance (c.f. Fig. 7.2 top row). For the inner radius of the steep scenario (#38420, $\rho_{\mathrm{pol}} = 0.740$) a variation of the normalized gradients within the uncertainties, however, can cause ITG/TEM transitions at ion scales. For the outer radius of the steep scenario (#38420, $\rho_{\mathrm{pol}} = 0.785$) the ITG dominance is more robust, but transitions to TEM are still possible by varying several gradients at the same time. The flat scenario at the inner radius (#38423, $\rho_{\mathrm{pol}} = 0.740$) turns out to have even more robust ITG turbulence, whereas a transition to TEM is only possible by variation of all gradients. The flat scenario at the outer radius (#38423, $\rho_{\mathrm{pol}} = 0.785$) is dominated by robust ITG turbulence, which does not transition to TEM when varying the gradients within the uncertainties. The dominance of ETG at small scales is robust and is expected to cause non-negligible but low transport. The observation that when increasing both $R/L_{T_\mathrm{e}}$ and $R/L_{n_\mathrm{e}}$, the plasma goes from a purely ITG-dominated state to a mixed state of comparably strong ITG and TEM drive, is consistent with theoretical predictions [217, 218] and has been seen in previous experiments at AUG [138].

Figures 7.2(g),(h) depict the wavenumber spectra of electron density fluctuations at $k_\mathrm{r} = 0$ to be in line with experimental conditions (c.f. Sec. 4.2). Figures 7.2(i),(j) show the wavenumber spectra of electron temperature fluctuations. Since all these wavenumber spectra come from nonlinear GENE runs, the finest resolved scale is $k_\perp \approx 18\,\mathrm{cm}^{-1}$. The energy injection scale is at $k_\perp$ slightly larger than $1\,\mathrm{cm}^{-1}$. At $k_\perp$ larger than this knee, the fluctuations decrease

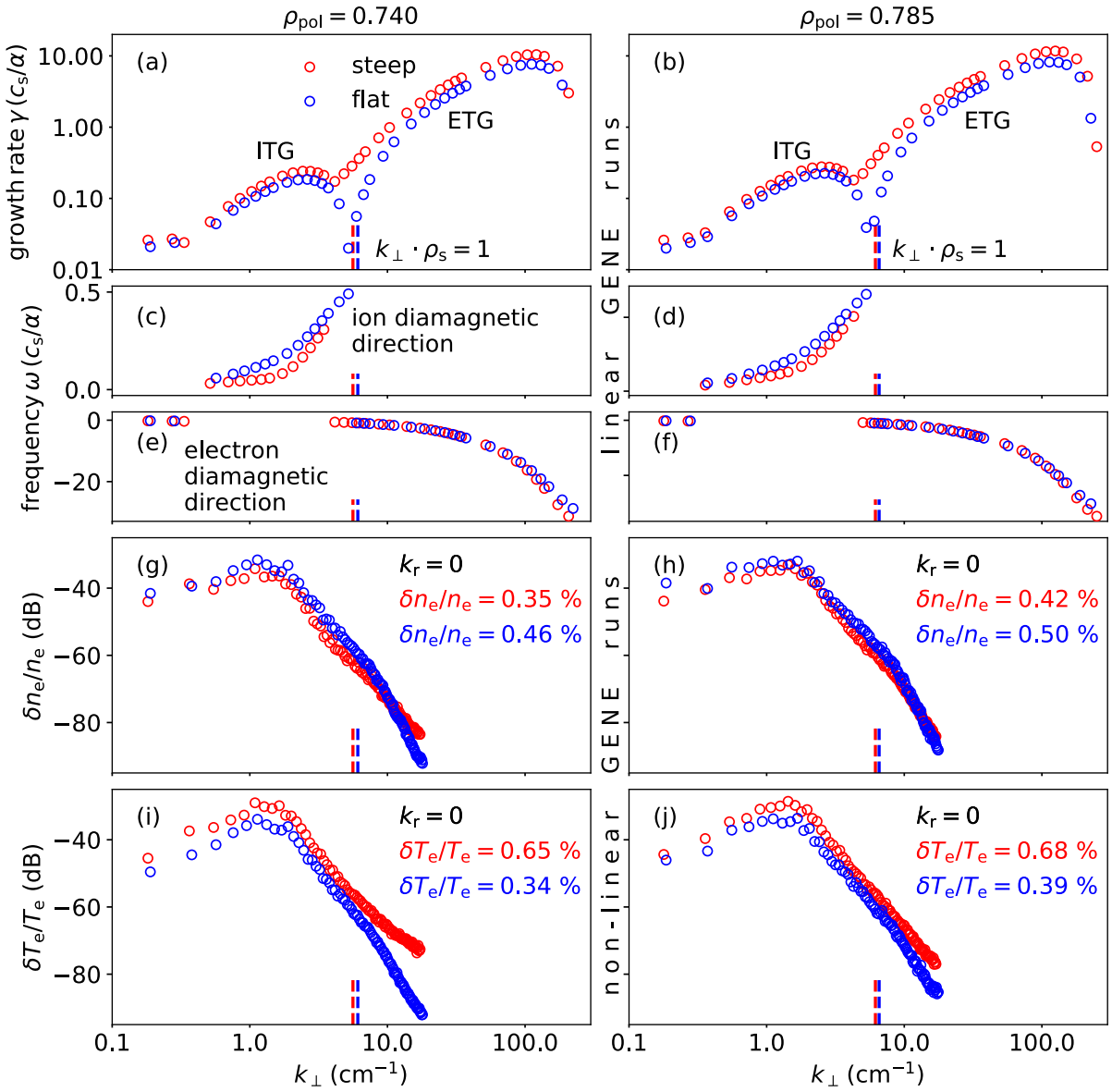


**Figure 7.2:** Linear growth rate (a),(b) and frequency (c)–(f) of the fastest growing mode in linear simulations for both radii and scenarios. The bottom plots depict the corresponding time averaged wavenumber spectra of electron density fluctuations in (g) and (h) and electron temperature fluctuations in (i) and (j) at zero radial wavenumber obtained from nonlinear simulations.

with increasing $k_\perp$ due to the cascade discussed in Sec. 2.2. The decrease of fluctuations with decreasing $k_\perp$ is likely an artifact of the finite size of the flux-tube simulation domain that cannot host as large turbulence scales as present in experimental plasma geometries. The faint knees around $k_\perp \approx 9\,\mathrm{cm}^{-1}$ ($k_\perp \rho_s \gtrsim 1$) indicate the vanishing of the ITG as fastest growing mode and the onset of ETG dominance. The relative temperature and density fluctuation amplitudes written in the plot are the integral of all scales. Whereas the temperature fluctuation amplitude in (i) and (j) increases from the flat to the steep scenario, the density fluctuation amplitude in (g) and (h) decreases. This is consistent with the experimental observations. As before, the behavior of the electron temperature fluctuations confirms simple turbulence pictures like

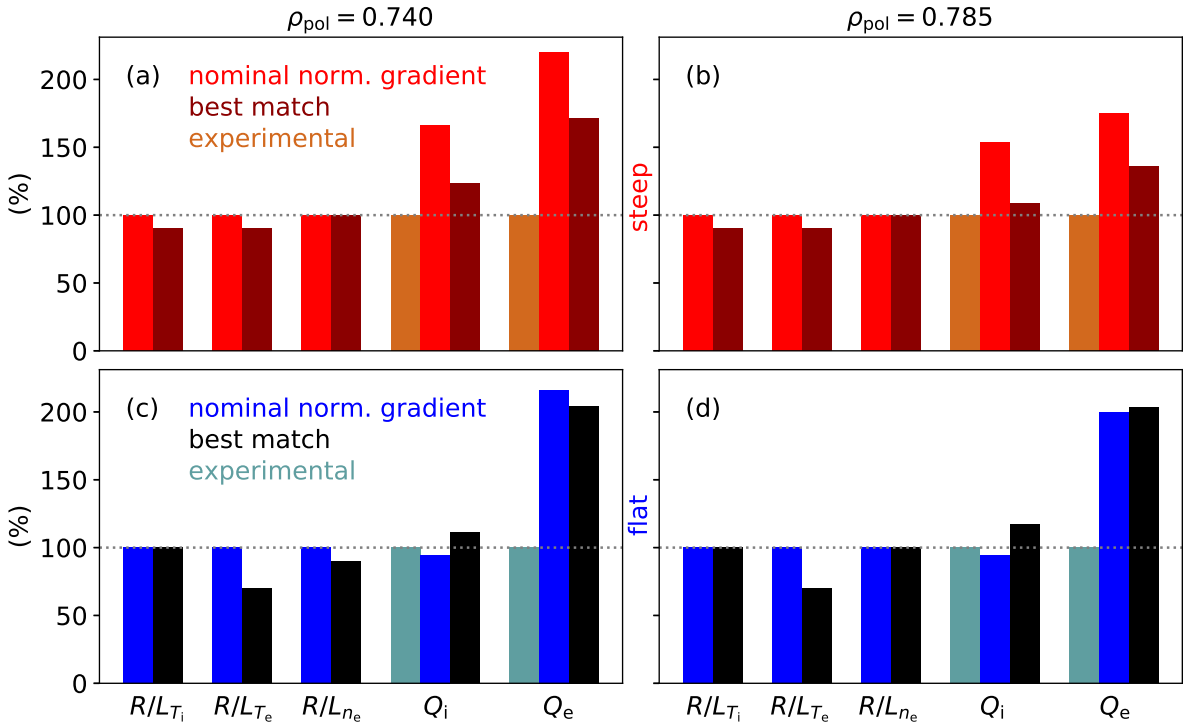


**Figure 7.3:** Nominal normalized gradients in comparison to best-match and experimental heat flux with the GENE heat fluxes for nominal normalized gradients and best-match, for both scenarios (rows) and radii (columns).

the mixing length model and the critical gradient model, whereas that of the electron density fluctuations contradicts them. It is interesting to note that the temperature fluctuation amplitude exceeds that of the density in the steep scenario, whereas this is reversed in the flat scenario.

## 7.4 Matching of fluxes and normalized kinetic gradients

Before comparing GENE turbulence to experimental turbulence measurements, validation efforts usually make sure that the heat fluxes of the simulations match the experimental heat fluxes. The reason for starting with heat fluxes is their comparatively simple extraction on the experimental side. In the context of this thesis, the TRANSP runs discussed in Sec. 6.1.4 provide the experimental fluxes. This chapter from now on discusses nonlinear GENE simulations. GENE runs based on the nominal normalized gradients from Fig. 6.4 find heat fluxes close to the experimental values. They are marked *nominal* in Fig. 7.3. However, a variation of the input normalized gradients brings the heat fluxes from the simulation closer to the experimental values. Here the *best match*, as labeled in Fig. 7.3, refers to the best match possible within the available computational resources. For the normalized gradients of ion temperature and electron density domains, the nominal values and 90 % of them are adequate for flux matching. For $R/L_{T_e}$, GENE requires smaller values than seen in the experiment, in particular for the flat scenario. Even though a difference of 30 % may seem large, this is within the experimental uncertainties of the ECE at the radial positions of interest, since there the hardware transitions from the edge

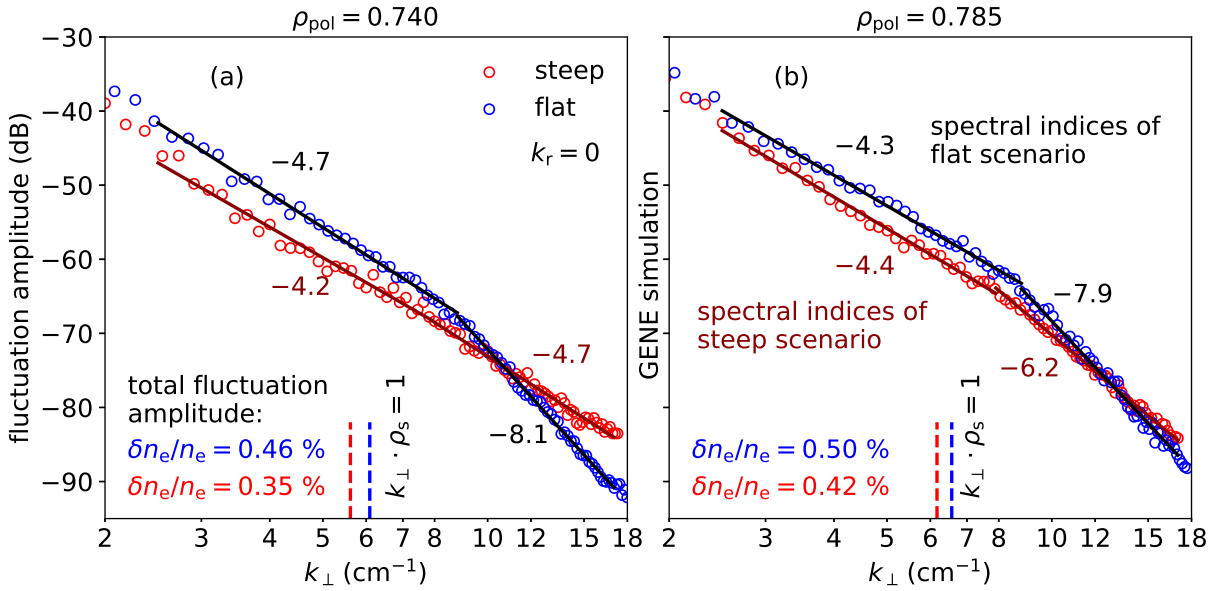


**Figure 7.4:** Time-averaged $k$-spectra simulated by GENE for both scenarios at both radii with linear fits and spectral indices. The fluctuation power in the flat scenario exceeds that of the steep scenario for a wide range of scales, the same is true for the total fluctuation power. For details refer to the text.

to the core system where the mixers are less reliable. In addition, currently ongoing simulations study the impact of a third species, Boron. These are expected to better match the electron heat fluxes with less severe deviations of the normalized gradients from their nominal values. Due to computational and temporal constraints experiment-simulations comparisons using GENE runs with a better match in $Q_e$ must be left to a future study.

## 7.5 Wavenumber spectrum of electron density fluctuations

The simulated turbulence field of electron density fluctuations allows to directly extract the fluctuation power of the different turbulence scales. The GENE output routines provide, among others, the perpendicular wavenumber spectrum of density fluctuations for zero radial wavenumber, which is close to what Doppler reflectometers measure, c.f. Sec. 4.2. This spectrum, shown in Fig. 7.4 for the experimentally covered spectral range, has a knee position of around $k_\perp = 8\,\mathrm{cm}^{-1}$ that separates a region with lower spectral index at low $k_\perp$ from a region with larger spectral index at large $k_\perp$. Note that this knee position, however, does not refer to the injection scale, that lies around $k_\perp \approx 1\,\mathrm{cm}^{-1}$ (c.f. Fig. 7.2), but to the onset of ETG influence on the turbulence. The spectral indices of linear fits to the two parts of the spectra are written in the plot. They compare well with the values found in a previous study, which compared a variety of GENE simulations with different turbulence drive [219] and reported spectral indices in the range $3-6$ in pure ITG/ETG/TEM turbulence as well as in mixtures. Whereas in the steep scenario the spectral indices below and above the knee position change only marginally, the change in the flat scenario is nearly a factor of 2. The fluctuation amplitude in the flat scenario is larger

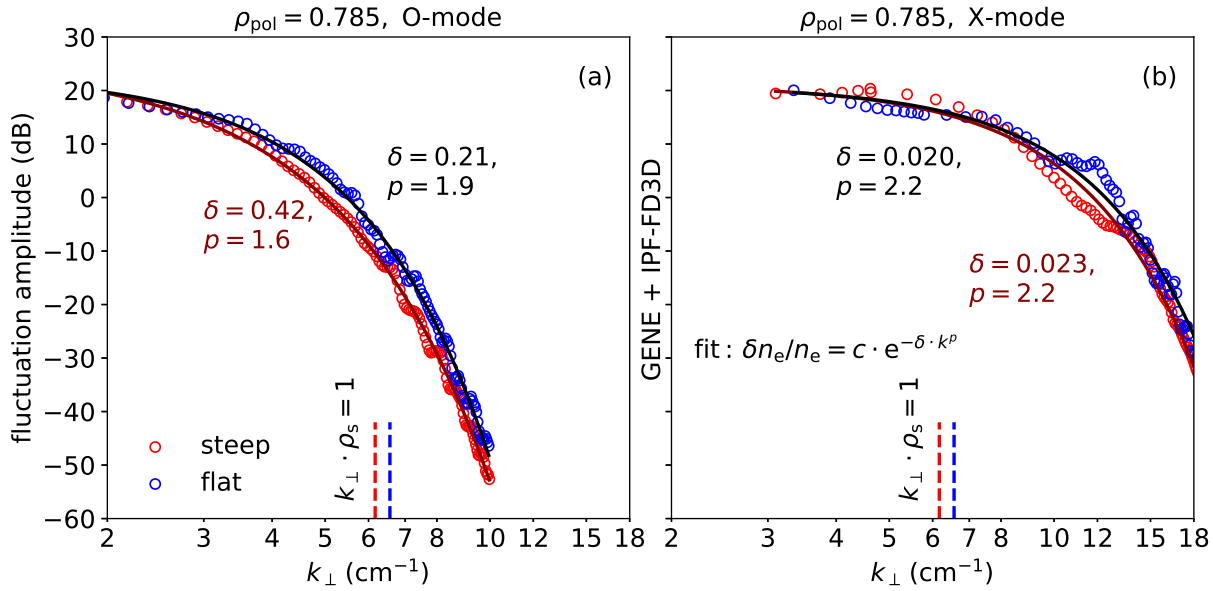


**Figure 7.5:** $k$-spectra from IPF-FD3D applied to GENE turbulence for the outer radius of both scenarios. The fluctuations in the flat scenario exceed those of the steep scenario for a wide range of wavenumbers. A general exponential function quantifies the spectra.

than in the steep scenario for a wide range of $k_\perp$. At high $k_\perp$ ($\rho_{pol} = 0.740$: $k_\perp < 10\,\mathrm{cm}^{-1}$, $\rho_{pol} = 0.785$: $k_\perp < 12\,\mathrm{cm}^{-1}$) fluctuations become stronger in the steep scenario. In total, the integral of the $k$-spectrum of the flat scenario exceeds the level of the steep scenario. In line with experiment and the references mentioned there [58, 138, 149, 178–181], the fluctuation power increases with radius. In these runs the instabilities that cause most of the transport are ITG and TEM, whereas the ETG contribution is non-negligible but small.

Following previous studies on $k$-spectra in AUG experiments and GENE [34, 35], the direct comparison of the GENE output to the measured $k$-spectra might not match due to nonlinear diagnostic effects (c.f. Secs. 4.5.1 and 6.3). Synthetic diagnostic modeling with the fullwave code IPF-FD3D (c.f. Sec. 4.6) can treat this effect. Figure 7.1(a) shows the absolute value of the simulated weighting function on top of the turbulent density fluctuations from GENE. Following Refs. [34, 35] the RMS of the IQ signal from IPF-FD3D serves as a measure of the fluctuation level. Note that the GENE runs in the context of this thesis provide enough timepoints at fine temporal spacing to go one step further and investigate Doppler spectra like in Fig. 4.3. For most $k_\perp$ values, the spectra look as expected: a Doppler shifted peak with one clear maximum well above the background noise. In that case the $k$-spectra obtained via RMS and by the area below the Gaussian fit give the same results. However, for some ranges of $k_\perp$, it is difficult to extract one clear peak from the simulated spectrum. Therefore, this thesis uses the RMS method and leaves the advanced synthetic modeling to future work. Figure 7.5 depicts the RMS power spectrum of the synthetic diagnostic modeling for O-mode in (a) and X-mode in (b). The X-mode measurements at the smallest scales ($k_\perp \lesssim 5-6\,\mathrm{cm}^{-1}$) originate from runs that only include every $8^{\mathrm{th}}$ turbulence sample, because of already solved issues. Due to computational constraints the focus is solely on the outer radial position.

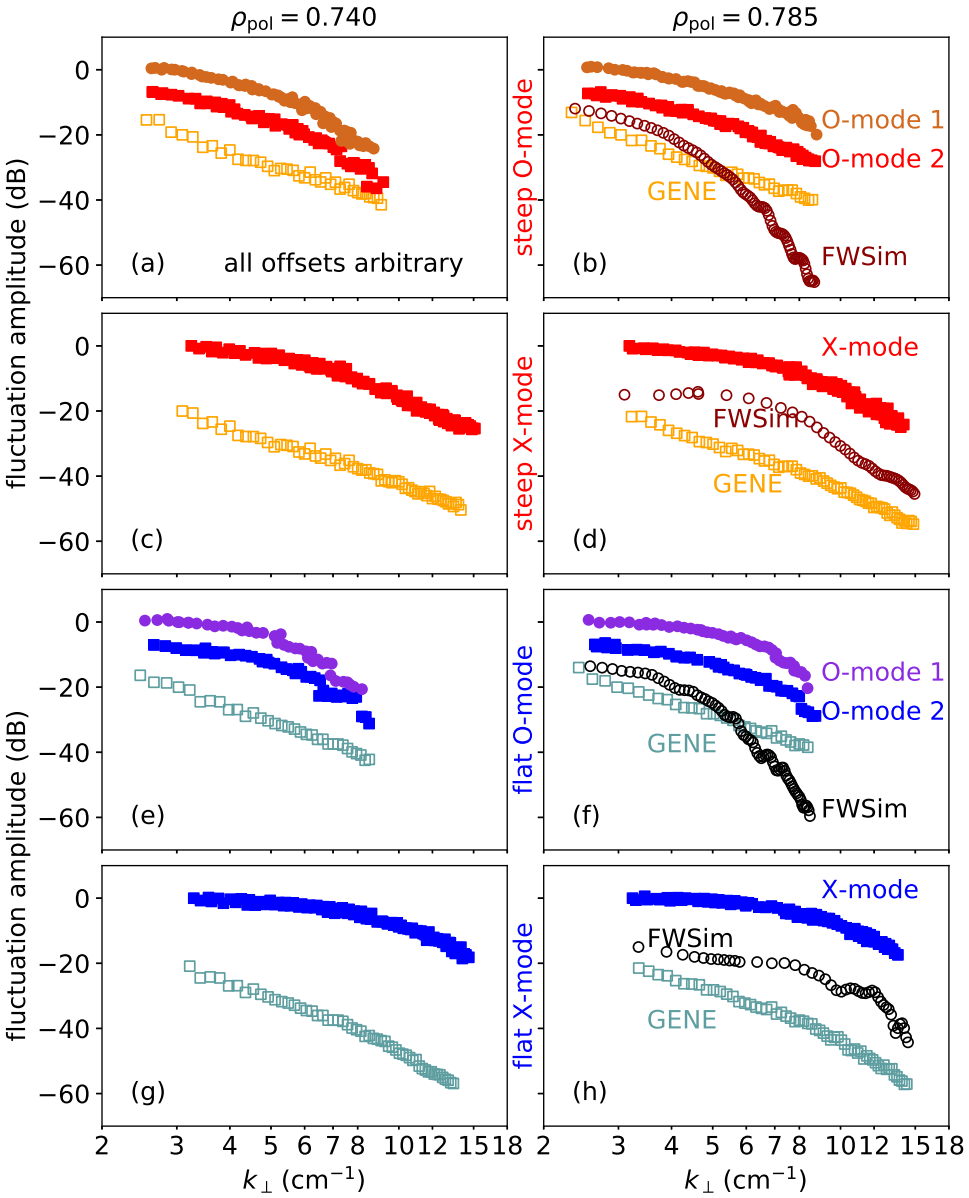


**Figure 7.6:** Wavenumber spectra for different polarizations and radii. Each plot depicts the experimental spectra together with GENE output and (for the outer radius) synthetic diagnostic modeling using IPF-FD3D for direct comparison.

The spectral shape of the fullwave simulations resembles the round shape of the experiments much better than the raw GENE output. Thus, following the experimental data analysis, the general exponential fit function $\delta n_e/n_e = c \cdot e^{-\delta \cdot k^p}$ is used to quantify the spectra. For O-mode the fit parameters (written in the plot) follow the same qualitative trend as in the experiment: going from the steep to the flat scenario $p$ increases and $\delta$ decreases. For X-mode this comparison is more difficult, since the fit does not describe the spectral shape as well as in O-mode. The oscillations in the spectrum seem to be an artifact of IPF-FD3D and are currently under investigation.

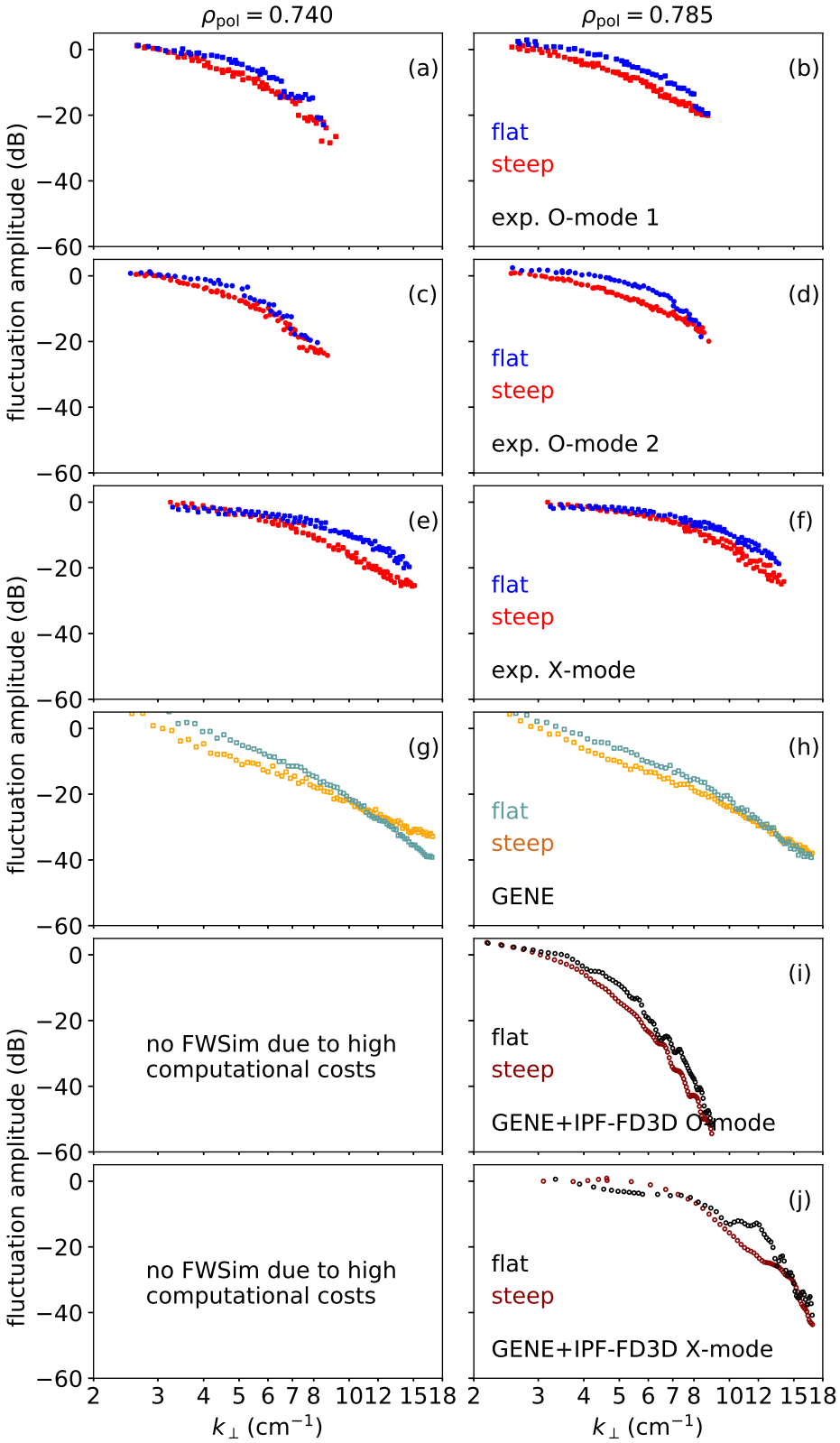


**Figure 7.7:** Comparison of all $k$-spectra from experiment, GENE output and synthetic diagnostic modeling using IPF-FD3D. The radii are separated in columns. X-mode and O-mode polarizations are distinguished. For all cases the fluctuation amplitude in the flat scenario exceeds that in the steep scenario.

The $k$-spectra from fullwave modeling recover a range of trends of the experimental wavenumber spectra, of which some are also visible in the raw GENE data. For a better comparison Fig. 7.6 plots all spectra of same radial position and – for experiment and fullwave simulations – same polarization in one plot. To enhance visibility the simulated spectra are cut to the $k_\perp$-range covered in experiment. The vertical offsets within the plots are arbitrary. As mentioned above, the fullwave simulations recover the curved shape of the experimental measurements. Whereas the GENE wavenumber spectrum consists of two linear cascades, the experimental measurements and fullwave simulations consistently see the O-mode spectra to bend at lower $k_\perp$ than the X-mode spectra, which is a direct consequence of the nonlinear power response and seen previously at AUG [34]. However, the question why the simulations, especially the fullwave simulations show a much stronger curving, i.e. a larger range of spectral indices, than experiment remains open.

To compare the difference between the two scenarios, Fig. 7.7 arranges the same data in different plots: the experimental spectra from the three Doppler reflectometers are shown in the top three plots, the GENE results in the middle and those from fullwave simulations in the bottom two plots. Note that the vertical offsets between different plots are arbitrary, but not within plots not. All plots state larger fluctuation amplitudes in the flat scenario than in the steep scenario and thus consistently oppose simple turbulence pictures like the mixing length model or the critical gradient model that fluctuations increase with the normalized gradient. The difference between the fluctuation levels of the two scenarios is most pronounced in the intermediate $k$-range, and less for fluctuations at small and large wavenumbers. While most of the literature observes increasing density fluctuation levels with normalized gradients, c.f. Ref. [214], an experimental study from DIII-D reports the density fluctuations at intermediate wavenumbers to drop with increasing $R/T_\mathrm{e}$ [170]. Subsequent gyrokinetic simulations, however, could not reproduce this finding [171]. The present study consistently observes the reduction of density fluctuations with increasing normalized electron temperature gradient in both experiment and simulation, being able to potentially come up with a physics explanation of this effect, for instance by varying the different kinetic gradients one after the other in future GENE runs. Comparing the shape of the wavenumber spectra reveals the experiment-simulation agreement that, as suggested above, the derivative of the spectral index, or simply the curvature, of the flat scenario's spectra is consistently stronger than for the steep scenario's spectra.

## 7.6 Radial correlation length of electron density fluctuations

The extraction of the radial correlation length of density fluctuations from the GENE output follows the analysis of $k$-spectra: first a rather simple correlation length analysis that only considers the scale-resolution of Doppler reflectometry is applied. Second a comparison with more comprehensive and computationally expensive fullwave simulations is performed. For the first approach, TORBEAM simulations provide the spectral resolution from the 3-ray method, c.f. Sec. 4.4.2. The interaction of the microwave beam with the turbulence in $k$-space is approximated

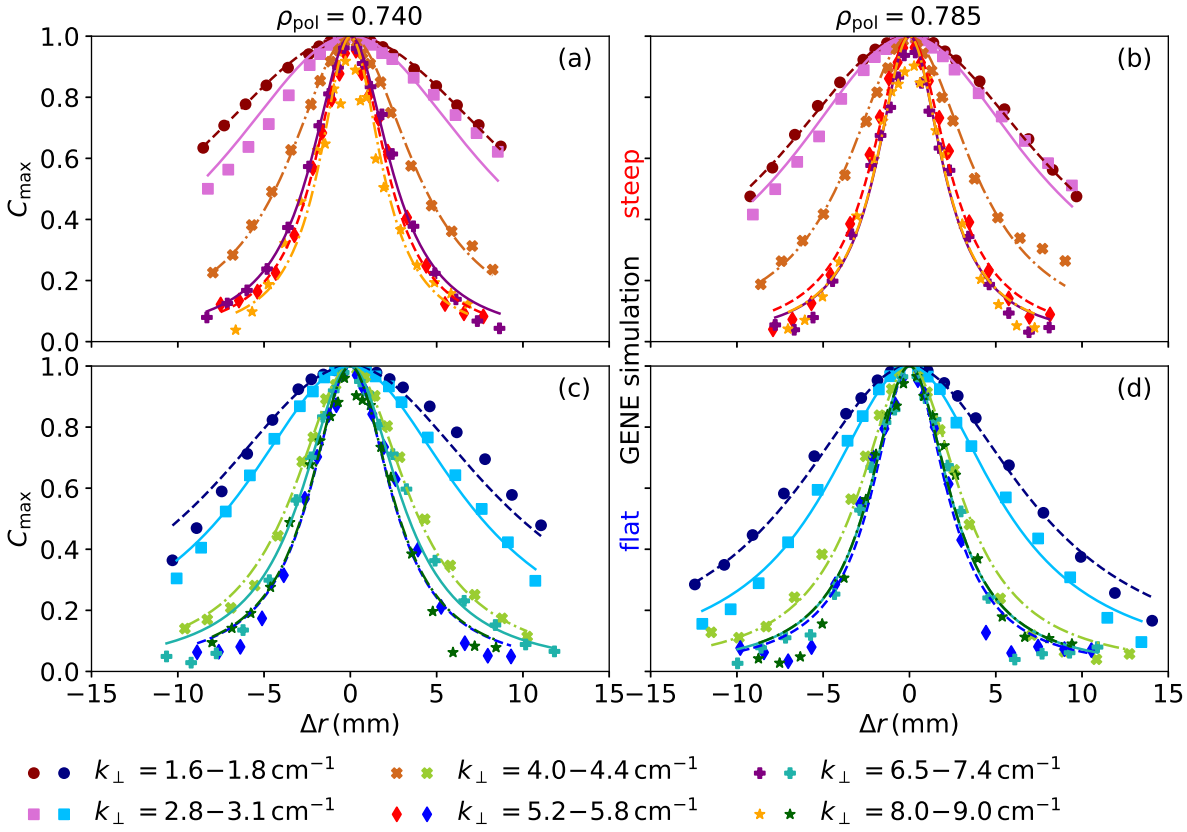


**Figure 7.8:** Maxima of the normalized correlation functions between experimental measurement points from analysis of GENE output including reduced synthetic diagnostic modeling for both scenarios (rows) and radii (columns). For details refer to the text.

by a Gaussian function with the spectral resolution from TORBEAM as width. Next, the GENE turbulence is convolved with the beam: it is Fourier transformed, then multiplied by this Gaussian filter function and transformed back. For simplicity, the Fourier transform is in $z$-direction rather than perpendicular to the flux surfaces and all hopping channels use the same spectral filtering as the reference channel. The resulting turbulence field only includes structures that the microwave beam is sensitive to. To improve statistics, four additional auxiliary reference channels (and thus 80 hopping channels) are placed at a radial distance of $\pm 2$ cm and $\pm 4$ cm to the original channels. This technique is justified, since in these flux-tube simulations the kinetic profiles and their gradients do not vary with radius. The spatial extent of the measurement regions from the 3-ray method would overestimate the experimental measurement volume, since correlating these volumes gives unreasonably large correlation. Thus, time traces of single points are correlated using ensemble averaging with $n_{\mathrm{fft}} = 256$. $C_{\mathrm{max}}$ is the maximum of the mean normalized cross-correlation function from the five different radial locations and plotted in Fig. 7.8. Both scenarios (rows) and radii (columns) show a decreasing correlation with radial distance, which depends on $k_\perp$. Figure 7.8 suggests that, in line with the experiment, the simulations do not predict an asymmetry in inner or outer radial direction and can be quantitatively described by Lorentzian functions rather than Gaussian functions (the latter is not shown). Following the experimental analysis the data are weighted with $1/C_{\mathrm{max}}^2$ for fitting.

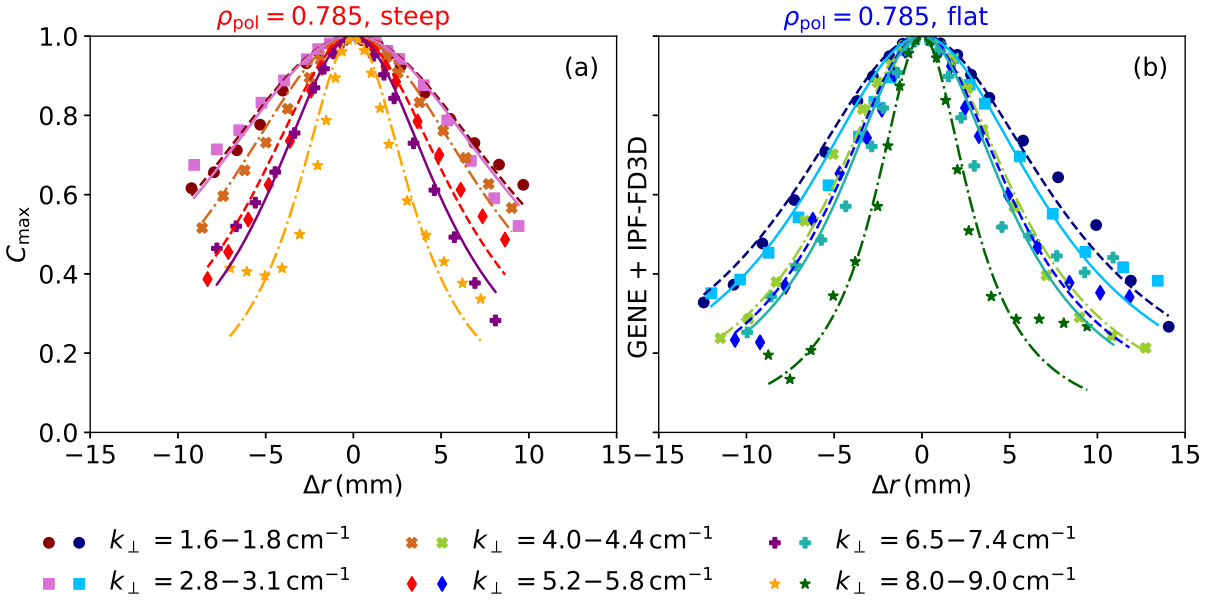


**Figure 7.9:** Maxima of the normalized cross correlation functions between measurement points using fullwave simulations with IPF-FD3D on GENE simulations as synthetic diagnostic for both scenarios.

Going one step further, the fullwave simulations take the experimental hardware settings (probing frequencies and mirror angles, c.f. Figs. 6.6(f),(i)) to model the measurement procedure of the Doppler reflectometers on a comprehensive level. Due to computational details, some of the probing frequencies are shifted by 10 MHz, which is, however, far below the measurement uncertainties. Other than in the experiment, where several sources of spurious noise contribute to the signal, the output signal of fullwave simulations only comprises contributions from the backscattered wave. The complex IQ signal enters into Eq. 2.14 using ensemble averaging with $n_{\mathrm{fft}} = 256$ (c.f. Sec. 2.7).

Figure 7.9 plots the maxima of the absolute of the normalized cross-correlation functions. Again, due to computational constraints, only the outer radial position is considered. Similar to the experiment and the reduced synthetic diagnostic on GENE, Lorentzian functions recover the shape of the spatial decay better than Gaussian functions. Figure 7.9 thus plots Lorentzian functions and uses the same weights for fitting as in the experiment and above. The data obtained from fullwave simulations shows more deviations from the Lorentzian shape than in Fig. 7.8. This partially goes back to the fact that the fullwave simulations lack statistics, since the GENE analysis shown above uses averaging over five samples instead of one sample. In addition, the short time window of the simulation might cause very low frequency oscillations, such as, for instance, zonal flows, to have cycle durations comparable to the total simulation time and thus impose systematic errors. Furthermore, it shall be mentioned that a scan of the input fluctuation amplitude for IPF-FD3D (not shown) found that the results from fullwave simulations highly depend on the absolute turbulence level. A detailed investigation is left for future studies, whereas this thesis highlights the satisfying agreement between experiment and fullwave simulations, the latter having been run for the first time with IPF-FD3D on GENE simulations for the purpose of correlation length analysis.

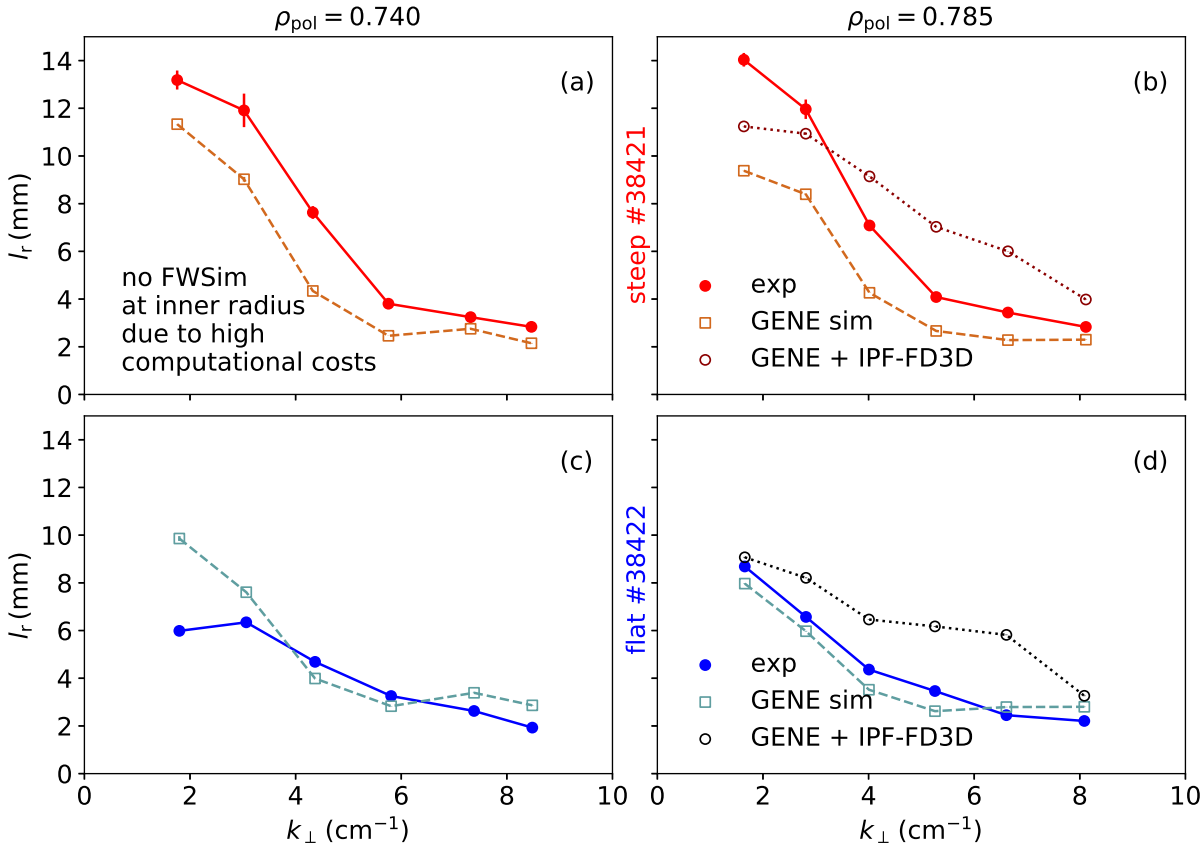


**Figure 7.10:** Radial correlation length versus the inverse turbulence structure size, for both scenarios (rows) and radii (columns). Experimental measurements as full symbols/solid line, IPF-FD3D supported analysis of GENE output as open circles/dotted line, pointwise analysis of GENE turbulence fields as open squares/dashed line.

Figure 7.10 shows the comparison between experiment and simulation of the radial correlation lengths, i.e. the HWHM of the Lorentzian fit functions, for both radii and scenarios. The decrease of $l_r$ with $k_\perp$ is in line with experiment and other experimental [187, 193] and simulation works [220] who report a scale-dependent measurement of radially correlated Doppler reflectometers, rather than a measurement of an average turbulence correlation length. The correlation lengths from GENE simulations (squares) only slightly increase from the flat to the steep scenario, which agrees with the concurrent increase of $\rho_s$. Since Doppler reflectometers correlate finite volumes rather than infinitesimally small points, the experimental correlation lengths (full circles) in general exceed those from GENE [149]: in the steep scenario, Figs. 7.10(a),(b) $l_r$ from experiment exceeds $l_r$ from GENE. However, since in the flat scenario in Figs. 7.10(c),(d) the diagnostic response is more nonlinear than in the steep scenario, the measured $l_r$ is smaller [190] and matches the GENE simulations. The fullwave simulations depicted as open circles exhibit larger correlation lengths than $l_r$ from GENE. However, the fullwave simulations yield values somewhat larger than the experimental observations.

Figure 7.11 plots the data of Fig. 7.10 using $2\pi/l_r$ for the vertical axis. This way of presentation relates to a radial wavenumber. The lines in Fig. 7.11 indicate linear fits through the origin, labeled with the slope. The reduction of the slope from the flat to the steep scenario seen in

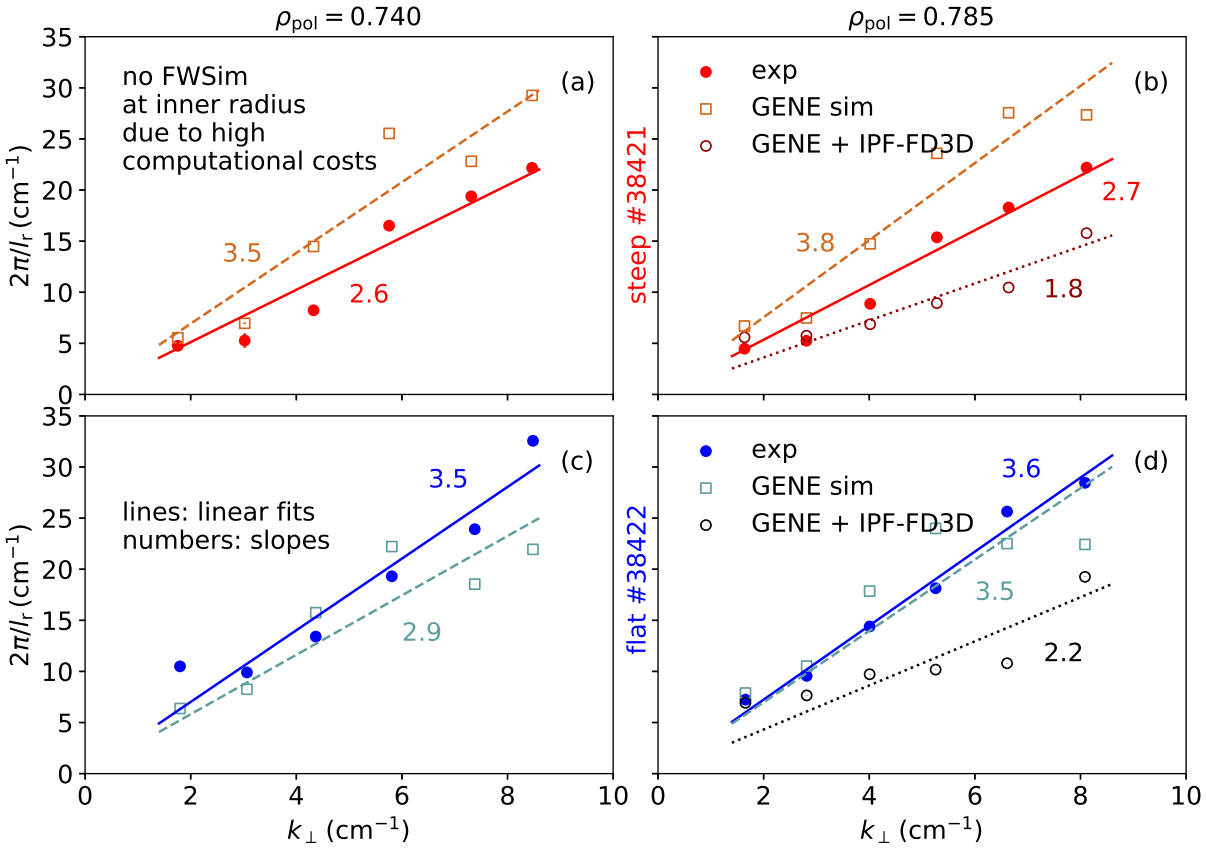


**Figure 7.11:** The inverse radial correlation length versus $k_\perp$ for both scenarios (rows) and radii (columns). These inverse radial and perpendicular structure sizes show an approximately linear relationship.

the experiment is not predicted by the pure GENE simulations. However, it is qualitatively recovered by synthetic diagnostic modeling.

In summary, the simulated values of $l_\mathrm{r}$ reasonably agree with that measured experimentally. Furthermore, the simulations recover the experimental reciprocal dependence of $l_r$ on $k_\perp$ and the weak radial dependence of $l_\mathrm{r}$. The experimentally observed trend of larger correlation lengths in the steep scenario is qualitatively modeled by the synthetic diagnostic, while pure GENE simulations predict no change. This analysis has been performed for the first time using IPF-FD3D on GENE turbulence. More detailed studies on synthetic modeling of radial correlation on Doppler reflectometry on gyrokinetic simulations, such as recently done for GYRO in Ref. [220], are desirable.

## 7.7 Eddy tilt and poloidally resolved velocity measurement of electron density fluctuations

The analysis of the eddy tilt angle from density fluctuations and the corresponding perpendicular velocity from GENE and IPF-FD3D are subject to a number of issues and is thus left open for

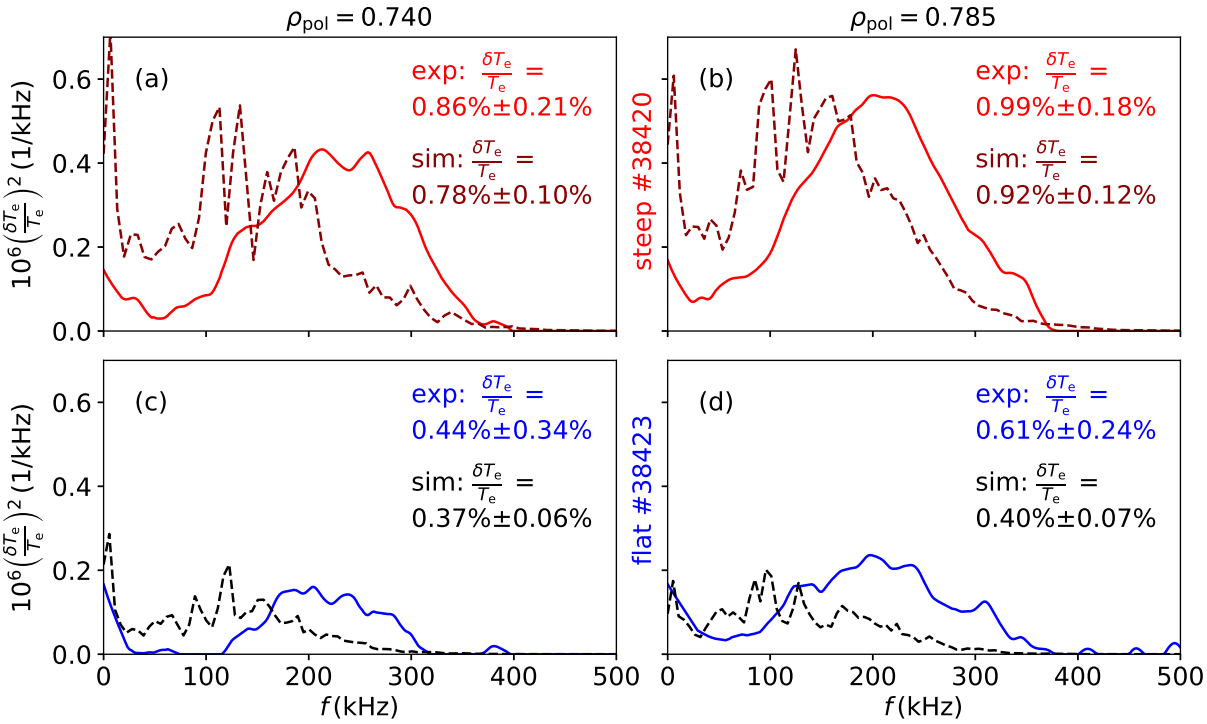


**Figure 7.12:** Simulated and experimental power spectra of electron temperature fluctuations for both scenarios and radii. Experimental measurements agree with GENE simulations.

further studies. For the tilt angle the limiting factor is probably lacking statistics (too short simulation times) as well as the time resolution of the GENE output, which is a factor of three more coarse than the DAQ sampling rates in the experiment.

On the velocity side, the IPF-FD3D runs to model the $k$-spectra cover a range of poloidal angles for the same radius and include synthetic velocity measurements. The Doppler spectra necessary to extract the velocity from the Doppler shift indicate consistent velocities between experiment and simulation for many data points. However, as discussed in Sec. 6.3 there are $k_\perp$ ranges where the position of the Doppler shifted peak in the spectrum of the backscattered wave is not clear, being likely an artifact of the short number of samples available from GENE and the resulting lacking statistical significance and noisy spectrum. Thus the analysis of the dependence of $v_\perp$ on the poloidal angle and the wavenumber needs a dedicated and detailed study, which is outside the scope of this thesis and left for future work.

## 7.8 Frequency spectrum and fluctuation amplitude of electron temperature fluctuations

The extraction of electron temperature fluctuation amplitudes from GENE turbulence requires synthetic CECE diagnostic modeling, which takes into account the extended spatial region from which each experimental CECE channel detects electron cyclotron radiation. The experimental

measurements of the fluctuation amplitudes (and radial correlation lengths) are carried out in sector 9. The specific antenna pattern serves as input into the ECRad code [120] to estimate the emission volumes. This procedure is picked up by a simultaneous validation work at AUG [118]. The synthetic CECE channels lie on the same line of sight as in the experiment, using the experimental radial channel separation. These measurement regions of the different CECE channels are indicated as black ellipses in Fig. 7.1(b) on top of the electron temperature fluctuation field from GENE, which denote the 1/e lines of the applied Gaussian filters. For a direct comparison with experiment one would correlate one of these channels with a neighboring channel and extract the coherence and thus the fluctuation amplitude. However, in order to improve statistics it is necessary to correlate all channels with their neighboring channel and extract the cross-power spectra using $n_{\mathrm{fft}} = 256$ number of samples for Fourier transformation and ensemble averaging with 50 % overlap.

The power spectra shown in Fig. 7.12 are the averages from correlating all channel-pairs shown in Fig. 7.1(b). This is justified since in flux-tube simulations radial variations are not considered. The noisy shape of the spectra is an artifact from the short time interval of the GENE runs. In compliance with the experimental analysis, the temperature fluctuation amplitude is the integral of the spectrum using the same boundaries as in the experimental data analysis performed in Sec. 6.7 (steep: 90–350 kHz, flat: 70–370 kHz). The uncertainties are the standard deviation from averaging the power spectra from all synthetic CECE channel pairs and thus give a lower limit of the total uncertainties. The fluctuation levels from both simulation and experiment quantitatively agree within uncertainties. They also consistently point out that temperature fluctuations increase with radius and with $R/L_{T_\mathrm{e}}$ from the flat to the steep scenario. This confirms reports that electron temperature fluctuations increase with $R/L_{T_\mathrm{e}}$ from DIII-D experiments [57, 173, 174], simulations with GYRO [214] and both [170, 171]. In addition, a radial increase of the fluctuation amplitude is reported for the core of AUG [118, 119], DIII-D [58, 180] and Alcator C-mod [214].

The experimental spectra show a stronger frequency shift than the simulation results. This is at variance with the velocity measurements from fullwave simulations (not shown) that match the experimental $v_\perp$ for most $k_\perp$. Note that Ref. [119] observed the reversed effect: a stronger shift in simulation than in experiment. Relating the electron temperature fluctuation amplitudes to simulated density fluctuation levels reveals $\delta T_\mathrm{e}/T_\mathrm{e} > \delta n_\mathrm{e}/n_\mathrm{e}$ in the steep scenario and $\delta T_\mathrm{e}/T_\mathrm{e} \approx \delta n_\mathrm{e}/n_\mathrm{e}$ in the flat scenario. This is in line with a range of past studies from DIII-D that report $\delta T_\mathrm{e}/T_\mathrm{e} > \delta n_\mathrm{e}/n_\mathrm{e}$ [173, 174, 221], $\delta T_\mathrm{e}/T_\mathrm{e} \gtrsim \delta n_\mathrm{e}/n_\mathrm{e}$ [58, 180] and $\delta T_\mathrm{e}/T_\mathrm{e} \approx \delta n_\mathrm{e}/n_\mathrm{e}$ [57]. Moreover, $\delta T_\mathrm{e}/T_\mathrm{e} > \delta n_\mathrm{e}/n_\mathrm{e}$ is found in GYRO simulations based on an Alcator C-mod plasma [214]. In conclusion, there is good quantitative agreement between the simulated and the experimentally measured electron temperature fluctuation amplitudes. The simulations recover both the increase of $\delta T_\mathrm{e}/T_\mathrm{e}$ with radius and with $R/L_{T_\mathrm{e}}$ seen in experiment.

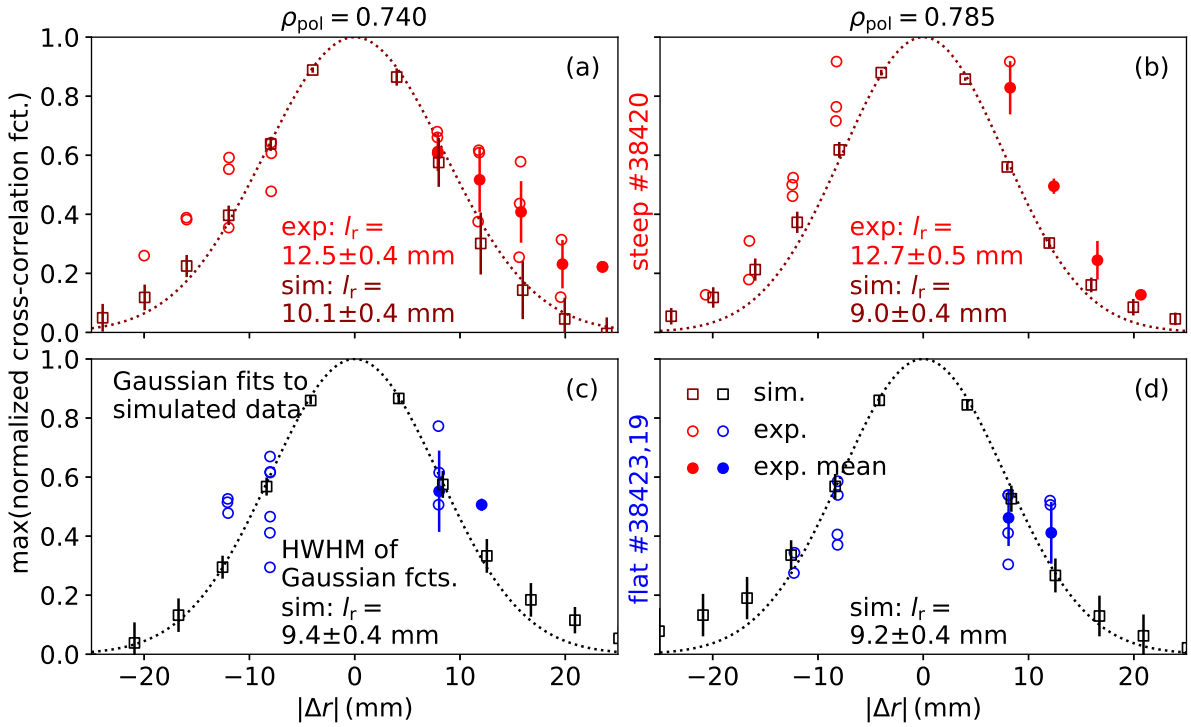


**Figure 7.13:** Radial decorrelation of electron temperature fluctuations and radial correlation lengths in experiment and simulation. The HWHM of the Gaussian fits on simulation slightly underestimate the experimental values. The correlation length for both scenarios and radii is the same in the simulation.

## 7.9 Radial correlation length of electron temperature fluctuations

The analysis of the radial correlation length of electron temperature fluctuations from GENE equals the extraction of $l_r$ of density fluctuations in terms of synthetic diagnostic modeling. The synthetic diagnostic signals from channels at different spatial distance up to channels pairs with five intermediate other channels are correlated using Eq. 2.14. Note that the GENE simulations do not include thermal noise, thus, the standard correlation procedure is applied. In line with experiment, the approximation $\max(c(\tau)) \approx c(\tau = 0)$ is applied. The mean values of $\max(c(\tau))$ from 10 channel pairs of each spatial separation along the experimental line of sight are plotted in Fig. 7.13 together with their standard deviation. Whereas in the experiment it is undecided whether a Gaussian or Lorentzian function recovers the trend of decorrelation better, here it is a Gaussian function that best fits the spatial decay of $\max(c(\tau))$. The corresponding HWHM of these fits and the experimental HWHM from Gaussian fits as written in Fig. 7.13 quantify that the simulation slightly underpredicts the experimental values of $l_r$. Both experiment and simulation agree that the correlation length does not change between the two radii. The GENE simulations additionally predict the flat scenarios to have a somewhat smaller correlation length than the steep scenario that likely sources from the difference in $\rho_s$. The difference of radial correlation lengths between scenarios is, however, within uncertainties.

Comparing the correlation length of temperature and density fluctuations indicates similar values for both domains. The $l_r$ from CECE includes scales up to $k_\perp \lesssim 3.3$–$4.1\,\mathrm{cm}^{-1}$ and thus compares

best to low $k_\perp$ measurements with Doppler reflectometry. The corresponding radial correlation length of density fluctuations from GENE is $8.3-10.6$ mm (c.f. Fig. 7.10), which is in the same range as radial correlation lengths of the electron temperature (c.f. Fig. 7.13). To my knowledge, these are the first comparisons between experiment and simulation touching radial correlation lengths in both density and temperature domains. The finding of similar electron temperature fluctuation correlation lengths for the steep and flat scenario supports reports from Alcator C-Mod [222] that study the dependence of $l_\mathrm{r}$ on the heat flux.

## 7.10 Cross-phase between electron density and temperature fluctuations

The extraction of the cross-phase between electron density and temperature fluctuations from GENE output requires the synthetic modeling of a reflectometer and a CECE channel. The line of sight through the plasma for $\alpha_{nT}$ measurements is shown in Fig. 6.7(b). The CECE spotsizes are an estimate of the vacuum antenna characteristics (vertical extent) and of the finite filter bandwidth of the CECE hardware (radial extent). The reflectometer spotsize is assumed identical in vertical direction, since the reflectometer beam uses the same launching/receiving mirror as the CECE. Following other AUG studies on the cross-phase [118, 119], the reflectometer spotsize in radial direction is approximated by the CECE spotsize as well. This assumption sources from the fact that the spectral resolution is determined by the smaller volume [33], in this case that of the CECE. Dedicated fullwave simulations on these scenarios confirm the wider radial extent of the reflectometer. In addition, a variation of the radial reflectometer width in the synthetic diagnostic from the CECE spotsize up to the largest possible radial extent that still lies within the GENE turbulence grid imposes only negligible changes on the cross-phase (not shown). This finding suggests that both O-mode and X-mode reflectometry would measure similar cross-phases if their only difference was the reflectometer beam size. Whereas for the present study, identical reflectometer and CECE spotsizes are used, an improved future approach could be to multiply the shape of the weighting function from fullwave simulations on the GENE turbulence to obtain a synthetic reflectometer timetrace. The most comprehensive solution would be to simulate the IQ signals with IPF-FD3D and correlate those with the CECE timetraces. Computational limitations, however, restrict to the procedure presented above as also used in the other experiment-simulation comparisons of the cross-phase on AUG [118, 119].

The solid lines in Figs. 7.14(a),(b) depict the cross-power spectra for both scenarios and radii (due to lacking statistics, the GENE runs do not permit to calculate the coherence). Their shape agrees with that of the experimentally measured coherence in (i). The cross-phases shown in (c),(d) confirm the experimental observation (j) that the cross-phase does not change between the scenarios. Following the discussion from Sec. 7.8 the statistics for extraction of $\alpha_{nT}$ are improved by averaging over 50 synthetic reflectometer and CECE channels that are equidistantly distributed along the experimental line of sight. This analysis uses $n_\mathrm{fft} = 256$ samples for Fourier transform and ensemble averaging with 50 % overlap. Note that Figs. 7.14(c),(d) assume the

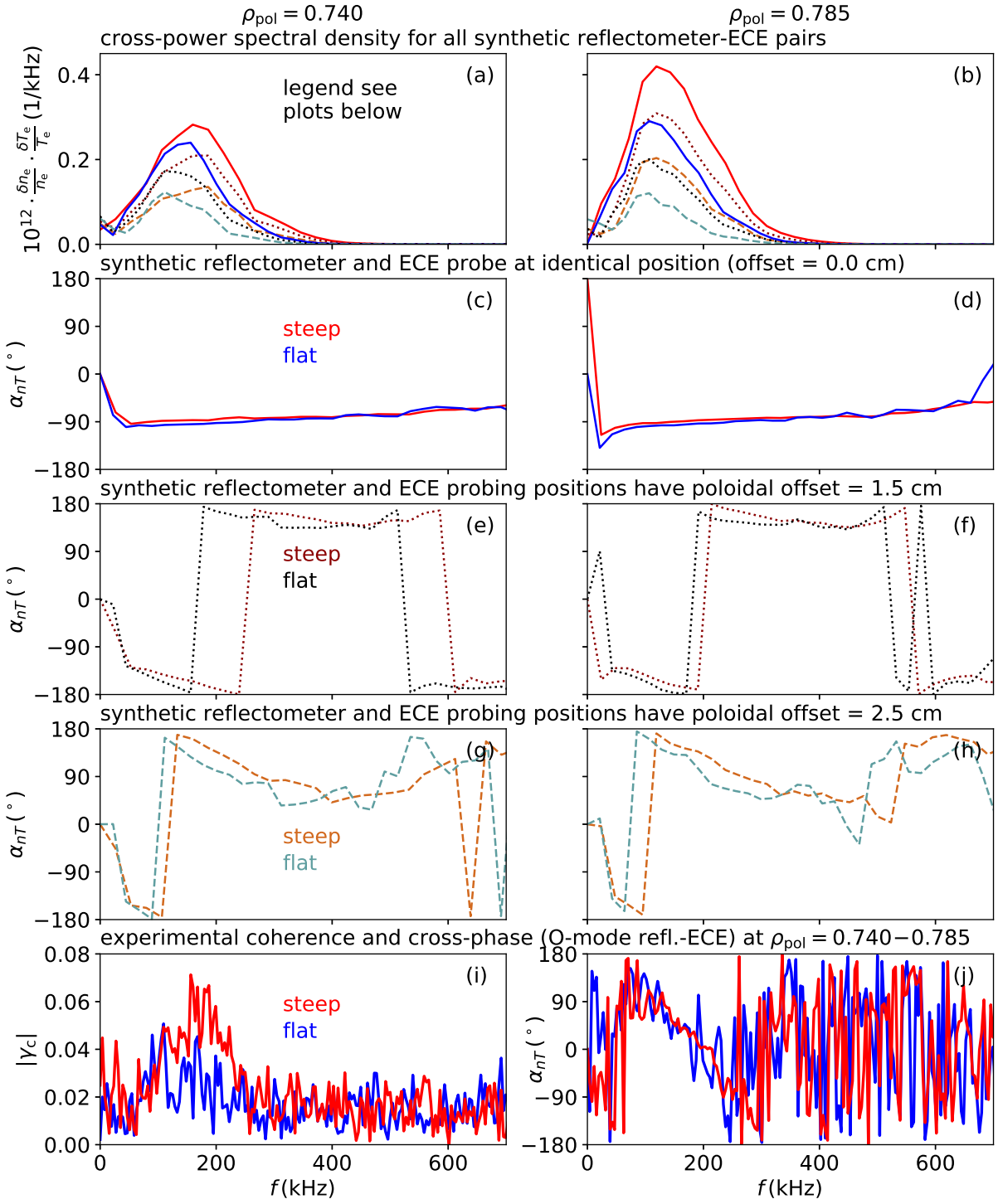


**Figure 7.14:** The cross-power spectra between simulated electron density and temperature fluctuations (a),(b) and the cross-phase (c)–(f) for both plasma scenarios and radii of interest. The middle row assumes the reflectometer and radiometer to probe at the same spatial location, the bottom row tackles cases where the density and temperature measurement locations are poloidally separated. The cross-phase does not change between scenarios. The bottom row shows the experimental measurements with O-mode reflectometry for $\rho_{pol} = 0.740-0.785$.

reflectometer and the ECE to probe at the exact same poloidal position, which is not the case in the experiment: ray tracing and LOS analysis predict a poloidal distance of 1.5 cm between reflectometer and CECE (c.f. Fig. 6.7(b)) whereas the phase-ramping of the cross-phase suggests a larger distance of 2.5 cm (c.f. Sec. 6.9). Figure 7.14 thus also includes the corresponding cross-phases (e)–(h) and power cross-power spectra (a),(b) for these two cases in dotted lines (offset=1.5 cm) and dashed lines (offset=2.5 cm). The poloidal offsets modify $\alpha_{nT}$ such that it agrees better with the experimental trend in (j). Note that the cross-phase in (j) is not defined in regions of low coherence in (i). However, the exact shape of the experimental observation in (j) is not recovered.

This thesis therefore restricts to the statement that both experiment and simulation consistently see that the cross-phase between electron density and temperature fluctuations does not change between the steep and the flat scenario. A detailed investigation and characterization of the ramping observed in experiment is left to future work, such as for instance done at DIII-D using gyrokinetic modeling with GYRO [58]. The conclusion to not see a change in the cross-phase between the steep and flat scenario is at variance with past reports that see $\alpha_{nT}$ to react on changes of the underlying kinetic gradients and turbulence. Changes up to 50 % were seen in DIII-D experiments and concurring GYRO simulations [58], as well as in dedicated GENE runs [200]. Slightly smaller changes were observed in DIII-D when varying $T_\mathrm{e}/T_\mathrm{i}$ [180]. Reference [173] observed marginal changes of the cross-phase with changes in gradient for low $1/L_{T_\mathrm{e}}$, whereas for larger $1/L_{T_\mathrm{e}}$ the cross-phase can significantly change even for variations in $1/L_{T_\mathrm{e}}$ on the order of a few percent. The normalized gradients in the study of this thesis, however, lie in the region where [173] reported significant changes.

## 7.11 Summary and discussion of overall match

The good agreement between the experimental measurements and the GENE simulations on a remarkable number of quantities in the two plasma scenarios highlights that contemporary turbulence models succeed in describing and understanding turbulence on a profound level. The accurate prediction of several turbulence features by GENE is a key element for successful fusion reactor designs including turbulence optimization. Plenty of validation works use metrics to quantify the agreement between experiment and gyrokinetic simulations. The commonly used metric introduced by Ref. [223] compares single values of turbulence quantities weighted within a primacy hierarchy between experiment and simulation, taking into account uncertainties of both measurement and modeling. However, a comparison of single values can only capture parts of the observed features (or cannot be applied to the $k$-spectra and $\alpha_{nT}$). In particular, it does not include trends between the two plasma scenarios, which are precisely designed to further constrain the validation. Thus, instead of applying a metric that excludes several interesting features, here, the match of all turbulence quantities between experiment and simulation, focusing additionally on the dependence of the fluctuations on frequency and shape, respectively, as well as the difference between steep and flat scenario and radial trends, is discussed in words. Still,

table 7.1 lists some key properties for comparison between experiment and simulation. This table, however, is only a rough overview and does not capture all of the detailed features of the different quantities, which will be discussed below.

The measured *wavenumber spectra of electron density fluctuations* show larger fluctuation amplitude in the flat than in the steep scenario for a wide range of intermediate scales, whereas at low and high $k_\perp$ the fluctuation amplitudes of both scenarios is similar. GENE consistently predicts the increase of density fluctuations at intermediate scales for decreasing $R/L_{T_\mathrm{e}}$ and $R/L_{n_\mathrm{e}}$. The raw GENE data do not model the curved experimental spectral shape, but rather show a linear dependence between fluctuation power and wavenumber (in a double-logarithmic scale). Only synthetic diagnostic modeling, i.e. fullwave simulations using the IPF-FD3D code on GENE turbulence, reproduce the curved shape. They additionally recover the increase of fluctuations at intermediate $k_\perp$ and the difference between O-mode and X-mode polarization. The curvature of the IPF-FD3D spectra is, however, larger than in the experiment. Both experiment and simulation agree on the radial increase of the fluctuation level.

The experimentally measured *radial correlation length of electron density fluctuations* decreases with $k_\perp$, which is consistent with both direct analysis of GENE turbulence fields and applying fullwave simulations to them. Experiment and simulations additionally agree that the spatial decorrelation of turbulence follows a Lorentzian function. The direct GENE analysis tends to reproduce the experimental measurements better than GENE including the fullwave simulations, which, however, cannot be excluded to be an artifact of low statistics. Whereas the correlation length from GENE only slightly changes with $R/L_{T_\mathrm{e}}$ and $R/L_{n_\mathrm{e}}$, experiment and fullwave simulations see a lower $l_\mathrm{r}$ in the flat scenario. This is probably due to the nonlinear diagnostic response of Doppler reflectometry. Both scenarios do not show a difference between the two radii, which is consistent between experiment and simulations.

The *electron temperature fluctuation amplitude* increases with $R/T_\mathrm{e}$ in both experiment and simulation and additionally matches quantitatively for both scenarios and radii. In line with density fluctuations it increases radially. The spectra from experiment are more Doppler shifted than the simulated spectra.

The *radial correlation length of electron temperature fluctuations* is the quantity of largest uncertainties in the experiment, which manifests itself in the way of spatial decorrelation: whereas Gaussian fits describe the decorrelation in the simulation, in the experiment it is sometimes a Gaussian or Lorentzian that fits the steep scenario data better, while in the flat scenario there is too few data to fit. Simulations slightly underestimate the measured correlation length in the steep scenario. In line with correlation lengths from density fluctuations GENE does not see any change between the flat and the steep scenario.

Both simulation and experiment consistently do not see any change of the *cross-phase between electron density and temperature fluctuations* from one scenario to the other. In the experiment the cross-phase ramps with frequency, which mostly sources from a poloidal offset of the measurement volumes. Introducing the experimental offset into the synthetic diagnostic modeling

causes the simulated cross-phase to tend towards the experimental ramping. For measurements using O-mode reflectometry the coherence between electron density and temperature fluctuations peaks at similar frequencies in both experiment and simulation. Correlation between ECE and X-mode reflectometry shows coherent features at the same frequency, but in addition a second peak at larger frequencies appears, which is not understood.

In summary, GENE remarkably well reproduces the qualitative trends between the flat and the steep scenario for all the investigated quantities where a comparison is possible. In addition, it matches various quantitative characteristics of all of them, leaving only a small number of features where a discrepancy between experiment and simulation persists.

| | | Experiment | | | | | | | | | | |
|---|---|---|---|---|---|---|---|---|---|---|---|---|
| | | normalized gradient ($m^{-1}$) | | | heat flux (MW) | | electron density fluct. | | | electron temperature fluct. | | cross-phase |
| | | $R/L_{n_e}$ | $R/L_{T_e}$ | $R/L_{T_i}$ | $Q_e$ | $Q_i$ | $k$-spectrum | $\delta n_e/n_e$ | $l_r$ (cm) | $\delta T_e/T_e$ (%) | $l_r$ (cm) | $\alpha_{n,T}$ (°) |
| $\rho_{pol,in}$ | steep | 4.8 | 13.4 | 7.9 | 0.7 | 0.8 | weak curvature | low | 0.3–1.3 | 0.9 | 1.3 | same value |
| | flat | 3.8 | 10.7 | 7.4 | 0.3 | 0.8 | intermediate curvature | high | 0.2–0.6 | 0.4 | - | |
| $\rho_{pol,out}$ | steep | 5.0 | 13.8 | 9.1 | 0.7 | 0.9 | weak curvature | low | 0.3–1.4 | 1.0 | 1.3 | |
| | flat | 3.6 | 10.9 | 8.8 | 0.2 | 0.9 | intermediate curvature | high | 0.2–0.9 | 0.6 | - | |
| see Fig. | | 6.4 | | | 6.5 | | 6.9 | 6.9 | 6.14 | 6.18 | 6.19 | 6.21 |
| | | GENE with synthetic diagnostics | | | | | | | | | | |
| $\rho_{pol,in}$ | steep | 4.8 | 12.0 | 7.1 | 1.1 | 1.1 | intermediate curvature | low | - (no FW sim) | 0.8 | 1.0 | $\approx -90$ |
| | flat | 3.4 | 7.5 | 7.4 | 0.5 | 0.9 | strong curvature | high | | 0.4 | 0.9 | $\approx -90$ |
| $\rho_{pol,out}$ | steep | 5.0 | 12.4 | 8.2 | 0.9 | 1.0 | intermediate curvature | low | 0.4–1.1 | 0.9 | 0.9 | $\approx -90$ |
| | flat | 3.6 | 7.6 | 8.8 | 0.5 | 1.0 | strong curvature | high | 0.3–0.9 | 0.4 | 0.9 | $\approx -90$ |
| see Fig. | | 7.3 | | | 7.3 | | 7.7 | 7.7 | 7.10 | 7.12 | 7.13 | 7.14 |

**Table 7.1:** Overview of some of the experimental (top) and simulated (bottom) values of turbulence quantities. It includes both radii and scenarios. Note that this list is intended only for a rough overview, but does not capture all of the detailed features of the different quantities, which are listed in the text of Chaps. 6 and 7 and in particular in the summary section, Sec. 7.11.

# 8 Conclusion and summary

Turbulence is the main driver of heat and particle transport in fusion plasmas and thus determines the performance of future fusion reactors. A detailed understanding of turbulence is necessary to predict the reactor size. The simulation codes used for modeling need to reliably predict the physics processes and turbulence behavior. This implies that they have been validated against existing experiments. The present work shows an encouraging example of code validation, where a remarkable number of measured physics quantities simultaneously agreed with predictions of the gyrokinetic code GENE. The number of parameters that were simultaneously compared exceeded that of past validation studies. In addition, the comparison included different plasma scenarios with different normalized gradients to further constrain the code and improve validation. In particular, two plasma scenarios with different normalized electron temperature gradients were comprehensively investigated experimentally. They were termed *steep* and *flat* electron temperature gradient scenario, where the normalized electron temperature gradient in the steep scenario exceeded the one in the flat scenario. Both, the quantitative predictions of GENE as well as the trends between the different scenarios showed excellent agreement with experimental measurements. The latter were performed with Doppler reflectometry measuring the electron density fluctuations and correlation electron cyclotron emission radiometry measuring the electron temperature fluctuations. A key element for the comparison was the extensive use of a fullwave code for synthetic diagnostic modeling on the simulated turbulence.

The main results and conclusions from the comparison were as follows:

The *normalized gradients* of electron temperature and electron density were found to increase from the flat to the steep scenario, whereas those of the ion temperature and toroidal rotation velocity remained mostly unchanged. Accordingly, the *ion heat flux* of both scenarios was similar, but the *electron heat flux* increased by more than a factor of two from the flat to the steep scenario. The final choice of the varied normalized gradients used as GENE input reproduced the trends of the experimental heat fluxes. However, further gradient variations or the inclusion of an impurity species would be desirable to obtain a better match in the electron heat flux.

The *wavenumber spectra of electron density fluctuations* were found to differ in shape between the two plasma scenarios. Surprisingly, the flat scenario exhibited higher fluctuation levels than the steep scenario for a wide range of scales. At large scales the spectral index of the steep scenario was larger than in the flat scenario, whereas for small scales it was the other way around. GENE consistently modeled these qualitative trends between the scenarios. The raw GENE data show a less curved spectrum than in experiment, but fullwave simulations with the IPF-FD3D code

on the GENE output confirmed the experimentally observed curvature of the spectrum. The average spectral decay was, however, somewhat stronger than the experiment.

The *electron temperature fluctuation amplitude* could only be provided for large scales. The fluctuation amplitude in the steep scenario exceeded the one in the flat scenario by a factor of two, which was consistent between experiment and simulation and reproduced the trend in the electron heat flux. The experimental frequency power spectrum had a similar spectral shape as in simulation. It peaked at higher frequencies, which points to a different perpendicular velocity.

The *radial correlation length of electron density fluctuations* was found to decrease with $k_\perp$. This indicated a correlation between the radial and poloidal eddy size. The flat scenario exhibited a smaller correlation length than the steep scenario, which was in line with the broader $k$-spectrum in the flat scenario. The experimentally measured correlation length was close to, but slightly smaller than the ones from both GENE and GENE including IPF-FD3D. The radial decay of the experimental and simulated correlation coefficients followed a Lorentzian function rather than a Gaussian. To sum up, the results of this first-of-its-kind extraction of the correlation length using IPF-FD3D on GENE agreed remarkably well with experimental data.

The experimental *radial correlation length of electron temperature fluctuations* of the steep scenario was slightly underestimated by the simulation. For the flat scenario, an experimental determination was not possible, but simulations found a similar value as in the steep scenario. The radial decay of the simulated correlation coefficients followed a Gaussian function rather than a Lorentzian, which is at variance with the observation for density fluctuations. Whether the decay of the experimental correlation coefficients in general follows either of these functions was difficult to determine due to the scatter of the data. Similar correlation lengths in $T_\mathrm{e}$ and $n_\mathrm{e}$ were found in both experiment and simulation.

The *cross-phase between electron density and electron temperature fluctuations* was found to remain unaffected from the underlying plasma scenario in both experiment and simulation. Its ramping with frequency was mainly related to a poloidal offset between the measurement locations of density and temperature, but hampered the comparison of an absolute value.

Furthermore, the *propagation velocity of electron density fluctuations perpendicular to the magnetic field* followed the poloidal trend of the $E \times B$ drift velocity for both scenarios. Due to a lack of statistics the velocity was not extracted from GENE runs directly. First fullwave simulations with IPF-FD3D on GENE turbulence showed promising initial results, but were too preliminary to be included.

The experimentally measured *tilt angle of turbulent electron density eddies* did not change between the scenarios. However, this feature has not been compared to gyrokinetic simulations, since there an extraction was not possible, likely due to lacking statistics impeding the extraction of time delays from correlation.

In addition to the validation effort described above, the poloidal dependence of the propagation velocity of electron density fluctuations perpendicular to the magnetic field was investigated for a variety of L-mode discharges using an X-mode Doppler reflectometer. In an extended poloidal region the velocity was found to only follow the poloidal dependence of the $E \times B$ drift velocity. Moreover, the full range of turbulence scales covered propagated at that same velocity. The impact of uncertainties of ray tracing on artificial asymmetries was investigated in a sensitivity study for both X-mode and O-mode polarization. Misalignment of the measurement hardware as well as an incorrect reconstruction of the magnetic equilibrium or the density profile were discussed to potentially introduce asymmetries outside the error bars. The artificial asymmetries were particularly pronounced for a wrong estimation of the injection angle when probing close to the midplane, as well as highly sensitive to the choice of the density profile. Whereas the velocity deviations caused by the first were systematic and observable over all radial regions, the distortion was more localized and potentially different on a shot to shot basis for the latter.

## Outlook

Even though the present study did everything to maximize the complexity of the validation efforts, there are several options for further enhancement, of which some shall be highlighted in the following.

First, there are some questions that remained open for single quantities. The analysis of the radial correlation lengths of density fluctuations left the question open, where the second peak in the spectrum of the Doppler reflectometer comes from. Furthermore, a study on the decreasing correlation length for increasing $\rho_s$ in the flat scenarios with additional heating power would be desirable. Regarding the cross-phase, a future investigation of the strong ramping with frequency would be of interest, in particular comparing measurements of both O-mode and X-mode reflectometry. Note that currently efforts are ongoing to build a combination of a reflectometer and a CECE radiometer that will routinely measure the cross-phase in AUG [224]. Moreover, the diagnostic effect of Doppler reflectometry that causes an underestimation of the perpendicular velocity could be further experimentally investigated by simultaneous measurements of $k$-spectra and the variation of $v_\perp$ with $k_\perp$ in different plasma scenarios.

Second, additional GENE runs could be done, such as simulations of the six additional scenarios with even steeper and flatter normalized gradients, new runs of the two original scenarios to obtain better matching of the heat fluxes and runs with longer time intervals to see if the improved statistics enable a consistent extraction of the time delay in correlation. Note that currently ongoing runs for three species will be analyzed. Finally, it would be interesting to also compare to global GENE [75] runs.

Another obvious extension of these validation efforts is the inclusion of more diagnostics and consequently more turbulence observables, which need to be simultaneously matched by the code. The poloidal correlation reflectometer [111] and two recently installed diagnostics, a W-band

comb-Doppler reflectometer [225] and a top launch Doppler reflectometer [168] could be used. In addition, the experiments in this thesis could potentially validate a variety of other gyrokinetic codes (c.f. Sec. 2.8 for a list). Note that currently dedicated runs with the fluid turbulence code TGLF [21] on both scenarios are ongoing. Furthermore, turbulence measurements in the steep gradient region of the pedestal could be compared to GENE or other edge specific turbulence codes. Finally, (further) modeling of the perpendicular velocity and cross-phase measurements with fullwave simulations would be desirable.

# Bibliography


[1] World meterological organisation. *State of Climate in 2021: Extreme events and major impacts.* [Online; 16. Mar. 2022]. URL: https://public.wmo.int/en/media/press-release/state-of-climate-2021-extreme-events-and-major-impacts.

[2] N. E. Stork. "Re-assessing current extinction rates". In: *Biodivers. Conserv.* 19 (2010), p. 357.

[3] European Environment Agency. *Greenhouse gas emissions by aggregated sector.* [Online; 27. Nov. 2020]. URL: https://www.eea.europa.eu/data-and-maps/daviz/ghg-emissions-by-aggregated-sector-5#tab-dashboard-02.

[4] Q. Meng. "The impacts of fracking on the environment: A total environmental study paradigm". In: *Sci. Total Environ.* 580 (2017), p. 953.

[5] A. E. Maczulak. *Renewable energy: sources and methods.* Infobase Publishing, 2010.

[6] J. Ongena et al. "Magnetic-confinement fusion". In: *Nat. Phys.* 12 (2016), p. 398.

[7] M. Asplund et al. "The chemical composition of the Sun". In: *Annu. Rev. Astron. Astrophys.* 47 (2009).

[8] H.-S. Bosch and G. M. Hale. "Improved formulas for fusion cross-sections and thermal reactivities". In: *Nucl. Fusion* 32 (1992), p. 611.

[9] J. D. Lawson. "Some criteria for a power producing thermonuclear reactor". In: *Proceedings of the physical society. Section B* 70 (1957), p. 6.

[10] U. Stroth. *Plasmaphysik. Phänomene, Grundlagen und Anwendungen.* Springer Spektrum, 2018.

[11] EUROfusion. *European Research Roadmap to the Realisation of Fusion Energy.* [Online; 27. Nov. 2020]. URL: https://www.euro-fusion.org/eurofusion/roadmap/.

[12] D. van Houtte et al. "Recent fully non-inductive operation results in Tore Supra with 6 min, 1 GJ plasma discharges". In: *Nucl. Fusion* 44 (2004), p. L11.

[13] A. Bock et al. "Non-inductive improved H-mode operation at ASDEX Upgrade". In: *Nucl. Fusion* 57 (2017), p. 126041.

[14] F. Wagner et al. "Regime of Improved Confinement and High Beta in Neutral-Beam-Heated Divertor Discharges of the ASDEX Tokamak". In: *Phys. Rev. Lett.* 49 (1982), p. 1408.

[15] Max Planck Institute for Plasmaphysics. *ASDEX Upgrade Introduction.* [Online; 27. Nov. 2020]. URL: https://www.ipp.mpg.de/16208/einfuehrung.

[16] P. C. Liewer. "Measurements of microturbulence in tokamaks and comparisons with theories of turbulence and anomalous transport". In: *Nucl. Fusion* 25 (1985), p. 543.

[17] A. J. Wootton et al. "Fluctuations and anomalous transport in tokamaks". In: *Phys. Fluids B: Plasma Physics* 2 (1990), p. 2879.

[18] F. Jenko et al. "Electron temperature gradient driven turbulence". In: *Phys. Plasma* 7 (2000), p. 1904.

[19] J. Candy and R. E. Waltz. "An Eulerian gyrokinetic-Maxwell solver ". In: *J. Comput. Phys.* 186 (2003), p. 545.

[20] G. M. Staebler, J. E. Kinsey, and R. E. Waltz. "Gyro-Landau fluid equations for trapped and passing particles". In: *Phys. Plasma* 12 (2005), p. 102508.

[21] G. M. Staebler, J. E. Kinsey, and R. E. Waltz. "A theory-based transport model with comprehensive physics". In: *Phys. Plasma* 14 (2007), p. 055909.

[22] B. D. Scott. "Edge turbulence and its interaction with the equilibrium". In: *Contrib. Plasma Phys.* 46 (2006), p. 714.

[23] A. Kendl, B. D. Scott, and T. T. Ribeiro. "Nonlinear gyrofluid computation of edge localized ideal ballooning modes". In: *Phys. Plasma* 17 (2010), p. 072302.

[24] M. Greenwald. "Verification and validation for magnetic fusion". In: *Phys. Plasma* 17 (2010), p. 058101.

[25] X. Lapillonne et al. "Nonlinear quasisteady state benchmark of global gyrokinetic codes". In: *Phys. Plasma* 17 (2010), p. 112321.

[26] R. Bravenec et al. "Benchmarking the GENE and GYRO codes through the relative roles of electromagnetic and E x B stabilization in JET high-performance discharges". In: *Plasma Phys. Controlled Fusion* 58 (2016), p. 125018.

[27] T. Görler et al. "Intercode comparison of gyrokinetic global electromagnetic modes". In: *Phys. Plasma* 23 (2016), p. 072503.

[28] G. Merlo et al. "Cross-verification of the global gyrokinetic codes GENE and XGC". In: *Phys. Plasma* 25 (2018), p. 062308.

[29] P. W. Terry et al. "Validation in fusion research: Towards guidelines and best practices". In: *Phys. Plasma* 15 (2008), p. 062503.

[30] A. E. White. "Validation of nonlinear gyrokinetic transport models using turbulence measurements". In: *J. Plasma Phys.* 85 (2019).

[31] A. E. White et al. "Simultaneous measurement of core electron temperature and density fluctuations during electron cyclotron heating on DIII-D". In: *Phys. Plasma* 17 (2010), p. 020701.

[32] A. E. White et al. "A correlation electron cyclotron emission diagnostic and the importance of multifield fluctuation measurements for testing nonlinear gyrokinetic turbulence simulations". In: *Rev. Sci. Instrum.* 79 (2008), p. 103505.

[33] R. V. Bravenec and A. J. Wootton. “Effects of limited spatial resolution on fluctuation measurements (invited)”. In: *Rev. Sci. Instrum.* 66 (1995), p. 802.

[34] T. Happel et al. “Comparison of detailed experimental wavenumber spectra with gyrokinetic simulation aided by two-dimensional full-wave simulations”. In: *Plasma Phys. Controlled Fusion* 59 (2017), p. 054009.

[35] C. Lechte et al. “X mode Doppler reflectometry k-spectral measurements in ASDEX Upgrade: experiments and simulations”. In: *Plasma Phys. Controlled Fusion* 59 (2017), p. 075006.

[36] C. Holland et al. “Implementation and application of two synthetic diagnostics for validating simulations of core tokamak turbulence”. In: *Phys. Plasma* 16 (2009), p. 052301.

[37] P. Manz. “The Microscopic Picture of Plasma Edge Turbulence”. Habilitation. Technische Universität München, 2018.

[38] A. N. Kolmogorov. “The Local Structure of Turbulence in Incompressible Viscous Fluid for Very Large Reynolds Numbers”. In: *Dokl. Akad. Nauk SSSR* 30 (1941). (reprinted in Proc. R. Soc. Lond. A **434**, 9 (1991)), p. 301.

[39] R. H. Kraichnan. “Inertial Ranges in Two-Dimensional Turbulence”. In: *Phys. Fluids* 10 (1967), p. 1417.

[40] T. Happel. “Doppler Reflectometry in the TJ-II Stellarator: Design of an Optimized Doppler Reflectometer and its Application to Turbulence and Radial Electric Field Studies”. PhD thesis. Universidad Carlos III de Madrid, 2010.

[41] A. Fujisawa. “A review of zonal flow experiments”. In: *Nucl. Fusion* 49 (2009), p. 013001.

[42] G. D. Conway, A. I. Smolyakov, and T. Ido. “Geodesic Acoustic Modes in magnetic confinement devices”. In: *Nucl. Fusion* 62 (2021), p. 013001.

[43] B. Coppi, M. N. Rosenbluth, and R. Z. Sagdeev. “Instabilities due to temperature gradients in complex magnetic field configurations”. In: *Phys. Fluids* 10 (1967), p. 582.

[44] W. Horton. “Drift waves and transport”. In: *Rev. Mod. Phys.* 71 (1999), p. 735.

[45] T. Görler and F. Jenko. “Scale Separation between Electron and Ion Thermal Transport”. In: *Phys. Rev. Lett.* 100 (2008), p. 185002.

[46] E. Mazzucato et al. “Short-Scale Turbulent Fluctuations Driven by the Electron-Temperature Gradient in the National Spherical Torus Experiment”. In: *Phys. Rev. Lett.* 101 (2008), p. 075001.

[47] B. B. Kadomtsev and O. P. Pogutse. “Trapped particles in toroidal magnetic systems”. In: *Nucl. Fusion* 11 (1971), p. 67.

[48] J. Weiland, A. B. Jarmen, and H. Nordman. “Diffusive particle and heat pinch effects in toroidal plasmas”. In: *Nucl. Fusion* 29 (1989), p. 1810.

[49] P. Manz et al. “Velocimetry analysis of type-I edge localized mode precursors in ASDEX Upgrade”. In: *Plasma Phys. Controlled Fusion* 56 (2014), p. 035010.

[50] P. Manz et al. “On the phase velocity in between weak and strong plasma edge turbulence”. In: *Plasma Phys. Controlled Fusion* 60 (2018), p. 085002.

[51] V. D. Shafranov. “Equilibrium of a toroidal pinch in a magnetic field”. In: *At. Energy* 13 (1963), p. 1149.

[52] G. D. Conway et al. “Suppression of Plasma Turbulence During Optimized Shear Configurations in JET”. In: *Phys. Rev. Lett.* 84 (2000), p. 1463.

[53] P. W. Terry. “Suppression of turbulence and transport by sheared flow”. In: *Rev. Mod. Phys.* 72 (2000), p. 109.

[54] P. Manz, M. Ramisch, and U. Stroth. “Physical Mechanism behind Zonal-Flow Generation in Drift-Wave Turbulence”. In: *Phys. Rev. Lett.* 103 (2009), p. 165004.

[55] U. Stroth, P. Manz, and M. Ramisch. “On the interaction of turbulence and flows in toroidal plasmas”. In: *Plasma Phys. Controlled Fusion* 53 (2011), p. 024006.

[56] P. H. Diamond and Y.-B. Kim. “Theory of mean poloidal flow generation by turbulence”. In: *Phys. Fluids B* 3 (1991), p. 1626.

[57] A. E. White et al. “Measurements of core electron temperature and density fluctuations in DIII-D and comparison to nonlinear gyrokinetic simulations”. In: *Phys. Plasma* 15 (2008), p. 056116.

[58] A. E. White et al. “Measurements of the cross-phase angle between density and electron temperature fluctuations and comparison with gyrokinetic simulations”. In: *Phys. Plasma* 17 (2010), p. 056103.

[59] G. R. Tynan, A. Fujisawa, and G. McKee. “A review of experimental drift turbulence studies”. In: *Plasma Phys. Controlled Fusion* 51 (2009), p. 113001.

[60] J. R. Pinzón Acosta et al. “Enhanced Doppler reflectometry power response: physical optics and 2D full wave modelling”. In: *Plasma Phys. Controlled Fusion* 59 (2017), p. 035005.

[61] E. Z. Gusakov, M. A. Irzak, and A. Yu Popov. “Radial correlation reflectometry at oblique probing wave incidence (linear scattering theory predictions)”. In: *Plasma Phys. Controlled Fusion* 56 (2014), p. 025009.

[62] T. Dannert. “Gyrokinetische Simulation von Plasmaturbulenz mit gefangenen Teilchen und elektromagnetischen Effekten”. PhD thesis. Technische Universität München, 2005.

[63] T. Görler. “Multiscale Effects in Plasma Microturbulence”. PhD thesis. Universität Ulm, 2009.

[64] D. Told. “Gyrokinetic Microturbulence in Transport Barriers”. PhD thesis. Universität Ulm, 2012.

[65] T. Dannert and F. Jenko. “Gyrokinetic simulation of collisionless trapped-electron mode turbulence”. In: *Phys. Plasma* 12 (2005), p. 072309.

[66] *Gyrokinetic Electromagnetic Numerical Experiment.* [Online; 30. Mar. 2022]. URL: `http://genecode.org/`.

[67] J. Candy, E. A. Belli, and R. V. Bravenec. "A high-accuracy Eulerian gyrokinetic solver for collisional plasmas". In: *J. Comput. Phys.* 324 (2016), p. 73.

[68] A. G. Peeters et al. "The nonlinear gyro-kinetic flux tube code GKW". In: *Comput. Phys. Commun.* 180 (2009), p. 2650.

[69] V. Grandgirard et al. "Computing ITG turbulence with a full-f semi-Lagrangian code". In: *Commun. Nonlinear Sci. Numer. Simul.* 13 (2008), p. 81.

[70] B. F. McMillan et al. "Long global gyrokinetic simulations: Source terms and particle noise control". In: *Phys. Plasma* 15 (2008), p. 052308.

[71] M. Maurer et al. "GENE-3D: A global gyrokinetic turbulence code for stellarators". In: *J. Comput. Phys.* 420 (2020), p. 109694.

[72] G. Jost et al. "Global linear gyrokinetic simulations in quasi-symmetric configurations". In: *Phys. Plasma* 8 (2001), p. 3321.

[73] A. Stegmeir et al. "GRILLIX: a 3D turbulence code based on the flux-coordinate independent approach". In: *Plasma Phys. Controlled Fusion* 60 (2018), p. 035005.

[74] D. Michels et al. "GENE-X: A full-f gyrokinetic turbulence code based on the flux-coordinate independent approach". In: *Comput. Phys. Commun.* 264 (2021), p. 107986.

[75] T. Görler et al. "The global version of the gyrokinetic turbulence code GENE". In: *J. Comput. Phys.* 230 (2011), p. 7053.

[76] F. Jenko et al. "Global and local gyrokinetic simulations of high-performance discharges in view of ITER". In: *Nucl. Fusion* 53 (2013), p. 073003.

[77] F. Merz. "Gyrokinetic simulation of multimode plasma turbulence". PhD thesis. Westfälische Wilhelms-Universität Münster, 2008.

[78] B. Streibl et al. "Chapter 2: Machine design, fueling, and heating in ASDEX Upgrade". In: *Fusion Sci. Technol.* 44 (2003), p. 578.

[79] J. Wesson. *Tokamaks*. New York: Oxford University Press Inc., 2004.

[80] J. P. Freidberg. *Plasma physics and fusion energy*. Cambridge university press, 2008.

[81] W. M. Stacey. *Fusion plasma physics*. John Wiley & Sons, 2008.

[82] Y. Kazakov, D. Van Eester, and J. Ongena. "Plasma heating in present-day and future fusion machines". In: *12th Carolus Magnus Summer School on Plasma and Fusion Energy Physics* (2015).

[83] V. Erckmann and U. Gasparino. "Electron cyclotron resonance heating and current drive in toroidal fusion plasmas". In: *Plasma Phys. Controlled Fusion* 36 (1994), p. 1869.

[84] E. Speth. "Neutral beam heating of fusion plasmas". In: *Rep. Prog. Phys.* 52 (1989), p. 57.

[85] R. Koch. "Plasma heating by neutral beam injection". In: *Fusion Sci. Technol.* 45 (2004), p. 183.

[86] S. S. Denk et al. "Analysis of electron cyclotron emission with extended electron cyclotron forward modeling". In: *Plasma Phys. Controlled Fusion* 60 (2018), p. 105010.

[87] H. Murmann et al. “The Thomson scattering systems of the ASDEX Upgrade tokamak”. In: *Rev. Sci. Instrum.* 63 (1992), p. 4941.

[88] A. Mlynek et al. “Design of a digital multiradian phase detector and its application in fusion plasma interferometry”. In: *Rev. Sci. Instrum.* 81 (2010), p. 033507.

[89] J. Schweinzer et al. “Reconstruction of plasma edge density profiles from Li I (2s-2p) emission profiles”. In: *Plasma Phys. Controlled Fusion* 34 (1992), p. 1173.

[90] M. Willensdorfer et al. “Characterization of the Li-BES at ASDEX Upgrade”. In: *Plasma Phys. Controlled Fusion* 56 (2014), p. 025008.

[91] R. J. Fonck. “Charge exchange recombination spectroscopy as a plasma diagnostic tool”. In: *Rev. Sci. Instrum.* 56 (1985), p. 885.

[92] E. Viezzer et al. “High-resolution charge exchange measurements at ASDEX Upgrade”. In: *Rev. Sci. Instrum.* 83 (2012), p. 103501.

[93] M. Cavedon et al. “A fast edge charge exchange recombination spectroscopy system at the ASDEX Upgrade tokamak”. In: *Rev. Sci. Instrum.* 88 (2017), p. 043103.

[94] A. Lebschy. “Experimental characterization of the core plasma flow at the ASDEX Upgrade tokamak”. PhD thesis. Technische Universität München, 2018.

[95] K. Brau et al. “Plasma rotation in the PDX tokamak”. In: *Nucl. Fusion* 23 (1983), p. 1643.

[96] R. E. Bell et al. “Comparison of poloidal velocity measurements to neoclassical theory on the National Spherical Torus Experiment”. In: *Phys. Plasma* 17 (2010), p. 082507.

[97] C. Chrystal et al. “Calculation of impurity poloidal rotation from measured poloidal asymmetries in the toroidal rotation of a tokamak plasma”. In: *Rev. Sci. Instrum.* 83 (2012), p. 10D501.

[98] A. Bortolon et al. “Indirect measurement of poloidal rotation using inboard–outboard asymmetry of toroidal rotation and comparison with neoclassical predictions”. In: *Nucl. Fusion* 53 (2013), p. 023002.

[99] R. Fischer et al. “Integrated Data Analysis of Profile Diagnostics at ASDEX Upgrade”. In: *Fusion Sci. Technol.* 58 (2010), p. 675.

[100] R. Fischer et al. “Estimation and Uncertainties of Profiles and Equilibria for Fusion Modeling Codes”. In: *Fusion Sci. Technol.* 76 (2020), p. 879.

[101] R. Fischer et al. “Magnetic equilibrium reconstruction using geometric information from temperature measurements at ASDEX Upgrade”. In: Proc. 40th EPS Conference on Plasma Physics, 2013.

[102] M. Bernert. “Analysis of the H-mode density limit in the ASDEX Upgrade tokamak using bolometry”. PhD thesis. Ludwig-Maximilians-Universität München, 2013.

[103] T. Happel et al. “Design of a new Doppler Reflectometer Front End for the ASDEX Upgrade Tokamak”. In: Padua, Italy: Proc. $10^{\text{th}}$ International Reflectometry Workshop, 2011.

[104] T. Happel et al. “The optimized steerable W-band Doppler reflectometer on ASDEX Upgrade: possibilities and issues”. In: Palaiseau, France: Proc. 11$^{\text{th}}$ International Reflectometry Workshop, 2013.

[105] S. J. Freethy et al. “Measurement of turbulent electron temperature fluctuations on the ASDEX Upgrade tokamak using correlated electron cyclotron emission”. In: *Rev. Sci. Instrum.* 87 (2016), p. 11E102.

[106] A. J. Creely et al. “Correlation electron cyclotron emission diagnostic and improved calculation of turbulent temperature fluctuation levels on ASDEX Upgrade”. In: *Rev. Sci. Instrum.* 89 (2018), p. 053503.

[107] H.-J. Hartfuß, T. Geist, and M. Hirsch. “Heterodyne methods in millimetre wave plasma diagnostics with applications to ECE, interferometry and reflectometry”. In: *Plasma Phys. Controlled Fusion* 39 (1997), p. 1693.

[108] H.-J. Hartfuß and T. Geist. *Fusion Plasma Diagnostics with mm-Waves*. Wiley-VCH, 2013.

[109] G. D. Conway et al. “Plasma rotation profile measurements using Doppler reflectometry”. In: *Plasma Phys. Controlled Fusion* 46 (2004), p. 951.

[110] A. Silva et al. “Ultrafast broadband frequency modulation of a continuous wave reflectometry system to measure density profiles on ASDEX Upgrade”. In: *Rev. Sci. Instrum.* 67 (1996), p. 4138.

[111] D. Prisiazhniuk et al. “Magnetic field pitch angle and perpendicular velocity measurements from multi-point time-delay estimation of poloidal correlation reflectometry”. In: *Plasma Phys. Controlled Fusion* 59 (2017), p. 025013.

[112] M. Weinlich and A. Carlson. “Flush mounted Langmuir probes in an oblique magnetic field”. In: *Phys. Plasma* 4 (1997), p. 2151.

[113] M. Griener et al. “Helium line ratio spectroscopy for high spatiotemporal resolution plasma edge profile measurements at ASDEX Upgrade”. In: *Rev. Sci. Instrum.* 89 (2018), p. 10D102.

[114] G. Birkenmeier et al. “Hardware developments and commissioning of the imaging heavy ion beam probe at ASDEX upgrade”. In: *Fusion Eng. Des.* 168 (2021), p. 112644.

[115] S. Sattler and H. J. Hartfuß. “Experimental evidence for electron temperature fluctuations in the core plasma of the W7-AS stellarator”. In: *Phys. Rev. Lett.* 72 (1994), p. 653.

[116] G. Cima et al. “Core temperature fluctuations and related heat transport in the Texas Experimental Tokamak-Upgrade”. In: *Phys. Plasma* 2 (1995), p. 720.

[117] C. Sung et al. “Changes in core electron temperature fluctuations across the ohmic energy confinement transition in Alcator C-Mod plasmas”. In: *Nucl. Fusion* 53 (2013), p. 083010.

[118] P. A. Molina Cabrera et al. “Changes in core electron temperature fluctuations and transport with isotopic mass in L-mode plasmas at ASDEX Upgrade”. In: *Plasma Phys. Controlled Fusion* (2022). to be submitted.

[119] S. J. Freethy et al. “Validation of gyrokinetic simulations with measurements of electron temperature fluctuations and density-temperature phase angles on ASDEX Upgrade”. In: *Phys. Plasma* 25 (2018), p. 055903.

[120] S. S. Denk et al. “ECRad: An electron cyclotron radiation transport solver for advanced data analysis in thermal and non-thermal fusion plasmas”. In: *Comput. Phys. Commun.* 253 (2020), p. 107175.

[121] E. Poli, A. G. Peeters, and G. V. Pereverzev. “TORBEAM, a beam tracing code for electron-cyclotron waves in tokamak plasmas”. In: *Comput. Phys. Commun.* 136 (2001), p. 90.

[122] E. Poli et al. “TORBEAM 2.0, a paraxial beam tracing code for electron-cyclotron beams in fusion plasmas for extended physics applications”. In: *Comput. Phys. Commun.* 225 (2018), p. 36.

[123] E. Holzhauer et al. “Theoretical and experimental investigation of the phase-runaway in microwave reflectometry”. In: *Plasma Phys. Controlled Fusion* 40 (1998), p. 1869.

[124] X. L. Zou et al. “Poloidal Rotation Measurement in Tore Supra by Oblique Reflectometry”. In: report EUR-CEA-FC-1674. Cadarache, France: Proc. 4$^{\text{th}}$ International Reflectometry Workshop, 1999.

[125] M. Hirsch et al. “Doppler reflectometry for the investigation of propagating density perturbations”. In: *Rev. Sci. Instrum.* 72 (2001), p. 324.

[126] M. Hirsch et al. “Doppler reflectometry for the investigation of propagating density perturbations”. In: *Plasma Phys. Controlled Fusion* 43 (2001), p. 1641.

[127] V. V. Bulanin et al. “Study of plasma fluctuations in the Tuman-3M tokamak using microwave reflectometry with an obliquely incident probing beam”. In: *Plasma Phys. Rep.* 26 (2000), p. 813.

[128] P. Hennequin et al. “Doppler backscattering system for measuring fluctuations and their perpendicular velocity on Tore Supra”. In: *Rev. Sci. Instrum.* 75 (2004), p. 3881.

[129] T. Happel et al. “Doppler reflectometer system in the stellarator TJ-II”. In: *Rev. Sci. Instrum.* 80 (2009), p. 073502.

[130] J. C. Hillesheim et al. “A multichannel, frequency-modulated, tunable Doppler backscattering and reflectometry system”. In: *Rev. Sci. Instrum.* 80 (2009), p. 083507.

[131] T. Tokuzawa et al. “Microwave Doppler reflectometer system in LHD”. In: *Rev. Sci. Instrum.* 83 (2012), p. 10E322.

[132] C. Zhou et al. “Recent Doppler Backscattering results from EAST tokamak”. In: *APS Division of Plasma Physics Meeting Abstracts*. Vol. 2013. 2013, TP8.

[133] J. C. Hillesheim et al. “Doppler backscattering for spherical tokamaks and measurement of high-k density fluctuation wavenumber spectrum in MAST”. In: *Nucl. Fusion* 55 (2015), p. 073024.

[134] T. Windisch et al. “Phased array Doppler reflectometry at Wendelstein 7-X”. In: *Rev. Sci. Instrum.* 89 (2018), p. 10H115.

[135] D. Carralero et al. “A feasibility study for a Doppler reflectometer system in the JT-60SA tokamak”. In: *Fusion Eng. Des.* 173 (2021), p. 112803.

[136] E. Viezzer et al. “High-accuracy characterization of the edge radial electric field at ASDEX Upgrade”. In: *Nucl. Fusion* 53 (2013), p. 053005.

[137] G. D. Conway et al. “Observations on core turbulence transitions in ASDEX Upgrade using Doppler reflectometry”. In: *Nucl. Fusion* 46 (2006), S799.

[138] T. Happel et al. “Core turbulence behavior moving from ion-temperature-gradient regime towards trapped-electron-mode regime in the ASDEX Upgrade tokamak and comparison with gyrokinetic simulation”. In: *Phys. Plasma* 22 (2015), p. 032503.

[139] G. R. McKee et al. “Impurity-induced turbulence suppression and reduced transport in the DIII-D tokamak”. In: *Phys. Plasma* 7 (2000), p. 1870.

[140] M. Hirsch et al. “Dynamics of poloidal flows and turbulence at the H-mode transition in W7-AS”. In: *Plasma Phys. Controlled Fusion* 48 (2006), S155.

[141] P. Hennequin et al. “Fluctuation spectra and velocity profile from Doppler backscattering on Tore Supra”. In: *Nucl. Fusion* 46 (2006), S771.

[142] E. Trier et al. “Radial electric field measurement in a tokamak with magnetic field ripple”. In: *Nucl. Fusion* 48 (2008), p. 092001.

[143] T. Estrada et al. “Sheared flows and transition to improved confinement regime in the TJ-II stellarator”. In: *Plasma Phys. Controlled Fusion* 51 (2009), p. 124015.

[144] G. D. Conway et al. “Assessment of Doppler reflectometry accuracy using full-wave codes with comparison to beam-tracing and analytic expressions”. In: Jülich, Germany: Proc. 12$^{\text{th}}$ International Reflectometry Workshop, 2015.

[145] G. D. Conway et al. “Recent progress in modelling the resolution and localization of Doppler reflectometry measurements”. In: Lausanne, Switzerland: Proc. 14$^{\text{th}}$ International Reflectometry Workshop, 2019.

[146] M. Hirsch and E. Holzhauer. “Doppler reflectometry with optimized temporal resolution for the measurement of turbulence and its propagation velocity”. In: *Plasma Phys. Controlled Fusion* 46 (2004), p. 593.

[147] V. Bulanin and M. Yafanov. “Spatial and spectral resolution of the plasma Doppler reflectometry”. In: *Plasma Phys. Rep.* 32 (2006), p. 47.

[148] Y Lin et al. “Plasma curvature effects on microwave reflectometry fluctuation measurements”. In: *Plasma Phys. Controlled Fusion* 43 (2001), p. L1.

[149] J. R. Pinzón Acosta. “Modelling and application of Doppler reflectometry for advanced turbulence studies on the ASDEX Upgrade tokamak and the TJ-II stellarator”. PhD thesis. Technische Universität München, 2018.

[150] P. Hennequin et al. “Analysis of density fluctuation frequency spectra in Tore Supra as a tool for studying plasma motion and transport properties”. In: ECA Vol. 23J, 3.006. Maastricht, Netherlands: Proc. 26$^{\text{th}}$ EPS Conference on Plasma Physics, 1999.

[151] C. Honoré et al. “Collective light scattering and instantaneous fluid velocity measurement”. In: *J. Atmos. Terr. Phys.* 58 (1996), p. 1025.

[152] G. V. Pereverzev. “Beam tracing in inhomogeneous anisotropic plasmas”. In: *Phys. Plasma* 5 (1998), p. 3529.

[153] J. R. Pinzón Acosta et al. “Experimental investigation of the tilt angle of turbulent structures in the core of fusion plasmas”. In: *Nucl. Fusion* 59 (2019), p. 074002.

[154] J. R. Pinzón Acosta et al. “Measurement of the tilt angle of turbulent structures in magnetically confined plasmas using Doppler reflectometry”. In: *Plasma Phys. Controlled Fusion* 61 (2019), p. 105009.

[155] E. Z. Gusakov and A. Y. Popov. “Two-dimensional non-linear theory of radial correlation reflectometry”. In: *Plasma Phys. Controlled Fusion* 46 (2004), p. 1393.

[156] A. Frank. “Impact of the Plasma Curvature and the Probing Beam Geometry on Doppler Reflectometer Velocity Measurements”. MA thesis. Technische Universität München, 2021.

[157] A. Frank et al. “Impact of the probing beam geometry and plasma curvature on Doppler reflectometry perpendicular velocity measurements”. In: *Plasma Phys. Controlled Fusion* (2022). to be submitted.

[158] C. Lechte. “Investigation of the Scattering Efficiency in Doppler Reflectometry by Two-Dimensional Full-Wave Simulations”. In: *IEEE Trans. Plasma Sci.* 37 (2009), p. 1099.

[159] C. Lechte et al. “Full-wave Doppler reflectometry simulations in 2D”. In: St. Petersburg, Russia: Proc. 8$^{\text{th}}$ International Reflectometry Workshop, 2007.

[160] A. Krämer-Flecken et al. “Poloidal rotation asymmetry and relation to turbulence”. In: vol. 36. Stockholm, Sweden: Proc. of the 39th EPS Conf. and 16th Int. Congress on Plasma Physics, 2012, P5.

[161] L. Vermare et al. “Poloidal asymmetries of flows in the Tore Supra tokamak”. In: *Phys. Plasma* 25 (2018), p. 020704.

[162] T. Estrada et al. “Turbulence and perpendicular plasma flow asymmetries measured at TJ-II plasmas”. In: *Nucl. Fusion* 59 (2019), p. 076021.

[163] K. Höfler et al. “Poloidally resolved measurements of the perpendicular propagation velocity of density fluctuations in ASDEX Upgrade L-mode plasmas”. In: *Plasma Phys. Controlled Fusion* 63 (2021), p. 035020.

[164] R. J. Groebner and T. H. Osborne. “Scaling studies of the high mode pedestal”. In: *Phys. Plasma* 5 (1998), p. 1800.

[165] P. A. Schneider. “Characterization and scaling of the tokamak edge transport barrier”. PhD thesis. Ludwig-Maximilians-Universität München, 2012.

[166] U. Plank. “The Effect of the Radial Electric Field around the Separatrix on the Access to the High Confinement Mode at ASDEX Upgrade”. PhD thesis. Ludwig-Maximilians-Universität München, 2021.

[167] P. J. McCarthy, P. Martin, and W. Schneider. *The CLISTE interpretive equilibrium code.* Tech. rep. Garching, Germany: IPP, 1999.

[168] G. D. Conway and P. Hennequin. *private communication (2022).*

[169] K. Höfler et al. "Study of poloidal asymmetries in the flow velocity perpendicular to the magnetic field of the ASDEX Upgrade tokamak". In: Lausanne, Switzerland: Proc. 14$^{\text{th}}$ International Reflectometry Workshop, 2019.

[170] J. C. DeBoo et al. "Probing plasma turbulence by modulating the electron temperature gradient". In: *Phys. Plasma* 17 (2010), p. 056105.

[171] C. Holland et al. "Testing gyrokinetic simulations of electron turbulence". In: *Nucl. Fusion* 52 (2012), p. 063028.

[172] C. Holland et al. "Validation studies of gyrofluid and gyrokinetic predictions of transport and turbulence stiffness using the DIII-D tokamak". In: *Nucl. Fusion* 53 (2013), p. 083027.

[173] J. C. Hillesheim et al. "Observation of a Critical Gradient Threshold for Electron Temperature Fluctuations in the DIII-D Tokamak". In: *Phys. Rev. Lett.* 110 (2013), p. 045003.

[174] J. C. Hillesheim et al. "Experimental characterization of multiscale and multifield turbulence as a critical gradient threshold is surpassed in the DIII-D tokamaka)". In: *Phys. Plasma* 20 (2013), p. 056115.

[175] C. Angioni et al. "Intrinsic Toroidal Rotation, Density Peaking, and Turbulence Regimes in the Core of Tokamak Plasmas". In: *Phys. Rev. Lett.* 107 (2011), p. 215003.

[176] R. J. Hawryluk. "An empirical approach to tokamak transport". In: *Physics of plasmas close to thermonuclear conditions.* Elsevier, 1981, p. 19.

[177] J. Breslau et al. *TRANSP.* Tech. rep. Princeton, NJ, United States: PPPL, 2018.

[178] A. Casati et al. "Turbulence in the TORE SUPRA Tokamak: Measurements and Validation of Nonlinear Simulations". In: *Phys. Rev. Lett.* 102 (2009), p. 165005.

[179] C. Bourdelle et al. "Collisionality scaling in Tore Supra: detailed energy confinement analysis, turbulence measurements and gyrokinetic modelling". In: *Nucl. Fusion* 51 (2011), p. 063037.

[180] T. L. Rhodes et al. "L-mode validation studies of gyrokinetic turbulence simulations via multiscale and multifield turbulence measurements on the DIII-D tokamak". In: *Nucl. Fusion* 51 (2011), p. 063022.

[181] M. W. Shafer et al. "2D properties of core turbulence on DIII-D and comparison to gyrokinetic simulations". In: *Phys. Plasma* 19 (2012), p. 032504.

[182] P. Hennequin et al. "Scaling laws of density fluctuations at high-k on Tore Supra". In: *Plasma Phys. Controlled Fusion* 46 (2004), p. B121.

[183] L. Vermare et al. "Wavenumber spectrum of micro-turbulence in tokamak plasmas". In: *C.R. Phys.* 12 (2011), p. 115.

[184] L. Vermare et al. "Impact of collisionality on fluctuation characteristics of micro-turbulence". In: *Phys. Plasma* 18 (2011), p. 012306.

[185] Ö. D. Gürcan et al. "Wave-Number Spectrum of Drift-Wave Turbulence". In: *Phys. Rev. Lett.* 102 (2009), p. 255002.

[186] Ö. D. Gürcan et al. "Shell models and the possibility of application to fusion plasmas". In: *Plasma Phys. Controlled Fusion* 52 (2010), p. 045002.

[187] J. Schirmer et al. "Radial correlation length measurements on ASDEX Upgrade using correlation Doppler reflectometry". In: *Plasma Phys. Controlled Fusion* 49 (2007), p. 1019.

[188] P. Hennequin et al. "Radial correlation of density fluctuations by coupling IPP and LPP W-band Doppler reflectometers on ASDEX Upgrade". In: Padova, Italy: Proc. 10$^{\text{th}}$ International Reflectometry Workshop, 2011.

[189] J. C. Hillesheim et al. "New plasma measurements with a multichannel millimeter-wave fluctuation diagnostic system in the DIII-D tokamak (invited)". In: *Rev. Sci. Instrum.* 81 (2010), p. 10D907.

[190] E. Blanco and T. Estrada. "Two-dimensional full-wave simulations of radial correlation Doppler reflectometry in linear and non-linear regimes". In: *Plasma Phys. Controlled Fusion* 55 (2013), p. 125006.

[191] G. R. McKee et al. "Non-dimensional scaling of turbulence characteristics and turbulent diffusivity". In: *Nucl. Fusion* 41 (2001), p. 1235.

[192] T. L. Rhodes et al. "Comparison of turbulence measurements from DIII-D low-mode and high-performance plasmas to turbulence simulations and models". In: *Phys. Plasma* 9 (2002), p. 2141.

[193] F. Fernández-Marina, T. Estrada, and E. Blanco. "Turbulence radial correlation length measurements using Doppler reflectometry in TJ-II". In: *Nucl. Fusion* 54 (2014), p. 072001.

[194] E. Mazzucato and R. Nazikian. "Radial scale length of turbulent fluctuations in the main core of TFTR plasmas". In: *Phys. Rev. Lett.* 71 (1993), p. 1840.

[195] R. Bielajew et al. "Edge turbulence measurements in L-mode and I-mode at ASDEX Upgrade". In: *Phys. Plasma* 29 (2022), p. 052504.

[196] S. J. Freethy et al. "Measurements of the density-temperature cross-phase angle of turbulent fluctuations at ASDEX Upgrade and comparison to theory". In: Lausanne, Switzerland: Proc. 14$^{\text{th}}$ International Reflectometry Workshop, 2019.

[197] F. Ryter et al. "Experimental evidence for gradient length-driven electron transport in tokamaks". In: *Phys. Rev. Lett.* 86 (2001), p. 2325.

[198] A. M. Dimits et al. "Comparisons and physics basis of tokamak transport models and turbulence simulations". In: *Phys. Plasma* 7 (2000), p. 969.

[199] J. Candy and R. E. Waltz. "Anomalous transport scaling in the DIII-D tokamak matched by supercomputer simulation". In: *Phys. Rev. Lett.* 91 (2003), p. 045001.

[200] T. Görler et al. "A flux-matched gyrokinetic analysis of DIII-D L-mode turbulence". In: *Phys. Plasma* 21 (2014), p. 122307.

[201] D. Told et al. “Characterizing turbulent transport in ASDEX Upgrade L-mode plasmas via nonlinear gyrokinetic simulations”. In: *Phys. Plasma* 20 (2013), p. 122312.

[202] R. E. Waltz, J. Candy, and R. V. Bravenec. “Revising the L-mode Edge Transport Shortfall with More Accurate Gyrokinetic Simulations”. In: *APS Division of Plasma Physics Meeting Abstracts*. Vol. 2017. 2017, TP11.

[203] U. Stroth et al. “Experimental turbulence studies for gyro-kinetic code validation using advanced microwave diagnostics”. In: *Nucl. Fusion* 55 (2015), p. 083027.

[204] C. Holland. “Validation metrics for turbulent plasma transport”. In: *Phys. Plasma* 23 (2016), p. 060901.

[205] N. T. Howard et al. “Quantitative comparison of experimental impurity transport with nonlinear gyrokinetic simulation in an Alcator C-Mod L-mode plasma”. In: *Nucl. Fusion* 52 (2012), p. 063002.

[206] A. E. White et al. “Multi-channel transport experiments at Alcator C-Mod and comparison with gyrokinetic simulations”. In: *Phys. Plasma* 20 (2013), p. 056106.

[207] C. Sung et al. “Quantitative comparison of electron temperature fluctuations to nonlinear gyrokinetic simulations in C-Mod Ohmic L-mode discharges”. In: *Phys. Plasma* 23 (2016), p. 042303.

[208] J. A. Heikkinen et al. “Full f gyrokinetic method for particle simulation of tokamak transport”. In: *J. Comput. Phys.* 227 (2008), p. 5582.

[209] S. Leerink et al. “Multiscale Investigations of Drift-Wave Turbulence and Plasma Flows: Measurements and Total-Distribution-Function Gyrokinetic Simulations”. In: *Phys. Rev. Lett.* 109 (2012), p. 165001.

[210] A. B. Altukhov et al. “Poloidal inhomogeneity of turbulence in the FT-2 tokamak by radial correlation Doppler reflectometry and gyrokinetic modelling”. In: *Plasma Phys. Controlled Fusion* 58 (2016), p. 105004.

[211] M. Kotschenreuther, G. Rewoldt, and W. M. Tang. “Comparison of initial value and eigenvalue codes for kinetic toroidal plasma instabilities”. In: *Comput. Phys. Commun.* 88 (1995), p. 128.

[212] F. van Wyk et al. “Ion-scale turbulence in MAST: anomalous transport, subcritical transitions, and comparison to BES measurements”. In: *Plasma Phys. Controlled Fusion* 59 (2017), p. 114003.

[213] A. J. Creely et al. “Perturbative thermal diffusivity from partial sawtooth crashes in Alcator C-Mod”. In: *Nucl. Fusion* 56 (2016), p. 036003.

[214] N. T. Howard et al. “Multi-scale gyrokinetic simulations: Comparison with experiment and implications for predicting turbulence and transport”. In: *Phys. Plasma* 23 (2016), p. 056109.

[215] J. Ruiz Ruiz et al. “Validation of gyrokinetic simulations of a National Spherical Torus eXperiment H-mode plasma and comparisons with a high-k scattering synthetic diagnostic”. In: *Plasma Phys. Controlled Fusion* 61 (2019), p. 115015.

[216] M. Kammerer, F. Merz, and F. Jenko. "Exceptional points in linear gyrokinetics". In: *Phys. Plasma (1994-present)* 15 (2008), p. 052102.

[217] X. Garbet et al. "Physics of transport in tokamaks". In: *Plasma Phys. Controlled Fusion* 46 (2004), B557.

[218] E. Fable, C. Angioni, and O. Sauter. "The role of ion and electron electrostatic turbulence in characterizing stationary particle transport in the core of tokamak plasmas". In: *Plasma Phys. Controlled Fusion* 52 (2010), p. 015007.

[219] T. Görler and F. Jenko. "Multiscale features of density and frequency spectra from nonlinear gyrokinetics". In: *Phys. Plasma* 15 (2008), p. 102508.

[220] J. Ruiz Ruiz et al. "Interpreting Radial Correlation Doppler Reflectometry using Gyrokinetic Simulations". In: *arXiv preprint arXiv:2201.06324* (2022).

[221] C. Holland et al. "Advances in validating gyrokinetic turbulence models against L- and H-mode plasmas". In: *Phys. Plasma* 18 (2011), p. 056113.

[222] A. E. White et al. "Feasibility study for a correlation electron cyclotron emission turbulence diagnostic based on nonlinear gyrokinetic simulations". In: *Plasma Phys. Controlled Fusion* 53 (2011), p. 115003.

[223] P. Ricci et al. "Approaching the investigation of plasma turbulence through a rigorous verification and validation procedure: A practical example". In: *Phys. Plasma* 22 (2015), p. 055704.

[224] R. Bielajew and C. Yoo. *private communication (2022).*

[225] T. Happel et al. "Design of a variable frequency comb reflectometer system for the ASDEX Upgrade tokamak". In: *Plasma Sci. Technol.* 22 (2020), p. 064002.

# A Acknowledgments

I would like to gratefully acknowledge the great help, which I received from my colleagues and friends.

First of all I would like to express my deep and sincere gratitude to my two main supervisors. Many thanks go to Ulrich Stroth, my academic supervisor, he gave me the great opportunity to work on plasma transport and turbulence since my Master thesis. I am very grateful for his continuous interest in my research and the valuable feedback and guidance. Additional great thanks go to Tim Happel, my daily supervisor, he accompanied my research and all my questions, be it concerning plasma physics, diagnostic's details or the soft-skill level. He introduced me to the huge and indispensable landscape of tools for ASDEX Upgrade data and supported and encouraged me to dig deep into my research. I honestly admire his patience and dedication in supervision and that I was always welcome in his office with all the time I needed.

I am particularly grateful to Pascale Hennequin, she deeply inspired and motivated me by patiently accompanying my first steps in Doppler reflectometry, diagnostic calibration, operation, data analysis and interpretation. My special thanks go to Pedro Molina Cabrera, his dedicated hardware work and discussions were crucial for the CECE measurements and analysis, in particular for the cross-phase on the hardware side and the correlation lengths on the analysis side.

I wish to acknowledge the help and dedication of Tobias Görler for running GENE and his continuous and time-consuming support in post-processing and discussion of results. I am additionally thankful and appreciate the time and effort of Carsten Lechte for the IPF-FD3D runs.

The advice and help provided by Anne White and Rachel Bielajew on CECE data analysis is greatly acknowledged. Special thanks go to Michael Bergmann and Rainer Fischer for their support on fitting the kinetic profiles. I would like to thank Garrard Conway and Elisee Trier for their support and discussions concerning Doppler reflectometry and poloidal correlation reflectometry. My sincere thanks go to Thomas Windisch for his immediate support on lending us the W7-X Doppler reflectometer for an extended time after hardware failure at ASDEX Upgrade. I am grateful for the inspiring discussions with Frank Jenko concerning the GENE comparison and for the helpful conversations with Gregor Birkenmeier and Peter Manz about turbulence in general. I would like to thankfully highlight the inspiring experience of (co-)supervising the theses of three TUM students, Antonia Frank, Florian Günzkofer and David Stockinger. In addition, the support of Elisabeth Wolfrum and Rachael McDermott on questions of any kind

concerning kinetic profiles has been of great help. Further thanks go to Matthias Willensdorfer and Wolfgang Suttrop for ECE related discussions. I would like to express my gratitude to Pierre David for providing me with the radiation profiles and to Philip Schneider for running TRANSP and Severin Denk for running ECRad. Additional thanks go to Martin Schubert and the ECRH group for their support. I would like to gratefully acknowledge Arne Kallenbach for his impressive management of ASDEX Upgrade operation with heart and mind. Additional thanks go to the experiment leaders and all other members of the ASDEX Upgrade team who are not mentioned in person. Furthermore, I would like to highly acknowledge Tim Happel, Ulrich Stroth, Tobias Görler, Jonathan Schilling, Michael Bergmann, Lieselotte J. Höfler and John Fitzurka for proof-reading the full/parts of this thesis.

Special acknowledgments go to the very helpful and kind team of technicians. In particular I would like to mention the great help of Johannes Friesen and Daniel Großmann with the in- and ex-vessel Doppler reflectometer hardware. Special gratitude goes to Michael Ebner and Wolfgang Zeidner for their tireless dedication in fixing a broken vacuum-flange crucial for Doppler reflectometer operation. The help with the data acquisition provided by Horst Eixenberger and his group, as well as the numerous support of the torus hall electricians around Maximilian Pichl is very much acknowledged. I would like to thank the IT team, in particular Christoph Fuchs, Antje Asbach, Michael Kölbl, Alexander Lenz, Roland Merkel, Annedore Buhler and Helmut Blank for their support. I wish to acknowledge the support of Biggy Perey and Gabriele Dörsch with several organizational matters.

I am deeply grateful for the fun time with a fantastic community of PhD researchers, postdocs or (young) permanent staff. Thank you so much for your support, your opinions, joking when things did not go as expected, evenings at Echinger See or Isar, etc. Risking to give an incomplete list, I would like to express my thanks to Michael Griener, Victoria Olevskaia, Michael Faitsch, Stephan Glöggler, Raheesty Devi Nem, Alexander Bock, Johannes Kurz, Christian Schuster, Francesco Sciortino and Andreas Redl and plenty of others who have been already acknowledged above. In addition, Daniel Wendler, my office mate with the largest temporal overlap, deserves special thanks for the great time I could spend with him. I would like to also thank Lennart Bock and Oleg Samoylov for their friendship and companionship during our time as PhD representatives. Furthermore, I wish to acknowledge the fun time while preparing for and performing at the IPP Christmas parties with several of the above mentioned colleagues and many more. :)

I am sincerely grateful for all the time I could spend with my friends outside IPP, in person or on the phone. They helped me enjoy all the other beautiful aspects of life outside work. Lastly, I would like express my deep thanks to my family for their unconditional support, their love and sympathy. I am incredibly grateful for their friendship and companionship. I would like to equally acknowledge the amazing support from my boyfriend, Jonathan Schilling. It is hard to decide which of the numerous facets to mention, thank you so much for all of them.